Numerical Investigation of Fluid Flow in Protruded Rotor-Stator Cavities

Elham Roshani Moghaddam

Submitted for the degree of Doctor of Philosophy

Thermo-Fluid Mechanics Research Centre

University of Sussex

Submitted: September 2014

Declaration

I hereby declare that this thesis has not been and will not be, submitted in whole or in part to another University for the award of any other degree.

Signature.....

Elham Roshani Moghaddam

September 2014

Acknowledgements

My deepest intellectual debts are owed to my supervisors, Professor Naser Sayma and Dr Christopher Long, for their support and professionalism. They always encouraged me to explore new directions in my thesis and they taught me how to develop my own ideas. They also taught me how to capture the reality. Their intellectual sharpness has shaped this research in numerous ways.

I would also like to thank my dear husband and parents for their love and compassions. I could not have completed this D.Phil without the support and encouragement of them.

University of Sussex

Elham Roshani Moghaddam

Submitted for the degree of Doctor of Philosophy

Numerical Investigation of Fluid Flow in Protruded Rotor-Stator Cavities

SUMMARY

The torque associated with overcoming the losses on a rotating disc is of particular importance to the designers of gas turbine engines. Not only does this represent a reduction in useful work, but it also gives rise to unwanted heating of metal surfaces and the adjacent fluid. This research presents a numerical study on the effect of rotor-mounted bolts on the moment coefficient and flow structure within a rotor–stator cavity under conditions representative of modern gas turbine engine design. Steady-state, two-dimensional and three-dimensional, computational fluid dynamics simulations are obtained using the FLUENT commercial code with a standard k-ε turbulence model. The model is firstly validated against experimental data and then used to study the effects of presence of rotor-mounted hexagonal bolts in the rotor-stator cavity under investigation using different dimensionless flow parameters. Also investigated were the effects of changing the number and size of rotor-mounted bolts on the flow structure and amount of losses for two test cases; one corresponding a throughflow dominated condition and the other corresponding a rotationally dominated one.

The simulation results showed that decreasing the throughflow rate reduces the area of the wake region causing the wakes to become more circumferential in their path around the

bolts. Also it was found that increasing the number and diameter of bolts respectively reduces and increases the area of the wake region. For N>18 a separation bubble forms above the bolt which its length increases with increasing the number of bolts.

The total moment coefficient of all bolts in the system increases with increasing the number of bolts. However, the rate of this increase reduces by mounting more bolts. While increasing the diameter of the bolts consistently increases the moment and drag coefficients for the rotationally dominated condition, for the throughflow dominated case an increase and a reduction was observed for respectively the moment and drag coefficients.

Index

1. CHAPTER 1: INTRODUCTION 1

1.1 PURPOSE OF THE STUDY 1

1.2 RESEARCH QUESTIONS 3

1.3 OVERVIEW OF THE THESIS 4

2. CHAPTER 2: REVIEW OF PREVIOUS WORK 7

2.1 INTRODUCTION 7

2.2 THEORETICAL AND EXPERIMENTAL INVESTIGATIONS 8

2.2.1 Rotating Disc Adjacent to a Quiescent Flow, Stationary Disc Adjacent to a Rotating Flow 10

2.2.2 Rotor-Stator Cavities 12

2.2.3 Rotor-Stator Cavities with Attached Protrusions 19

2.3 NUMERICAL METHODS 25

2.4 THE BOLT WINDAGE TEST RIG 27

2.5 SUMMARY 31

3. CHAPTER 3: COMPUTATIONAL MODEL VALIDATION 32

3.1 INTRODUCTION 32

3.2 SELECTING THE VALIDATION CASES 32

3.3 VALIDATION CASE NO. 1: EXPERIMENTAL MEASUREMENTS OF COREN (2007) 34

3.4 VALIDATION CASE NO.2: NUMERICAL ANALYSIS OF VAUGHAN (1987) 52

3.5 VALIDATION CASE NO.3: EXPERIMENTAL MEASUREMENTS OF DAILY ET AL. (1964) 58

3.6 SUMMARY 65

4. CHAPTER 4: PLAIN DISC SIMULATIONS 67

4.1 INTRODUCTION 67

4.2 SIMULATION PROCEDURE 67

4.3 TWO-SIDED CAVITY SIMULATIONS 70

4.4 PLAIN DISC FLOW STRUCTURE 75

4.5 MOMENT COEFFICIENT RESULTS 87

4.6 SUMMARY 91

5. CHAPTER 5: ROTOR-STATOR SYSTEM WITH MOUNTED BOLTS: INVESTIGATION OF THE EFFECTS OF FLOW CONDITION VARIATIONS 93

5.1 INTRODUCTION 93

5.2 SIMULATION SPECIFICATIONS OF THE BWR SYSTEM 94

5.3 FLOW STRUCTURE INVESTIGATION 96

5.3.1 Investigation of the effects of mounting protrusions on the flow structure out of the range of interference of the bolts 96

5.3.2 Investigation of the effects of mounting protrusions on the flow structure in the range of interference of the bolts for a specific flow condition 105

5.3.3 Investigation of the effects of changing the flow conditions on the flow structure in the range of interference of the bolt..... 121

5.4 INVESTIGATION OF BOLT DRAG COEFFICIENT 133

5.5 MOMENT COEFFICIENT VARIATIONS 137

5.6 THE STANDARD K-ε MODEL AND PROTRUSIONS 143

5.7 SUMMARY 146

6. ROTOR-STATOR SYSTEM WITH MOUNTED BOLTS: INVESTIGATION OF THE EFFECTS OF CHANGING THE NUMBER AND DIAMETER OF BOLTS 148

6.1 INTRODUCTION 148

6.2 INVESTIGATION OF THE VARIATIONS OF FLOW STRUCTURE AND THE AMOUNT OF LOSSES FOR A SPECIFIC DIAMETER AND DIFFERENT NUMBER OF BOLTS 148

6.2.1 Flow structure analysis 150

6.2.2 Moment and drag coefficients 163

6.3 INVESTIGATION OF THE VARIATIONS OF FLOW STRUCTURE AND AMOUNT OF LOSSES FOR A SPECIFIC NUMBER AND DIFFERENT DIAMETERS OF BOLTS 172

6.4 INVESTIGATION OF THE MOMENT AND DRAG COEFFICIENT VARIATIONS BY VARYING THE DIAMETER AND NUMBER OF BOLTS SIMULTANEOUSLY 182

6.5 INVESTIGATION OF THE VALIDITY OF EXPERIMENTAL MEASUREMENT ASSUMPTIONS: EQUAL AMOUNTS OF DISC MOMENT COEFFICIENTS FOR A SYSTEM WITH BOLTS AND A SYSTEM WITHOUT BOLTS 186

6.6 SUMMARY 190

7. CONCLUSIONS AND RECOMMENDATIONS FOR FUTURE WORK 192

7.1 INTRODUCTION 192

7.2 RECOMMENDATIONS FOR FUTURE WORK 199

REFERENCES 201

APPENDIX 1: CFD PROCEDURE 215

APPENDIX 2: TURBULENCE MODELLING 217

List of Figures

Figure 1.1: The Internal Air Paths in a Gas Turbine Engine, courtesy of Rolls-Royce plc. 2
Figure 2.1: Fluid Initially at Rest Adjacent to a Rotating Disc, from Schlichtling and Gersten (1999) 10
Figure 2.2: Rotating Fluid over a Stationary Disc, from Schlichtling and Gersten (1999) 12
Figure 2.3: Schematic Diagram of an Enclosed Rotor-Stator System 13
Figure 2.4: Schematic Diagram of the Bolt Windage Test Rig 30
Figure 2.5: Orientation of the Bolts with Respect to Rotation 31
Figure 3.1: Schematic Diagram of the Two-dimensional Simulated Geometry 36
Figure 3.2: Comparison between the Axial Distribution of Dimensionless Radial Velocity for Different Turbulence Models with the Experimental Data of Coren (2007) at r/b = 0.79; Re_ϕ = 0.81 x 10^7, C_w = 0.3 x 10^5 (λ_T = 0.09) 38
Figure 3.3: Comparison between Axial Distribution of Dimensionless Tangential Velocity for Different Turbulence Models with the Experimental Data of Coren (2007) at r/b = 0.79; Re_ϕ = 0.81 x 10^7, C_w = 0.3 x 10^5, (λ_T = 0.09) 39
Figure 3.4: Comparison between the Axial Distribution of Dimensionless Radial Velocity for Different Turbulence Models with the Experimental Data of Coren (2007) at r/b = 0.79; Re_ϕ = 0.271 x 10^7, C_w = 0.3 x 10^5, (λ_T = 0.21) 40
Figure 3.5: Comparison between the Axial distribution of Dimensionless Tangential Velocity for Different Turbulence Models with the Experimental Data of Coren (2007) at r/b = 0.79; Re_ϕ = 0.271 x 10^7, C_w = 0.3 x 10^5, (λ_T = 0.21) 41
Figure 3.6: Comparison of the Moment Coefficient Results of Different Turbulence Models with the Experimental Data of Coren (2007) 42
Figure 3.7: Simulation Results of Radial Velocity at r/b = 0.79 for Different near Wall Treatments, Using the Standard k-ε Model for Re_ϕ = 0.81 x 10^7, C_w = 0.3 x 10^5, (λ_T = 0.09) 44
Figure 3.8: Simulation Results of Tangential Velocity at r/b = 0.79 for Different near Wall Treatments, Using the Standard k-ε Model for Re_ϕ = 0.81 x 10^7, C_w = 0.3 x 10^5, (λ_T = 0.09) 44
Figure 3.9: Simulation Results of Radial Velocity at r/b = 0.79 for Different near Wall Treatments, Using the Standard k-ε Model for Re_ϕ = 0.271 x 10^7, C_w = 0.3 x 10^5, (λ_T = 0.21) 45
Figure 3.10: Simulation Results of Tangential Velocity at r/b = 0.79 for Different near Wall Treatments, Using the Standard k-ε Model for Re_ϕ = 0.271 x 10^7, C_w = 0.3 x 10^5, (λ_T = 0.21) 45
3.11:Comparison of the Radial Velocity for Different Inlet Pipe Lengths and Inlet Turbulent Intensities Using the Standard k-ε Model with Enhanced Wall Treatment for Re_ϕ = 0.81 x 107, C_w = 0.3 x 105, (λ_T = 0.09) at (a): r/b = 0.31, and (b) r/b = 0.79 47
Figure 3.12: Comparison of β at r/b = 0.5 for Different Turbulence Models; Re_ϕ = 8 x 10^5, C_w = 2000 56

Figure 4.1: Schematic Diagram of the Two-dimensional Simulated Geometry with a Cut of Generated Grids 69
Figure 4.2: Schematic Diagram of the Two-sided Simulated Geometry 71
Figure 4.3: Contribution to the Total Moment Coefficient Produced by the Different Rotating Components in the Simulated Two-sided Plain Disc Geometry, $C_w = 0.3 \times 10^5$....73
Figure 4.4: Contribution to the Total Moment Coefficient Produced by the Different Rotating Components in the Simulated Two-sided Plain Disc Geometry, $C_w = 10^5$ 74
Figure 4.5: Flow Streamlines for the Plain Disc System under Different Flow Conditions: .76
Figure 4.6: Tangential Velocity Distributions at the radial locations of r/b = 0.62 and r/b = 0.8 for:.....77
Figure 4.7: Radial Velocity Distributions at the radial locations of r/b = 0.62 and r/b = 0.8 for: 78
Figure 4.8: Axial Velocity Distributions at the radial locations of r/b = 0.62 and r/b = 0.8 for: 79
Figure 4.9: Variations of β / β^* with $\lambda_T(r/b)^{-13/5}$ 84
Figure 4.10: Radial Pressure Distribution for the Plain Disc System for the Flow Conditions of:.....85
Figure 4.11: Variation of Moment Coefficient with Rotational Reynolds number. Comparison between Numerical and Experimental Results for plain disc, $C_w = 0.3 \times 10^5$...87
Figure 4.12: Variation of Moment Coefficient with Turbulent Flow Parameter. Comparison between Numerical and Experimental Results for plain disc, $C_w = 0.3 \times 10^5$.....88
Figure 4.13: Variation of Moment Coefficient with Rotational Reynolds number. Comparison between Numerical and Experimental Results for plain disc, $C_w = 10^5$.....88
Figure 5.1: The Computational Domain Used for the Three-dimensional Simulations of the Protruded Rotor-Stator System with 18 Bolts, Showing the Mesh in: (a) r-ϕ Plane, and (b) r-z Plane.....95
Figure 5.2: Flow Streamlines for the Plain Disc and Protruded Disc Systems; $Re_\phi = 0.177 \times 10^7$, $C_w = 0.3 \times 10^5$, ($\lambda_T = 0.31$) 97
Figure 5.3: Flow Streamlines for the Plain Disc and Protruded Disc Systems; $Re_\phi = 0.72 \times 10^7$, $C_w = 0.3 \times 10^5$, ($\lambda_T = 0.09$) 98
Figure 5.4: Side view of the Rotor-Stator System with Bolts (The Two Radial Locations where Tangential and Radial Velocities Distributions were obtained are shown).....99
Figure 5.5: Comparison of the Dimensionless Tangential Velocity Distribution between the Plain Disc and Protruded Disc Systems for $Re_\phi = 0.177 \times 10^7$, $C_w = 0.3 \times 10^5$, ($\lambda_T = 0.31$) at (a) r/b =0.62 and (b) r/b = 0.8.....100
Figure 5.6: Comparison of the Dimensionless Tangential Velocity Distribution between the Plain Disc and Protruded Disc Systems for $Re_\phi = 0.72 \times 10^7$, $C_w = 0.3 \times 10^5$, ($\lambda_T = 0.09$) at (a) r/b =0.62 and (b) r/b = 0.8 101

Figure 5.7: Comparison of the Dimensionless Radial Velocity Distribution between the Plain Disc and Protruded Disc Systems for $Re_\phi = 0.177 \times 10^7$, $C_w = 0.3 \times 10^5$, ($\lambda_T = 0.31$) at (a) r/b =0.62 and (b) r/b = 0.8 102
Figure 5.8: Comparison of the Dimensionless Radial Velocity Distribution between the Plain Disc and Protruded Disc Systems for $Re_\phi = 0.72 \times 10^7$, $C_w = 0.3 \times 10^5$, ($\lambda_T = 0.09$) at (a) r/b =0.62 and (b) r/b = 0.8 103
Figure 5.9: Comparison of the Radial Pressure Distribution between the Plain Disc and Protruded Disc Systems for the Rotationally Dominated Condition ($Re_\phi = 0.72 \times 10^7$, $C_w = 0.3 \times 10^5$, ($\lambda_T = 0.09$)) and Throughflow Dominated Condition ($Re_\phi = 0.177 \times 10^7$, $C_w = 0.3 \times 10^5$, ($\lambda_T = 0.31$)) at z/s = 0.52 104
Figure 5.10: Relative Velocity Vectors around the Bolt at z/s = 0.045 for $Re_\phi = 0.177 \times 10^7$, $C_w = 0.3 \times 10^5$ ($\lambda_T = 0.31$) 107
Figure 5.11: Static Pressure Distribution on the Bolt Surface at z/s = 0.045 for $Re_\phi = 0.177 \times 10^7$, $C_w = 0.3 \times 10^5$ ($\lambda_T = 0.31$); (a) Pressure Coefficient Distribution, (b) Static Pressure Contour 108
Figure 5.12: ϕ-Wall Shear Stress Distribution on the Bolt Surface at z/s = 0.045 for $Re_\phi = 0.177 \times 10^7$, $C_w = 0.3 \times 10^5$ ($\lambda_T = 0.31$) 109
Figure 5.13: Total Relative Velocity Contour at z/s = 0.045 for $Re_\phi = 0.177 \times 10^7$, $C_w = 0.3 \times 10^5$ ($\lambda_T = 0.31$) 109
Figure 5.14: Relative Velocity Vectors around the Bolt for $Re_\phi = 0.177 \times 10^7$, $C_w = 0.3 \times 10^5$ ($\lambda_T = 0.31$) at (a): z/s = 0.4 and (b): z/s = 0.22 113
Figure 5.15: Pressure Coefficient Distribution on the Bolt Surface at z/s = 0.4 and z/s = 0.22 for $Re_\phi = 0.177 \times 10^7$, $C_w = 0.3 \times 10^5$ ($\lambda_T = 0.31$ 114
Figure 5.16: Total Relative Velocity Contour for $Re_\phi = 0.177 \times 10^7$, $C_w = 0.3 \times 10^5$ ($\lambda_T = 0.31$) at (a): z/s = 0.4 and (b): z/s = 0.22 116
Figure 5.17: Flow Streamlines around the Bolt for $Re_\phi = 0.177 \times 10^7$, $C_w = 0.3 \times 10^5$ ($\lambda_T = 0.31$) at (a) r/b = 0.92, (b) r/b = 0.89 and (c) r/b = 0.86 121
Figure 5.18: Comparison of Relative Velocity Vectors at z/s = 0.045 for Different Flow Conditions 126
Figure 5.19: Comparison of the Pressure Distribution around the Bolt at z/s = 0.045 between (a): $C_w = 0.3 \times 10^5$, $Re_\phi = 0.9 \times 10^7$, ($\lambda_T = 0.064$) and (b): $C_w = 0.3 \times 10^5$, $Re_\phi = 0.177 \times 10^7$ ($\lambda_T = 0.31$) 127
Figure 5.20: Comparison of the ϕ-wall Shear Stress Distribution around the Bolt at z/s = 0.045 between (a) $C_w = 0.3 \times 10^5$, $Re_\phi = 0.177 \times 10^7$ ($\lambda_T = 0.31$) and (b) $C_w = 0.3 \times 10^5$, $Re_\phi = 0.9 \times 10^7$, ($\lambda_T = 0.064$) 127

Figure 5.21: Comparison of the Pressure Distribution around the Bolt at z/s = 0.045 between (a): C_w = 0.3 x 10^5, Re_ϕ = 0.9 x 10^7, (λ_T = 0.064) and (b): C_w = 10^5, Re_ϕ = 0.9 x 10^7, (λ_T = 0.25).....128
Figure 5.22: Comparison of the ϕ-wall Shear Stress Distribution around the Bolt at z/s = 0.045 between (a): C_w = 10^5, Re_ϕ = 0.9 x 10^7, (λ_T = 0.25) and (b): C_w = 0.3 x 10^5, Re_ϕ = 0.9 x 10^7, (λ_T = 0.064).....128
Figure 5.23: Variations of the Drag Coefficient as a Function of Re_Δ. Comparison between the Drag Coefficient of Hexagonal Bolts Mounted on Rotor with the Drag Coefficient of Circular Cylinder and Sphere using the Results Obtained by Schlichting and Gersten (1999) 135
Figure 5.24: Variation of Moment Coefficient with Rotational Reynolds Number, C_w = 0.3 x 10^5.....137
Figure 5.25: Variation of Moment Coefficient with Turbulent Flow Parameter, C_w = 0.3 x 10^5.....138
Figure 5.26: Variation of Moment Coefficient with Rotational Reynolds Number, C_w = 10^5 138
Figure 5.27: Variation of Moment Coefficient with Turbulent Flow Parameter, C_w = 10^5.139
Figure 5.28: Comparison of the Drag Coefficient Obtained by the Simulation Results with Those Calculated Using Equation 5.7.....142
Figure 5.29: Comparison of the Pressure Distribution Predicted by the Standard k$-\varepsilon$ Model with that Predicted by the Realizable k-ε, SST-k-ω and RSM at *z/s* = 0.045; Re_ϕ = 0.27 x 10^7, C_w = 0.3 x 10^5 (λ_T = 0.22).....144
Figure 5.30: Comparison of the ϕ-Wall Shear Stress Distribution Predicted by the Standard k-ε Model with that Predicted by the Realizable k-ε, SST-k-ω and RSM at *z/s* = 0.045; Re_ϕ = 0.27 x 10^7, C_w = 0.3 x 10^5 (λ_T = 0.22) 144
Figure 6.1: Simulated Geometries for Different Number of Bolts in r-ϕ Plane.....150
Figure 6.2: Relative Velocity Vectors at z/s = 0.045 for Different Number of Bolts; Re_ϕ = 0.72 x 10^7 and C_w = 0.3 x10^5 (λ_T = 0.09) 152
Figure 6.3: Relative Velocity Vectors at z/s = 0.045 for Different Number of Bolts; Re_ϕ = 0.67 x 10^7 and C_w = 10^5 (λ_T = 0.35) 153
Figure 6.4: ϕ-wall Shear Stress Distribution on the Bolt at *z/s* = 0.045 for Re_ϕ = 0.67 x 10^7, C_w = 10^5 (λ_T= 0.35); *N* = 3, 18, 45 and 60 155
Figure 6.5: Pressure Coefficient Distribution on the Bolt at *z/s* = 0.045 for Re_ϕ = 0.67 x 10^7, C_w = 10^5 (λ_T = 0.35); *N* = 3, 18, 45 and 60.....156
Figure 6.6: ϕ-wall Shear Stress Distribution on the Bolt at *z/s* = 0.045 for Re_ϕ = 0.72 x 10^7, C_w = 0.3 x 10^5 (λ_T= 0.09); *N* = 3, 18, 45 and 60.....156

Figure 6.7: Pressure Coefficient Distribution on the Bolt at z/s = 0.045 for Re_ϕ = 0.72 x 10^7, C_w = 0.3 x 10^5 (λ_T = 0.09); N = 3, 18, 45 and 60 157
Figure 6.8: Relative Velocity Vectors around the Bolt for N = 45, Re_ϕ = 0.67 x 10^7, C_w = 10^5 (λ_T = 0.35), Zooming on the Locations of the First and Second Separation (S1 and S2) and Reattachment (R) Points 158
Figure 6.9: Predicted Axial Variation of Dimensionless Tangential Velocity at r/b = 0.9, Re_ϕ = 0.67 x 10^7 and C_w = 10^5 (λ_T = 0.35) 161
Figure 6.10: Predicted Axial Variation of Dimensionless Tangential Velocity at r/b = 0.9, Re_ϕ = 0.72 x 10^7 and C_w = 0.3 x10^5 (λ_T = 0.09).....162
Figure 6.11: Variation of Moment Coefficient with Number of Bolts N. Comparison Between Numerical and Experimental Results for 3, 9 and 18 Bolts and a Plain Disc: Re_ϕ = 0.67 x 10^7, C_w = 10^5 (λ_T = 0.35) 164
Figure 6.12: Variation of Moment Coefficient with Number of Bolts N. Comparison Between Numerical and Experimental Results for 3, 9 and 18 Bolts and a Plain Disc: Re_ϕ = 0.72 x 10^7, C_w = 0.3 x 10^5 (λ_T = 0.09) 165
Figure 6.13: Predicted Variation of Moment Coefficient with Number of Bolts, N for Re_ϕ = 0.67 x 10^7, C_w = 10^5 (λ_T = 0.35).....165
Figure 6.14: Predicted Variation of Moment Coefficient with Number of Bolts, N for Re_ϕ = 0.72 x 10^7, C_w =0.3 x 10^5 (λ_T = 0.09).....166
Figure 6.15: Variation of the Overall Moment Coefficient, Viscous and Pressure-related (Form Drag and Radial Pumping) Contributions with Number of Bolts (Re_ϕ = 0.67 x 10^7, C_w = 10^5 and λ_T = 0.35).....166
Figure 6.16: Variation of the Overall Moment Coefficient, Viscous and Pressure-related (Form Drag and Radial Pumping) Contributions with Number of Bolts (Re_ϕ = 0.72 x 10^7, C_w =0.3 x10^5 and λ_T = 0.09).....167
Figure 6.17: Comparison of the Drag Coefficient of Individual Bolts as a Function of N for (a): Re_ϕ = 0.67 x 10^7, C_w = 10^5 (λ_T = 0.35), and (b): Re_ϕ = 0.72 x 10^7, C_w = 0.3 x 10^5 (λ_T = 0.09) 170
Figure 6.18: Comparison of the Moment Coefficient of Individual Bolts as a Function of N for (a): Re_ϕ = 0.67 x 10^7, C_w = 10^5 (λ_T = 0.35), and (b): Re_ϕ = 0.72 x 10^7, C_w = 0.3 x 10^5 (λ_T = 0.09).....170
Figure 6.19: Relative Velocity Vectors for Re_ϕ = 0.67 x 10^7, C_w = 10^5 (λ_T = 0.35) at z/s = 0.045; N =18, (a) D =1 6 mm, (b) D = 13 mm, and (c) D = 10 mm 173
Figure 6.20: Relative Velocity Vectors for Re_ϕ = 0.72 x 10^7, C_w = 0.3 x 10^5 (λ_T = 0.09) at z/s = 0.045, N =18, (a) D =1 6 mm, (b) D = 13 mm, and (c) D = 10 mm 174
Figure 6.21: Variations of ϕ-wall Shear Stress Distribution on the Bolt for Different Diameters of Bolts at z/s = 0.045, Re_ϕ = 0.72 x 10^7, C_w = 0.3 x 10^5 (λ_T = 0.09), N =18.....175

Figure 6.22: Variations of Pressure Distribution on the Bolt for Different Diameters of Bolts at z/s = 0.045, Re_ϕ = 0.72 x 10^7, C_w = 0.3 x 10^5 (λ_T = 0.09), N =18.....175
Figure 6.23: Variations of ϕ-wall Shear Stress Distribution on the Bolt for Different Diameters of Bolts at z/s = 0.045, Re_ϕ = 0.67 x 10^7, C_w = 10^5 (λ_T = 0.35), N = 18.....176
Figure 6.24: Variations of Pressure Distribution on the Bolt for Different Diameters of bolts at z/s = 0.045, Re_ϕ = 0.67 x 10^7, C_w = 10^5 (λ_T = 0.35), N =18.....176
Figure 6.25: Variations of the Drag Coefficient of Individual Bolts for N = 18 (a): Re_ϕ = 0.67 x 10^7, C_w = 10^5 (λ_T=0.35) and (b): Re_ϕ = 0.72 x 10^7, C_w = 0.3 x 10^5 (λ_T=0.09) 180
Figure 6.26: Variations of the Moment Coefficient of Individual Bolts for N = 18 (a): Re_ϕ = 0.67 x 10^7, C_w = 10^5 (λ_T=0.35) and (b): Re_ϕ = 0.72 x 10^7, C_w = 0.3 x 10^5 (λ_T=0.09) 180
Figure 6.27: Variations of Total Moment Coefficient as a Function of Bolts Spacing for Different Diameters of Bolts; Re_ϕ = 0.67 x 10^7, C_w = 10^5 (λ_T = 0.35).....183
Figure 6.28: Variations of Total Moment Coefficient as a Function of Bolts Spacing for Different Diameters of Bolts; Re_ϕ = 0.72 x 10^7, C_w =0.3 x10^5 (λ_T = 0.09).....184
Figure 6.29: Variations of Drag Coefficient of Individual Bolts as a Function of Bolts Spacing for Re_ϕ = 0.67 x 10^7, C_w = 10^5 (λ_T = 0.35) 184
Figure 6.30: Variations of Drag Coefficient of Individual Bolts as a Function of Bolts Spacing for Re_ϕ = 0.72 x 10^7, C_w =0.3 x10^5 (λ_T = 0.09) 185
Figure 6.31: Variations of Moment Coefficient Results Produced by the Rotor Between (a): Rotor-mounted Bolts System with C_w = 10^5, (b): Rotor-mounted Bolts System with C_w = 0.3 x 10^5, (c): Plain Disc System with C_w = 10^5, and (d): Plain disc System with C_w = 0.3 x 10^5 187
Figure 6.32: Variations of Moment Coefficient Produced by the Rotor with Different Number of Mounted Bolts, D = 16 mm; (a) Re_ϕ = 0.67 x 10^7, C_w = 10^5 (λ_T = 0.35) and (b) Re_ϕ = 0.72 x 10^7, C_w =0.3 x10^5 (λ_T = 0.09).....187

List of Tables

Table 3.1: Comparison of Moment Coefficient for Different Inlet Pipe Lengths and Different Inlet Turbulent Intensities Using the Standard k-ε Model with Enhanced Wall Treatment for Re_ϕ = 0.81 x 10^7, C_w = 0.3 x 10^5, (λ_T = 0.09) 51
Table 3.2: Comparison of Moment Coefficient for Different Inlet Pipe Lengths and Different Inlet Turbulent Intensities Using the Standard k-ε Model for Re_ϕ = 0.271 x 10^7, C_w = 0.3 x 10^5, (λ_T = 0.21) 52
Table 3.3: Comparison between the Rotor Moment Coefficient results of Different Turbulence Models and Daily et al.'s and Owen's Correlations 57

Table 3.4: Comparison between the Simulation Result of Swirl Ratio Using the Standard k-ε Model and Different Near Wall Treatments....57
Table 3.5: Comparison between the Simulation Results of Moment Coefficient Using the Standard k-ε Model and Different Near Wall Treatments....58
Table 3.6: Comparison between the Rotor Moment Coefficients of Different Turbulence Models, with Daily et al.'s and Owen's Correlations....62
Table 3.7: Comparison of Rotor Moment Coefficients using standard k-ε Model between Enhanced Wall Treatment and Standard Wall Function....65
Table 4.1: Boundary and Simulation Conditions of the Plain Disc System....70
Table 4.2: Matrix of Flow Conditions for the Plain Disc System (Miles, 2011)....70
Table 4.3:Contribution to the Total Moment Coefficient Produced by the Different Rotating Components in the Simulated Two-sided Plain Disc Geometry, $C_w = 0.3 \times 10^5$....74
Table 4.4: Contribution to the Total Moment Coefficient Produced by the Different Rotating Components in the Simulated Two-sided Plain Disc Geometry, $C_w = 10^5$....74
Table 4.5: Rotor Boundary Layer Thickness at r/b = 0.8....82
Table 4.6: Rotor Boundary Layer Thickness at r/b = 0.6....82
Table 4.7: Comparison of the Numerical Results of Rotor Boundary Layer Thickness (mm) for $Re_\phi = 0.171 \times 10^7$ and Cw = 0.3×10^5....83
Table 5.1: Matrix of Flow Conditions for the Rotor-Mounted Bolt System; D = 16 mm, N = 18....96
Table 5.2: Results of the Free-stream Reynolds Number, Angle of Attack and Mach Number of The Flow Approaching the Bolt for $Re_\phi = 0.177 \times 10^7$ and $C_w = 0.3 \times 10^5$, (λ_T = 0.31)....118
Table 5.3: Comparison of the Local Free-stream Reynolds Number and Angle of Attack at z/s = 0.045 for Different Flow Conditions....129
Table 5.4: Comparison of the Stagnation and Separation Points on a Plane Cut at z/s = 0.045 for Different Flow Conditions....129
Table 5.5: Comparison of the Rossby Number at the Location of the Bolts for Different Flow Conditions....133
Table 5.6: Comparison of the Total Free-stream Reynolds Number and Angle of Attack of the Flow Approaching the Bolt as well as the Individual Bolts Drag Coefficient for Different Flow Conditions....135
Table 5.7:Comparison of the Drag Coefficient and Free-stream Reynolds Number Obtained by the Simulation Results with Those Calculated Using Equations 5. 6 and 5.7 for the Simulated Matrix of Flow Conditions....141
Table 5.8: Comparison of the Total Free-stream Reynolds Number and Angle of Attack of the Flow approaching the Bolt as well as the drag coefficient and Moment coefficient of

Individual Bolts Resulted from the Predictions of Realizable k–ε, Standard k–ε , SST-k–ω and RSM Turbulence Models; $Re_\phi = 0.27 \times 10^7$, $C_w = 0.3 \times 10^5$ ($\lambda_T = 0.22$).....145
Table 6.1: Matrix of Flow Conditions.....149
Table 6.2: Comparison of the Free-stream Reynolds Number and Angle of Attack of the Flow Approaching the Bolt at z/s =0.045 as well as the Location of the Stagnation and Separation Points for Different Number of Bolts; $Re_\phi = 0.72 \times 10^7$, $C_w = 0.3 \times 10^5$ ($\lambda_T = 0.09$) 157
Table 6.3: Comparison of the Free-stream Reynolds Number and Angle of Attack of the Flow Approaching the Bolt at z/s =0.045 as well as the Location of the Stagnation and Separation Points for Different Number of Bolts; $Re_\phi = 0.67 \times 10^7$, $C_w = 10^5$ ($\lambda_T = 0.35$) ...158
Table 6.4: Comparison of the Rotor Boundary Layer Thickness for Different Number of attached Bolts at r/b = 0.91 and $\phi = 87.28^\circ$.....163
Table 6.5: Comparison of the Total Free-stream Reynolds Number and Angle of Attack of the Flow Approaching the Bolts as well as the Drag Coefficient of Individual Bolts for N = 3, 9, 18, 36, 45, and 60; $Re_\phi = 0.72 \times 10^7$, $C_w = 0.3 \times 10^5$ ($\lambda_T = 0.09$).....169
Table 6.6: Comparison of the Total Free-stream Reynolds Number and Angle of Attack of the Flow Approaching the Bolts as well as the Drag Coefficient of Individual Bolts for N = 3, 9, 18, 36, 45, and 60;$Re_\phi = 0.67 \times 10^7$, $C_w = 10^5$ ($\lambda_T = 0.35$).....169
Table 6.7: Comparison of the Local Free-stream Reynolds Number and Angle of Attack of the Flow Approaching the Bolt at z/s =0.045 as well as the Location of the Stagnation and Separation Points for Different Diameters of bolts, $Re_\phi = 0.67 \times 10^7$, $C_w = 10^5$ ($\lambda_T = 0.35$), N = 18.....177
Table 6.8: Comparison of the Local Free-stream Reynolds Number and Angle of Attack of the Flow Approaching the Bolt at z/s =0.045 as well as the Location of the Stagnation and Separation Points for Different Diameters of bolts, $Re_\phi = 0.72 \times 10^7$, $C_w = 0.3 \times 10^5$ ($\lambda_T =$ 0.09), N = 18.....177
Table 6.9: Comparison of the Boundary Layer Thickness of the Rotor for Different Diameters of attached Bolts at r/b = 0.91 and $\phi = 87.28^\circ$.....178
Table 6.10: Variations of Total Free-stream Reynolds Number and Angle of Attack of the Flow Approaching the Bolts as well as the Drag and Moment Coefficients of Individual Bolts for Different Diameters, $Re_\phi = 0.67 \times 10^7$, $C_w = 10^5$ ($\lambda_T = 0.35$), N =18 179
Table 6.11: Variations of the Total Free-stream Reynolds Number and Angle of Attack of the Flow Approaching the Bolts as well as the Drag and Moment Coefficients of Individual Bolts for Different Diameters of Bolts, $Re_\phi = 0.72 \times 10^7$, $C_w = 0.3 \times 10^5$ ($\lambda_T = 0.09$), N =18 179
6.12:Table 6.33: Comparison of the Results of Bolts Moment Coefficient Obtained by the CFD Results with those Obtained Using Equation 6.3 for Different Number of Bolts, D = 16 mm; $Re_\phi = 0.67 \times 10^7$, $C_w = 10^5$ ($\lambda_T = 0.35$) 188

Nomenclature

A	Cross sectional area	m^2
A_p	Projected area of the body on a plane perpendicular to the direction of flow	m^2
a	Disc inner radius	m
b	Disc outer radius	m
C	Experimental constant	
D	Diameter of bolts	m
F_D	Drag force	N
H	Bolt height	m
M	Torque	N.m
$\dot{m}$	Mass flow rate	kg/s
N	Number of bolts	
p, p_s, p_∞	Total, static and free-stream pressure	pa
Q	Volumetric flow rate	m^3
r	Local radius	m
r_b	Bolt radius	m
s	Axial gap between the discs	m

s_a	Axial clearance between rotor/stator and shroud	m
s_r	Radial clearance between rotor/stator and shroud	m
V_{rel}	Relative total velocity	m/s
V_r	Radial velocity	m/s
V_ϕ	Tangential velocity	m/s
$V_{\phi-rel}$	Relative tangential velocity	m/s
X_b	Ratio of bolts pitch arc length to bolts across-flats distance	
x_{pr}	Bolts pitch arc length,	mm
z	Axial coordinate	

Greek Symbols

α	Angle of attack	°
δ	Boundary layer thickness	mm
ε_m	Constant	
ϕ	Tangential coordinate	
μ	Dynamic viscosity	kg/m s
ν	Kinematic viscosity	m^2/s
π	pi = 3.142	

ρ	Density	kg/m^3
ω	Rotational speed	rad/s

Dimensionless Groups

$C_m = \frac{M}{1/2\,\rho\omega^2 b^5}$	Moment coefficient
$C_W = \frac{\dot{m}}{\mu b}$	Throughflow Reynolds number
$C_p = \frac{(p_s - p_\infty)}{1/2\,\rho V^2}$	Pressure coefficient
$\lambda_T = \frac{C_w}{\mathrm{Re}_\phi^{0.8}}$	Turbulent flow parameter
$\mathrm{Re}_\phi = \frac{\rho\omega b^2}{\mu}$	Rotational Reynolds number
Re_r	Radial Reynolds number
$\mathrm{Re}_D = \frac{\rho V D}{\mu}$	Free-stream Reynolds number
$Ro = 1 - \frac{V_\varphi}{r\omega}$	Rossby number
$G = \frac{s}{b}$	Gap ratio

$\beta = \frac{V_\phi}{r\omega}$ Core swirl ratio

Acronyms

BWR Bolt windage rig

CFD Computational fluid dynamics

CPU Central processing unit

LDA Laser Doppler Anemometry

RSM Reynolds stress model

RNG Renormalization group model

SST Shear stress transport model

1. Introduction

1.1 Purpose of the Study

Improving engine performance, reducing the cost of new products and complying with environmental regulations are areas of intense interest for the turbomachinery industry. In order to increase the specific power output of a gas turbine and consequently reduce the size of the power plant, higher turbine entry temperatures of the main gas flow are accompanied by higher pressure ratios. Turbine entry temperatures in modern civil engines are currently above 1600˚C, and components in contact with a flow at such high temperatures will rapidly exceed their creep and fatigue limits, leading to catastrophic failure. It is only possible to operate at these elevated temperatures because of the internal air system, which uses some of the compressor's air to cool the turbine discs, blades and nozzle guide vanes. Figure 1.1 shows a typical gas turbine internal air system.

The air used for cooling will be heated as a result of viscous dissipation as it flows over both rotating and stationary surfaces. A torque needs to be provided to overcome the irreversible losses, and this parasitic phenomenon is referred to as windage. Skin friction is the source of windage for a smooth surface. However, it is not uncommon for protrusions such as bolts to be attached to the rotating and stationary surfaces. In such cases, form drag also contributes to windage. It is worth noting that there will also be a torque associated with the so-called pumping losses that occur as a result of the work done by a protrusion changing the angular momentum of the fluid. It is important to make the distinction between these and windage because the pumping loss term is isentropic. The sum of the irreversible torque (due to windage) and the reversible torque (due to pumping work) is embodied in the moment coefficient, which is defined in the next chapter. A detailed knowledge of the influence of protrusions on flow physics as well as more accurate

predictions of windage offer potential for improved design of the internal air system, with associated increases in thrust and efficiency.

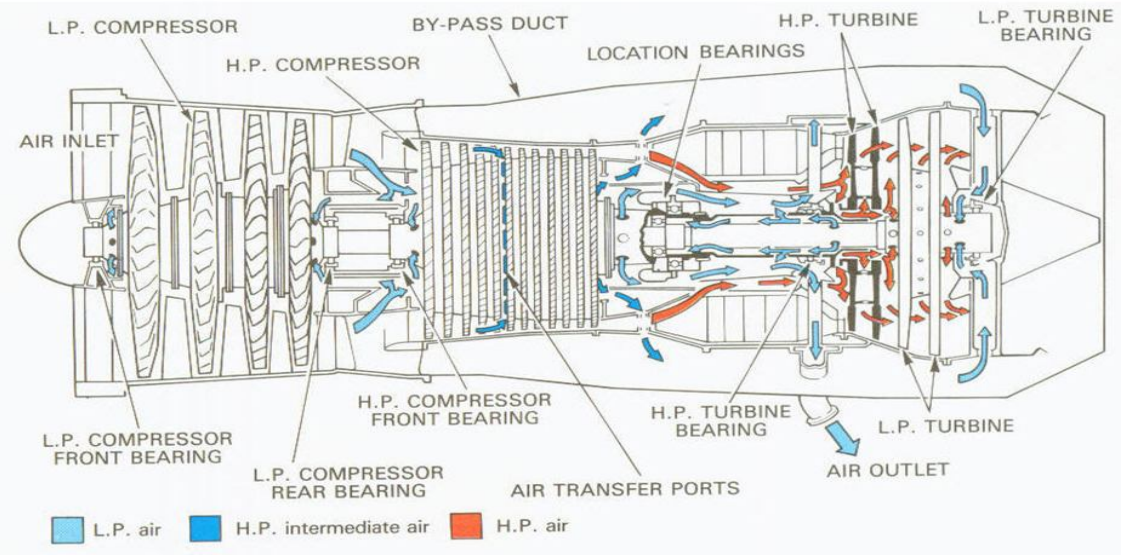

Figure 1.1: The Internal Air Paths in a Gas Turbine Engine, courtesy of Rolls-Royce plc.

Computational fluid dynamics (CFD) is now widely recognised as an established tool for modelling the internal air system of a gas turbine engine. CFD developments started around 1960. However, due to limitations in computing power its usage was limited to simple two-dimensional flows. The rapid growth of computer power in addition to advancements in numerical techniques improved CFD methods and made it a powerful and essential tool for modelling turbomachinery flows. CFD solutions in combination with theoretical and experimental approaches can improve gas turbine design by offering a powerful way to develop a physical understanding of the flow phenomena through the system under investigation. Experimental measurements can provide reliable data. However, they are often limited to a narrow scope of variables. This is because of the high cost of experiments. Furthermore, some variables are almost impossible to be measured at some

specific locations. Therefore, experimental measurements are not able to obtain a continuous picture of variables in the system. In these circumstances, CFD methods can be applied to represent the flow phenomena and to account for all the major flow parameters in each turbine component.

Based on CFD improvements, different simulation packages have been developed. One of these packages is FLUENT, which is a well-recognised validated commercial package and provides the features needed for the analysis of almost all components of the system. In addition, the turbulence models in FLUENT are well-validated and have the ability to be coupled with mesh adaptation in the near-wall regions. Based on these considerations, FLUENT is used for flow simulations in this thesis.

This research work aims to improve the physical understanding of the fluid flow phenomena caused by mounting protrusions in a rotor-stator cavity and to quantify the amount of their power loss. This will provide best practice for the design of all rotating surfaces with attached protrusions in a gas turbine engine. These aims will be achieved by a combination of experimental, theoretical and numerical approaches. This thesis will use the outcomes of previous research to validate the CFD software and assess its ability to model the flow in the rotor-stator cavity and, consequently, will use the CFD to answer those questions that have not been answered before. Since a commercial CFD software package (FLUENT) is used as the simulator in this research, validation does not have its common meaning. Instead, it means finding suitable controls of the software's features in order to obtain results that are acceptable in comparison to the relevant experimental or validated numerical data and that also are cost- and time-effective.

1.2 Research Questions

The central question that this thesis examines is:

What are the influences of protrusions on the flow structure, flow parameter distributions, and power loss in a rotor-stator cavity with radial outflow?

The central research question will be approached by answering three specific supporting research questions:

1- What are the effects of adding protrusions in a rotor-stator cavity in terms of flow structure and flow parameter distributions such as velocity and pressure? How do these parameters vary around protrusions? Do Taylor columns occur on top of a bolt and extend across the axial width of the cavity from rotor to stator?
2- What are the effects of adding protrusions in a rotor-stator cavity in terms of losses? How does the drag coefficient of the protrusions vary with Reynolds numbers? Does the drag from the bolts have substantially different behaviour in regimes where it is expected to be notionally laminar or notionally turbulent?
3- To what extent do the number and size of protrusions affect the flow structure and amount of losses in the cavity?

The above set of questions provides a reasonable opportunity for a more detailed investigation of the influence of protrusions in a rotor-stator cavity.

1.3 Overview of the Thesis

The thesis is composed of seven chapters. The chapters are as follows:

Chapter 1: Introduction

Chapter 1 gives an introductory description of the subject of the research. A brief explanation is also given of how the research can contribute to knowledge, as well as an overview of the thesis.

Chapter 2: Review of previous work

Chapter 2 aims to establish the theoretical and empirical framework for the thesis. The thesis builds upon literature on fluid flows in rotor-stator cavities and power loss prediction in these systems, in particular on studies that have examined the effects of attached

protrusions. In this chapter, a review of the theoretical and experimental work conducted in fluid flows in rotor-stator cavities is first presented. Subsequently, a critical analysis of the previous literature about the flow in rotor-stator cavities with protrusions is given, aiming to understand what has been done before, and to find gaps for further work. The chapter then reviews the progress of numerical methods in modelling the fluid flows particularly within rotor-stator cavities. Finally, a brief description of the experimental test rig that is modelled and used for simulations in this thesis is given.

Chapter 3: Computational model validation

The CFD modelling package, FLUENT, is validated in this chapter. As mentioned, what is referred to as validation in this chapter is the process of finding suitable controls for the software to produce results that are computationally both time- and cost-effective and that also have acceptable accuracy, compared to relevant experimental or validated numerical results. Three rotor-stator test cases are selected from literature and simulated using the CFD model. The selection of the cases for validation is based on different considerations, such as similarities in geometric configuration and flow conditions with the cases investigated in this research, as well as the availability of experimental or validated numerical data. The validation results are drawn out in order to be used in simulations of main rotor-stator cases in the research.

Chapter 4: Plain disc simulations

This chapter is concerned with investigating the simulation results of the plain disc (i.e. without protrusions) configuration. Plain disc simulations are used to provide baseline data to study the effect of adding protrusions to the system. Hence, complete analysis of different aspects of flow for the plain disc system under different flow conditions is presented in this chapter.

Chapter 5: Rotor-stator system with mounted bolts: investigation of the effects of flow condition variations

This chapter is concerned with detailed analyses of the flow phenomena in the rotor-stator cavity with rotor-mounted bolts. The results of these analyses present the main aerodynamics of the flow as well as the impact of protrusions on the flow behaviour and the amount of losses. Simulations are performed for a fixed number and diameter of bolts. Detailed 3-dimensional variations of flow parameters both in the vicinity of and far from the bolts under different flow conditions are investigated.

Chapter 6: Rotor-stator system with mounted bolts: investigation of the effects of changing the number and diameter of bolts

This chapter extends the work presented in Chapter 5 to consider the effects of varying the number and diameter of bolts. Rotor-stator cavity with different numbers and diameters of bolts are simulated under two different dominating flow conditions. In addition, the validity of the assumption used during experimental measurements that there is an equal amount of rotor moment for the cavity with and without protrusions is investigated.

Chapter 7: Conclusions

Chapter 7 summarises the main findings of the thesis and answers the research questions. It also outlines the research limitations and suggests some directions for future work.

2. Review of Previous Work

2.1 Introduction

The purpose of this chapter is to review the current state of knowledge regarding the fluid flow in rotor-stator systems, particularly on those with mounted protrusions, and to establish a theoretical framework for the case study chapters. Interest is centred on studies that examine the turbulent flow regime and give results about the power loss or moment coefficient within the rotor-stator systems. The relevant literature is divided into two sections: a review of both experimental and theoretical work, and a review of numerical investigations. First, a review is given of the main work conducted on the fluid flow in rotor-stator cavities, considering the main focus of this research. Subsequently, a critical review of existing studies about the effects of protrusions in rotor-stator cavities is presented, aiming to identify their gaps and limitations. Finally, a review of the progress of numerical methods in modelling the fluid flows particularly within rotor-stator cavities is given.

The chapter is composed of five sections. Section 2.2 reviews analytical and experimental investigations about the fluid flow in rotor-stator cavities. It first describes the simple cases of a rotating disc adjacent to a quiescent flow and a stationary disc adjacent to a rotating flow as an introduction to rotating flow associated with discs. It then moves toward the common configurations of a stationary housing in close proximity to a rotating disc and reviews the fluid flow investigations of rotor-stator systems with and without superimposed flow. Subsequently it examines the main literature on which this thesis is built, relating to the rotor-stator cavities with protrusions. Section 2.3 reviews the numerical methods of modelling the rotating flows. Section 2.4 describes the details of the test rig assembly that was used in the Thermo Fluid Mechanics Research Centre at Sussex University for experimental measurements. The geometric specifications of the test rig are the same as those used for CFD simulations in this thesis. In addition, the experimental measurements

conducted on this test rig are used in this research for validating the computational CFD model. Finally, Section 2.5 gives a summary of the chapter.

2.2 Theoretical and Experimental Investigations

There is a large range of applications and geometric configurations for the flow associated with discs. The range extends from simple configurations of rotating or stationary discs in an initially quiescent or rotating flow to complicated configurations of two rotating discs or rotor-stator discs with throughflow. A complete review of flow associated with rotating discs for different geometric configurations has been conducted by Owen and Rogers (1989), Owen and Rogers (1995) and Childs (2007). Here, only those investigations within the literature about the fluid flow in rotor-stator cavities with protrusions on which the basic concepts of this thesis are built will be reviewed. Prior to this review, it is necessary to define a series of non-dimensional parameters that are used to describe the flow associated with discs. The definitions of these dimensionless parameters are as follows:

- Rotational Reynolds number Re_ϕ

$$\mathrm{Re}_\phi = \frac{\rho\omega^2 b}{\mu} \tag{2.1}$$

Where b is the outer radius of the disc, μ and ρ are the dynamic viscosity and density of the fluid respectively, and ω is the angular velocity of the disc.

- Mass flow coefficient or throughflow Reynolds number C_w, which describes the radial flow in the rotor-stator cavity.

$$C_w = \frac{\dot{m}}{\mu b} \tag{2.2}$$

Where $\dot{m}$ is the mass flow rate pumped by the disc.

- Turbulent flow parameter, $\lambda_{T,}$ which is a useful parameter developed by Owen and Rogers (1989) that takes its definition from a momentum integral solution of the boundary layer equations using $1/7^{th}$ power law velocity profile (Von Karman, 1921). It relates the rotational Reynolds number to the throughflow Reynolds number in order to describe the flow in rotor-stator cavities with throughflow. In addition, based on the results obtained by Owen and Rogers, for $\lambda_T < 0.2$ the flow regime is described as rotationally dominated and for $\lambda_T \geq 0.2$ is described as throughflow dominated.

$$\lambda_T = \frac{C_w}{\mathrm{Re}_\phi^{0.8}} \tag{2.3}$$

- Moment coefficient C_m

$$C_m = \frac{M}{\frac{1}{2}\rho\omega^2 b^5} \tag{2.4}$$

Where M is the moment on one side of the disc.

- Gap ratio, which describes the dimensions of rotor-stator systems as the ratio of the rotor-stator spacing to disc radius.

$$G = \frac{s}{b} \tag{2.5}$$

Where s is the axial distance between the rotor and the stator.

- Swirl ratio

$$\beta = \frac{V_\phi}{r\omega} \tag{2.6}$$

Where V_ϕ is the tangential velocity of the core of fluid between the rotor and the stator.

2.2.1 Rotating Disc Adjacent to a Quiescent Flow, Stationary Disc Adjacent to a Rotating Flow

It is instructive to study the flow over a rotating disc as the basis of all rotating flows before looking at more complex rotating flow cases. The initial studies on flow characteristics near rotating discs were conducted by Von Karman (1921). He considered the simple case of a disc with radius b rotating with an angular velocity ω in an initially quiescent fluid. This simple case is referred to as "free disc". The general flow structure of the free disc system is composed of a boundary layer attached to the disc with a radially outward flow. The formation of this outflow is known as the free disc pumping effect. There is an axial entrainment flow that balances the mass flow rate within the system. Figure 2.1 shows a schematic configuration of the free disc case.

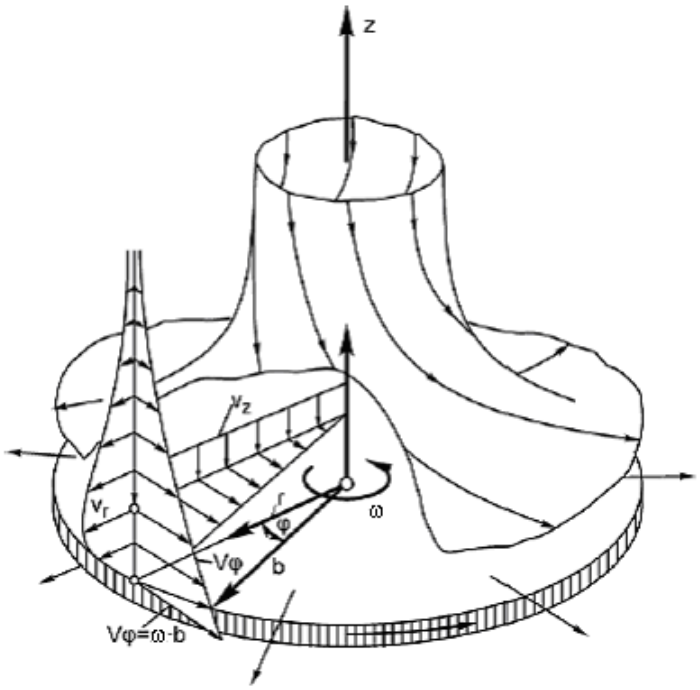

Figure 2.1: Fluid Initially at Rest Adjacent to a Rotating Disc, from Schlichtling and Gersten (1999)

Assuming that the fluid is incompressible and isothermal and that the system is axisymmetric, Von Karman simplified the equations of motion to a set of ordinary differential equations. He also provided solutions to these equations both for laminar and turbulent flows. For the turbulent flow, he used the momentum integral method and the $1/7^{th}$ power law velocity profile for both the radial and tangential velocities to calculate the moment coefficient and the mass flow coefficient.

The free disc problem has been analysed by different researchers (Cochran (1934), Goldstein (1935), Theodorsen and Regier (1944), Dorfman (1963), Bayley and Owen (1969), Owen and Rogers (1989), Schlichtling and Gersten (1999)), and different correlations have been suggested for the mass flow coefficient and disc moment coefficient.

In 1940, Bodewadt followed the Von Karman analysis and investigated numerically the case of an infinite stationary disc adjacent to a flow with solid body rotation. This configuration was also studied by Rogers and Lance (1960), Nydahl (1971), Owen and Rogers (1989) and Schlichtling and Gersten (1999). Contrary to the free disc case, the boundary layer close to the disc was found to have a radial inward flow, which produces axial flow pumping outside the boundary layer due to conservation of mass (see Figure 2.2). The thickness of this boundary layer is greater than the free disc boundary layer, because the axial outflow tends to thicken the boundary layer while the axial inflow in the free disc case suppresses the boundary layer.

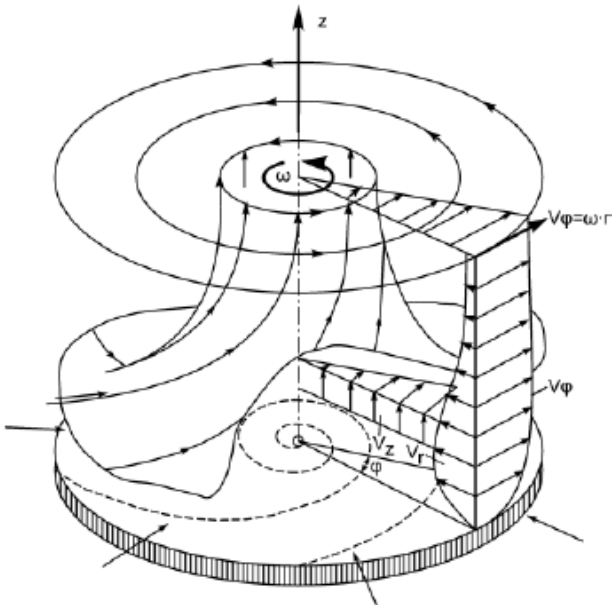

Figure 2.2: Rotating Fluid over a Stationary Disc, from Schlichtling and Gersten (1999)

2.2.2 Rotor-Stator Cavities

Rotor-stator systems are common configurations in rotating flow applications. The early studies of the fluid flow between two finite rotating and stationary discs with no throughflow were conducted by Schultz-Grunow (1935). Although the application of engines with rotor-stator cavities without throughflow is very limited, experimental and numerical investigations of these systems have been widely considered to date. This has been with the aim of providing a database for better understanding of systems with throughflow and also for CFD validation of rotating cavity cases.

Having a stationary disc adjacent to a rotating disc significantly alters each of the flow structures examined in the previous section. Schultz-Grunow found that for high Re_ϕ, there is a radially outward flow on the rotor and a radially inward flow on the stator. He showed that outside these two boundary layers, there is a core of fluid that rotates about half of the angular velocity of the rotor.

The general problem of flow between an infinite rotating disc co-axially located adjacent to an infinite stationary disc was investigated by Batchelor (1951). Batchelor used Von Karman's solutions of Navier-Stokes equations and predicted that there was a core of fluid between the rotor and the stator that rotates with an intermediate velocity between that of the rotor and the stator. In contrast, Stewartson (1952) found that for low rotational Reynolds numbers there is no core rotation and the non-zero tangential velocity only exists in the disc boundary layer. Later, Mellor *et al.* (1968) conducted numerical investigations and found that the two flow patterns suggested by Batchelor and Stewartson could be found in rotor-stator systems.

Daily and Nece (1960) performed experimental measurements to investigate the flow in a shrouded enclosed rotor-stator system. A schematic diagram of an enclosed rotor-stator system is shown in Figure 2.3. The axial distance between the rotor and stator was varied during the experiments. The variations were so that the range of the gap ratio, *G,* was from 0.0127 to 0.217. Both laminar and turbulent flows were studied during the experiments.

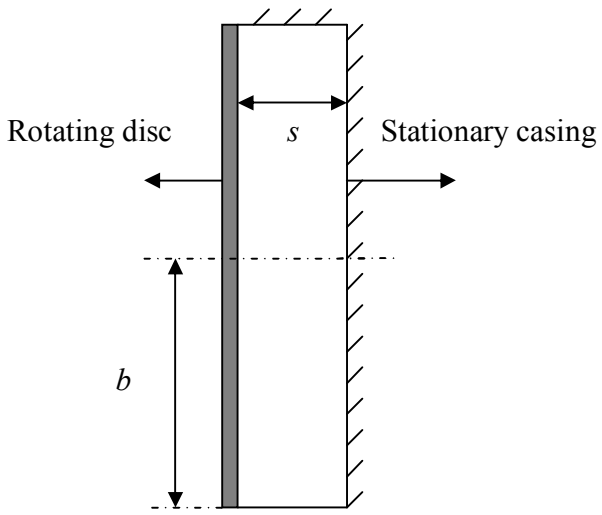

Figure 2.3: Schematic Diagram of an Enclosed Rotor-Stator System

Four flow regimes were identified by Daily and Nece:

1. Regime 1: small G (merged boundary layers), laminar flow
2. Regime 2: small G (merged boundary layers), turbulent flow
3. Regime 3: large G (separate boundary layers), laminar flow
4. Regime 4: large G (separate boundary layers), turbulent flow

As a rough guide, the flow is turbulent for $\mathrm{Re}_\phi > 10^5$ and for turbulent flow, G is considered to be large when $G > 0.04$.

Daily and Nece also measured the disc frictional torque at different rotational Reynolds numbers and correlated the moment coefficient for each flow regime as follows:

Regime 1: $$C_m = \frac{2\pi}{G\,\mathrm{Re}_\phi} \tag{2.7}$$

Regime 2: $$C_m = \frac{0.08}{G^{0.167}\,\mathrm{Re}_\phi^{\,0.25}} \tag{2.8}$$

Regime 3: $$C_m = \frac{3.7G^{0.1}}{\mathrm{Re}_\phi^{\,0.5}} \tag{2.9}$$

Regime 4: $$C_m = \frac{0.0102G^{0.1}}{\mathrm{Re}_\phi^{\,0.2}} \tag{2.10}$$

Owen (1969) measured the moment coefficient of a rotating disc adjacent to a stationary disc and concluded that the disc moment coefficient is strongly dependent on the gap ratio, G, and for the values of $G > 0.12$, it reduces to the free disc values.

Gartner (1987) performed both experimental measurements and numerical analysis to determine the moment coefficient of an enclosed rotating disc. A range of rotational Reynolds numbers up to 10^7 was used with a variable gap ratio. For lower gap ratios, he found merged boundary layers with the swirl ratio, β, below 0.4 for high radial locations. For higher gap ratios, separate boundary layers were found with a core region rotating with

$\beta = 0.4$. Gartner also found a 20% increase of the moment coefficient for higher gap ratios in comparison to that for lower gap ratios. Furthermore, he used his own velocity measurements and the Euler equation for angular momentum in order to calculate the moment coefficient. According to his conclusions, about 60% of power loss was found to be due to the losses occurring in the rotor boundary layer, 30% in the stator boundary layer, and 10% due to pushing the flow axially between the rotor and stator. Gartner's numerical results show good agreement with his experimental measurements.

Graber *et al.* (1987) performed experimental measurements on different closed geometries of rotating discs, as well as discs with mounted bolts. They found that while radial inflow reduces the disc moment coefficient, radial outflow increases it. The results of the moment coefficient for the systems with bolts mounted on the rotor showed an increase of about two times that of the rotor without mounted bolts.

Romero-Hernandez *et al.* (2001) performed experiments on a small enclosed rotor-stator rig and measured the windage friction for speeds of the rotor up to 30,000 rpm. The experimental results were used for the validation of their numerical approach in which the k-ε turbulence model was used. The CFD results were about 10% lower than the correlations used by Daily and Nece. This discrepancy was explained as the result of turbulence modelling inaccuracies.

All the above-mentioned investigations into rotor-stator systems did not consider throughflow in the cavity. Rotor-stator cavities with throughflow have a wide range of applications in industry, especially in gas turbine engines. Bayley and Conway (1964) conducted experimental measurements on an un-shrouded rotor-stator disc system with radial inflow and measured the moment coefficient. They concluded that increasing the mass flow coefficient from zero to the order of 10^4 doubles the disc moment coefficient.

Daily *et al.* (1964) performed both experimental measurements and analytical analysis on a rotor-stator system with radial outflow. The gap ratio of $0.01 \leq G \leq 0.1$ and rotational Reynolds numbers up to 10^6 were tested using water as the working fluid. Based on the results of their experiments, they correlated the moment coefficient results. This correlation uses a modification of the correlation given by Daily and Nece (Equation 2.10) for closed

cavities, so that the percentage of the increased moment coefficient due to throughflow effects is added to the Daily and Nece's correlation.

$$\%C_m = 1390K_0 \frac{T_F}{[G]^{-0.125}} \tag{2.11}$$

Where:

$$T_F = \frac{Q}{\omega b^3} \mathrm{Re}_\phi^{\,0.2} \tag{2.12}$$

K_0 is the non-dimensional tangential velocity of the core of fluid for the no-throughflow case and is dependent on the gap ratio. For $G = 0.1$, K_0 is 0.42. Q is the volumetric flow rate of fluid.

In addition, Daily *et al.* found the following correlation for the moment coefficient based on their analytical analysis:

$$C_m = \left[\frac{0.663}{b^{4.6}\,\mathrm{Re}_\phi^{\,0.2}} \right] \int_0^b r^{3.6} \left(1 - K_r\right)^{1.25} \left[1 + \left[\frac{0.162}{1 - K_r} \right]^{\frac{23}{8}} \right] dr \tag{2.13}$$

Where:

$$K_r = \frac{K_0}{CT_F \left(\frac{b}{r} \right)^{2.6} + 1} \tag{2.14}$$

C is a constant and a function of rotational Reynolds number.

Considering both the experimental and analytical correlations, it is found that the moment coefficient of the disc with throughflow is higher than that with no throughflow. This increase can be attributed to the reduction of core rotation by increasing the throughflow rate.

Bayley and Owen (1970) used a rotor-stator rig with radial outflow in order to investigate the effects of throughflow on the moment coefficient. The gap ratio was varied throughout their measurements. They found that the moment coefficient is dependent upon whether a shroud is used in the system or not. According to their conclusions, a shrouded system with no throughflow has a lower moment coefficient than that without a shroud. This is due to the increased amount of ingress of fluid for un-shrouded rotor-stator systems. Accordingly, the amount of relative velocity between the core and the disc increases and, as a result, it increases the drag on the rotor. In contrast, they found that for cases with throughflow, shrouded systems have a higher moment coefficient in comparison with un-shrouded ones. Bayley and Owen also found that increasing the throughflow rate and reducing the rotational Reynolds number reduces the tangential velocity of the core, but increases the moment coefficient of the disc. Furthermore, they found that having a rotor-stator system with lower gap ratios produces higher moment coefficients.

Owen (1988) suggested a solution for the moment coefficient of rotor-stator system with throughflow that accounts for the core rotation using a term that is dependent on λ_T.

For $\lambda_T < 0.2$:

$$C_m = \mathrm{Re}_\phi^{-0.2}\{0.0729x_c^{4.6} + 0.0389[(1-x_c^{4.6}) + 14.7\lambda_T(1-x_c^{2}) + 90.4\lambda_T^{2}(1-x_c^{-0.6})]\} \quad 2.15$$

Where:

$$x_c = 1.79\lambda_T^{5/13} \quad 2.16$$

And for $\lambda_T > 0.2$:

$$C_m = 0.333\lambda_T\,\mathrm{Re}_\phi^{-0.2} \quad 2.17$$

Owen and Rogers (1989) found that the presence of superimposed radial flow complicates the boundaries between the four flow regimes suggested by Daily and Nece. In particular, a large superimposed flow can cause the flow to be turbulent even when there is no rotation. They also considered the more general case of a rotating disc in a rotating fluid. This is a

good approximation of the flow behaviour in un-shrouded rotor-stator systems where the axial gap between the discs exceeds boundary layer thickness. The flow entrained by the rotor is given by:

$$C_{w,ent} = \varepsilon_m \, \mathrm{Re}_\phi^{0.8} \qquad 2.18$$

Where the coefficient ε_m depends on β. For $\lambda_T < \varepsilon_m$, the flow structure is dominated by rotation, and for $\lambda_T > \varepsilon_m$, the throughflow dominates. There is no simple closed form relationship to express $\varepsilon_m(\beta)$, but using a quadratic fit of the tabulated data by Owen and Rogers gives:

$$C_{w,ent} = (0.2242\beta^2 - 0.441\beta + 0.219)\,\mathrm{Re}_\phi^{0.8} \qquad 2.19$$

For $\beta = 0$ (free disc) this gives the well-known result:

$$C_{w,ent} = 0.219\,\mathrm{Re}_\phi^{0.8} \qquad 2.20$$

For $\beta = 0.42$, which corresponds to a rotor stator system with $C_w = 0$:

$$C_{w,ent} = 0.073\,\mathrm{Re}_\phi^{0.8} \qquad 2.21$$

Since β depends on λ_T, the above equations suggest that there is no single value of ε_m that can be used to delineate the flow regime. However, for a superimposed radial outflow, a value of $\lambda_T = 0.219$ represents an upper limit to the value of ε_m and consequently an upper limit to a flow that is dominated by rotation effects.

Gartner (1997) developed a semi-empirical correlation that gives satisfactory agreement for the moment coefficient from a rotor-stator cavity over a wide range of dimensionless mass flows. He also suggested solutions for the moment coefficient of a rotor-stator system with throughflow based on the value of λ_T.

2.2.3 Rotor-Stator Cavities with Attached Protrusions

Protrusions are common features attached to the rotating or the stationary discs in practical applications of rotor-stator systems. These three-dimensional features significantly alter the flow structure in the system, particularly in their vicinity, and produce additional losses due to their viscous and form drags. Investigations into the effects of these protrusions on the fluid flow within the system have been conducted over the most recent two decades.

Dibelius *et al*. (1984) performed the first studies on the effects of protrusions in rotor-stator cavities. They used a test rig with a rotor disc in an enclosed housing. For rotor-mounted bolts, they noted a significant increase in the moment coefficient above that of a plain disc. This occurred for both zero superimposed flow and large values of superimposed flow. They also used the radial pressure gradient to derive an axial thrust term in order to demonstrate the effects of protrusions. Comparing the axial thrust values, they noticed that the effect of protrusions on the flow structure was more pronounced when the flow was dominated by rotational effects.

Subsequently, Zimmerman *et al*. (1986) measured the effect of various bolt designs on shaft torque. Those designs considered were: staged (i.e. axially stacked concentric bolts of reducing diameter), cylindrical rotor bolts, partially-covered (by a fin) rotor bolts, and fully-covered (by an annular ring) rotor bolts. It was found that 18 staged bolts on a disc at a radius ratio of $r_p/b = 0.75$ increased the measured torque over the plain disc by a factor of 2.5, with further increases for cylindrical shaped bolts. Partially-covered bolts gave little benefit in reducing the overall torque compared to uncovered bolts. However, fully-covered bolts gave a significant reduction in the moment coefficient compared with uncovered bolts, and a moment coefficient of approximately 25% above that of a plain disc.

Zimmermann *et al*. explained the results of their torque measurements by plotting the moment coefficient for different rotational Reynolds numbers for no-throughflow and throughflow with $C_w = 2.6 \times 10^4$. The effect of the superimposed flow was to increase the moment coefficient by 50% for all the bolt designs investigated. The non-dimensional flow conditions used by Zimmermann *et al*. during their measurements ($Re_\phi \leq 10^7$ and $C_w \leq 2.6$

x 10^4) were lower than the real conditions of a gas turbine engine (2.5 x $10^6 \leq Re_\phi \leq$ 2.5 x 10^7 and 3 x $10^4 \leq C_w \leq$ 1 x 10^5). Therefore, it is necessary to extend these ranges and re-examine the variations of moment coefficient under higher non-dimensional parameters.

Additionally, Zimmermann *et al*. carried out a theoretical analysis and attributed the increase in moment coefficient in the presence of rotor-mounted protrusions to the superposition of three elements: form drag, skin friction and pumping losses. They found that for a small number of bolts (N<13), form drag dominates the additional moment produced, whereas for a large number of bolts the pumping losses become more important. They suggested three equations for the moment coefficient produced by each of the three elements (Equations 2.22 to 2.24). However, since there is no empirical method to measure these three components separately, their equations have not yet been investigated. In addition, Zimmerman *et al.* suggested a theoretical limit where increasing the number of bolts will actually cause a decrease in the moment coefficient. The validity of the presence of this theoretical limit has not yet been investigated either empirically or numerically.

For pumping losses:

$$P_{pr} = \omega \, \dot{m}_{pr}(V_{\varphi,b} r_{b,pr} - V_{\phi,a} r_{a,pr}) \qquad 2.22$$

Where $V_{\phi,b}$ is the tangential velocity of the fluid driven by the bolt at its outer radius, $V_{\phi,a}$ is the tangential velocity of the fluid driven by the bolt at its inner radius, $r_{b,pr}$ is the bolt's outer radius, $r_{a,pr}$ is the bolt's inner radius and $\dot{m}_{pr}$ is the mass flow pumped by the bolt heads.

Form drag:

$$\Delta C_{m,pr,form} = N C_D (1-\beta)^2 \left(\frac{r_p}{b}\right)^3 \frac{HD}{b^2} F \qquad 2.23$$

Where C_D is the drag coefficient of the bolt, N is the number of bolts, r_p is the bolt's circle radius, H is the height of the bolt, D is the diameter of the bolt and F is a drag correction factor due to interference with the wakes of neighbouring bolts.

Boundary layer losses:

$$C_{m,pr,BL} = 0.073\,\mathrm{Re}_{\phi}^{-0.2}\left(\frac{r_{b,pr}}{b}\right)^{4.6}\left[1-\left(\frac{r_{a,pr}}{r_{b,pr}}\right)^{5.7}\right]^{0.8} \qquad 2.24$$

The next experiments on the effects of protrusions in rotor-stator cavities were carried out by Millward and Robinson (1989), who measured enthalpy rise in supplied flow. These experiments were carried out by varying the number of bolts, their diameter and circumferential pitch, and the projected cross-sectional area with bolts attached to both the rotor and the stationary casing. Millward and Robinson obtained a correlation of their results for bolts attached to the rotor. Equation 2.25 shows the rewritten correlation in terms of C_m. They also noted that the effect on enthalpy rise of bolts located towards the outer radius was very significant, whereas those located towards the inner radius had little effect. For stator-mounted bolts, there was insufficient data to derive a correlation, but it was noted that the enthalpy rise due to stator bolts was about one-third of the corresponding conditions with rotor bolts. Tests were also carried out with full and partial covering of both stator and rotor bolts. No measurable effect was found by partially covering the rotor bolts but the stator bolts showed a reduction in enthalpy rise at high mass flows. Fully covered bolts, however, gave similar results to a plain disc, and in some cases a reduction was actually observed.

$$C_m = \left[\frac{C_w}{\mathrm{Re}_{\phi}}\left(\frac{b}{r}\right)^3\right]^{\left(1.4-\frac{1}{3}\frac{r}{a}\right)}\left(\frac{p}{D}\right)^{0.44}\frac{r^3 An}{b^5} \qquad 2.25$$

The correlation is valid for the following ranges:

$$2.3\left[\frac{C_w}{\mathrm{Re}_{\phi}}\left(\frac{b}{r}\right)^3\right]^{\left(1.4-\frac{1}{3}\frac{r}{a}\right)}\left(\frac{p}{D}\right)^{0.44} \le 1$$

$$0.001 < \left[\frac{C_w}{\mathrm{Re}_{\phi}}\left(\frac{b}{r}\right)^3\right] < 0.1$$

$$3<\frac{p}{D}<20$$

$$1.5<\frac{r}{a}<2.25$$

Similar to Zimmermann *et al.*'s measurements, the range of non-dimensional flow conditions used by Millward and Robinson were $Re_\phi \leq 10^7$ and $C_w \leq 10^4$, which were again lower than real gas turbine flow conditions. The applicability of their correlation beyond these ranges should therefore be investigated.

Gartner (1998) used a momentum integral method to predict the frictional torque from a single disc with protrusions. The predictions agree well with available data, provided that the spacing between the bolts is not so small that wake effects become significant. Gartner used a theoretical model as well as experimental measurements to calculate the power loss due to protrusions. However, the integral method used for his theoretical model was confined to the free disc case; it is the same with his experimental measurements. This confines the usage of his correlation to rotor-stator systems. In addition, theoretical calculations of the moment coefficient were based on the $1/7^{th}$ power law for the velocity profiles in the disc boundary layer, while the validity of this assumption is doubted. Furthermore, the correlation suggested for the moment coefficient was based on the drag coefficient correlation suggested by Taniguchi *et al.* (1981) for isolated cylinders attached to a stationary wall in wind tunnel. Therefore, the limitations of that correlation (neglecting the viscous drag in comparison to pressure drag, assuming a uniform two-dimensional boundary layer for cylindrical protrusions mounted on the stationary wall) should also be considered.

The effects of protrusions in rotor-stator systems were also experimentally investigated by Coren (2007). The geometric specifications of the test rig he used as well as the range of dimensionless parameters are the same as those used for CFD simulations in this thesis. Coren performed an experimental study on windage effects in rotor-stator cavities. Tests were carried out on a smooth disc with and without mounted protrusions inside an enclosed pressurised housing. The gap ratio was kept constant ($G = 0.1$) during the experiments and

the range of the rotational Reynolds number and mass flow coefficient were 2.5 x $10^6 \leq \mathrm{Re}_\phi \leq$ 2.5 x 10^7 and 3 x $10^4 \leq C_w \leq$ 1 x 10^5 respectively, which corresponds with modern gas turbine conditions. Coren compared the experimental results of the moment coefficient for the rotor-stator system without bolts (plain disc) with the correlations suggested by Daily *et al.* (1964), Owen (1988) and Gartner (1997), and found the best match for cases where $\lambda_T <$ 0.2 with the model of Owen, and for cases where $\lambda_T >$ 0.2 with the model of Gartner. In addition, Coren used the results of his experiments to find a correlation for the moment coefficient of the plain disc system (Equation 2.26).

$$C_m = 0.52[C_w]^{0.37}[\mathrm{Re}_\phi]^{-0.57} + 0.0028 \qquad 2.26$$

Coren also carried out an experimental study on the windage effects of rotor and stator mounted bolts in the same rotor-stator cavity. Measurements were carried out for N = 3, 9, and 18 bolts of diameter D = 16mm mounted on both rotor and stator. He suggested a correlation for the moment coefficient as a function of the rotational Reynolds number, mass flow coefficient, number, and radius of mounted bolts (see Equation 2.27). He found that stator mounted bolts give the highest moment coefficient for rotationally dominated flow conditions. In contrast, for rotor-mounted bolts, the highest moment coefficient was produced by radially dominated flow conditions. Laser Doppler Anemometry (LDA) was also used to measure the radial and tangential components of velocity. Coren found that for rotor-mounted bolts and rotationally dominated flow conditions, the core rotational speed could reach that of the disc.

$$C_m = X\{0.115\,[C_w]^{0.63}\,[\mathrm{Re}_\varphi]^{-0.57}\,[Y]^{0.38} + 0.005\} \qquad 2.27$$

Where X is 1 for rotor-mounted bolts and 0.32 for stator-mounted bolts. Also, $Y = \dfrac{r_p}{B_p}$ where r_p is the radius at which the bolts are mounted and B_p is the bolt's pitch arc length.

Although the effect of the number of bolts is indirectly considered in Coren's correlation by considering B_p, the validity of this correlation for a large number of bolts, where the space between the bolts is significantly lower than that used in his measurements, is doubted considerably. In addition, the effect of the diameter of bolts is not examined in Coren's correlation.

Miles (2011) conducted experimental measurements on the same test rig that was used by Coren (2007). A set of plain disc tests as well as tests with rotor- and stator-mounted protrusions were carried out under a range of flow conditions that are typical for gas turbine engines. Different numbers (N = 3, 9, and 18) and diameters (D = 10mm, 13mm, and 16mm) of hexagonal bolts were used during the experiments. Miles also carried out a set of tests with bi-hexagonal bolts and pockets. She found that increasing the number and diameter of bolts increases the moment coefficient. She also suggested a correlation for the moment coefficient as a function of dimensionless flow parameters and the ratio of diameter to the circumferential pitch of the bolts (see Equation 2.28). For the rotor-stator system with bi-hexagonal bolts, Miles found that the moment coefficient is reduced, in comparison with the system with hexagonal bolts. The use of pockets showed little effect in comparison to protrusions. Although the measurements conducted by Miles correlated windage as a function of flow parameters and the number and size of protrusions, she added little information about the flow structure and flow parameter variations in the range of interference of the protrusions. In addition, she estimated the drag coefficient of the bolts with the drag coefficient of a circular cylinder by defining a Reynolds number based on the core velocity and diameter of the bolts. Using this estimation, she proposed that the drag coefficient of the bolts could be in the range of laminar to turbulent separation. Although the drag coefficient of the bolts could be roughly estimated by assuming them to be cylinders, there is still a need for the drag coefficient of the bolts to be accurately calculated.

$$C_m = 12.15\,\mathrm{Re}_\phi^{-0.67}\, C_w^{0.44}\left(\frac{D}{p}\right)^{0.27} \qquad 2.28$$

2.3 Numerical Methods

In addition to experimental and theoretical investigations, rotating flows have been the subject of many numerical simulation investigations. Today, Computational Fluid Dynamics (CFD) is recognised as an established tool for use in areas such as turbomachinery applications where rotating flows are one of the most important flow phenomena. Modelling these flows requires the solution of a set of simultaneous, non-linear, partial-differential equations resulting from a strong coupling of the momentum conservation equation components. For the case of non-isothermal turbulent flows, the energy conservation equation and the difficulties of finding a suitable turbulence model are added to the numerical difficulties of the system. In addition, it is now well-recognised that the experimental and theoretical approaches are essential complementary parts of developing computational methods. Hence, the lack of suitable experimental measurements as well as the previously-mentioned numerical difficulties have slowed down the process of developing CFD techniques. Nevertheless, CFD is now a powerful tool for modelling fluid flow and heat transfer, including within the turbomachinery industry.

Early numerical methods solving the fluid flow in rotating cavities were developed for incompressible laminar flows, which were restricted to low rotational Reynolds numbers (Pao (1970), Gosman and Splalding (1970), Patankar and Spalding (1972), Gosman and Ideriah (1976)). Different pressure correction methods, due to the incompressible assumption of the fluid, were used during these investigations. It was around the mid-1990s that steady, axisymmetric, incompressible CFD methods were established in industry (Virr et al. (1993)). However, with the progress of computing power, more and more restrictions have been relaxed. Compressibility effects were added to the system by extending the algorithms for pressure correction methods, and density-based methods were extended for low Mach number regimes (Chew and Hills (2007)).

The low rotational Reynolds number assumptions that were the other restriction of early computations were gradually eliminated by the development of turbulence modelling methods. Modelling highly turbulent flows is now common using the large eddy simulation (LES) and Reynolds-averaged Navier-Stokes (RANS) equations. Today, the main problem

is to find the most appropriate turbulence model based on the flow characteristics and the money and time available. Some researchers recommend the k-ε model with standard wall function for rotating flows due to its satisfactory results and lower time and cost requirements in comparison to Reynolds stress models (RSM) (Virr et al. (1994)). Others prefer using RSM due to its improvements in modelling rotating flows in certain cases over the k-ε model (Lee et al. (2004)). However, still there is no single turbulence model that can be recommended for CFD methods in all cases. Hence, finding a suitable model largely depends on comparing the results of different models with relevant experimental data and simultaneously considering the available time and money.

One of the first numerical investigations into the special rotating flow case of rotor-stator cavities was conducted by Chew (1984), who modelled a rotor-stator system with throughflow using a low Reynolds number k-ε model. Consequently, Chew and Vaughan (1988) examined this type of flow with and without throughflow using a model based on mixing length hypothesis, and obtained acceptable velocity profile and moment coefficient results compared to the experimental measurements of Daily and Nece (1960) and Daily et al. (1964).

Later, Iacovides and Toumpanakis (1993) modelled a closed rotor-stator cavity using four turbulence models including a k-ε model coupled with a one-equation model, the Launder and Sharma k-ε model, a k-ω model and RSM, and showed that RSM provides the appropriate level of closure for the system. Consequently, Kilic *et al*. (1994) modelled a similar rotor-stator cavity to Daily and Nece's using the Launder and Sharma low Reynolds number k-ε turbulence model. The results of their computations showed good agreement with the experimental data.

The development of improved turbulence models for use in numerical analysis of rotor-stator systems has been an area of extensive research. A review of these investigations was conducted by Iacovides and Launder (1995). Improved results were obtained using Reynolds stress models (RSM). Elena and Schiestel (1996) tested these models and found that they give better results, especially for systems with rotation. However, using RSM is very expensive and often has stability problems. The results of investigations conducted by

Iacovides and Launder (1995) and Ton and Lin (1994) show that the k-ε model is able to reach a compromise between accuracy and CPU time for numerical simulations of rotor-stator systems.

In the previous section, the gaps and limitations of the main literature investigating the effects of adding protrusions to rotor-stator cavities were presented. There are some gaps in common in all the literature, and these include the limitations of theoretical and experimental work in comparison with CFD simulations. One of these limitations is that it is not possible to measure the torque produced by individual bolts through experimental techniques. The only possible method is to measure the produced torque in two cases: the system with attached bolts and the system without them. The result of subtracting one of these values from the other could be considered as the torque due to bolts. Although this is the only applicable method, it is based on an assumption that the amount of torque produced by the disc remains constant for the system with bolts and the system without bolts. The validity of this assumption is questionable. In addition, most experimental measurements have been carried out only at discrete points, usually far from the bolts. In contrast, CFD simulations are able to produce a continuous picture of all parameters variations and distributions in the system, even in the vicinity of the bolts. Another advantage of CFD methods is that changing the flow conditions or protrusion dimensions and repeating the data acquisition is not as time-consuming and costly a process as using experimental methods. These concerns motivated this research in order to investigate flow in a rotor-stator cavity with protrusions using CFD simulations.

2.4 The Bolt windage test rig

Figure 2.4 shows a general assembly of the test rig used for experimental measurements at the Thermo Fluid Mechanics Research Centre (TFMRC) at Sussex University (Miles, 2011) . This consists of a shaft-mounted titanium alloy disc with an outer radius of b = 225mm enclosed within a sealed steel pressure casing. The maximum clearance between the rotor and the casing is s = 22mm. Around the outer rim of the disc is a labyrinth seal

and a stator-mounted shroud encases the cavities on either side of the disc. The disc is driven by a 50 kW motor through a 5:1 step-up gearbox. Mounted between the gearbox and the disc is an in-line torquemeter. The test side of the disc (labelled 'front cavity' in Figure 2.4) carries the majority of the instrumentation, whereas the balance side (labelled 'rear cavity' in Figure 2.4) has sufficient instrumentation to balance the flow conditions on both sides of the disc. A superimposed flow of air enters the rig centrally on the test side, flows radially outward through the cavity and leaves through the labyrinth seal at the perimeter. An equal amount of air is supplied to the balance side, where it enters through four inlet pipes equally spaced around the central shaft. There are four orifice plates positioned upstream and downstream of the test rig on both the test and balance side to measure the mass flow of air into and out of the rig, and this ensures both sides are balanced. The air is supplied at pressures of up to 7.5 bar (absolute), and mass flows (to both sides) of up to 0.82 kg/s by an Atlas Copco screw type compressor, and treated with an Atlas Copco air conditioning unit to provide dry air in the range of 15 to 25 ºC prior to delivery to the rig.

The simulations covered the following range of dimensionless parameters that are typical for a gas turbine engine:

$0.27 \times 10^7 \leq \mathrm{Re}_\phi \leq 1.4 \times 10^7$

$0.3 \times 10^5 \leq C_w \leq 1 \times 10^5$

$0.06 \leq \lambda_T \leq 0.58$

A shaft-mounted Vibrometer TM112 in-line torquemeter measures torque and rotational speed. The 95% confidence interval in torque measurement is less than ± 1 N m. The uncertainty in speed measurement is less than ± 5 rev/min. The torque due to bearing friction in the test rig depends on rotational speed and was obtained from a previous calibration. This driveline torque was subtracted from all of the measured values of torque to obtain a value of the torque transmitted to the fluid, M. The magnitude of the driveline torque varied from approximately 2% of the total at high rotational speeds to approximately 20% at low values of rotational speed.

It is important to note that the test rig was designed with the intention of making the torque on the test and balance sides equal. The two sides have the same geometrical configuration with bolts located on both sides of the disc at the same radius. Furthermore, the pressure was kept equal on both sides of the cavity to provide the same flow conditions. The cooling flow enters into the balance side at a much higher radius (r/b = 0.55) than on the test side (r/b = 0.1). As a result, the flow travels over a smaller section of the disc before exiting the system. There are two reasons why this difference in inlet radius is thought to have an insignificant effect on the torque. Firstly, the torque on a plain disc is a strong function of the radius. Consequently, most of the contribution to the torque experienced by the balance side comes from that radially outward of the inlet. Secondly, the tangential velocity of the disc at this higher radius will also be proportionally higher, leading to greater shear between the disc and the non-rotating fluid near the entry point. This will increase the local moment coefficient in this region, which will act to balance the torque experienced on each side of the disc.

Tests were carried out with N = 3, 9 and 18 and D = 10mm, 13mm, and 16mm hexagonal bolts of height H = 11mm. These were attached, at a radius of 0.2m, r_b/b = 0.889, to both sides of the disc surface to ensure similar conditions on either side and to minimise axial heat conduction. For reference, the orientation of the bolts relative to the direction of rotation is shown in Figure 2.5.

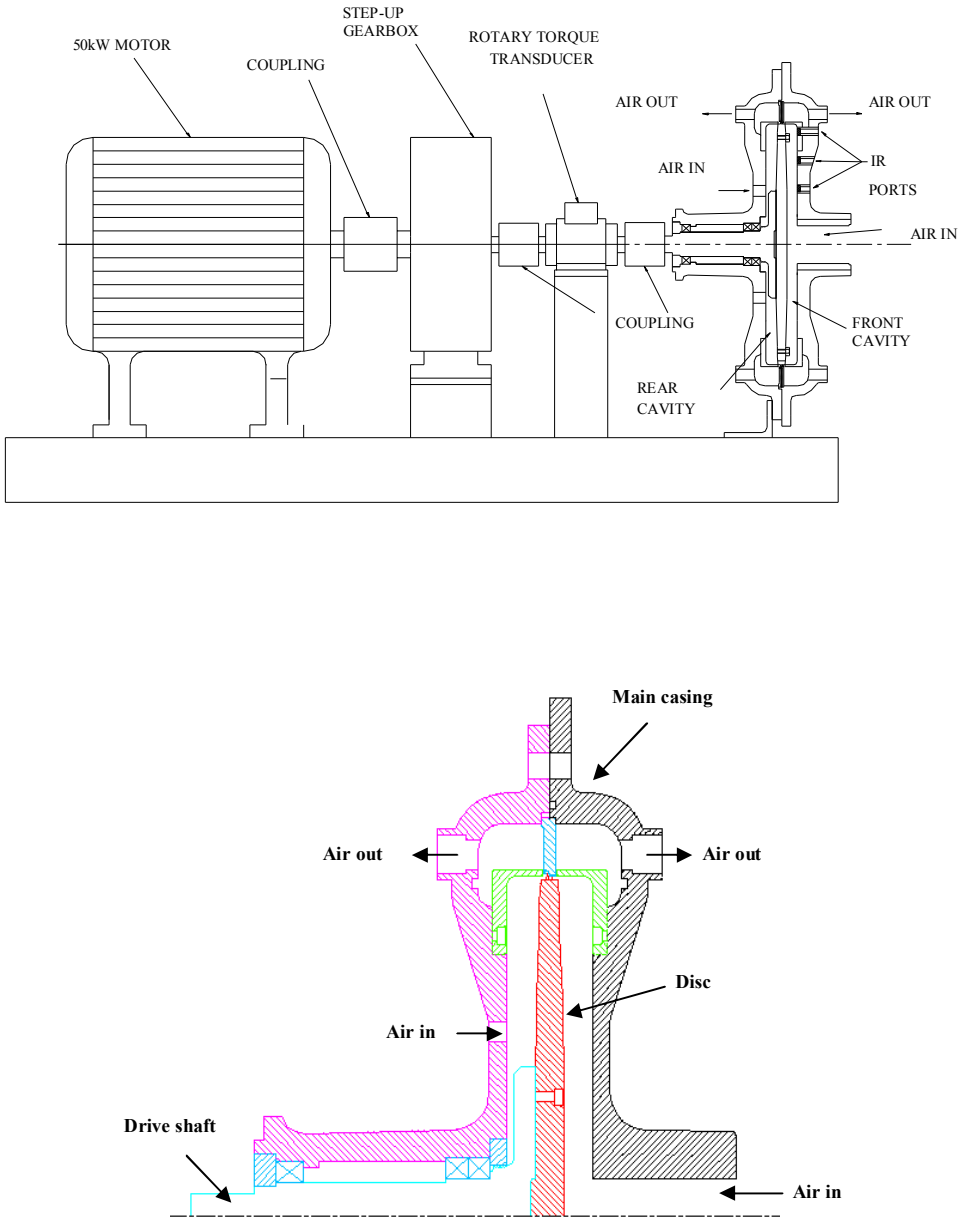

Figure 2.4: Schematic Diagram of the Bolt Windage Test Rig (Miles, 2011)

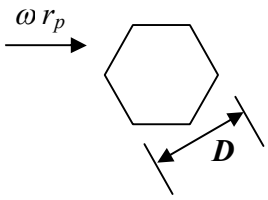

Figure 2.5: Orientation of the Bolts with Respect to Rotation

2.5 Summary

This chapter has established the theoretical and empirical framework for the thesis by reviewing the literature about fluid flow in rotor-stator cavities, particularly that which has examined the effects of attached protrusions. From this review it is clear that a certain amount of theoretically- and experimentally-gathered information regarding power loss and fluid flow in rotor-stator systems with protrusions is available. However, a detailed picture of flow parameters variations in the cavity, particularly in the range of interference of bolts, has not yet been obtained. In addition, it was found that all of the experimental measurements of power loss due to protrusions have been based on the assumption that there is an equal amount of disc moment coefficient for systems with bolts and systems without bolts. The validity of this assumption is questionable and should also be investigated. Therefore, this study was initiated with the objective of utilising CFD to provide detailed information about fluid flow in rotor-stator systems with protrusions so that a better understanding of flow behaviour in such systems can be established.

3. Computational Model Validation

3.1 Introduction

Validation of the CFD code, ANSYS FLUENT, against three rotor-stator test cases is presented in this chapter. Since commercial CFD software is used as the simulator in this research, validation does not have its common meaning. What is referred to as validation in this chapter is finding suitable controls for the software to produce results that are both computationally time- and cost-effective and also have acceptable accuracy compared to relevant experimental or validated numerical results. It should be noted that further validation of the CFD code for the case of three-dimensional rotor-stator systems with protrusions will be continued in Chapters 5 and 6.

The chapter is composed of four sections. In Section 3.2, the rotor-stator cavity with superposed radial outflow that was used by Coren (2007) during his experimental measurements is simulated. In Section 3.3, simulations are carried out for the rotor-stator cavity with superposed radial outflow that was used by Vaughan (1987) during his numerical analysis. Section 3.4 validates the modelling software against the experimental measurements conducted by Daily *et al*. (1964) in a rotor-stator cavity with superposed radial outflow. Finally, Section 3.5 summarises the chapter.

3.2 Selecting the Validation Cases

As mentioned, three test cases have been selected from literature in order to validate the CFD simulation software. The selection of the validation cases was based on different considerations, such as similarities in geometric configurations and flow conditions with the cases investigated in this research, as well as the availability of experimental or validated numerical data. Some considerations are similar between the three cases, and

some reasons are specific to each individual case. The geometric specification of the three selected cases is in the category of shrouded rotor-stator systems with large clearances. For all of the cases there is an axial throughflow and radial outflow. In addition, the flow is expected to be turbulent for all three validation cases. Aside from these considerations, the cases were also selected for the following reasons:

- **Validation Case No. 1: Experimental Measurements of Coren (2007)**

The geometric specification of the test rig and the range of non-dimensional parameters used by Coren were the same as those used in this thesis. Hence, it provides good information for evaluating the CFD results. Data of both power loss (moment coefficient) and velocity variations through the width of the cavity were provided in Coren's measurements.

- **Validation Case No.2: Numerical Analysis of Vaughan (1987)**

Vaughan carried out numerical calculations of the flow in a shrouded rotor-stator system with radial outflow. He provided useful data about the core swirl ratio, as well as the moment coefficient. He plotted the variations of β/β^* for different turbulent flow parameters in the plane midway through the cavity, and compared his results with earlier experimental and numerical investigations. Since similar comparisons are made for plain disc system, this validation is useful.

- **Validation Case No.3: Experimental Measurements of Daily *et al.* (1964)**

This test case has been selected due to the completeness of the investigations of different aspects of flow in rotor-stator cavities with throughflow. Radial and tangential velocity distributions in different radial locations were reported by the researchers. The researchers also measured and correlated the radial pressure variation as well as core swirl ratio and rotor boundary layer thickness. Results of the mentioned correlations are used in Chapter 4 for flow analysis in the plain disc system. The data were provided for different throughflow rates and rotational Reynolds numbers. The moment coefficient produced by the disc was

also measured and correlated by the researchers. This set of information could be used to validate the CFD code very effectively.

3.3 Validation Case No. 1: Experimental Measurements of Coren (2007)

Validation was performed against the plain disc experimental measurements that Coren (2007) carried out on the rotor-stator test rig described in Section 2.4. No bolts were attached to either the rotor or stator. The computations were carried out for two cases of interest: 1) throughflow dominated (λ_T = 0.21, C_w = 0.3 x 10^5, Re_ϕ = 0.26 x 10^7); and 2) rotationally dominated (λ_T = 0.09, C_w = 0.3 x 10^5, Re_ϕ = 0.81 x 10^7). The absolute inlet air pressure and temperature for the throughflow dominated case are 2.07 bar and 306 K, while for the rotationally dominated case they are 3.04 bar and 301 K.

A schematic diagram of the geometry modelled is shown in Figure 3.1. A model of the geometry in two dimensions was built and meshed for use with enhanced wall treatment. Further details about the near wall treatment may be found in Appendix 2. There is an extended geometry after the outlet, which is used to avoid reversed flow through the outflow boundary. This extended geometry provides a uniform flow before the outlet boundary, and prevents it from changing direction and re-entering through the outlet, which could cause numerical instability. A grid independence study was carried out in order to make sure that the computational results were unaffected by grid size. To achieve this, the number of grid cells was doubled. The results were then compared with the coarser mesh. If the discrepancies between the two results were considered to be negligible, the coarser mesh was selected for further simulations. The number of points for the grid independent simulation in this case is 18,000 for use with the enhanced wall treatment. The Pressure-based, steady state solver was used with the 2nd order discretisation method (see Appendix 1 for further explanations about the CFD procedure).

The air is taken to be compressible, and ideal gas law provides a relationship between density, pressure and temperature. The pressure and temperature boundary conditions used at the inlet for each case were obtained from the experimental data. The outlet static pressure was set so that it produced the measured mass flow rate. A rotating reference frame with an angular velocity of the rotor speed was used.

During the solution process the residuals and the lift, drag, and moment coefficients can be monitored continuously in order to identify the convergence. The convergence criteria were as follows:

1. Iterations residual for all the variables except the energy equation are less than 10^{-5}. For the energy equation, the residual is less than 10^{-6}.
2. Fluctuations of outlet mass flow rate are less than 0.1% of inlet mass flow rate.

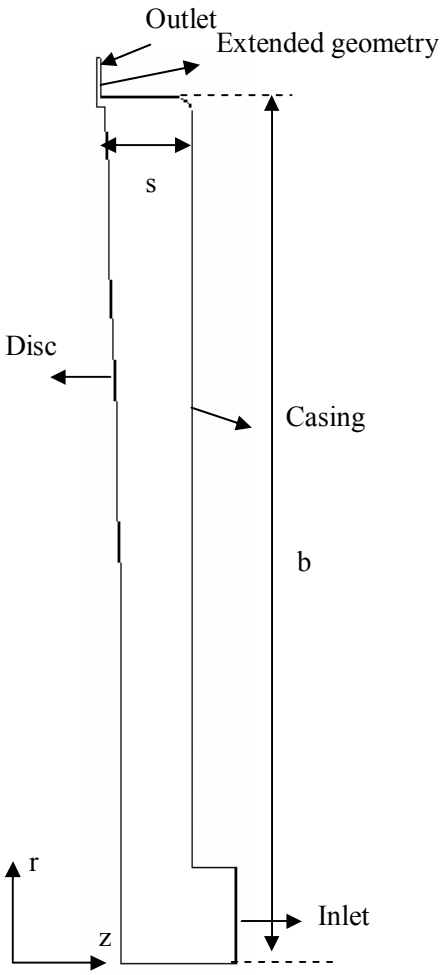

Figure 3.1: Schematic Diagram of the Two-dimensional Simulated Geometry

Six different turbulence models available within FLUENT were used to assess and compare the functionality of each model: standard k-ε, realizable k-ε, RNG (Renormalisation group) k-ε, standard k-ω, SST k-ω and RSM (Reynolds Stress Model) (see Appendix 2). The output of this comparison will be the most appropriate model to be used in this thesis.

In general, finding an appropriate turbulence model for each particular class of application is both a challenging and a critical step during CFD simulations. The level of accuracy of the model, and the computational effort and cost in terms of CPU time and memory usage are the points that should be considered. It is now well known that the RSM provides better

predictions for situations in which the flow is anisotropic, including separated flows, flows with strong streamline curvature, vortices and rotating flows. However, it should be noted that application of RSM is still limited, particularly for three-dimensional flows. This is mainly due to the large resources required. In addition, the RSM that is used within FLUENT does not always predict more accurately than the two equation models. This is due to the closure assumptions used to model various terms in the transport equations for Reynolds stresses (Jones and Clarke, 2005 and Rodi, et al., 1998). For both of the simulated flow conditions in this validation case, the RSM required about five times more CPU time on average for reaching the convergence compared to the standard k-ε model. In addition, obtaining a converged solution for RSM was also more challenging compared to the two equation models.

Figures 3.2 and 3.3 show comparisons of the simulation results between the dimensionless radial and tangential velocities at $r/b = 0.79$ for the rotationally dominated case ($\lambda_T = 0.09$) using the experimental data of Coren. Note that $z/s = 0$ (local amount of s is used) corresponds to the rotor surface, and $z/s = 1$ to the stator surface. Figures 3.4 and 3.5 show similar comparisons of results for the throughflow dominated case ($\lambda_T = 0.21$). It should be noted that Coren performed his experimental measurements at three discrete axial locations through the width of the cavity. However, these points are located outside the boundary layer thickness of both the rotor and the stator. Therefore, it is only possible to validate the results obtained for the core of flow between the rotor and the stator.

Additionally, Figure 3.6 illustrates comparisons of the computed values of the moment coefficient with the experimental measurements for $\lambda_T = 0.09$ and 0.21.

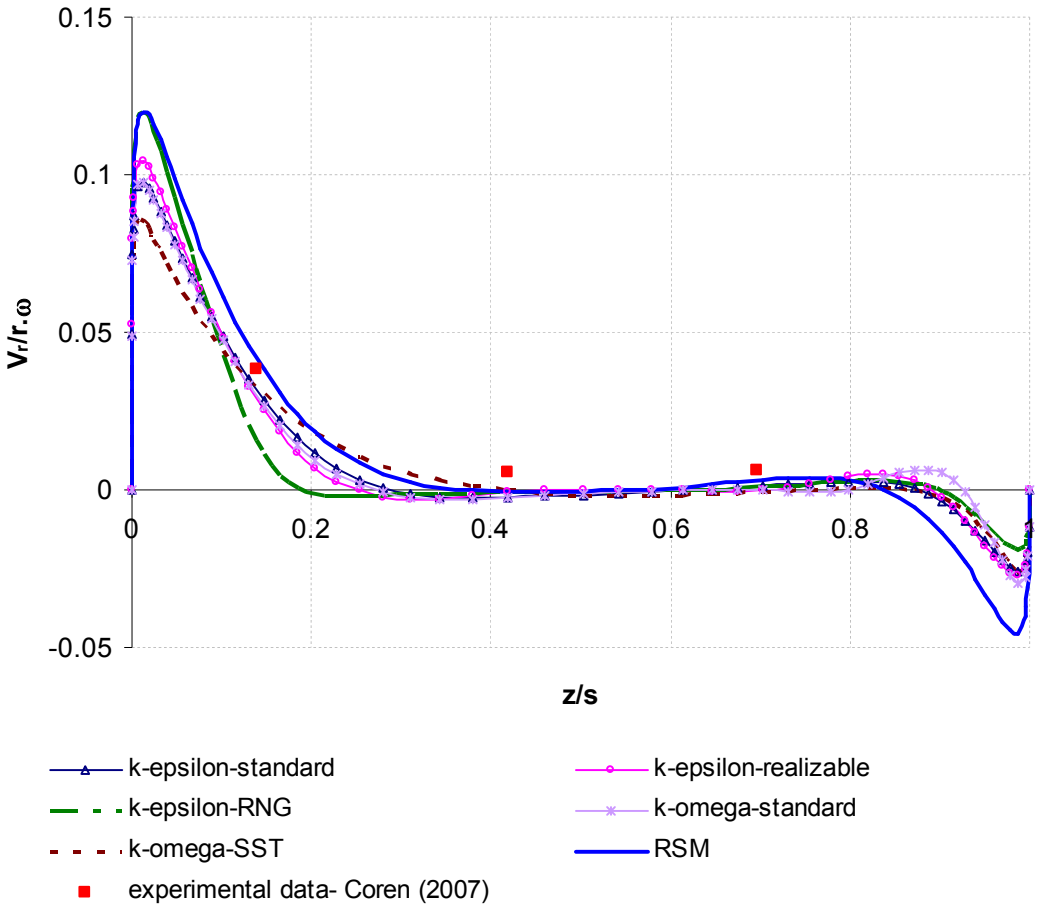

Figure 3.2: Comparison between the Axial Distribution of Dimensionless Radial Velocity for Different Turbulence Models with the Experimental Data of Coren (2007) at $r/b = 0.79$; $Re_\phi = 0.81 \times 10^7$, $C_w = 0.3 \times 10^5$ ($\lambda_T = 0.09$)
Note: z/s = 0 is located on the rotor. This is also the case for Figures 3.3 to 3.9.

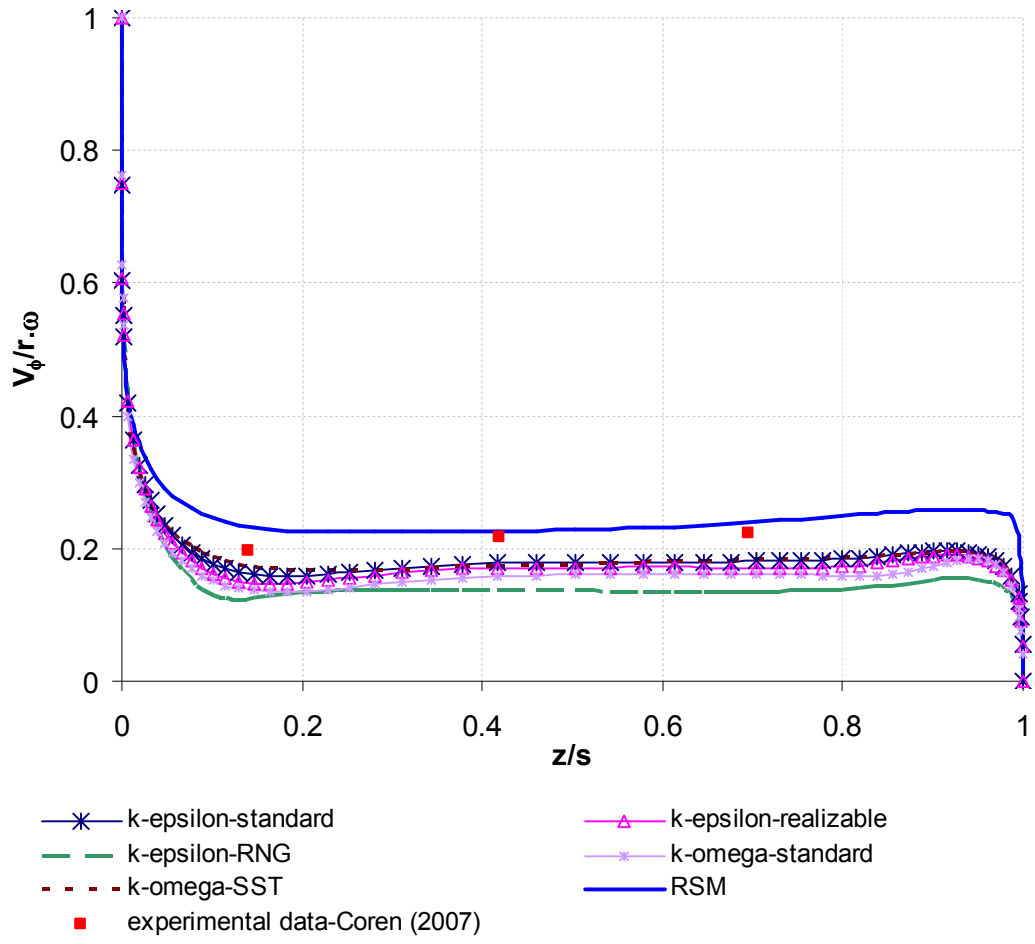

Figure 3.3: Comparison between Axial Distribution of Dimensionless Tangential Velocity for Different Turbulence Models with the Experimental Data of Coren (2007) at $r/b = 0.79$; $Re_\phi = 0.81 \times 10^7$, $C_w = 0.3 \times 10^5$, ($\lambda_T = 0.09$)

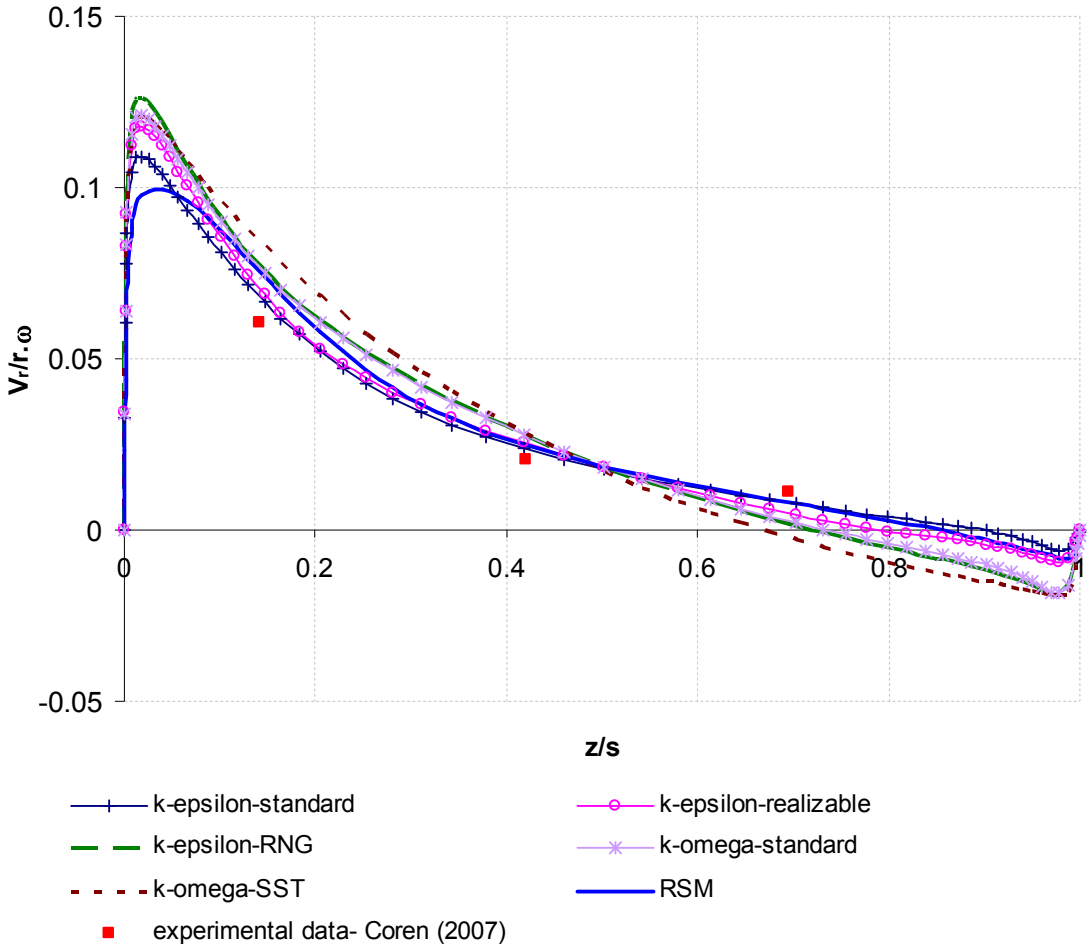

Figure 3.4: Comparison between the Axial Distribution of Dimensionless Radial Velocity for Different Turbulence Models with the Experimental Data of Coren (2007) at $r/b = 0.79$; $Re_\phi = 0.271 \times 10^7$, $C_w = 0.3 \times 10^5$, ($\lambda_T = 0.21$)

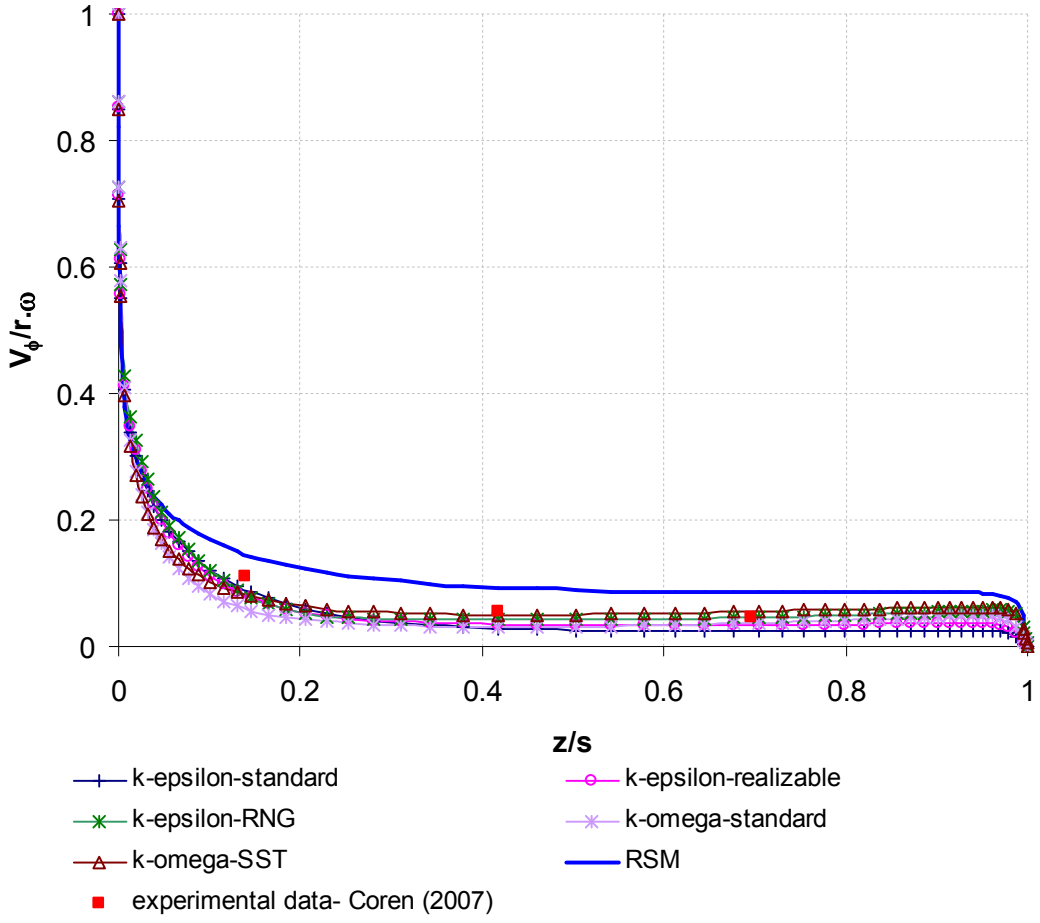

Figure 3.5: Comparison between the Axial distribution of Dimensionless Tangential Velocity for Different Turbulence Models with the Experimental Data of Coren (2007) at $r/b = 0.79$; $Re_\phi = 0.271 \times 10^7$, $C_w = 0.3 \times 10^5$, ($\lambda_T = 0.21$)

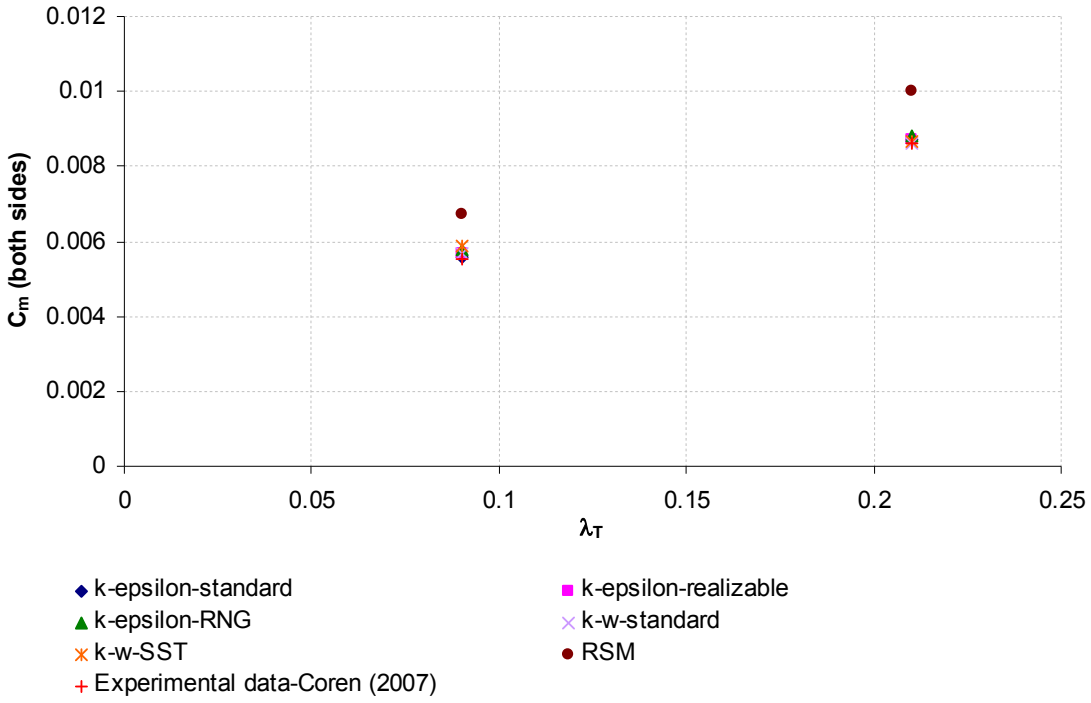

Figure 3.6: Comparison of the Moment Coefficient Results of Different Turbulence Models with the Experimental Data of Coren (2007)

It can be seen from Figures 3.2 and 3.4 that there are noticeable differences between the results obtained for the radial velocity distribution using different turbulence models. The differences are more pronounced within the boundary layers. Considering the tangential velocity and the moment coefficient, it can be observed that acceptable agreement exists between the experimental data and the simulation results (with the exception of RSM). Furthermore, it can be seen that the results of tangential velocity and moment coefficient that were obtained using different turbulence models (with the exception of RSM) show only small discrepancies. As a result, it can be concluded that the tangential velocity and moment coefficient have low sensitivity to the selection of turbulence model.

Reaching convergence was also difficult for the RNG k-ε model, and it took about three times more CPU time for reaching a converged solution compared to the standard k-ε model. The maximum number of iterations for achieving a stabilised solution for the standard and realizable k-ε and the two k-ω (standard and SST) models was about 2500. However, for the RNG model, the solution was stabilised after about 8000 iterations. This could be due to the additional non-linear terms in the governing equations of the RNG model.

Based on the simulation results, the RSM was noticeably less accurate than all other models in predicting the tangential velocity and moment coefficient, while the remaining models showed similar level of accuracy. However, RSM, standard k-ε and realizable k-ε models showed to have better predictions for radial velocity in comparison to the experimental data. In addition, although the realizable k-ε model has been shown to provide better performance for several applications including separated flows and flow features having strong rotation and vortices, it requires about twice of the CPU time and more solution features tuning to reach a converged solution than the standard k-ε model.

It is also worth commenting on the effect of near wall treatments on the moment coefficient and velocity distributions. Using the enhanced wall treatment requires sufficiently fine meshes near the walls in order to model the viscous sub-layer. This increases the total number of points and, as a result, the computational time. Therefore, another mesh was generated for use with standard wall function. The number of points for the grid independent simulation for use with the standard wall function was 18,000. The effect of near wall treatments on the velocity distribution across the cavity at $r/b = 0.79$ is shown in Figures 3.7, 3.8, 3.9 and 3.10. The radial and tangential velocities for $\lambda_T = 0.09$ are shown in Figures 3.7 and 3.8, and those for $\lambda_T = 0.21$ in Figures 3.9 and 3.10 respectively. Two wall treatment schemes were used: standard wall function and enhanced wall treatment both with the standard k-ε turbulence model (see Appendix 2 for an explanation of different near wall modelling types).

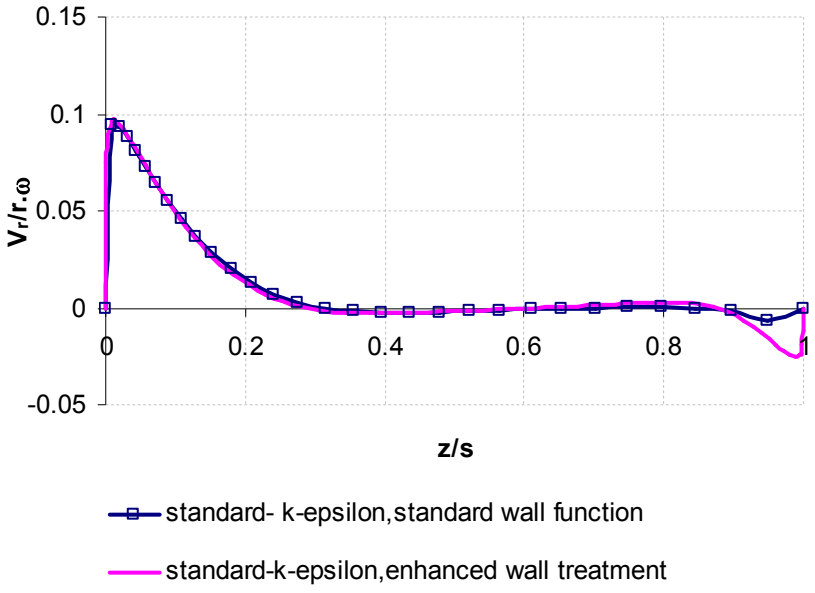

Figure 3.7: Simulation Results of Radial Velocity at *r/b* = 0.79 for Different near Wall Treatments, Using the Standard k-ε Model for $Re_\phi = 0.81 \times 10^7$, $C_w = 0.3 \times 10^5$, ($\lambda_T = 0.09$)

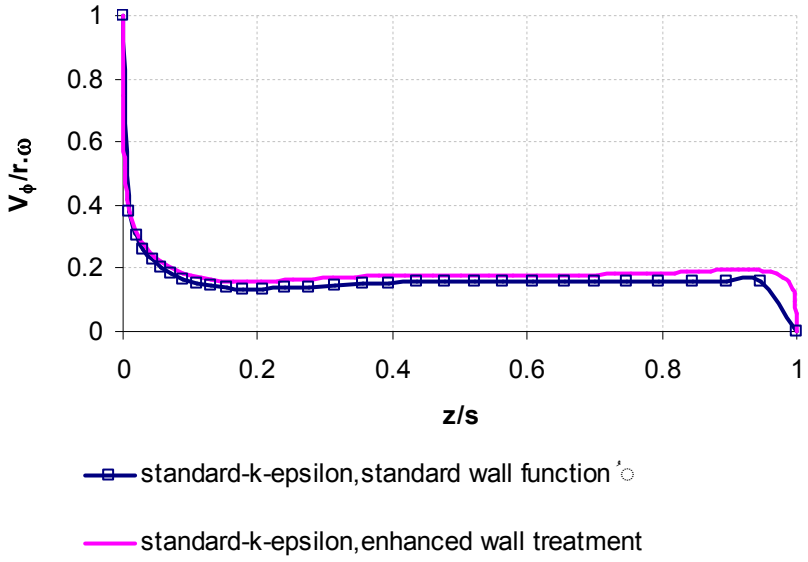

Figure 3.8: Simulation Results of Tangential Velocity at *r/b* = 0.79 for Different near Wall Treatments, Using the Standard k-ε Model for $Re_\phi = 0.81 \times 10^7$, $C_w = 0.3 \times 10^5$, ($\lambda_T = 0.09$)

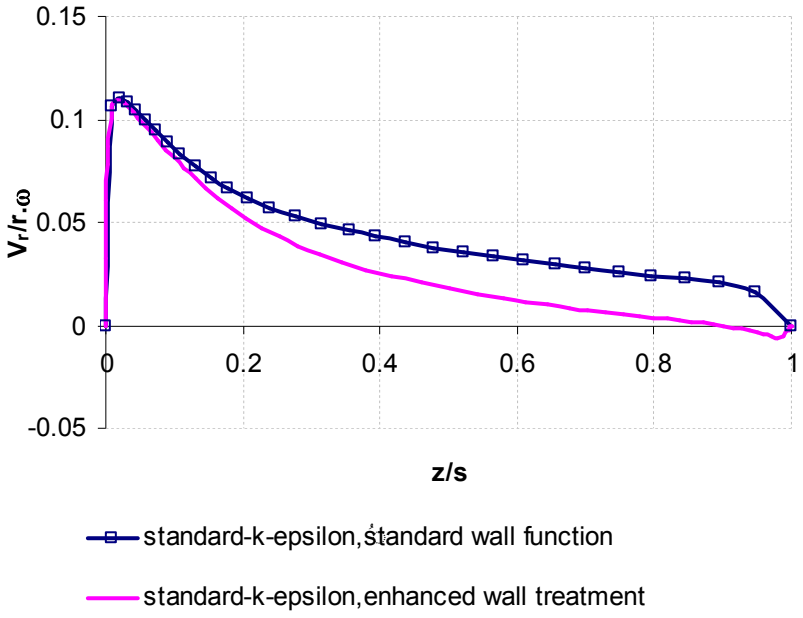

Figure 3.9: Simulation Results of Radial Velocity at *r/b* = 0.79 for Different near Wall Treatments, Using the Standard k-ε Model for $Re_\phi = 0.271 \times 10^7$, $C_w = 0.3 \times 10^5$, ($\lambda_T = 0.21$)

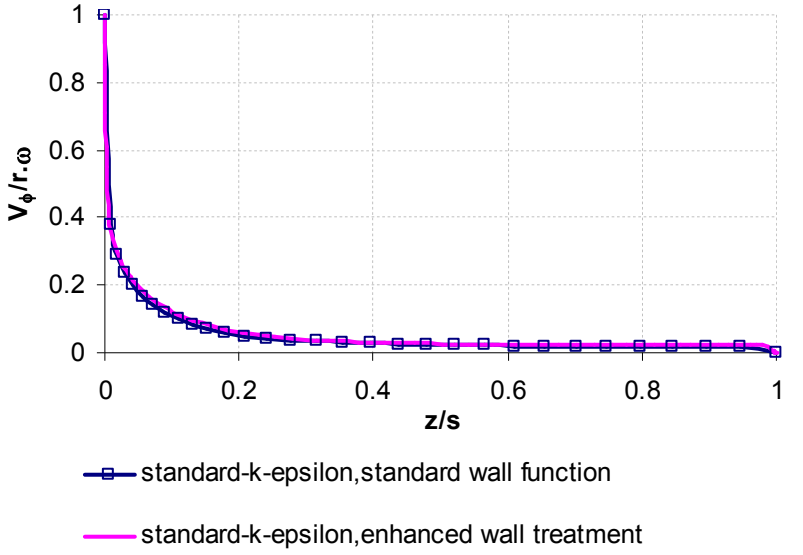

Figure 3.10: Simulation Results of Tangential Velocity at *r/b* = 0.79 for Different near Wall Treatments, Using the Standard k-ε Model for $Re_\phi = 0.271 \times 10^7$, $C_w = 0.3 \times 10^5$, ($\lambda_T = 0.21$)

For λ_T = 0.09 there is generally good agreement between the two methods of wall treatment outside the boundary layers. However, it can be seen from Figure 3.9 that the standard wall function approach fails to predict a negative radial velocity near the stator. This results in an over-prediction of radial velocity in that region, and since the radial velocity continues to increase away from the stator, this over-prediction will accordingly continue across the whole width of the cavity. However, it appears that the enhanced wall treatment is able to predict the negative radial velocity region near the stator and give results that are more consistent with the theoretical data in the literature. The better prediction of the enhanced wall treatment was not un-expected due to the improved modelling level of the near wall region in comparison with the standard wall function (see Appendix 2).

A comparison was also made between the simulation results of the moment coefficient for λ_T = 0.09 and λ_T = 0.21 using the two different near wall treatments. It was found that the standard wall function gives a lower value of the moment coefficient (by about 8%) compared to the results from the enhanced wall treatment. This happens because the standard wall function does not model the details of the laminar sub-layer and the buffer layer regions, and hence fails to accurately predict the viscous losses in those areas.

In order to further inspect the simulated results of the rotor-stator system, it is interesting to investigate the effects of inlet boundary conditions on the flow structure within the cavity and the amount of losses. Normally, attaching a pipe to the entrance of rotating cavities provides a fully developed velocity profile. Since the simulated geometry includes an inlet pipe (L = 25cm), investigation of the effects of changing its length would be of interest. As a result, a sensitivity analysis was performed by simulating another geometry with a long inlet pipe (L = 125cm). Simulations were also carried out using different turbulent intensities of I = 2%, 5%, and 10% at the inlet boundary condition to investigate the influence of turbulent intensity variations on the flow behaviour within the system. Figures 3.11 and 3.12 show respectively the dimensionless radial and tangential velocities at two radial locations of r/b = 0.31 and r/b = 0.79 for λ_T = 0.09 using different inlet pipe lengths and turbulent intensities. Figures 3.13 and 3.14 show similar comparisons for λ_T = 0.21.

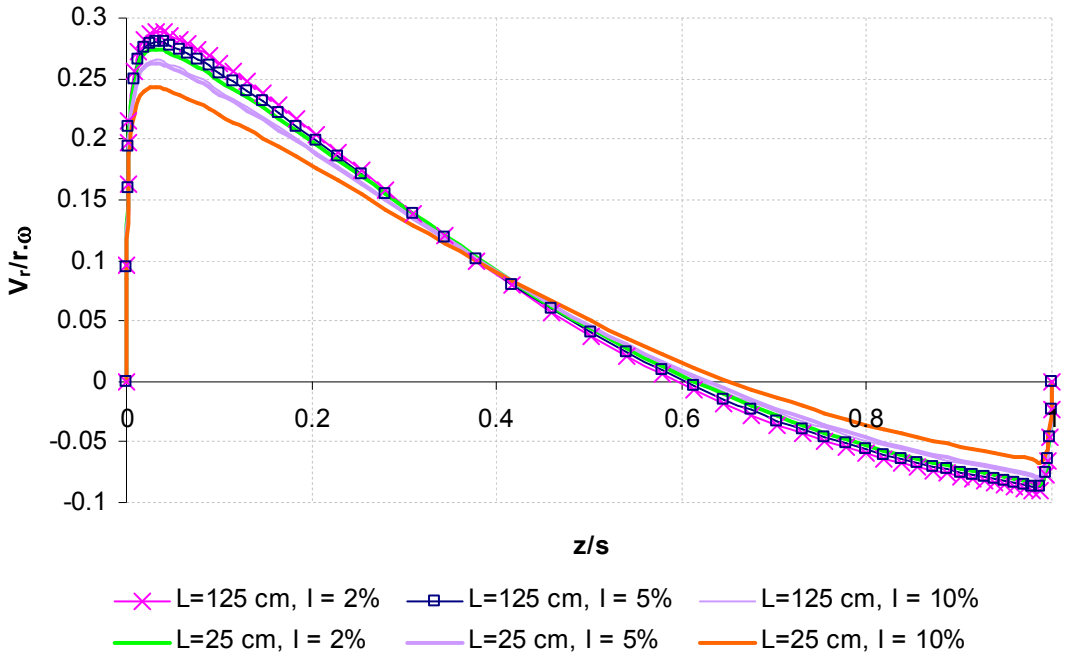

(a)

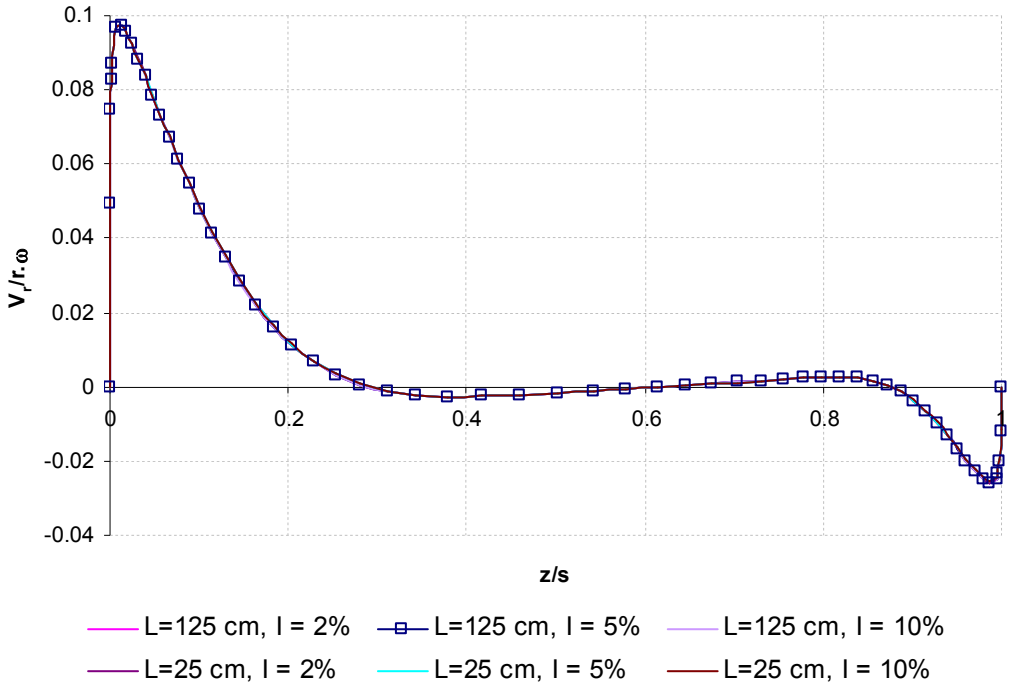

(b)

3.11:Comparison of the Radial Velocity for Different Inlet Pipe Lengths and Inlet Turbulent Intensities Using the Standard k-ε Model with Enhanced Wall Treatment for Re_ϕ = 0.81 x 107, C_w = 0.3 x 105, (λ_T = 0.09) at (a): r/b = 0.31, and (b) r/b = 0.79

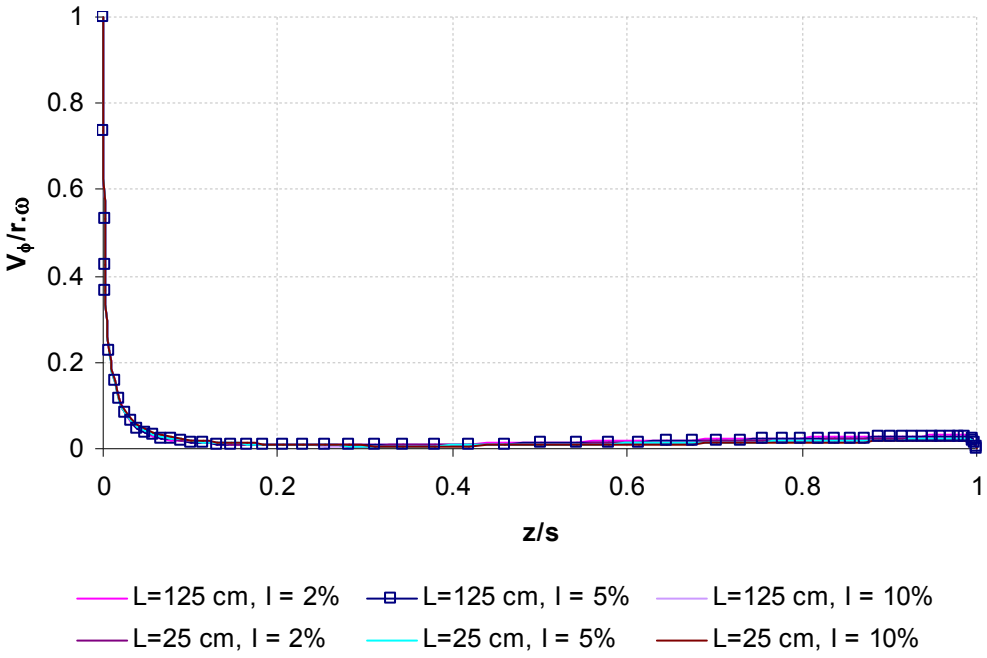

(a)

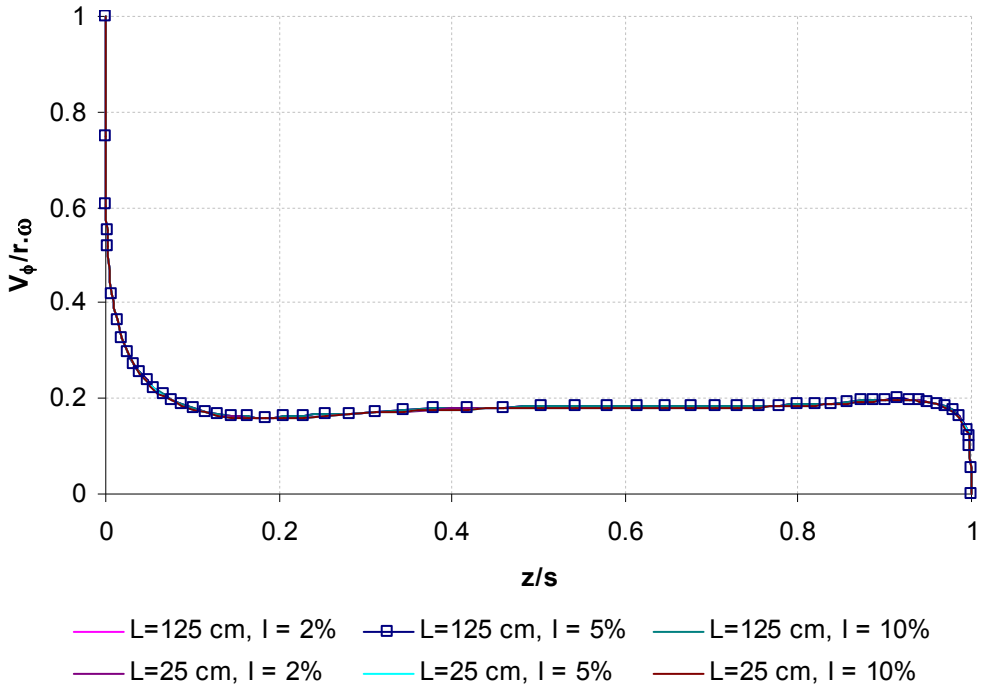

(b)

Figure 3.12: Comparison of the Tangential Velocity for Different Inlet Pipe Lengths and Inlet Turbulent Intensities Using the Standard k-ε Model with Enhanced Wall Treatment for $Re_\phi = 0.81 \times 10^7$, $C_w = 0.3 \times 10^5$, ($\lambda_T = 0.09$) at (a): $r/b = 0.31$, and (b) $r/b = 0.79$

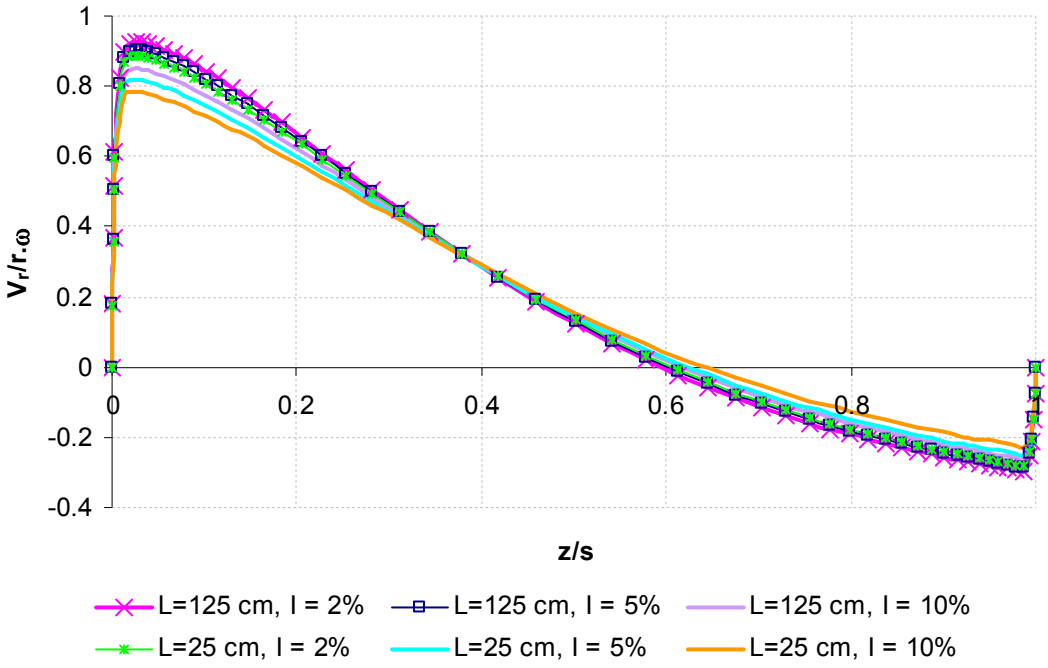

(a)

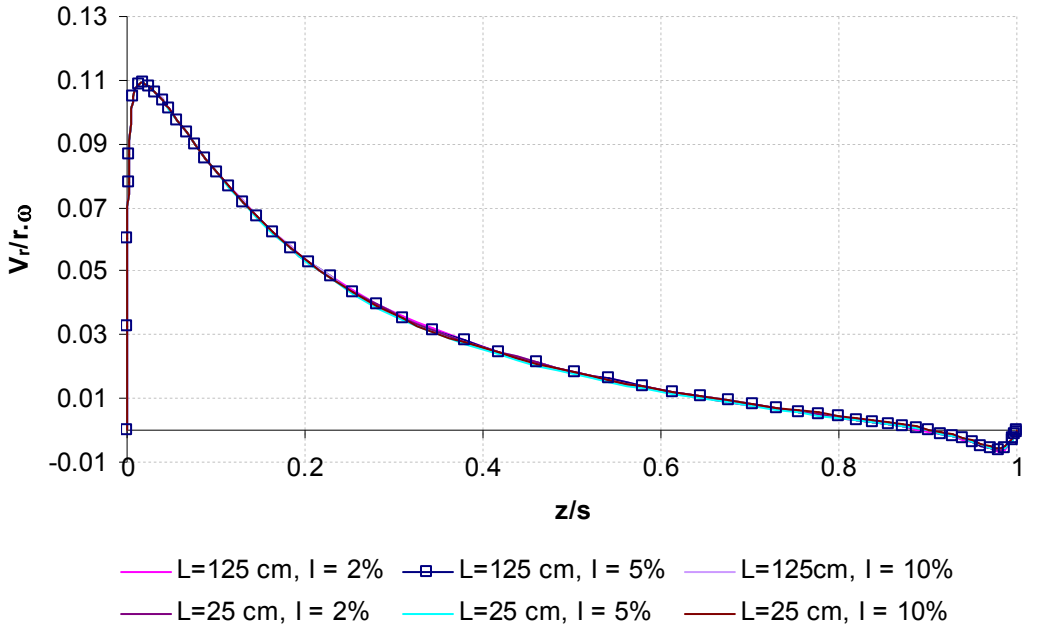

(b)

Figure 3.13: Comparison of the Radial Velocity for Different Inlet Pipe Lengths and Inlet Turbulent Intensities Using the Standard k-ε Model with Enhanced Wall Treatment for $Re_\phi = 0.271 \times 10^7$, $C_w = 0.3 \times 10^5$, ($\lambda_T = 0.21$) at (a): $r/b = 0.31$, and (b) $r/b = 0.79$

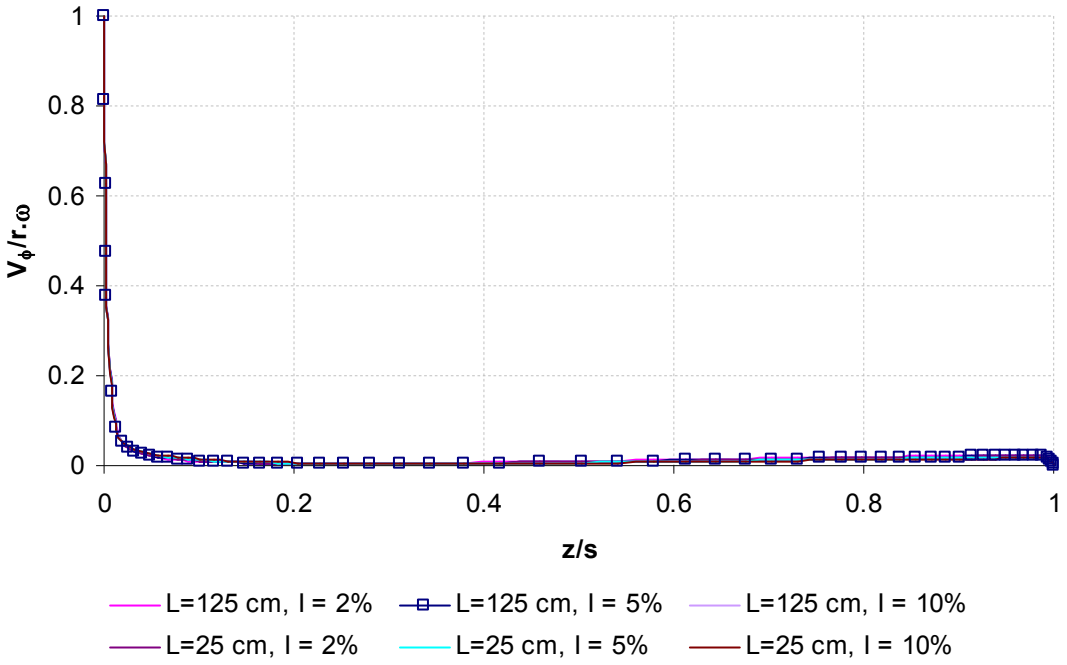

(a)

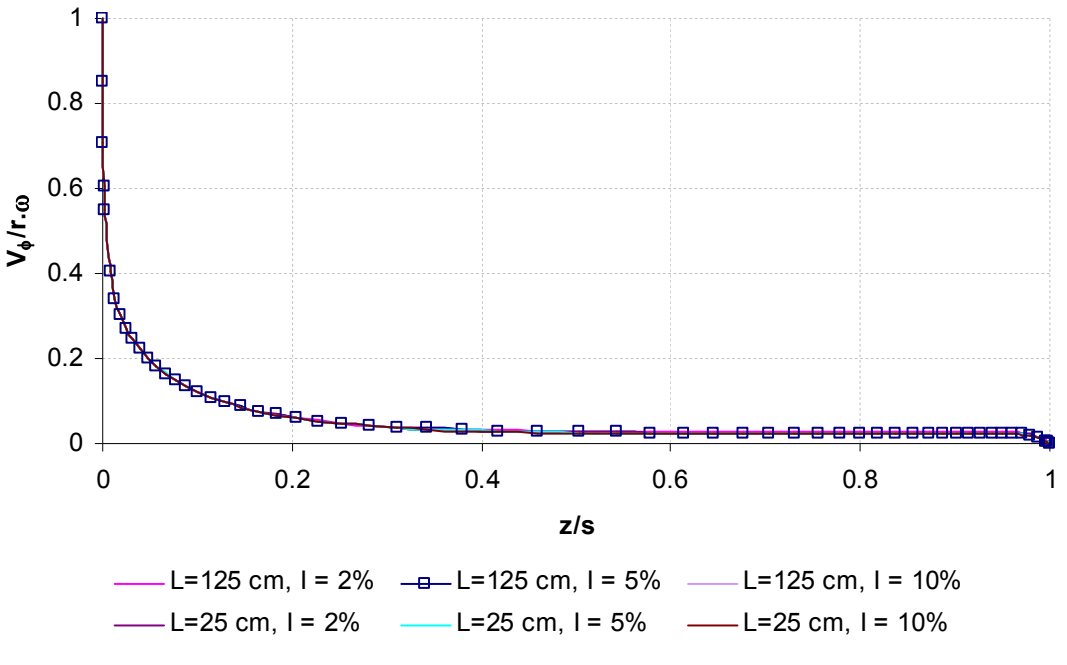

(b)

Figure 3.14:Comparison of the Tangential Velocity for Different Inlet Pipe Lengths and Inlet Turbulent Intensities Using the Standard k-ε Model with Enhanced Wall Treatment for Re_ϕ = 0.271 x 10^7, C_w = 0.3 x 10^5, (λ_T = 0.21) at (a): *r/b* = 0.31, and (b) *r/b* = 0.79

It can be seen that changing the inlet pipe length and the inlet turbulent intensities does not change the tangential velocity distribution, even for small radial locations where the effects of entering fluid have not fully vanished. Considering the radial velocity distribution, it appears that changing the inlet pipe length does not change the radial velocity profile at higher radii. However, small differences could be observed at lower radial locations close to the entrance of the cavity. Regarding the inlet turbulent intensity, it appears that its variations have no effect on the radial velocity distribution using the long pipe (L = 125cm). This is because flow has the chance to eliminate the irregularities of high-turbulence before entering the cavity. In contrast, for the short pipe (L = 25cm), increasing the inlet turbulent intensity decreases the peak of radial velocity in the boundary layer attached to the rotor.

Tables 3.1 and 3.2 show a comparison between the simulation results of the moment coefficient for different inlet pipe lengths and inlet turbulent intensities under the two mentioned flow conditions. It can be seen that changing both the inlet pipe length and the inlet turbulent intensity do not affect the moment coefficient results.

Table 3.1: Comparison of Moment Coefficient for Different Inlet Pipe Lengths and Different Inlet Turbulent Intensities Using the Standard k-ε Model with Enhanced Wall Treatment for $Re_\phi = 0.81 \times 10^7$, $C_w = 0.3 \times 10^5$, ($\lambda_T = 0.09$)

	C_m (two sides)
L = 125 cm, I = 2%	0.005766
L = 125 cm, I = 5%	0.005763
L = 125 cm, I = 10%	0.005761
L = 25 cm, I = 2%	0.005768
L = 25 cm, I = 5%	0.005767
L = 25 cm, I = 10%	0.005766

Table 3.2: Comparison of Moment Coefficient for Different Inlet Pipe Lengths and Different Inlet Turbulent Intensities Using the Standard k-ε Model for $Re_\phi = 0.271 \times 10^7$, $C_w = 0.3 \times 10^5$, ($\lambda_T = 0.21$)

	C_m (two sides)
L = 125 cm, I = 2%	0.00876
L = 125 cm, I = 5%	0.00875
L = 125 cm, I = 10%	0.00874
L = 25 cm, I = 2%	0.00875
L = 25 cm, I = 5%	0.00874
L = 25 cm, I = 10%	0.00873

3.4 Validation Case No.2: Numerical Analysis of Vaughan (1987)

In this case, validation of the code is given using the numerical calculations of Vaughan (1987). Vaughan compared his numerical results with the experimental measurements of Pincombe and El-Oun (1986). Air at an ambient temperature enters a rotor-stator cavity through a gap at the centre of the stator and leaves it from a periphery in the shroud. In addition to the inlet throughflow, there is an external flow above the rotor-stator system. Figure 3.15 shows a schematic diagram of the geometry with the following dimensions: s = 19mm, b = 190mm (G = 0.1), a = 19mm, r_{sh} = 186mm, r_e = 233mm, s_c = 1.9mm. Computations were carried out for the following three flow conditions: 1- C_w = 1000 and $Re_\phi = 8 \times 10^5$ (λ_T = 0.019), 2- C_w = 2000 and $Re_\phi = 8 \times 10^5$ (λ_T = 0.038), and 3- C_w = 1000 and $Re_\phi = 4 \times 10^5$ (λ_T = 0.033). For all cases, the external flow Reynolds number was 6×10^5, which is calculated using Equation 3.1.

$$Re_w = \frac{\rho u_e b}{\mu} \qquad 3.1$$

Where u_e is the velocity of external flow.

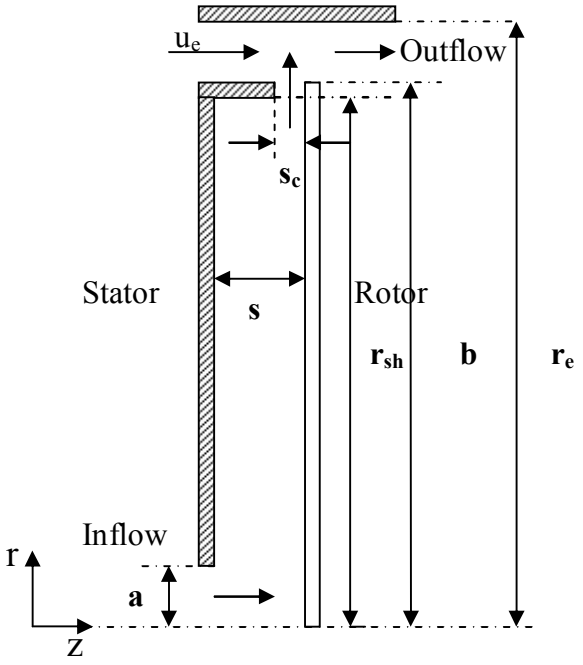

Figure 3.15: Schematic Diagram of Validation Test Case No.2

Meshes were generated for use with the enhanced wall treatment. The grid independence study was also performed. There is an extended geometry at the outlet and an attached pipe at the inlet, which provides sufficient length for a fully developed velocity profile.

Although Vaughan considered the fluid to be incompressible, it is worth comparing his computations with computations considering the fluid to be compressible, and comparing both results with the experimental measurements. Hence, the ideal gas law was used for modelling the density, and Sutherland's law for modelling the viscosity. The inlet mass flow rate and rotational speed for each of the flow conditions were calculated using the relevant mass flow coefficient and rotational Reynolds numbers. 2^{nd} discretisation was used for all variables. The convergence criteria were the same as those used in the first validation case. The six turbulence models that were used in previous section were used here as well.

Vaughan plotted the variations of β/β^* for different turbulent flow parameters in the plane midway through the cavity and at r/b = 0.5. β is the dimensionless tangential

velocity or swirl ratio, and β^* is the value of β for zero throughflow. The figure compares the experimental measurements of Pincombe and El-Oun (1986) and the correlations of Daily *et al*. (1964) and Owen (1988) with the numerical calculations of Vaughan.

Daily *et al*.'s correlation is based on their measurements of the core rotation at three different radius ratios of *r/b* = 0.469, 0.648, and 0.828 and at three gap ratios of *G* = 0.0273, 0.069, 0.124 (see Equation 3.2).

$$\frac{\beta}{\beta^*} = \left(1 + 12.74 \frac{\lambda_T}{(\frac{r}{b})^{\frac{13}{5}}} \right)^{-1} \qquad 3.2$$

The measured values of β^* for the three gap ratios are 0.475, 0.45, and 0.42 respectively.

Owen (1988) suggested two correlations for core rotation in turbulent flows (Equations 3.3 and 3.4); each correlation corresponds to a specific approximation method for calculating β. Based on Owen's approximate theory (Owen, 1988), β^* was taken as 0.426, and it is this value that was used in Equation 3.2 by Vaughan. This is a reasonable estimate of β^* for $G = 0.1$, considering Daily *et al*.'s measurements.

$$(1-\beta)^{1.6}(1-0.51\beta) - 0.638\beta^{0.8} = 4.57\lambda_T(\frac{r}{b})^{-2.6} \qquad 3.3$$

$$\mathrm{sgn}(1-\beta)\left|1-\beta\right|^{1.6} - \beta^{0.8} = \frac{\lambda_T}{0.1395(\frac{r}{b})^{2.6}} \qquad 3.4$$

Figure 3.16 compares the simulation results of different turbulence models with the experimental measurements of Pincombe and El-Oun (1986), the correlations of Daily *et al*. (1964) and Owen (1988), and the numerical calculations of Vaughan (1987), zooming in on the regions where the flow conditions of this case are located.

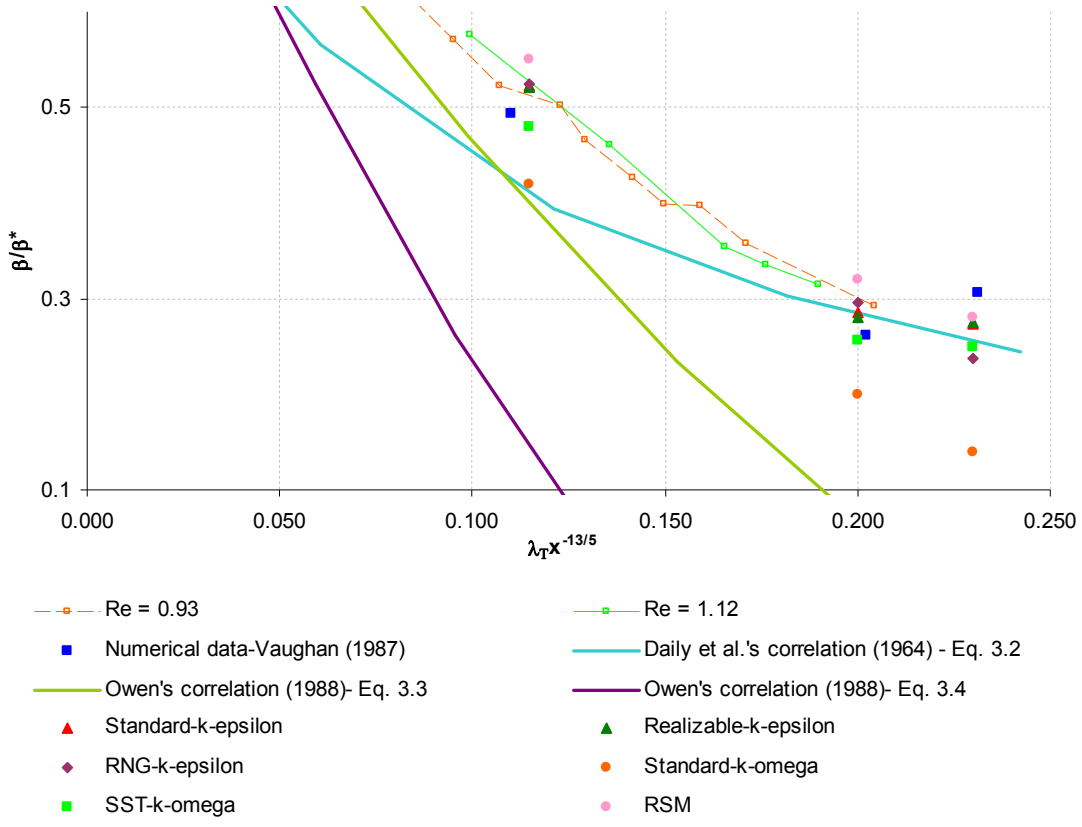

Figure 3.16: Comparison of β/β^* for the Simulation Results Using Different Turbulence Models with the Experimental Measurements of Pincombe and El-Oun (1986) (for $Re_\phi = 0.93 \times 10^5$ and 1.12×10^5), the Correlations of Daily et al. (1964) and Owen (1988), and Numerical Calculations of Vaughan (1987)

It can be seen that all of the turbulence models except the standard k-ω have acceptable results comparable with the experimental measurements of Pincombe and El-Oun. Regarding the standard k-ω model, it is known that the ω-equation in the standard k-ω model shows a strong sensitivity to the values of ω in the free stream region outside the boundary layer (Menter, 1994). This could be the reason for the weak predictions of the standard k-ω model. However, it should be noted that dividing β over β^* approximately doubles the difference between the results of dimensionless tangential velocity for different turbulence models. The observable differences between the data may be understood by plotting β for different turbulence models where $Re_\phi = 8 \times 10^5$ and $C_w = 2000$ (see Figure 3.17). Accordingly, it can be seen that the difference between the results of the standard k-ω and the other models becomes less noticeable when β is the subject of comparison.

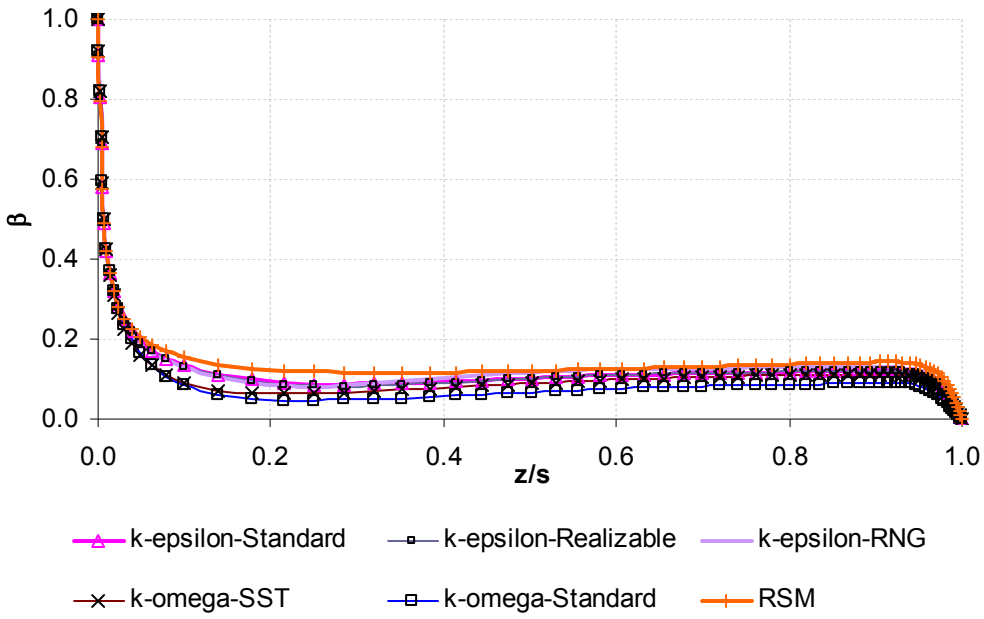

Figure 3.12: Comparison of β at r/b = 0.5 for Different Turbulence Models; $Re_\phi = 8 \times 10^5$, $C_w = 2000$
Note: *z/s* = 0 is located on the rotor.

Table 3.3 compares the simulation results of the moment coefficient using different turbulence models with the correlations of Daily *et al.* (Equation 2.11) and Owen (Equation 2.15) for the three simulated flow conditions. According to the results given in Table 3.3, the variations of the moment coefficient using different turbulence models can be considered to be negligible.

Table 3.3: Comparison between the Rotor Moment Coefficient results of Different Turbulence Models and Daily et al.'s and Owen's Correlations

Turbulence Model	C_m (One-sided)		
	$Re_\phi = 8 \times 10^5$ $C_w = 1000$	$Re_\phi = 8 \times 10^5$ $C_w = 2000$	$Re_\phi = 4 \times 10^5$ $C_w = 1000$
Standard- k-ε	0.003003	0.003395	0.004151
Realizable- k-ε	0.003007	0.003423	0.004149
RNG- k-ε	0.00302	0.003421	0.004153
Standard- k-ω	0.002885	0.00325	0.004042
SST- k-ω	0.002958	0.003327	0.004108
RSM	0.0033	0.00375	0.0048
Daily et al.'s correlation (Equation 2.11) (Averaged 3 % of difference from the results of Standard k-ε model)	0.003	0.0034	0.0038
Owen's correlation (Equation 2.15)	0.0025	0.00333	0.00363

Similar to the first validation case, another mesh was generated to use with the standard wall function using the standard k-ε model. Tables 3.4 and 3.5 compare the results of the swirl ratio and the moment coefficient for the enhanced wall treatment and the standard wall function for the three flow conditions explored in this section. It can be seen that the differences between the values of the moment coefficient and the swirl ratio, using the two near wall treatments, are not significant.

Table 3.4: Comparison between the Simulation Result of Swirl Ratio Using the Standard k-ε Model and Different Near Wall Treatments

Model	β		
	$Re_\phi = 8 \times 10^5$ $C_w = 1000$	$Re_\phi = 8 \times 10^5$ $C_w = 2000$	$Re_\phi = 4 \times 10^5$ $C_w = 1000$
Standard- k-ε- Enhanced wall treatment	0.22	0.114	0.14
Standard- k-ε - Standard wall function	0.2	0.09	0.12

Table 3.5: Comparison between the Simulation Results of Moment Coefficient Using the Standard k-ε Model and Different Near Wall Treatments

Model	C_m		
	$Re_\phi = 8 \times 10^5$ $C_w = 1000$	**$Re_\phi = 8 \times 10^5$ $C_w = 2000$**	**$Re_\phi = 4 \times 10^5$ $C_w = 1000$**
Standard- k-ε- Enhanced wall treatment	0.003	0.003395	0.0041
Standard- k-ε - Standard wall function	0.0029	0.0033	0.004

3.5 Validation Case No.3: Experimental Measurements of Daily et al. (1964)

This case is taken from the experiments of Daily *et al*. (1964). Air at an ambient temperature enters a rotor-stator cavity axially through an opening between the stator and the shaft and leaves the cavity radially through a gap between the shroud and the stator. Figure 3.18 shows a schematic diagram of the cavity, with the following dimensions: s = 15.83mm, b = 230.2mm (G = 0.0687), a = 37.6mm, r_s = 25.4mm, and s_c = 3.57mm. The dimensionless flow conditions are: $Re_\phi = 6.9 \times 10^5$ and C_w = 472 (λ_T = 0.01).

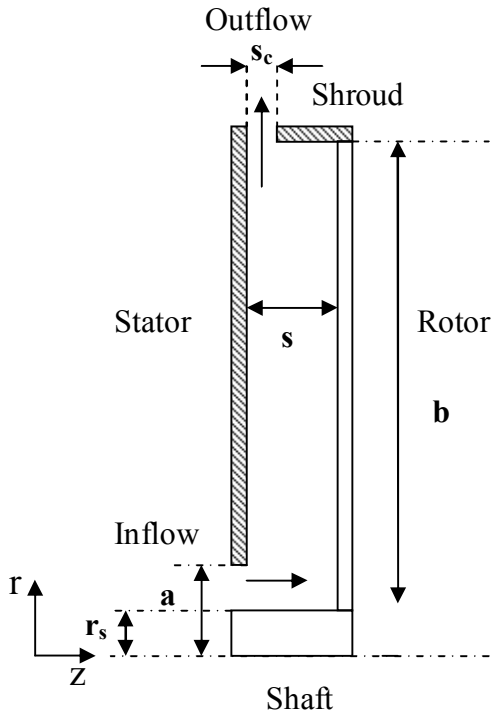

Figure 3.18: Schematic Diagram of Validation Test Case No.3

Meshes were generated for use with the enhanced wall treatment. The grid independence study was also performed. An extended geometry was used at the outlet and an attached pipe at the inlet. The fluid was taken to be compressible; the ideal gas law was used for modelling the density and Sutherland's law was used for modelling the viscosity. The inlet mass flow rate and the rotational speed of the rotor were set from the rotational Reynolds number and the mass flow coefficient. 2nd order discretisation was used for all variables. Similar to the previous cases, six turbulence models were examined. The convergence criteria are the same as those used in previous sections.

Figure 3.19 compares the simulation results of the non-dimensional radial velocity with the experimental results of Daily *et al*. at r/b = 0.648 and r/b = 0.828. Figure 3.20 illustrates similar comparisons for the dimensionless tangential velocity. Additionally, Table 3.6 compares the moment coefficient obtained using different turbulence models with the results obtained using Daily *et al*.'s (Equation 2.11) and Owen's (Equation 2.15) correlations.

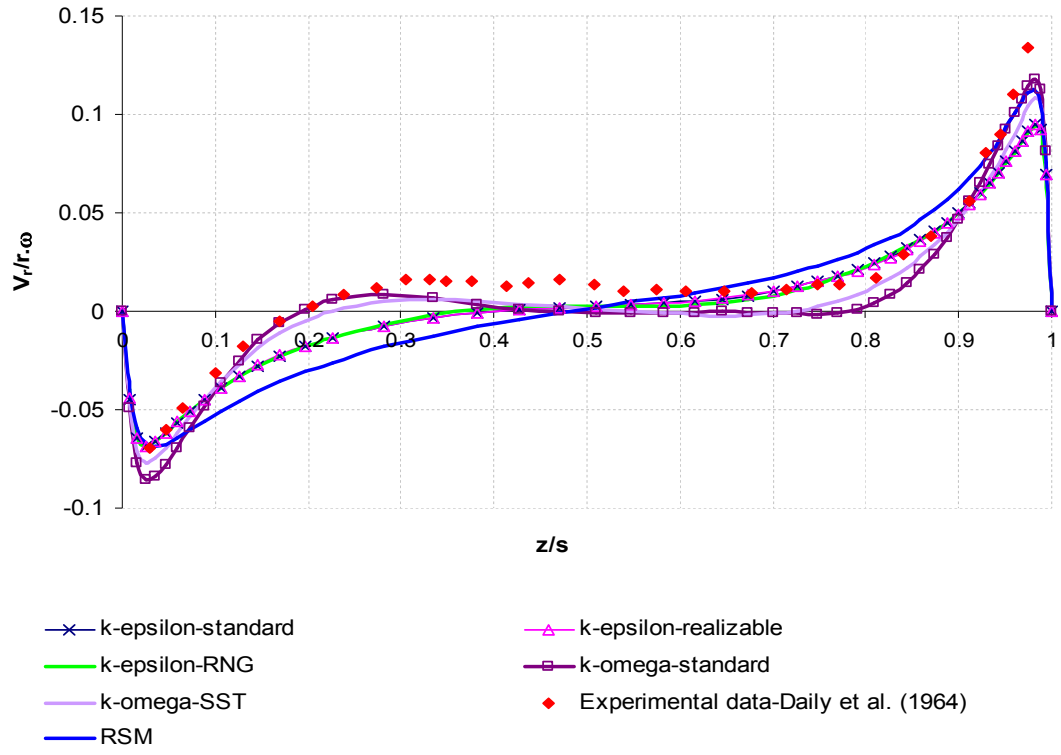

(a)

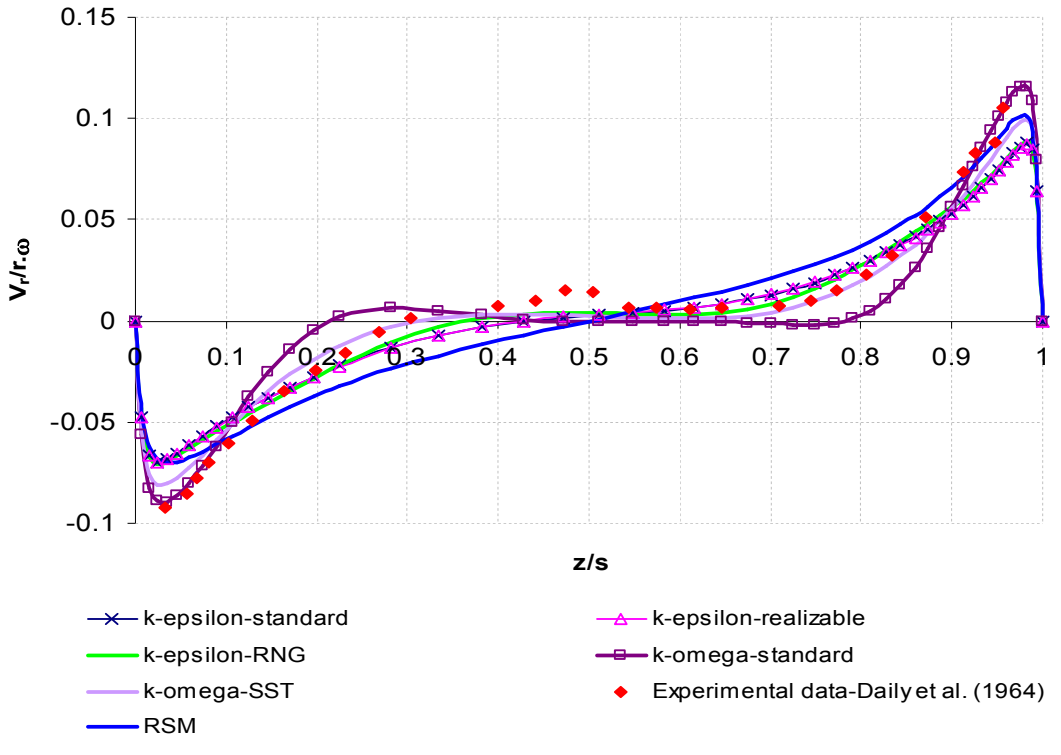

(b)

Figure 3.19: Comparison of the Radial Velocity Using Different Turbulence Models with the Experimental Data of Daily et al. (1964) at (a): *r/b*=0.648 and (b): *r/b*=0.828
Note: *z/s* = 0 is located on the rotor. This is also the case for Figure 3.20.

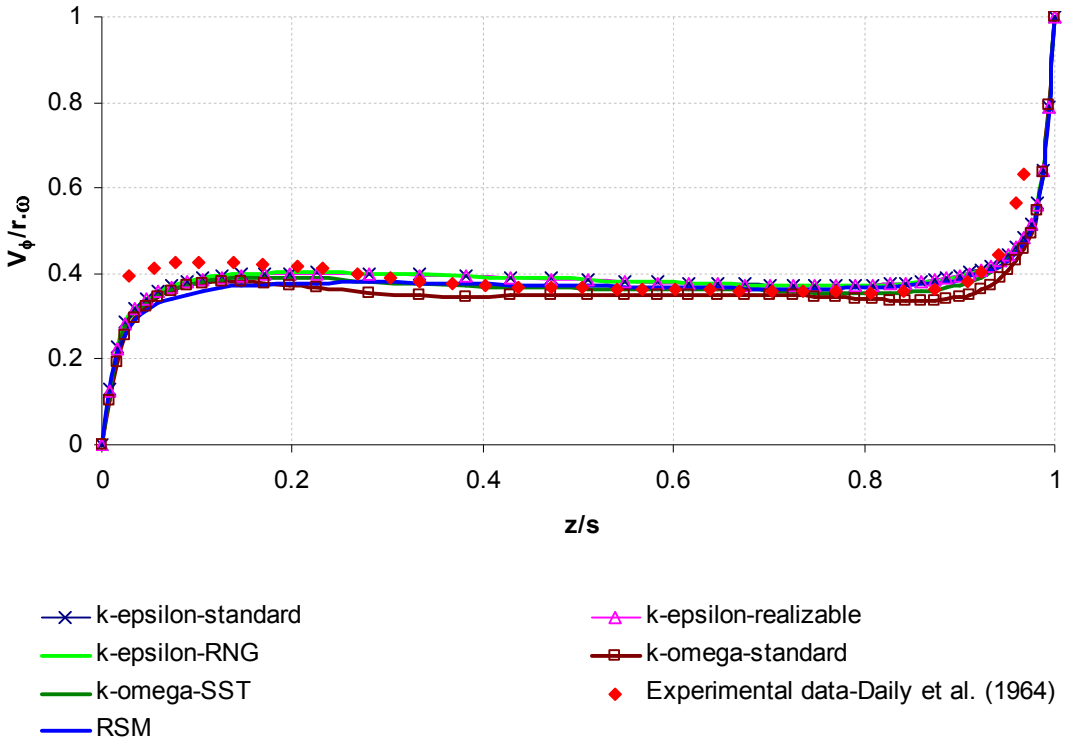

(a)

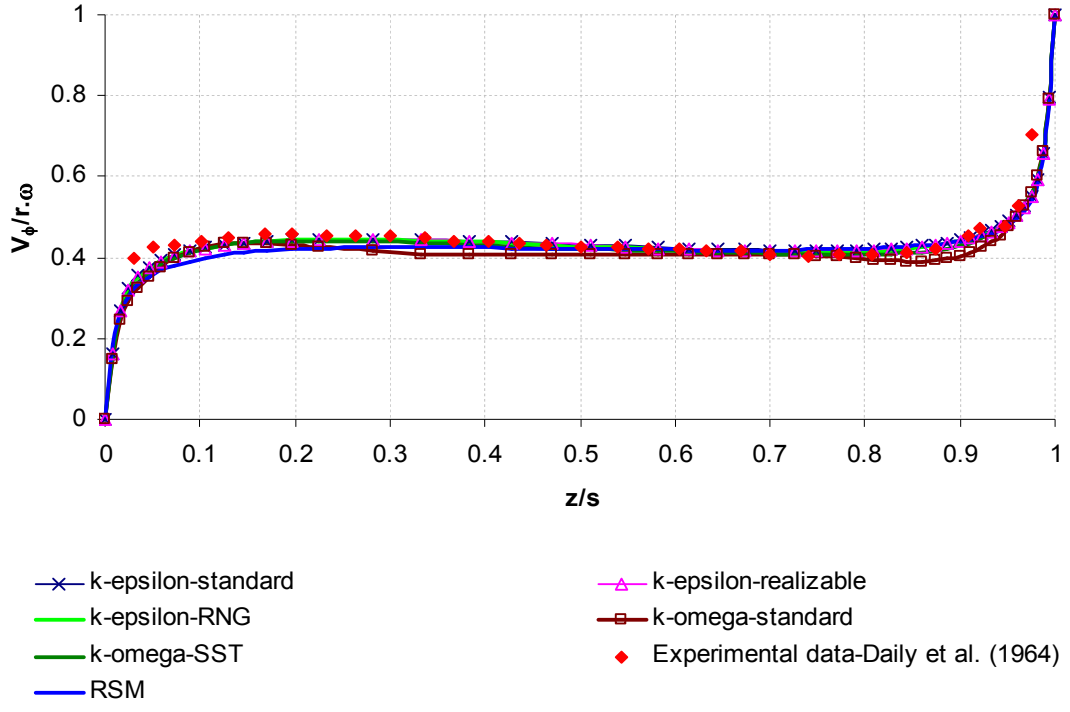

(b)

Figure 3.20: Comparison of the Tangential Velocity Using Different Turbulence Models with the Experimental Data of Daily et al. (1964) at (a): *r/b*=0.648 and (b): *r/b*=0.828

Table 3.6: Comparison between the Rotor Moment Coefficients of Different Turbulence Models, with Daily et al.'s and Owen's Correlations

Model	C_m (One-sided)
Standard- k-ε	0.003308
Realizable- k-ε	0.003313
RNG- k-ε	0.003314
Standard- k-ω	0.00323
SST- k-ω	0.003285
RSM	0.003815
Daily et al.'s correlation (Equation 2.11)	0.0029
Owen's correlation (Equation 2.15)	0.00423

Based on the results displayed in Figures 3.19 and 3.20, all of the turbulence models show similar predictions for the radial velocity outside the boundary layer. The results show good agreement with the experimental data. However, the standard-k-ω and SST-k-ω models have better predictions inside the boundary layers. Considering the tangential velocity, the predictions of all the models are broadly similar and show good agreement with the experimental measurements.

Regarding the moment coefficient, it can be seen from Table 3.6 that the different models have extremely similar predictions with the exception of the RSM. It can be seen that RSM has an over-prediction for the moment coefficient and, as it was explained in the first validation case, this could be due to the closure assumptions used within FLUENT to model various terms in the transport equations for Reynolds stresses. Also, as it was concluded in the previous validation cases, moment coefficient has low sensitivity to the selected turbulence model. In addition, it appears that both the simulation results and the results obtained from Owen's correlation overestimate the moment coefficient in comparison with Daily *et al.*'s correlation.

Similar to the previous validation cases, another simulation was implemented using the standard k-ε model with standard wall function, and the results were compared with the results of the standard k-ε model with enhanced wall treatment. Hence, another mesh was produced for use with the standard wall function. Figures 3.21 and 3.22 display the

non-dimensional radial and tangential velocity distributions at two radial locations of *r/b* = 0.648 and *r/b* = 0.828 using the two mentioned near wall treatments. A comparison of the moment coefficient for the two near wall treatments is also given in Table 3.7.

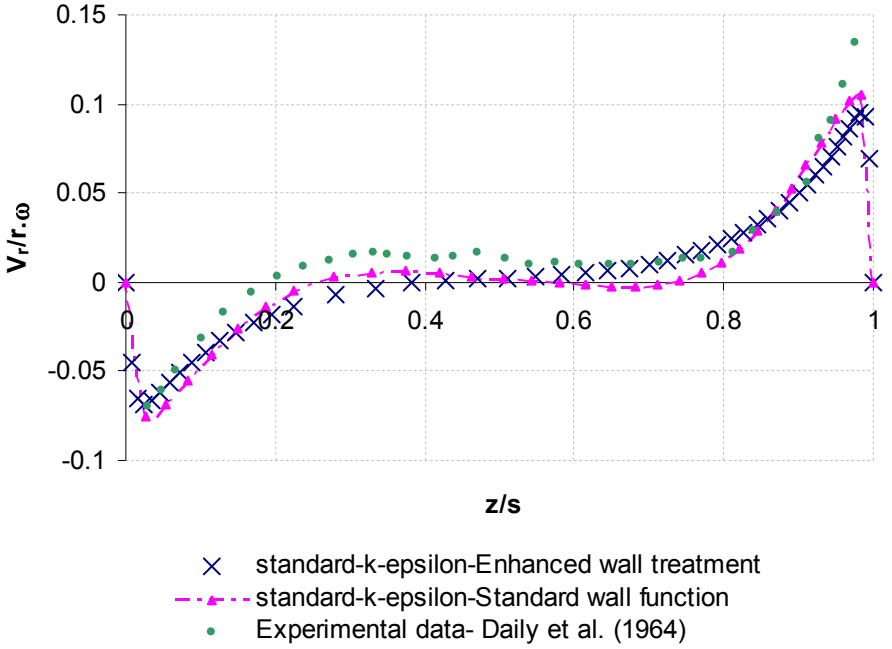

(a)

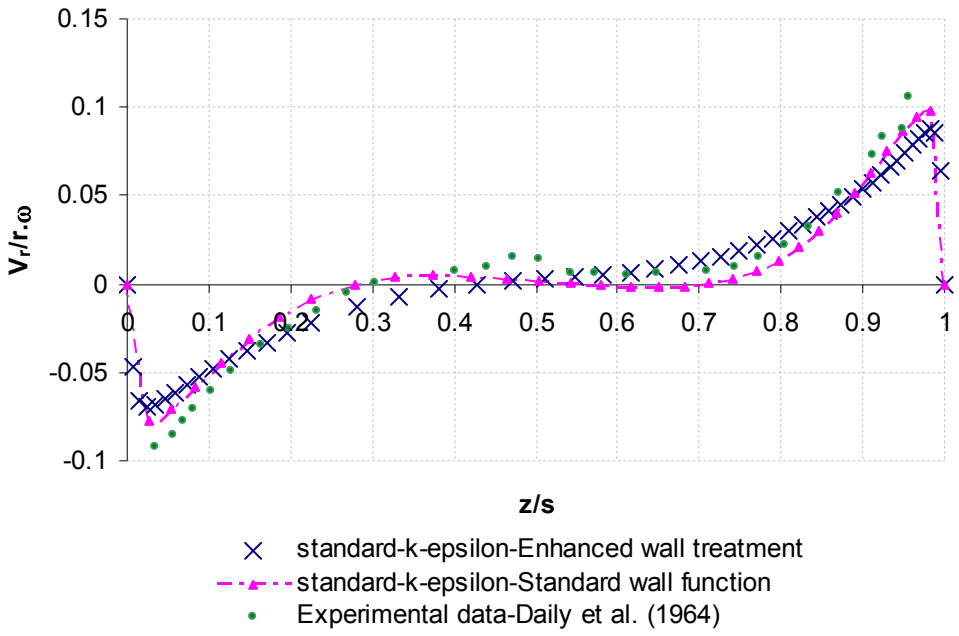

(b)

Figure 3.21: : Comparison of Axial Variation of Radial Velocity Using Standard k-ε Model between Enhanced Wall Treatment and Standard Wall Function at (a): r/b=0.648 and (b): r/b = 0.828

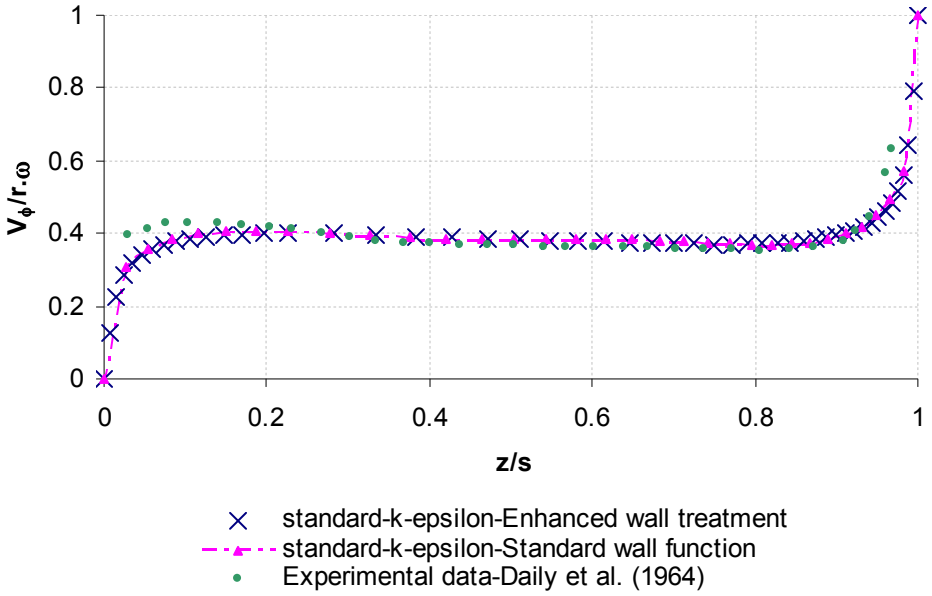

(a)

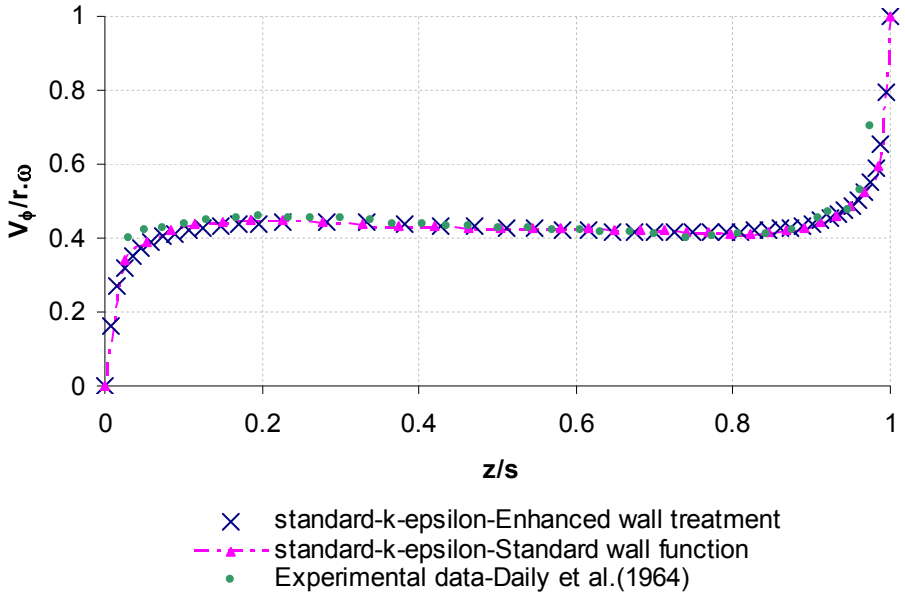

(b)

Figure 3.22: Comparison of Axial Variation of Tangential Velocity Using Standard k-ε Model between Enhanced Wall Treatment and Standard Wall Function at (a): *r/b*=0.648 and (b): *r/b* = 0.828

Table 3.7: Comparison of Rotor Moment Coefficients using standard k-ε Model between Enhanced Wall Treatment and Standard Wall Function

Model	C_m
Standard-k-ε- Enhanced wall treatment	0.0033
Standard-k-ε- Standard wall function	0.0032

According to Figures 3.21 and 3.22, the results of the two near wall treatments do not show significant differences. This is also confirmed in Table 3.7, which compares the simulation results of the moment coefficient for the two near wall treatments.

3.6 Summary

Three validation cases were selected from the literature and simulated in this chapter. Simulations were performed using six different turbulence models, including the RSM.

Based on the results gathered in this chapter, the moment coefficient showed a relatively low sensitivity to the selection of turbulence model (with the exception of RSM). The RSM noticeably over-predicts the moment coefficient of the disc. In addition, the results obtained using RSM for the radial and tangential velocity distributions were no better than the simpler linear eddy viscosity models. Comparing the results obtained by k-ε and k-ω models, it was found that k-ω models have similar level of accuracy for calculating the disc moment coefficient in comparison with other two equation turbulence models. However, the number of iterations for reaching a converged solution, in particular, for the SST k-ω model was about twice of that for the standard k-ε model. Regarding the three types of the k-ε models, the RNG k-ε showed poor predictions for the radial and tangential velocity distributions of the first validation case. Also, the number of iterations for reaching a converged solution using the RNG k-ε model was about three times more than of that for the standard k-ε model. Analysis of

the results obtained by the standard k-ε and the realizable k-ε showed acceptable predictions for tangential and radial velocity distributions in the three validation cases. While both models showed similar level of accuracy, realizable k-ε model required twice of the required time and more solution features tuning to reach a converged solution than the standard k-ε model. Based on the above considerations, it would appear that the standard k-ε model offers the best combination of computational accuracy combined with simplicity of reaching convergence and acceptable computational costs. Hence, this model was selected as the turbulence model for the simulations in this thesis. However, since the flow in the protruded rotor-stator cavity is highly three-dimensional and the effects of rotation and boundary layer separation complicate the flow phenomena in vicinity of the bolts, the validity of the results obtained by the standard k-ε model will be re-examined in Chapter 5.

Comparison was also made to examine the effects of near wall treatments on the velocity distributions and moment coefficient. Accordingly, the standard wall function and enhanced wall treatment were applied to the simulations using the standard k-ε model. It was found that simulations using the enhanced wall treatment predicted the moment coefficient and the tangential and radial velocities more accurately, particularly in the boundary layers, than the standard wall function. Therefore, the enhanced wall treatment is selected as the near wall function for modelling the near wall regions of the rotor-stator system with mounted bolts.

4. Plain disc simulations

4.1 Introduction

In this chapter the simulation results of the plain disc configuration (i.e. the rotor-stator system without protrusions) are investigated. This chapter extends the numerical analysis of the plain disc cavity investigated in Section 3.2 to different flow conditions and tries to gather all the fluid flow information that can be found from the numerical simulation of the system. Before any attempt can be made to analyse the effects of protrusions on the flow structure in a rotor-stator cavity, flow physics and the amount of losses should be examined in the plain disc system. Such an investigation provides baseline data to study the impacts of adding protrusions to the system. Complete analysis of different aspects of flow for the plain disc system under different flow conditions is therefore essential.

The chapter is composed of six sections. Section 4.2 describes the simulation procedure for the two-dimensional plain disc system. In Section 4.3, simulations of the complete system (two-sided cavity) are provided, and the results of the disc moment coefficient for the rear and front sides of the cavity are compared. This analysis examines the possibility of simulating only one side of the cavity and reducing the mesh size by 50%. Section 4.4 illuminates different flow aspects of the rotationally dominated and throughflow dominated regimes. The moment coefficient of the plain disc system is presented for different flow conditions in Section 4.5. Finally, Section 4.6 summarises the chapter.

4.2 Simulation procedure

The geometry of the plain disc system is the same as the geometry used by Coren (2007), which was explained in Section 3.2. Similarly, two-dimensional simulations have been used in this chapter due to the axially symmetric geometry of the plain disc

configuration. Figure 4.1 shows a schematic diagram of the simulated system with a cut of the generated grids. There is an extended geometry at the outlet, and a pipe attached to the inlet. A 200 x 60 mesh in the *r*-*z* plane proved to be sufficient to get grid-independent solutions using the enhanced wall treatment. The boundary conditions are summarised in Table 4.1. A more detailed explanation of the selected boundary conditions and the convergence criteria were given in Section 3.2, as well as in Appendix 1. Based on the results described in Chapter 3, the standard k-ε model with enhanced wall treatment was used for the simulations in this and the following chapters. However, for the three-dimensional rotor-stator system with protrusions, simulations were also carried out using the realizable k-ε, SST-k-ω and RSM models, in order to validate the accuracy of the standard k-ε model in the three-dimensional system where the effects of rotation and boundary layer separation simultaneously exist in the vicinity of the bolt (see Section 5.6).

Different flow conditions were used for the simulations, providing a large database for analysis. The flow conditions are grouped into two matrices with nominal values of throughflow Reynolds numbers: C_w = 0.3 x 10^5, and C_w = 10^5. Rotational Reynolds numbers range from 0.171 x 10^7 to 1.61 x 10^7. The flow conditions were obtained from the experimental measurements carried out by Miles (2011), which cover a range of non-dimensional parameters found in modern gas turbine engines. The data are given in Table 4.2.

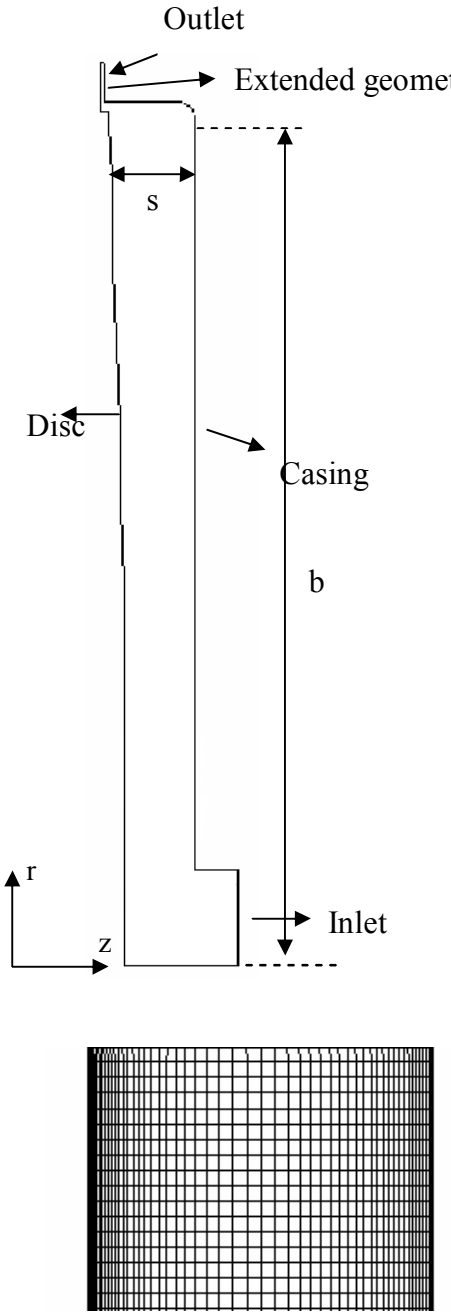

Figure 4.1: Schematic Diagram of the Two-dimensional Simulated Geometry with a Cut of Generated Grids Between the Rotor and the Stator

Table 4.1: Boundary and Simulation Conditions of the Plain Disc System

Solution methods	2nd order discretisation scheme set for all variables
Material	Air, ideal gas is used for modelling density and Sutherland's law used for modelling viscosity, constant specific heat capacity of 1006.43 J/kg K
Rotor	Adiabatic rotating wall at speed of ω
Stator, shroud, pipe	Adiabatic Stationary wall
Inlet	Pressure inlet, total pressure and total temperature are set from experimental data. Hydraulic diameter of 50 mm, and turbulent intensity of 5%
Outlet	Pressure outlet, static pressure is set so that the pressure difference of the inlet and outlet provides the desired mass flow rate

Table 4.2: Matrix of Flow Conditions for the Plain Disc System (Miles, 2011)

ω (rad/s)	$\dot{m}$ (kg/s)	Re_φ (/10^7)	C_w (/10^5)	λ_T	P_{in}^* (bar)	T_{in}^{**} (K)
261.9	0.125	0.171	0.31	0.32	1.98	293.5
407.9	0.122	0.271	0.3	0.21	2.04	294.45
617.1	0.124	0.578	0.299	0.12	3.02	297.75
915.7	0.123	0.802	0.284	0.085	3.04	298.65
1057.4	0.123	1.167	0.286	0.063	4.03	297.75
207.5	0.413	0.348	1.029	0.6	5.05	294.5
415.4	0.419	0.68	1.029	0.35	5.02	296.25
628.1	0.418	1.012	1.018	0.25	5.03	296.65
912.2	0.4177	1.42	1	0.19	5.08	297.45
1060.6	0.418	1.61	0.986	0.17	5.12	298.15

*: Static pressure
**: Static temperature

4.3 Two-sided cavity simulations

As mentioned in Chapter 2, the bolt windage rig has a double-sided disc, and the experiments were carried out by balancing the flow to both sides. Balancing the test (front) and balance (rear) sides of the cavity was achieved by matching the mass flow together with the inlet and outlet pressures. As well as reducing the net axial load on the rotor, this also ensures minimum leakage at the peripheral seals between the front and rear sides of the disc. Consequently, it is possible to simulate one side of the cavity in

isolation to reduce the mesh size by 50%. In order to ensure that little leakage occurred in the experiment between the rear and front sides of the cavity, the two-sided geometry of the plain disc was meshed and modelled with the CFD code. The flow conditions used for the simulations included two sets of throughflow Reynolds numbers, each including four different rotational Reynolds numbers: 1- $C_w = 0.3 \times 10^5$ with ($Re_\phi = 0.27 \times 10^7$, 0.578×10^7, 0.802×10^7 and 1.17×10^7 ($0.063 < \lambda_T < 0.21$), and 2- $C_w = 10^5$ with ($Re_\phi = 0.68 \times 10^7$, 1.012×10^7, 1.42×10^7 and 1.61×10^7 ($0.17 < \lambda_T < 0.35$). Figure 4.2 shows the simulated geometry of the two-sided cavity.

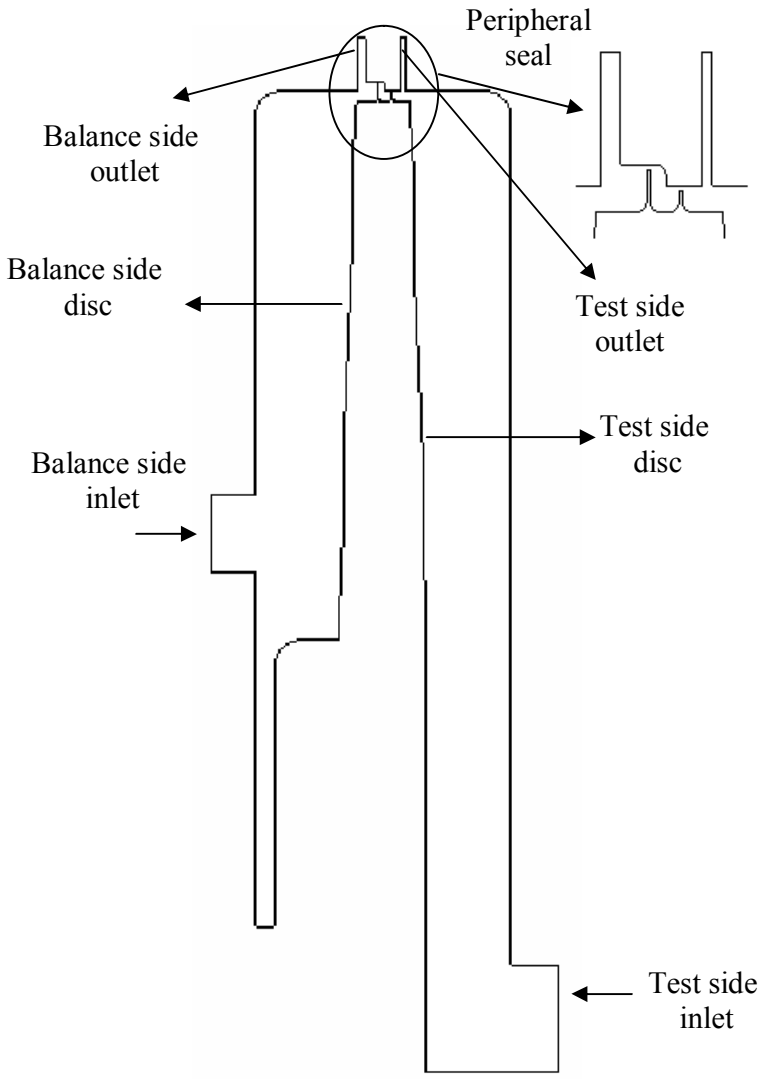

Figure 4.2: Schematic Diagram of the Two-sided Simulated Geometry

According to the simulation results, the maximum amount of flow leakage (about 3% of the total mass flow rate) occurred for $C_w = 10^5$ and $\mathrm{Re}_\phi = 0.68 \times 10^7$. Comparison of the flow leakage for the simulated flow conditions reveals that this value reduces when reducing the inlet mass flow rate or increasing the rotational Reynolds number. Although the maximum amount of flow leakage is very small, it is still necessary to investigate whether this amount of leakage changes the moment produced by the disc in the rear and front sides of the cavity.

The total viscous moment coefficient of the disc can be divided into three sources: that from the front side of the disc, that from the rear side of the disc, and that from the peripheral seal. Figures 4.3 and 4.4 respectively show the contributions of these sources of moment coefficient to the total for $C_w = 0.3 \times 10^5$ and $C_w = 10^5$ and the different rotational Reynolds numbers. It can be seen that the moment coefficient of the front and rear sides are almost the same. This is also shown in Tables 4.3 and 4.4, which give the percentage contribution of each component to the total moment coefficient for $C_w = 0.3 \times 10^5$ and $C_w = 10^5$ respectively. Accordingly, it appears that the flow was balanced in the front and rear sides of the cavity and the leakage of flow between the two sides could be disregarded.

It is also relevant to note that the moment coefficient for the peripheral seal is generally around 11% of the total moment coefficient (or $1/9^{\text{th}}$ of the value obtained from the two disc surfaces). This fact is used in subsequent computations where just one side of the cavity without the peripheral seal is modelled. The experimentally measured values of the moment coefficient take account of the frictional toques experienced on both sides of the disc and the peripheral seal. Thus, computed values from a one-sided model of the cavity can be compared with the experimental values by halving 89% (the amount of moment coefficient produced by the peripheral seal was subtracted) of the total moment coefficient obtained during experiments.

The moment produced by the labyrinth seal was also predicted by Millward and Edwards (1994), using the following correlations.

$$C_{m,seal} = \left(\frac{C_w}{\mathrm{Re}_\varphi} \right)^{0.55} n_f^{-0.65} \qquad 4.1$$

$$M_L = C_{m,seal}\pi L\omega^2 b^4 \rho \qquad 4.2$$

Where L is the length of the seal, and n_f is the number of the fins. For the test rig under investigation, L = 0.0212m and n_f = 2 (Miles, 2011).

Miles (2011) used this mentioned correlation in order to calculate the moment coefficient produced by the peripheral seal. The calculated moment was then subtracted from the total moment in order to find the moment produced by the disc alone. Accordingly, Miles found that the labyrinth seal contributes between 16% and 23% of the total measured moment, depending on the flow condition. However, based on the simulation results, the amount of moment produced by the peripheral seal is lower than that value, between 9% and 12% of the total moment.

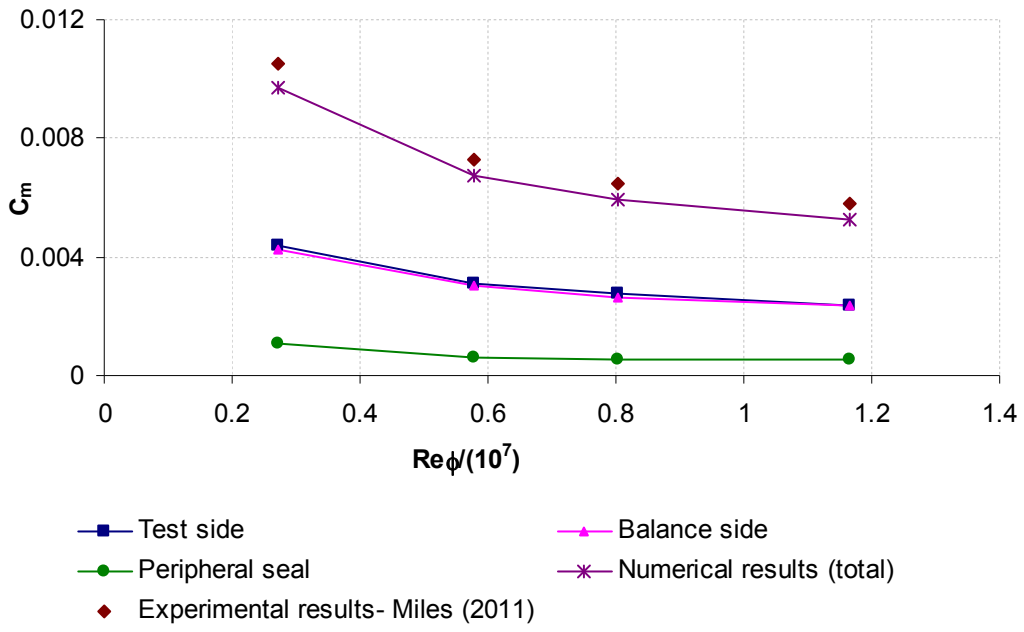

Figure 4.3: Contribution to the Total Moment Coefficient Produced by the Different Rotating Components in the Simulated Two-sided Plain Disc Geometry, C_w = 0.3 x 10^5

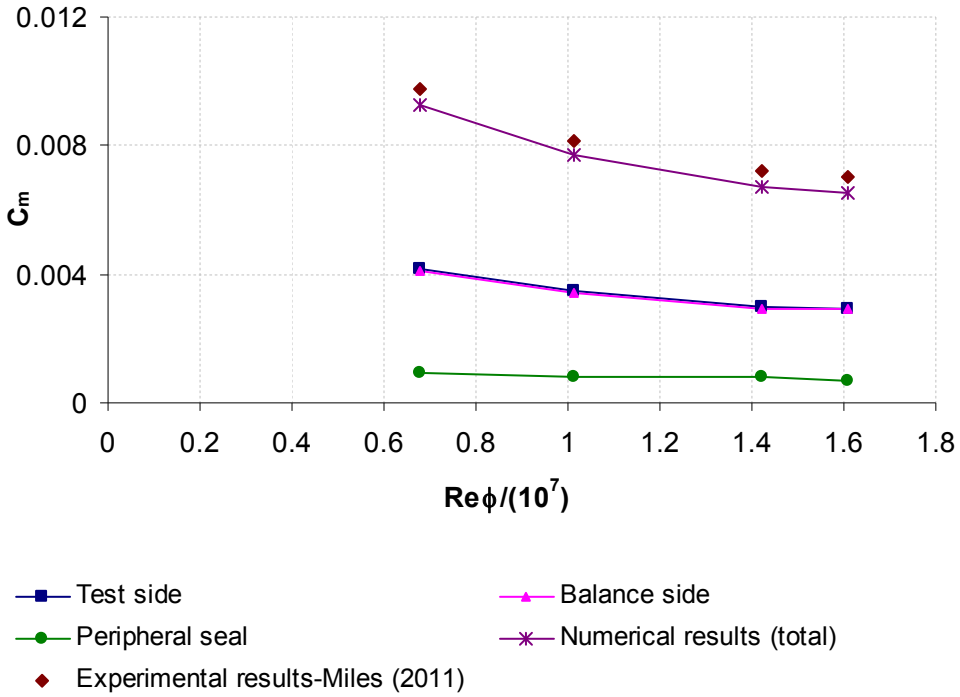

Figure 4.4: Contribution to the Total Moment Coefficient Produced by the Different Rotating Components in the Simulated Two-sided Plain Disc Geometry, Cw = 10^5

Table 4.3:Contribution to the Total Moment Coefficient Produced by the Different Rotating Components in the Simulated Two-sided Plain Disc Geometry, C_w = 0.3 x 10^5

$Re_\phi / 10^7$	Percentage of total moment coefficient		
	Test side	Balance side	Peripheral seal
0.271	0.46	0.43	0.11
0.578	0.46	0.45	0.09
0.802	0.46	0.45	0.09
1.167	0.46	0.44	0.1

Table 4.4: Contribution to the Total Moment Coefficient Produced by the Different Rotating Components in the Simulated Two-sided Plain Disc Geometry, C_w = 10^5

$Re_\phi / 10^7$	Percentage of total moment coefficient		
	Test side	Balance side	Peripheral seal
0.68	0.45	0.45	0.1
1.012	0.45	0.44	0.11
1.42	0.45	0.43	0.12
1.61	0.45	0.44	0.11

4.4 Plain disc flow structure

The plain disc system is a widely investigated case. Hence, flow structure and energy losses in this system have been reported in the literature under different flow conditions and geometric specifications. Detailed reviews of previous studies were presented by Owen and Rogers (1989) and Childs (2007). For the applications analysed in this work, the flow is expected to be turbulent, and for the geometries analysed G = 0.1.

Simulation results of four different typical flow conditions were selected from Table 4.2 to be analysed: 1- $Re_\phi = 1.61 \times 10^7$, $C_w = 10^5$ ($\lambda_T = 0.17$), 2- $Re_\phi = 1.167 \times 10^7$, $C_w = 0.3 \times 10^5$ ($\lambda_T = 0.063$), 3- $Re_\phi = 0.171 \times 10^7$, $C_w = 0.3 \times 10^5$ ($\lambda_T = 0.31$), and 4- $Re_\phi = 0.348 \times 10^7$, $C_w = 10^5$ ($\lambda_T = 0.6$). The first two flow conditions are representative of the rotationally dominated flow pattern, and the second two flow conditions are representative of the throughflow dominated flow regime.

Figures 4.5 through 4.8 show a set of different flow parameters variations in the plain disc system for the mentioned flow conditions. Typical circumferentially averaged structure of the mean flow in the plain disc system is shown in Figure 4.5 (a) to (d). The tangential velocity distributions of the mentioned flow conditions are shown in Figure 4.6 at two different radial locations of $r/b = 0.62$ and $r/b = 0.8$. Figures 4.7 and 4.8 show similar plots for the radial and axial velocity distributions respectively.

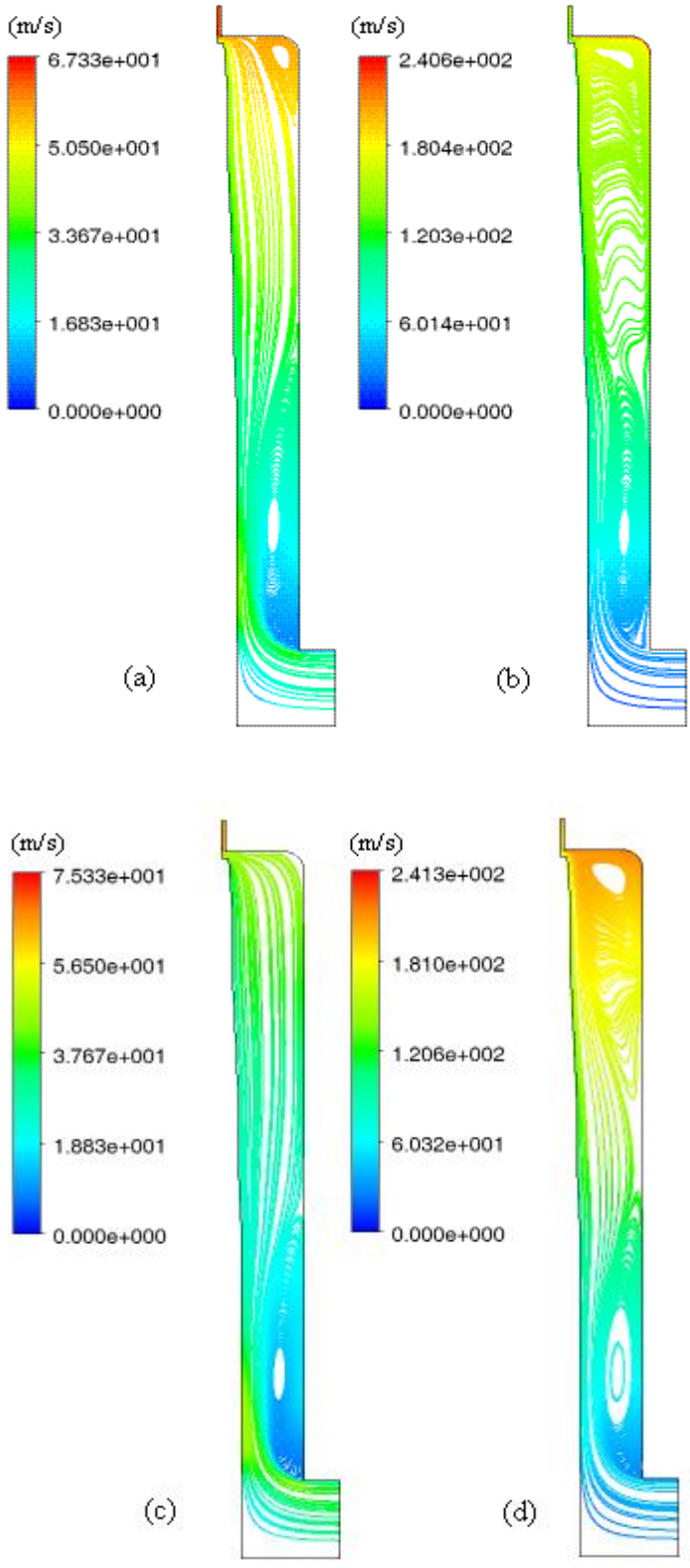

Figure 4.5: Flow Streamlines (relative total velocity) for the Plain Disc System under Different Flow Conditions:

(a) $Re_\phi = 0.171 \times 10^7$, $C_w = 0.3 \times 10^5$ ($\lambda_T = 0.31$)

(b) $Re_\phi = 1.167 \times 10^7$, $C_w = 0.3 \times 10^5$ ($\lambda_T = 0.063$)

(c) $Re_\phi = 0.348 \times 10^7$, $C_w = 10^5$ ($\lambda_T = 0.6$)

(d) $Re_\phi = 1.61 \times 10^7$, $C_w = 10^5$ ($\lambda_T = 0.17$)

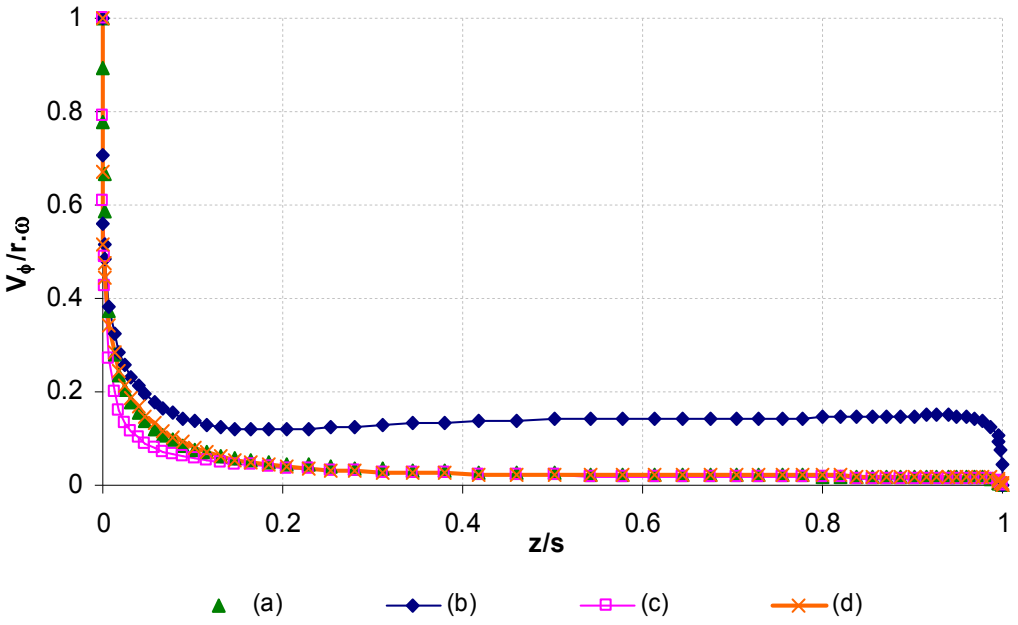

(a): *r/b* = 0.62

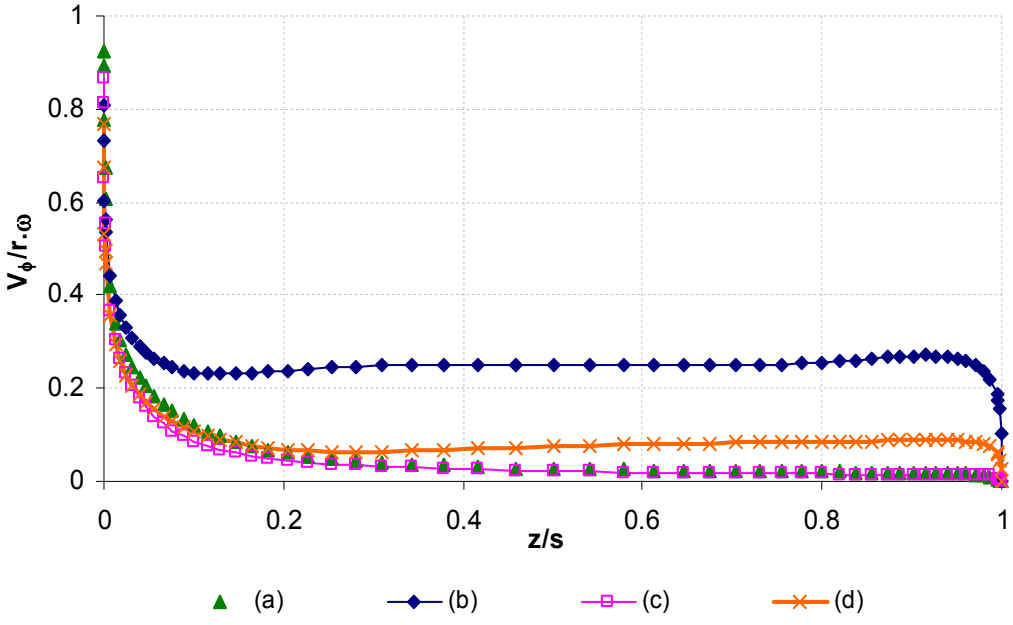

(b): *r/b* = 0.8

Figure 4.6: Tangential Velocity Distributions at the radial locations of r/b = 0.62 and r/b = 0.8 for:
(a) $Re_\phi = 0.171 \times 10^7$, $C_w = 0.3 \times 10^5$ ($\lambda_T = 0.32$)
(b) $Re_\phi = 1.167 \times 10^7$, $C_w = 0.3 \times 10^5$ ($\lambda_T = 0.063$)
(c) $Re_\phi = 0.348 \times 10^7$, $C_w = 10^5$ ($\lambda_T = 0.6$)
(d) $Re_\phi = 1.61 \times 10^7$, $C_w = 10^5$ ($\lambda_T = 0.17$)
Note: *z/s* = 0 is located on rotor. This is also the case for Figures 4.7 and 4.8.

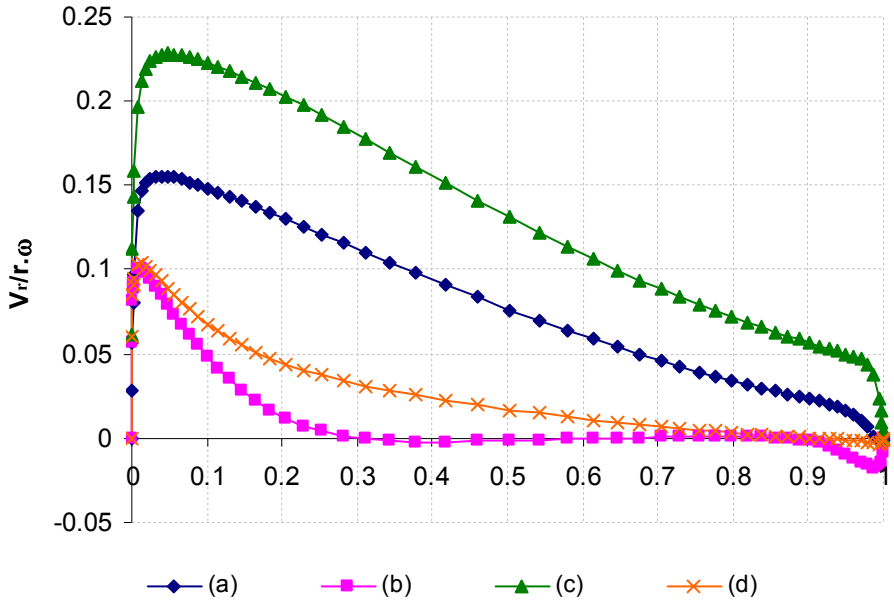

(a): *r/b* = 0.62

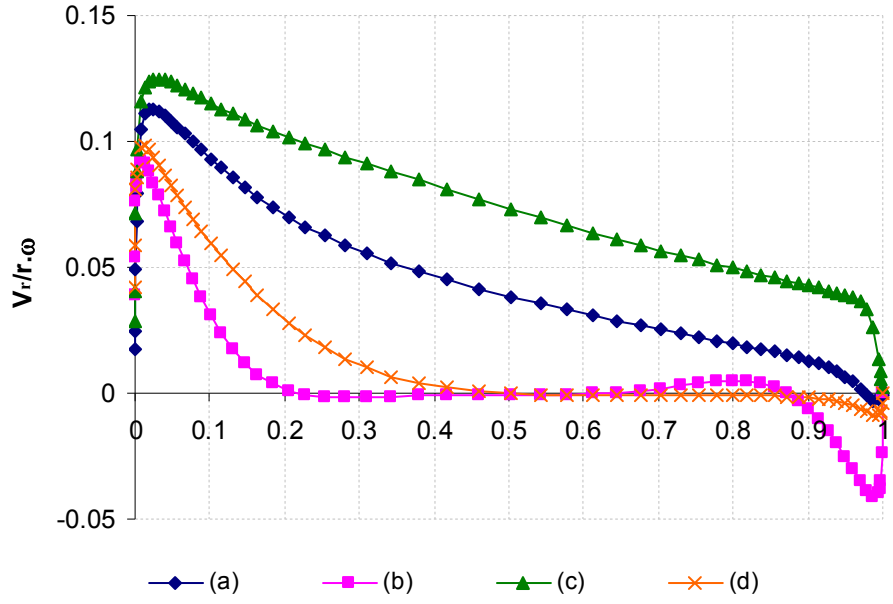

(b): *r*/b = 0.8

Figure 4.7: Radial Velocity Distributions at the radial locations of r/b = 0.62 and r/b = 0.8 for:
(a) $Re_\phi = 0.171 \times 10^7$, $C_w = 0.3 \times 10^5$, ($\lambda_T = 0.32$
(b) $Re_\phi = 1.167 \times 10^7$, $C_w = 0.3 \times 10^5$, ($\lambda_T = 0.063$),
(c) $Re_\phi = 0.348 \times 10^7$, $C_w = 10^5$, ($\lambda_T = 0.6$)
(d) $Re_\phi = 1.61 \times 10^7$, $C_w = 10^5$, ($\lambda_T = 0.17$)

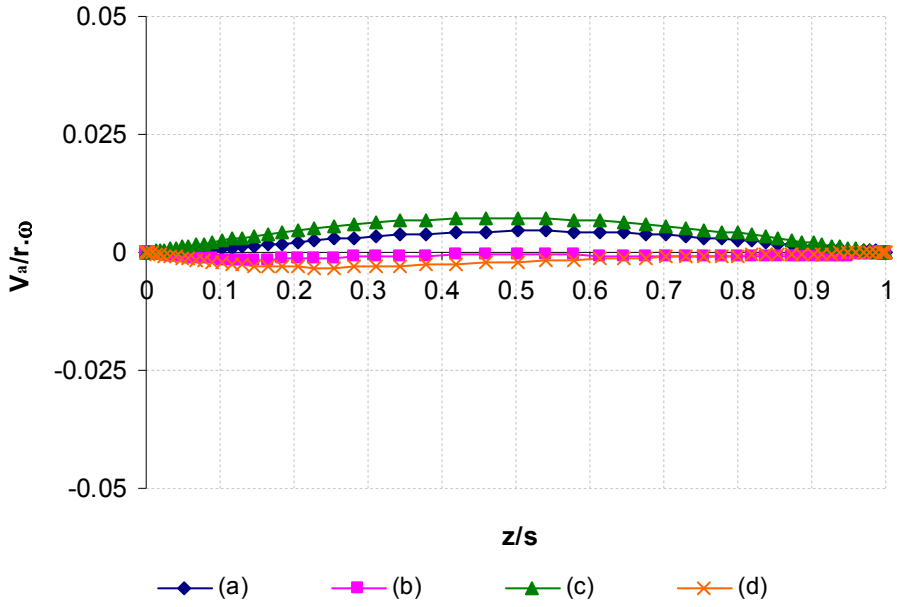

(a): *r/b* = 0.62

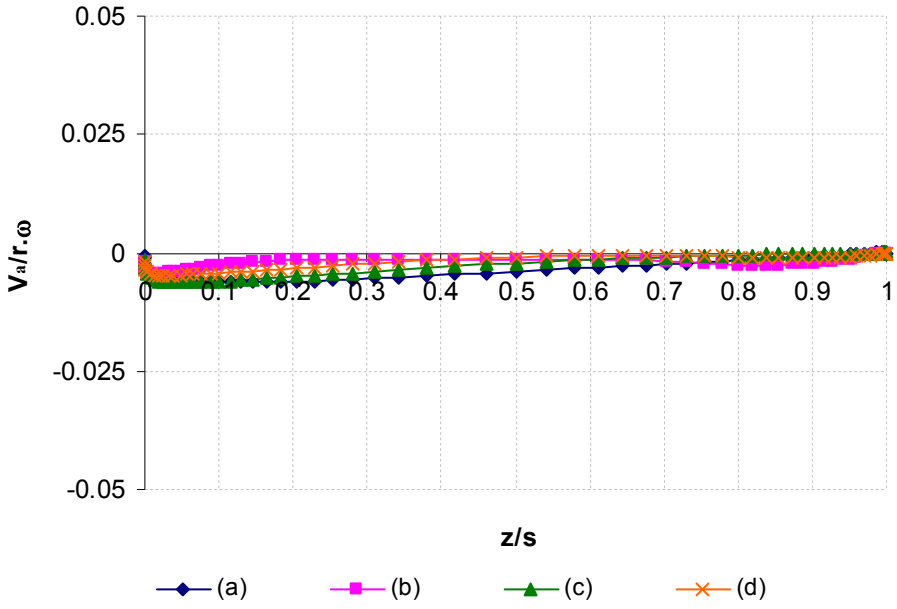

(b): *r/b* = 0.8

Figure 4.8: Axial Velocity Distributions at the radial locations of r/b = 0.62 and r/b = 0.8 for:
(a) $Re_\phi = 0.171 \times 10^7$, $C_w = 0.3 \times 10^5$, ($\lambda_T = 0.32$)
(b) $Re_\phi = 1.167 \times 10^7$, $C_w = 0.3 \times 10^5$, ($\lambda_T = 0.063$)
(c) $Re_\phi = 0.348 \times 10^7$, $C_w = 10^5$, ($\lambda_T = 0.6$)
(d) $Re_\phi = 1.61 \times 10^7$, $C_w = 10^5$, ($\lambda_T = 0.17$)

The results obtained from the simulations (shown in Figures 4.5 to 4.8) are quite comparable to the experimental observations of Daily *et al*. (1964) and the predictions of Owen and Rogers (1989) for the turbulent flow structure in rotor-stator cavities with large clearances. Accordingly, the flow structure in the rotor-stator wheel-space could be categorised into the two models of Stewartson (1952) and Batchelor (1950). Stewartson's model explains the flow with a throughflow dominated condition in which rotation has a small influence on the flow structure. In contrast, Batchelor's flow pattern models the flow with a rotationally dominated condition. Here, rotation plays an important role in the flow structure inside the cavity.

In rotor-stator cavities, the parameter that is most important to categorise the flow regime is the turbulent flow parameter, λ_T. It is used as an indicator in Batchelor and Stewartson's flow structures. The turbulent flow parameter of 0.219 is the transitional point above which transition from a rotationally dominated condition (Batchelor's flow pattern) to a throughflow dominated condition (Stewartson's flow pattern) occurs (Owen and Rogers, 1989). The effects of the turbulent flow parameter variations on the flow structure can be seen by comparing the velocity streamlines in Figure 4.5 (a) to (d), as well as the velocity distributions in Figures 4.6 to 4.8. Keeping the throughflow rate constant and increasing the disc speed, and, as a result, the rotational Reynolds number, moves the flow pattern to Batchelor's model, where the flow is divided into three distinct zones: separate boundary layers near the rotor and stator with a rotating core in between. In this model, a net radial outflow and inflow exist, close to the rotor and stator respectively. This is shown by the negative and positive radial velocities close to the stator and rotor respectively in Figure 4.7. The core has zero radial velocity and a swirl ratio of β. Increasing the rotational Reynolds number increases the tangential velocity of the core (compare the tangential velocity of the core displayed in Figure 4.6).

Increasing the throughflow rate influences the flow field to a great extent. By increasing C_w, the central core disappears and an outward radial flow ($V_r > 0$) forms everywhere, even in the stator boundary layer. The flow then follows Stewartson's model. In this model, tangential velocity variation only exists in the rotor boundary layer and is almost zero outside it (see Figures 4.6 and 4.7). According to the simulation results, at high

throughflow rates the change in tangential velocity in the disc boundary layer is close to $r\omega$.

Effects of the radius on the radial and tangential velocity distributions can be observed in Figures 4.6 to 4.8 by comparing the velocity distribution results at the radial locations of $r/b = 0.62$ and $r/b = 0.8$. It can be seen that for high rotational Reynolds numbers, the zero radial velocity of the core only exists for higher radial locations. In addition, for lower values of Re_ϕ particularly at low radii, radial velocity has a very steep profile. Furthermore, while the radial velocity distribution does not vary very much with radius for higher values of Re_ϕ, it varies significantly for lower values of Re_ϕ. Regarding the tangential velocity distribution, it is clear that the core speeds up with an increase in radius.

Inspecting the axial velocity distributions, which are shown in Figure 4.8, it can be observed that there is almost a zero axial velocity for all flow conditions through the whole width of the cavity.

It is also interesting to investigate the boundary layer growth on the rotor surface for different flow conditions, and to compare it with the relevant correlations suggested in the literature. Calculation of the rotor boundary layer thickness is required in almost all of the analytic modelling of flow in rotor-stator cavities that emerges from the integral boundary layer theory. Smaller boundary layer thicknesses result in stronger velocity gradients between the core and the wall, and consequently higher values of viscous moment coefficient. Due to the dominance of the tangential shear stress component in developing the boundary layers on both walls, it is the tangential velocity distribution that specifies the boundary layer thickness (Daily *et al*., 1964). The boundary layer thickness of the rotor can be defined as the axial distance away from the wall where the non-dimensional tangential velocity reaches 1.1β.

The simulation results of rotor boundary layer thickness could be compared with the boundary layer thickness obtained from solutions of Ekman boundary layer equations assuming $1/7^{th}$ power law velocity profiles (Owen and Rogers, 1989). Accordingly, Equation 4.3 gives the boundary layer thickness for a rotating fluid over a rotating wall (Owen, 1987). In addition to Owen's correlation for rotor boundary layer thickness, Daily *et al*. (1964) also proposed a relation between the rotor boundary layer thickness

and Re_ϕ as well as β (see Equation 4.4) based on their experimental measurements. Comparison of the results of boundary layer thickness obtained from the simulations with those obtained using Equations 4.3 and 4.4 are tabulated in Tables 4.5 and 4.6 at r/b = 0.8 and r/b = 0.62 respectively. The numerical results were obtained by plotting the dimensionless tangential velocity distribution and finding the axial location where it reaches approximately 1.1β.

$$\frac{\delta}{r} = 0.0983(1-\beta)^{0.6}\left(\left(\frac{r}{b}\right)^2 \mathrm{Re}_\phi\right)^{-0.2} \tag{4.3}$$

$$\delta = 0.4(1-\beta)^2 \frac{r}{\mathrm{Re}_\varphi^{\,0.2}} \tag{4.4}$$

Table 4.5: Rotor Boundary Layer Thickness at r/b = 0.8

$Re_\phi/10^7$	$C_w/10^5$	δ_{rotor} (mm) Numerical results	δ_{rotor} (mm) Owen (1987)	δ_{rotor} (mm) Daily et al. (1964)
0.171	0.3	4.4	1.078	3.9
1.167	0.3	1.916	0. 73	2.6
0.348	1	4.3	0. 94	3.3
1.61	1	3.9	0. 67	2.5

Table 4.6: Rotor Boundary Layer Thickness at r/b = 0.6

$Re_\phi/10^7$	$C_w/10^5$	δ_{rotor} (mm) Numerical results	δ_{rotor} (mm) Owen (1987)	δ_{rotor} (mm) Daily et al. (1964)
0.171	0.3	3.3	0.84	3
1.167	0.3	1.55	0.53	1.6
0.348	1	3.7	0.73	2.6
1.61	1	3.3	0.54	1.94

The first point that can be gleaned from Tables 4.5 and 4.6 is that the difference between the solution of Ekman boundary layer equations and the CFD results is quite significant. This could be explained due the assumption made regarding the mentioned equations: that the equations are strictly valid for $\beta \to 1$ (Owen, 1987) and also the limitations of the numerical methodology and the associated assumptions. However, β is noticeably far from 1 in the simulated cases. The highest amount of β that occurs for the flow condition of $C_w = 0.3 \times 10^5$ and $Re_\phi = 1.167 \times 10^7$ is 0.14 at r/b = 0.6 and 0.25 at r/b = 0.8.

Inspection of the data shown in Tables 4.5 and 4.6 indicates that increasing Re_ϕ decreases the rotor boundary layer. This could be explained due to the increase in centrifugal forces compressing the boundary layer on the rotor. In addition, as it is evident in the correlation suggested by Daily *et al*., rotor boundary layer thickness is a function of (1-β). Hence, increasing Re_ϕ increases β and, as a result, reduces the rotor boundary layer thickness. Moreover, with an increase in throughflow rate, the degree of turbulence in rotor boundary layer increases, resulting in its thickening. Finally, as is clearly shown in Tables 4.5 and 4.6, the rotor boundary layer thicknesses increase with increasing radius, which is characteristic of turbulent flows.

It is also necessary to investigate the extent to which the numerical results of the rotor boundary layer thickness change with changing the type of turbulence model. Simulations were therefore carried out for a typical flow condition of $Re_\phi = 0.171 \times 10^7$ and $C_w = 0.3 \times 10^5$ using the RSM and realizable k-ε turbulence models with enhanced wall treatment. The results of these simulations are displayed in Table 4.7.

Table 4.7: Comparison of the Numerical Results of Rotor Boundary Layer Thickness (mm) for $Re_\phi = 0.171 \times 10^7$ and $C_w = 0.3 \times 10^5$

r/b	RSM with enhanced wall treatment	Realizable k-ε with enhanced wall treatment	Standard k-ε with enhanced wall treatment
0.6	4	3.27	3.3
0.8	4.9	4.36	4.4

Based on the simulation results of tangential velocity distributions, similar to the cases discussed in Section 3.2, RSM over-predicts the tangential velocity of the core as well as the rotor boundary layer thickness. The standard and realizable k-ε models also had similar predictions of tangential velocity and the thickness of the rotor boundary layer.

It is also interesting to investigate how the core swirl ratio is affected by different flow conditions in the plain disc system. Owen and Rogers (1989) modelled the core rotation using the generalised solution of momentum integral equations. Similar investigations were performed by Daily *et al*. (1964), Owen (1986) and Dadkhah (1989). Figure 4.9 compares the simulation results of the core swirl ratio with the results obtained by these researchers.

Comparison of the analytical correlations of Owen and the empirical correlations of Daily *et al*. and Dadkhah with the simulation results show that for $\lambda_T x^{-2.6} < 0.25$ the analytical results of Owen, for $0.25 < \lambda_T x^{-2.6} < 1.5$ the empirical correlation of Dadkhah, and for $1.5 < \lambda_T x^{-2.6}$ the empirical correlation of Daily *et al*. give closer results to the numerical predictions. This could be explained by the range of non-dimensional parameters in which each of the correlations is valid. Similar results were also obtained by Childs (2007).

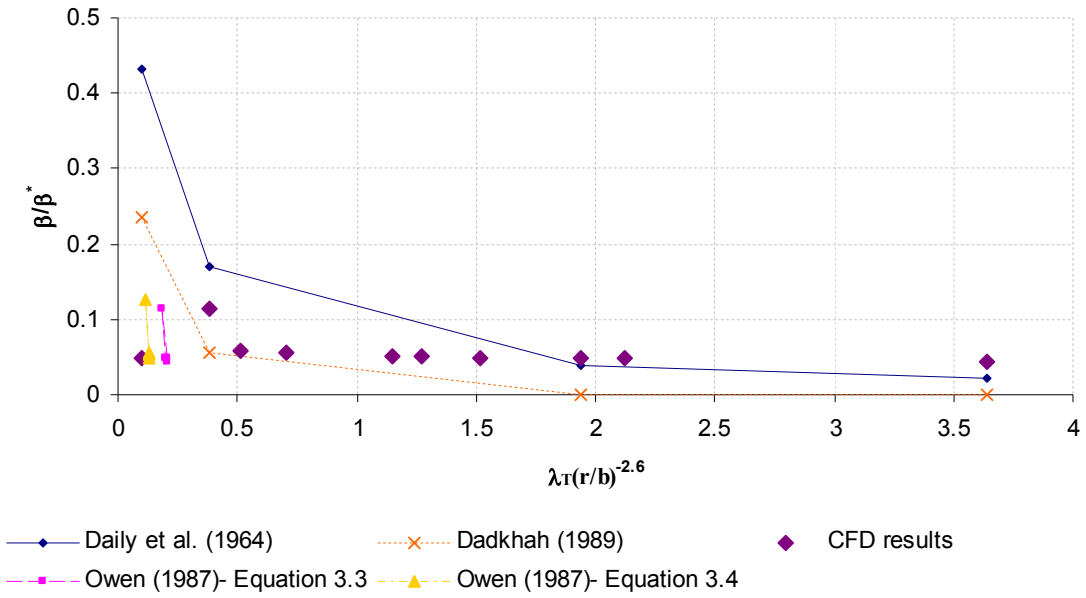

Figure 4.9: Variations of β / β^* with $\lambda_T(r/b)^{-13/5}$

To complement the analysis of flow phenomena in the plain disc system, radial pressure distribution was also examined. Figure 4.10 shows the simulation results of the dimensionless pressure coefficient $Cp = \frac{(p_b - p_r)\rho b^2}{\mu^2}$, used by Daily *et al.* (1964) and Bayley and Owen (1969), as a function of radius for different C_w and Re_ϕ.

Variations of radial pressure could be explained considering Equation 4.5, which was derived from the radial momentum equation (Daily *et al.*, 1964).

$$\frac{\partial p}{\partial r} = \rho\left(\frac{v_\varphi^{\,2}}{r} - v_r \frac{\partial v_r}{\partial r}\right) \qquad 4.5$$

According to Equation 4.5, the radial pressure is controlled by two mechanisms: radial flow effect and rotational (tangential velocity) effect. For the conditions where both the radial and tangential velocities are small, the radial pressure gradient remains constant and very close to zero.

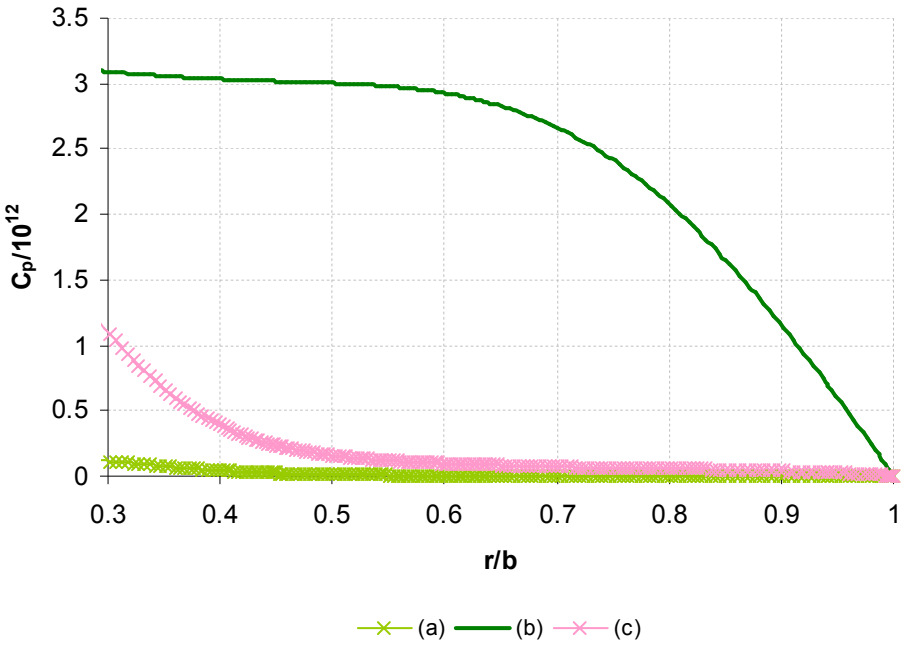

Figure 4.10: Radial Pressure Distribution for the Plain Disc System for the Flow Conditions of:
(a) $Re_\phi = 0.171 \times 10^7$, $C_w = 0.3 \times 10^5$, ($\lambda_T = 0.32$)
(b) $Re_\phi = 1.167 \times 10^7$, $C_w = 0.3 \times 10^5$, ($\lambda_T = 0.063$)
(c) $Re_\phi = 1.012 \times 10^7$, $C_w = 10^5$, ($\lambda_T = 0.25$)

As can be seen in Figure 4.10, pressure rises towards the peripheral seal of the cavity. Comparison of the presented plots reveals that for a constant value of C_w, the radial pressure difference between the inlet and outlet of the cavity increases significantly by increasing the rotational Reynolds number. In contrast, increasing the throughflow rate for approximately similar values of Re_ϕ slightly decreases the radial pressure gradient. Therefore, as was expected, the pressure gradient in the cavity is primarily determined by rotation. It can also be seen that the effect of the rotational Reynolds number becomes less significant by increasing the throughflow rate. It is interesting to note that for the rotationally dominated cases, there is a small pressure variation from the inlet to the center of the cavity. Subsequently, pressure rapidly increases from the centre to the periphery of the system. This is contrary to the throughflow dominated condition where the pressure varies noticeably from the inlet to the center of the cavity and then stays at a constant value for higher radial locations. The trend of radial pressure difference variations with Re_ϕ and C_w is quite compatible with those variations obtained by the experimental measurements of Bayley and Owen (1969).

It is also interesting to investigate whether any axial pressure gradients exist in the cavity from the rotor to the stator or in the opposite direction. Hence, the axial pressure difference was calculated for three flow conditions: $Re_\phi = 0.348 \times 10^7$, $C_w = 10^5$, ($\lambda_T = 0.6$), $Re_\phi = 0.171 \times 10^7$, $C_w = 0.3 \times 10^5$, ($\lambda_T = 0.32$) and $Re_\phi = 1.167 \times 10^7$, $C_w = 0.3 \times 10^5$, ($\lambda_T = 0.063$) at $r/b = 0.6$ and $r/b = 0.8$. It was found that the maximum axial pressure difference (about 8 Pa) occurs at lower radii and for the flow condition with the highest turbulent flow parameter ($Re_\phi = 1.012 \times 10^7$, $C_w = 10^5$, $\lambda_T = 0.25$). For the other two flow conditions, particularly at higher radial locations, the pressure difference is less than 2 Pa. Therefore, it appears that there is a minor axial pressure difference between the rotor and stator. This could also be confirmed by looking at the axial velocity distribution along the z-axis (see Figure 4.8). Accordingly, there is almost zero axial velocity through the width of the cavity.

4.5 Moment coefficient results

An important requirement in analysing rotor-stator systems is not only to understand the physics of flow and the mechanisms of losses but also to quantify the amount of losses associated with the systems. The tangential shear stress at the surface of the disc produces viscous friction and, consequently, a viscous moment. As was mentioned in the previous chapter, it is more convenient to use the moment coefficient, rather than the moment, for power loss calculations in rotor-stator systems. Accordingly, Figures 4.11 and 4.12 show variations of the moment coefficient for $C_w = 0.3 \times 10^5$ as a function of the rotational Reynolds number and turbulent flow parameter, respectively. Figures 4.13 and 4.14 show similar variations for $C_w = 10^5$. Comparisons were made with the experimental measurements carried out by Miles (2011).

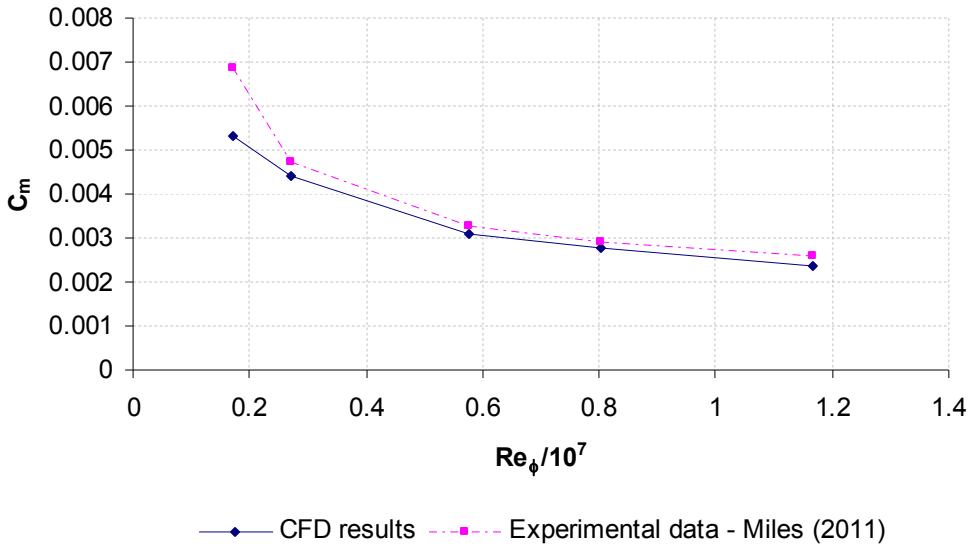

Figure 4.11: Variation of Moment Coefficient with Rotational Reynolds number. Comparison between Numerical and Experimental Results for plain disc, $C_w = 0.3 \times 10^5$

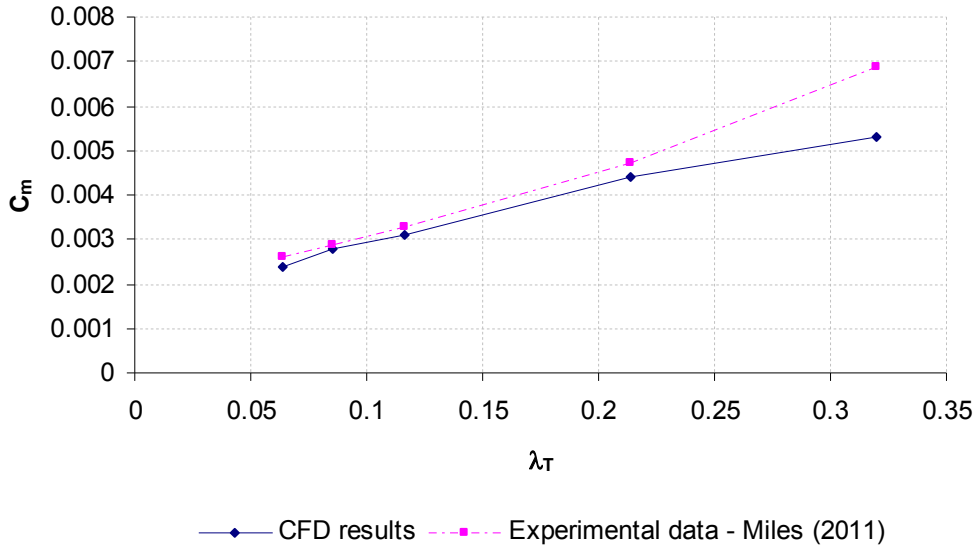

Figure 4.12: Variation of Moment Coefficient with Turbulent Flow Parameter. Comparison between Numerical and Experimental Results for plain disc, $C_w = 0.3 \times 10^5$

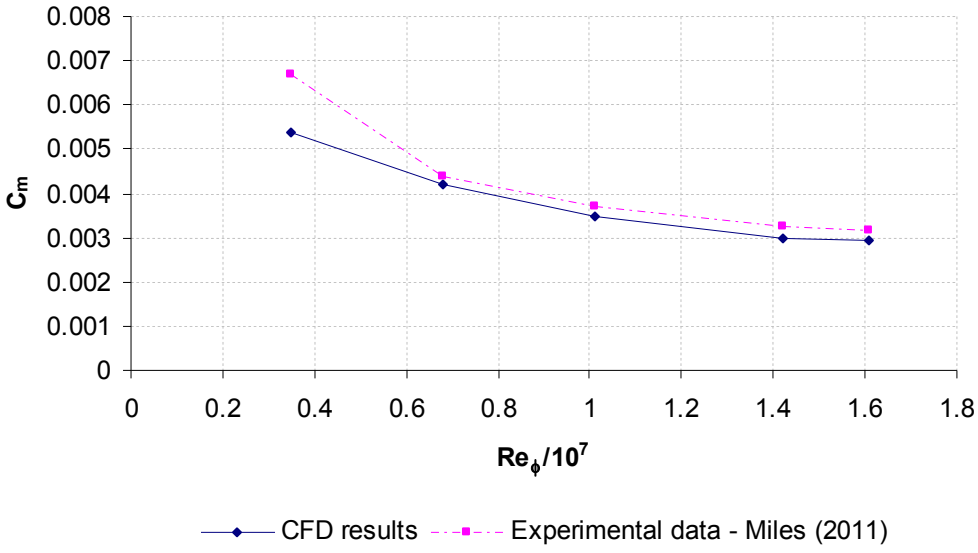

Figure 4.13: Variation of Moment Coefficient with Rotational Reynolds number. Comparison between Numerical and Experimental Results for plain disc, $C_w = 10^5$

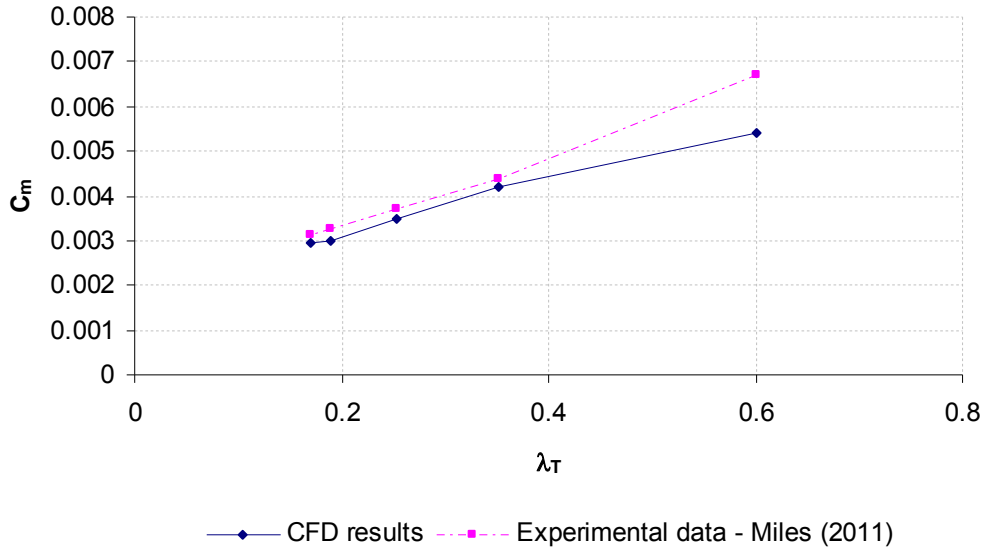

Figure 4.14: Variation of Moment Coefficient with Turbulent Flow Parameter. Comparison between Numerical and Experimental Results for plain disc, $C_w = 10^5$

Examination of Figures 4.11 to 4.14 reveals that there is very good agreement between the numerical and the experimental data for most of the rotational Reynolds numbers and turbulent flow parameters. However, there is a divergence for the lower values of Re_ϕ and the higher values of λ_T. This can be explained by considering the experimental uncertainties in measuring the moment for lower values of rotational Reynolds numbers. According to the experimental uncertainty analysis, the relative uncertainty was about 24% (Miles, 2011). Since the amount of moment produced by the disc is very low for lower values of the disc speed, the measured moment approaches the same order of magnitude as the measured uncertainties.

Further inspection of Figures 4.11 to 4.14 illustrates that increasing the turbulent flow parameter, which is associated with a reduction in Re_ϕ or an increase in the throughflow rate, increases the moment coefficient of the disc. For a constant value of C_w, increasing the rotational speed of the disc makes rotation the dominant mechanism in the system. Having a disc with higher rotational velocity speeds up the core and, as a result, increases the core swirl ratio (see Figure 4.6). This will increase the velocity gradient between the core and the disc and consequently produce higher shear stress. This leads to the production of higher disc moments. However, since the rotational speed is

squared in the moment coefficient formula, the moment coefficient decreases when increasing the disc's rotational speed.

For a constant value of Re_ϕ, increasing the throughflow rate brings about a reduction in the tangential velocity of the core. This occurs due to the conservation of angular momentum, and is a well-known phenomenon in plain disc systems (Owen and Rogers, 1989). Consequently, increasing C_w increases the relative (rotor to core) tangential velocity, resulting in an increase in the moment coefficient produced by the skin friction.

It is also of interest to compare the numerical results of the moment coefficient with earlier experimental data. The work of Daily *et al.* (1964) (see Equation 2.11), Coren (2007) (see Equation 4.6) and Owen (1988) (see Equations 2.15 and 2.17) were compared against the CFD data. Figures 4.15 and 4.16 demonstrate such a comparison for $C_w = 0.3 \times 10^5$ and $C_w = 10^5$, respectively.

$$C_m = \{0.52[C_w]^{0.37}[\mathrm{Re}_\varphi]^{-0.57} + 0.0028\}/2 \qquad 4.6$$

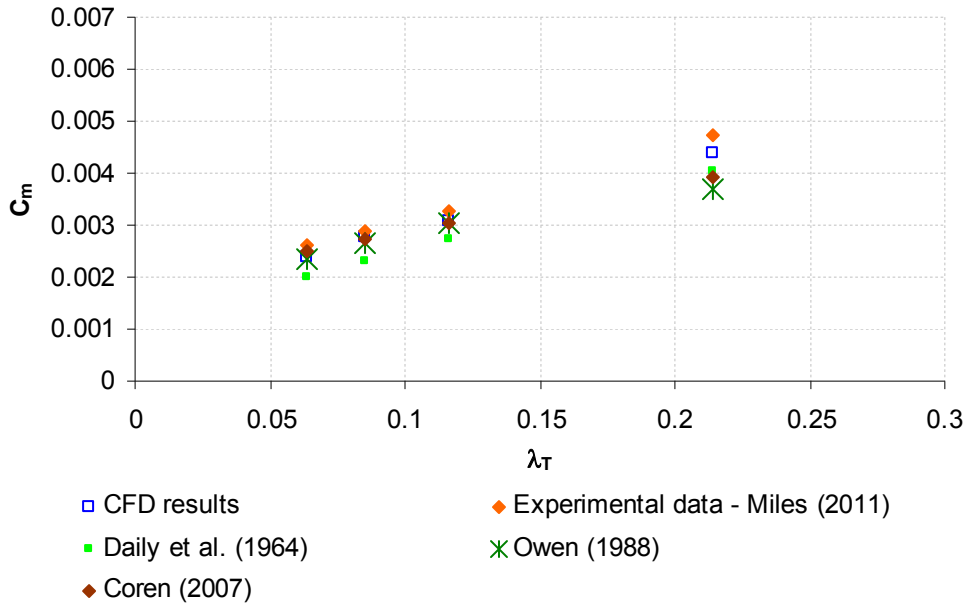

Figure 4.15: Comparison of the Simulation Results of Moment Coefficient with the Experimental and Analytical Correlations as well as the Experimental Measurements of Miles (2011); $C_w = 0.3 \times 10^5$

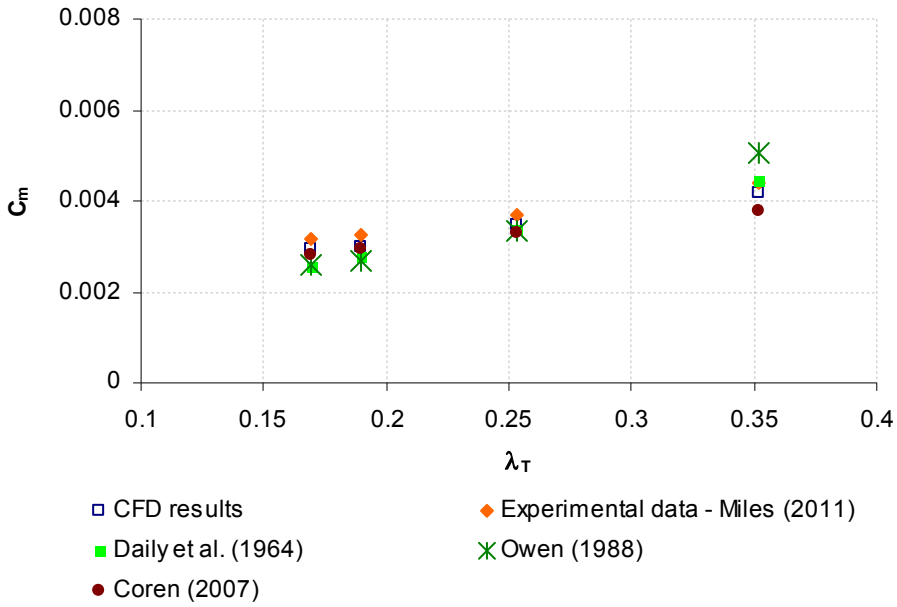

Figure 4.16: Comparison of the Simulation Results of Moment Coefficient with the Experimental and Analytical Correlations as well as the Experimental Measurements of Miles (2011); $C_w = 10^5$

As can be observed, there is good agreement between the data, particularly for $\lambda_T < 0.2$. Among the correlations, the correlation suggested by Coren gives the closest moment coefficient to that obtained by the numerical results. This could be explained due to the similarity of the geometric configuration as well as the range of non-dimensional parameters used in both investigations. Considering the work conducted by Owen and Daily *et al*., the differences between the results could result from the low ranges of Re_ϕ and C_w used in their experiments.

4.6 Summary

The rotor-stator cavity with no protrusions (plain disc configuration) was simulated in two dimensions using the standard k-ε turbulence model. A complete analysis of different aspects of flow as well as loss coefficients under different dimensionless conditions has been presented in this chapter. The data will be used in the following chapters for investigating the effects of adding protrusions to the system.

Simulations of the complete system (two-sided cavity) have also been provided, and the results of the disc moment coefficient for the rear and front sides of the cavity were compared. It was found that very little leakage exists between the rear and front sides of the cavity. It was also found that the moment coefficient for the peripheral seal is generally around 11% of the total moment coefficient, and the moment coefficient produced by the front side and the rear side of the cavity are almost equal.

Investigating the flow pattern in the simulated rotor-stator cavity under different non-dimensional flow conditions showed that, as was expected from the literature, the two flow patterns of Batchelor and Stewartson could be distinguished in the system: the former corresponds to rotationally dominated flow with two boundary layers and a rotating core, and the latter corresponds to a throughflow dominated condition with one boundary layer attached to the rotor. In addition, the moment coefficient of the plain disc system was compared with the results of the experimental correlations suggested by Coren (2007), Daily *et al.* (1964) and Owen (1988). It was found that the correlation suggested by Coren gives the closest moment coefficient to that obtained from the numerical results.

5. Rotor-Stator System with Mounted Bolts: Investigation of the Effects of Flow Condition Variations

5.1 Introduction

A detailed analysis of flow structure and energy losses in the rotor-stator cavity with rotor-mounted bolts is presented in this chapter. According to the literature review (see Sections 2.2.3 and 2.3), a complete and detailed analysis of flow phenomena in rotor-stator cavities with mounted protrusions has not yet been systematically conducted. This could be because of the difficulties in using experimental techniques to perform measurements in the vicinity of protrusions and to directly measure the losses caused by them, or the complexities of numerical methods in predicting flow mechanisms, particularly around protrusions. This chapter is therefore strategically focused on what flow phenomena can be explored from the CFD simulations of the rotor-stator system with mounted bolts. Discussions are provided for constant numbers and geometric specifications of hexagonal bolts. The effects of changing the diameter and number of bolts will be explored in the next chapter.

This chapter comprises seven sections. In Section 5.2, the general simulation specifications of three-dimensional systems are described. Section 5.3 deals with the analysis of simulation results investigating the flow structure under different flow conditions. A comparison of flow phenomena between the plain disc and protruded disc systems is presented in this section. In addition, different flow parameter variations are examined in three dimensions around the bolts. Section 5.4 provides the simulation results of the bolt drag coefficient for different flow conditions. The results of the flow structure analysis are used to distinguish those parameters affecting the drag coefficient variations for different flow conditions. Section 5.5 provides a discussion of the moment coefficient of individual bolts as well as the total rotor-stator system. Section 5.6 investigates the simulation results obtained by using the standard k-ε, the realizable k-ε, the SST k-ω and the RSM turbulence models for a typical flow condition, and compares them with those obtained using the standard k-ε turbulence model. The

comparison reveals the extent to which the standard k-ε model is able to predict reliable results in three dimensions, in particular around the protrusions. Finally, Section 5.7 presents a summary of the chapter.

5.2 Simulation specifications of the BWR system

The presence of bolts in the rotor-stator cavity disturbs the two-dimensional characteristics of the system and necessitates three-dimensional simulations. Figure 5.1 shows the computational domain and two cuts of the three-dimensional mesh used in the computational model for the rotor-stator cavity with rotor-mounted bolts. This chapter presents the simulation results for 18 bolts, 16mm in diameter and 11mm in height, which were attached to the disc at a radius of 0.2 m, r/b = 0.889. The bolts cover about half of the width of the cavity (z/s of the tip of the bolts is 0.5). The angular extent of the sector simulated for 18 bolts is 20°.

The required number of elements for the three-dimensional meshing of the rotor-stator system with mounted bolts was significantly larger than for the equivalent two-dimensional model. The approximate number of elements used for modelling the two-dimensional plain disc system was about 18,000, while it was about 810,000 for the 20° sector of the three-dimensional system. Unstructured grids were used in the r-ϕ plane only. Finer grids were used near the bolt. The distance between the first point of the meshes and the walls was specified to allow the use of enhanced wall treatments. The standard k–ε model was used for the simulations. However, comparisons were also made between the results of the standard k-ε model, realizable k-ε, SST k-ω and RSM model in order to ensure whether the use of the standard k-ε model is suitable for three-dimensional simulations. The results of these comparisons are presented in Section 5.6. All other simulation specifications were the same as those mentioned in Section 4.2.

Similar to the plain disc simulations, the simulation results for 18 bolts were grouped in two matrices with two values of throughflow Reynolds number: $C_w = 0.3 \times 10^5$, and $C_w = 10^5$. Different rotational speeds of rotor were used for the simulations, providing a large database for analysis. The arranged cases are given in Table 5.1.

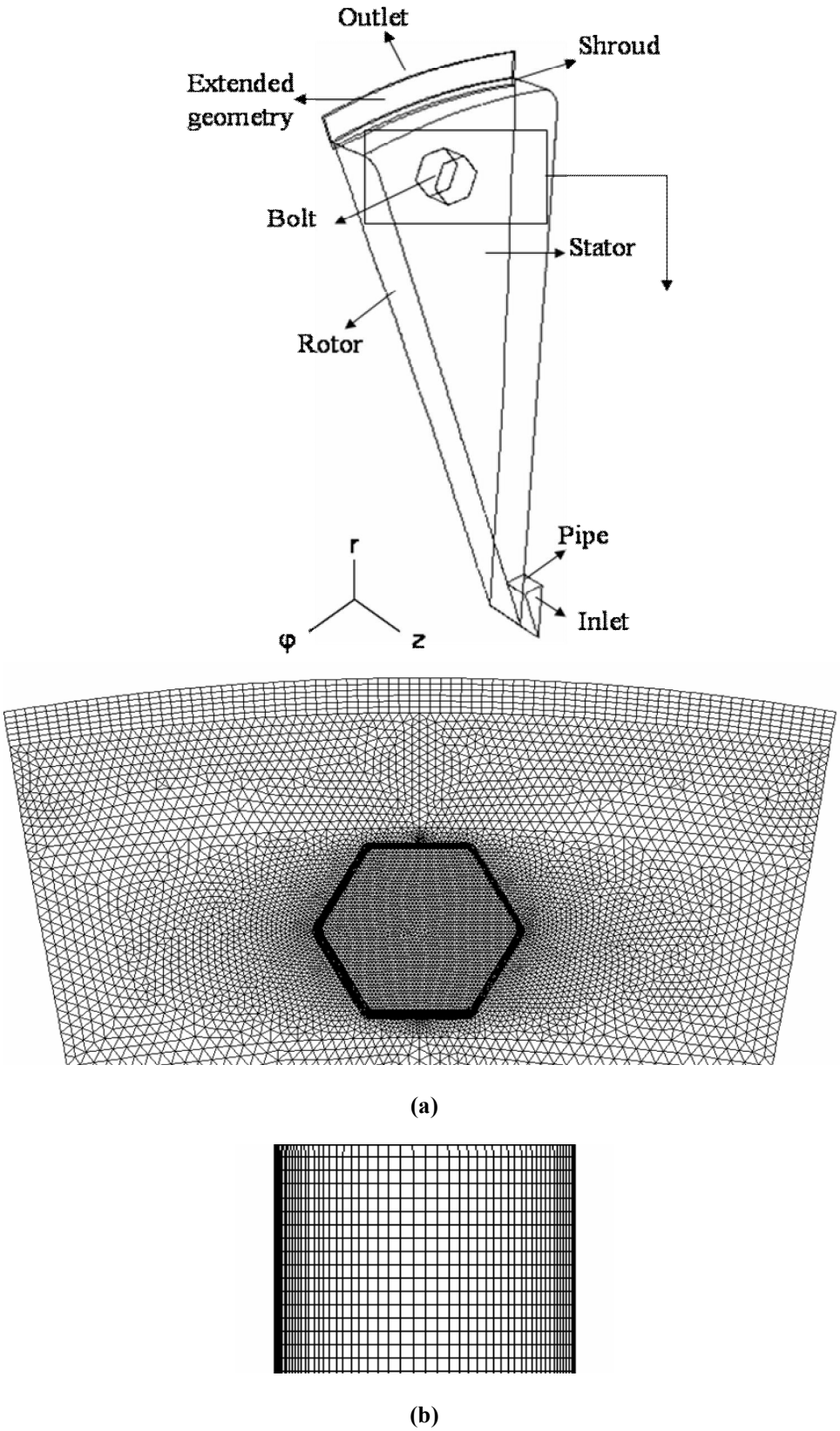

(a)

(b)

Figure 5.1: The Computational Domain Used for the Three-dimensional Simulations of the Protruded Rotor-Stator System with 18 Bolts, Showing the Mesh in: (a) r-φ Plane, and (b) r-z Plane

Table 5.1: Matrix of Flow Conditions for the Rotor-Mounted Bolt System; D = 16 mm, N = 18

ω (rad/s)	$\dot{m}$ (kg/s)	Re_φ ($/10^7$)	C_w ($/10^5$)	λ_T	P_{in}* (bar)	T_{in}** (K)
264.5	0.1248	0.177	0.311	0.31	2	288.45
411	0.1242	0.272	0.307	0.22	2.02	289
902.5	0.1188	0.716	0.268	0.09	3	292
1060.1	0.1149	0.933	0.242	0.06	4.08	300.55
211.9	0.4104	0.362	1.022	0.58	5.11	292.1
409.5	0.4152	0.668	1.017	0.35	5.1	296.7
618.8	0.4121	0.999	0.994	0.25	5.17	292.35
889.5	0.4119	1.323	0.963	0.19	5.15	288.1

*: Static pressure
**: Static temperature

5.3 Flow structure investigation

A complete and detailed analysis of flow phenomena in the plain disc system were presented in Chapter 4. However, mounting protrusions in the plain disc system significantly alters the flow structure and the amount of losses. Protrusions such as bolts are common features in rotating machineries. Hence, an investigation of the effects of these features on the flow physics and the amount of losses is needed for detailed design of those systems. In order to investigate the impacts of mounting protrusions in the plain disc system, it is more convenient to first examine different parameter variations at radial locations out of the range of interference of the bolts, and subsequently investigate the flow structure in the range of their interference.

5.3.1 Investigation of the effects of mounting protrusions on the flow structure out of the range of interference of the bolts

Two typical flow conditions were selected for comparing the flow structure in the plain disc and protruded disc systems: $Re_\phi = 0.177 \times 10^7$, $C_w = 0.3 \times 10^5$, ($\lambda_T = 0.31$)

representing a throughflow dominated condition, and Re_ϕ = 0.72 x 10^7, C_w = 0.3 x 10^5, (λ_T = 0.09) representing a rotationally dominated flow condition. Figures 5.2 and 5.3 show comparisons of the flow streamline in the plain disc system with that in the protruded system at $\phi = 90^\circ$ for the two mentioned flow conditions.

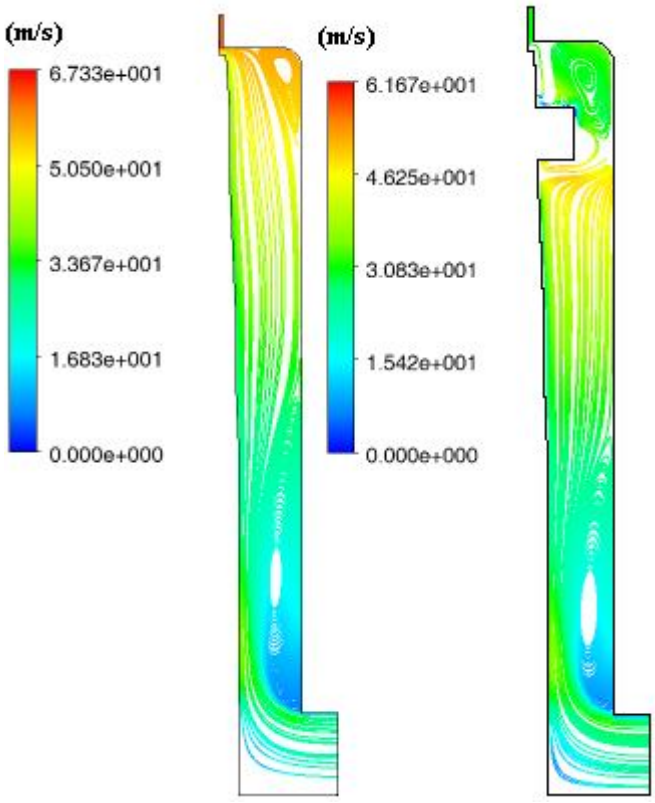

Figure 5.2: Flow Streamlines (relative total velocity) for the Plain Disc and Protruded Disc Systems; Re_ϕ = 0.177 x 10^7, C_w = 0.3 x 10^5, (λ_T = 0.31)

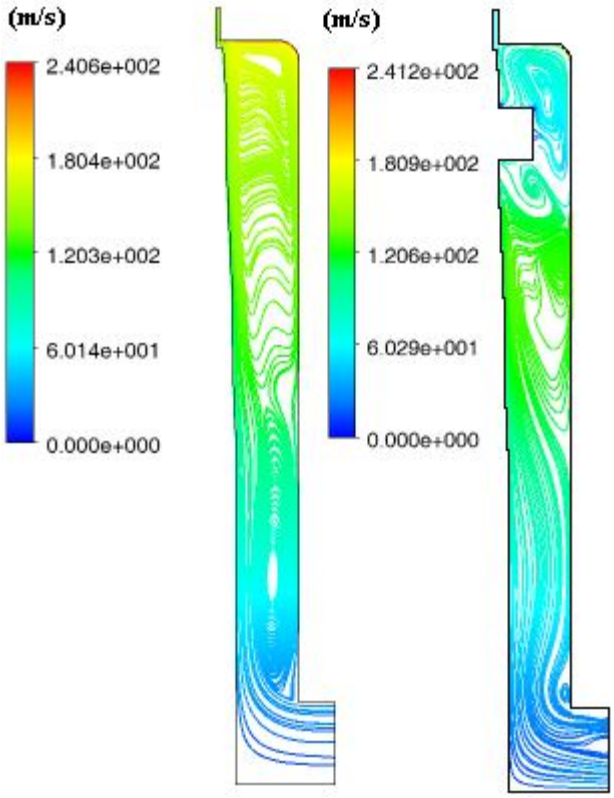

Figure 5.3: Flow Streamlines (relative total velocity) for the Plain Disc and Protruded Disc Systems; $Re_\phi = 0.72 \times 10^7$, $C_w = 0.3 \times 10^5$, ($\lambda_T = 0.09$)

It appears that the presence of bolts on the rotor reduces the recirculation zone close to the inlet, particularly for lower values of the turbulent flow parameter. This recirculation region is produced due to the 90° turn of the fluid from the axial to the radial direction as it enters the cavity. In addition, it can be seen that for the system with mounted bolts, the recirculation area close to the outlet is enlarged and covers almost the whole area above the bolts.

Figures 5.5 and 5.6 illustrate the simulation results of tangential velocity for the plain disc and rotor-mounted bolt systems at r/b = 0.62 and r/b = 0.8 (Figure 5.4 shows a side-view of the cavity with the selected two radial locations), for $Re_\phi = 0.177 \times 10^7$, $C_w = 0.3 \times 10^5$, ($\lambda_T = 0.31$) and $Re_\phi = 0.72 \times 10^7$, $C_w = 0.3 \times 10^5$, ($\lambda_T = 0.09$) respectively. Figures 5.7 and 5.8 show the results for radial velocity. It can be seen that for both of the flow conditions, the radial and tangential velocities of the plain disc system are almost equal with the rotor-mounted bolt system at lower radial locations. However, as

was expected, for higher radial locations the tangential velocity of the protruded disc system is higher than the plain disc system. In contrast, the radial velocity of the plain disc system is higher than the radial velocity of the protruded disc system.

Further inspection of the tangential velocity profiles reveals that for the throughflow dominated condition, the boundary layer thicknesses of the plain disc system are almost equal with those of the protruded disc system at both higher and lower radial locations. This is also the case for the rotationally dominated condition at lower radial locations. However, for the rotationally dominated condition at higher radii, the boundary layer thickness of the plain disc system is noticeably larger than that for the protruded system. This agrees with the results obtained in the previous chapter and also the results proposed by Daily *et al*. (1964) that the boundary layer thickness of the rotating disc increases with a reduction in the tangential velocity of the core.

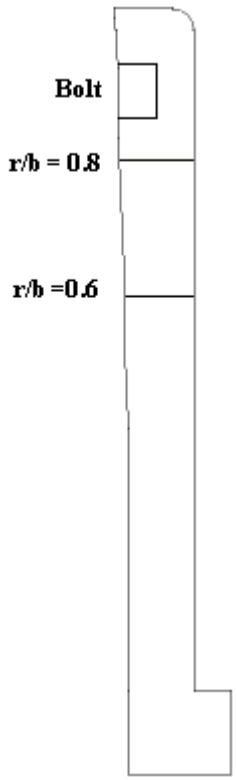

Figure 5.4: Side view of the Rotor-Stator System with Bolts (The Two Radial Locations where Tangential and Radial Velocities Distributions were obtained are shown)

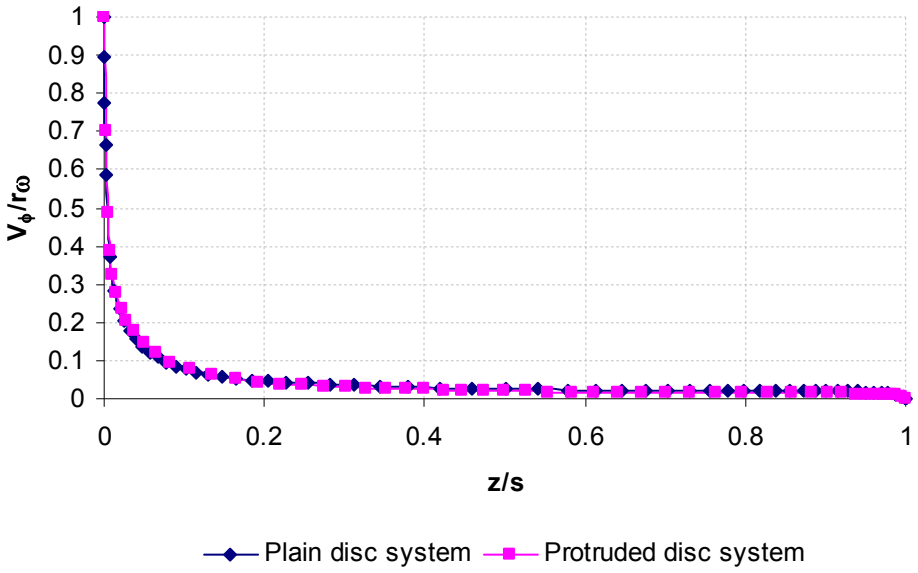

(a)

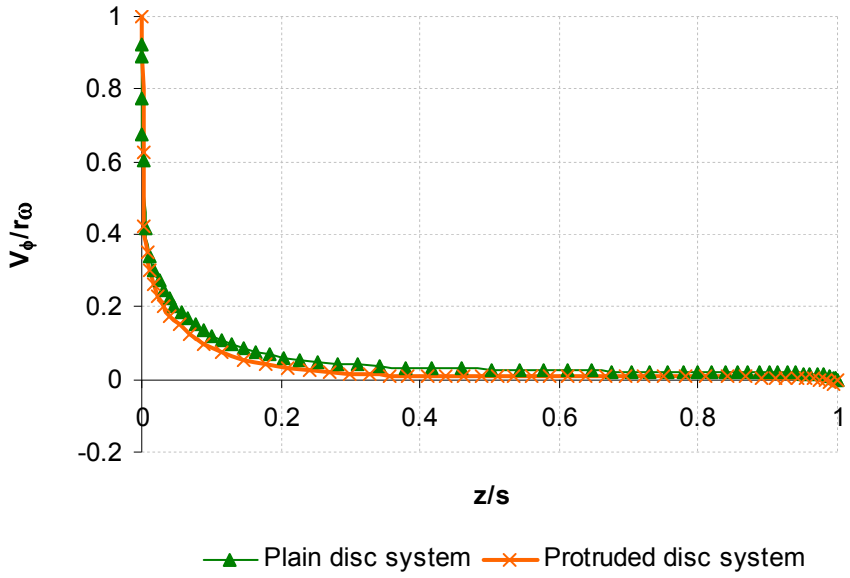

(b)

Figure 5.5: Comparison of the Dimensionless Tangential Velocity Distribution between the Plain Disc and Protruded Disc Systems for $Re_\phi = 0.177 \times 10^7$, $C_w = 0.3 \times 10^5$, ($\lambda_T = 0.31$) at (a) r/b =0.62 and (b) r/b = 0.8

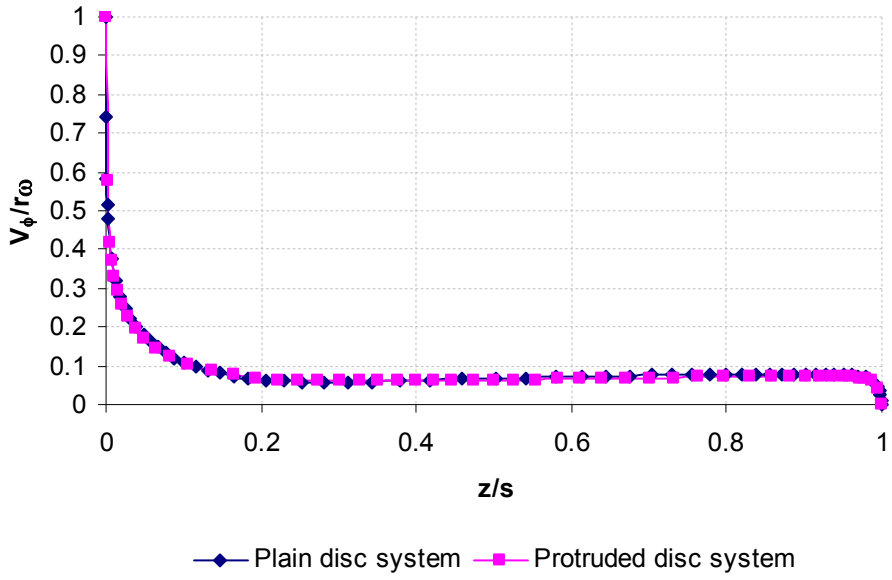

(a)

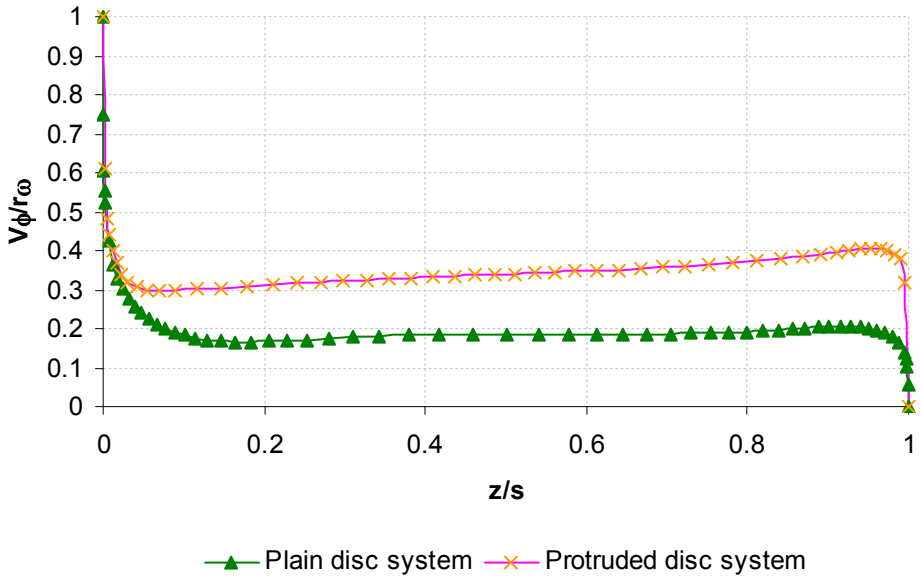

(b)

Figure 5.6: Comparison of the Dimensionless Tangential Velocity Distribution between the Plain Disc and Protruded Disc Systems for $Re_\phi = 0.72 \times 10^7$, $C_w = 0.3 \times 10^5$, ($\lambda_T = 0.09$) at (a) r/b =0.62 and (b) $r/b = 0.8$

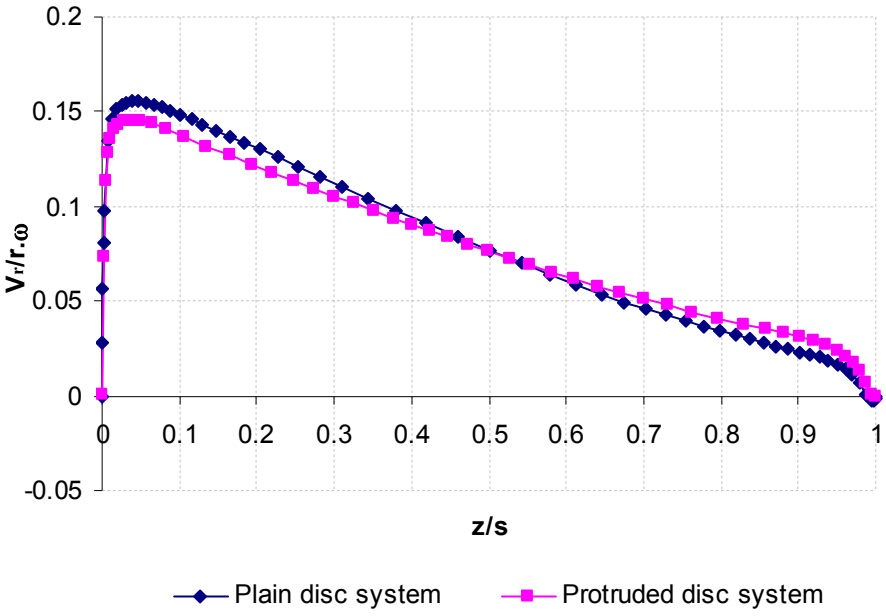

(a)

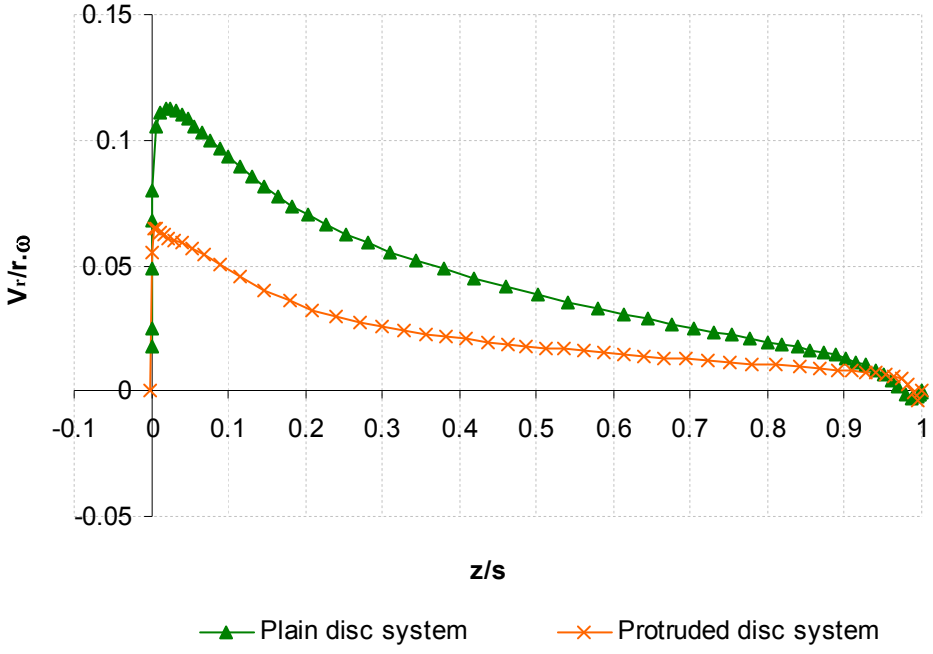

(b)

Figure 5.7: Comparison of the Dimensionless Radial Velocity Distribution between the Plain Disc and Protruded Disc Systems for $Re_\phi = 0.177 \times 10^7$, $C_w = 0.3 \times 10^5$, ($\lambda_T = 0.31$) at (a) r/b =0.62 and (b) r/b = 0.8

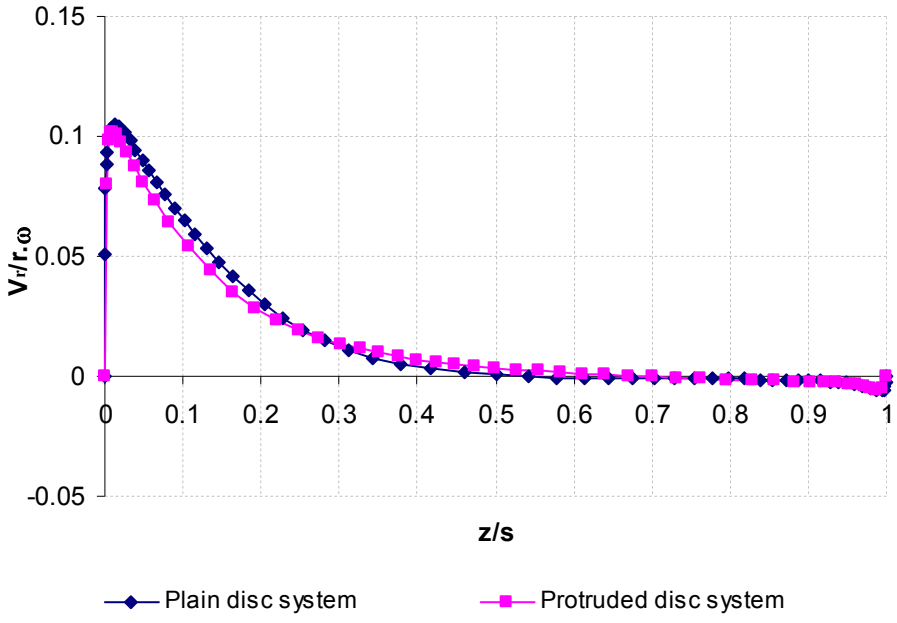

(a)

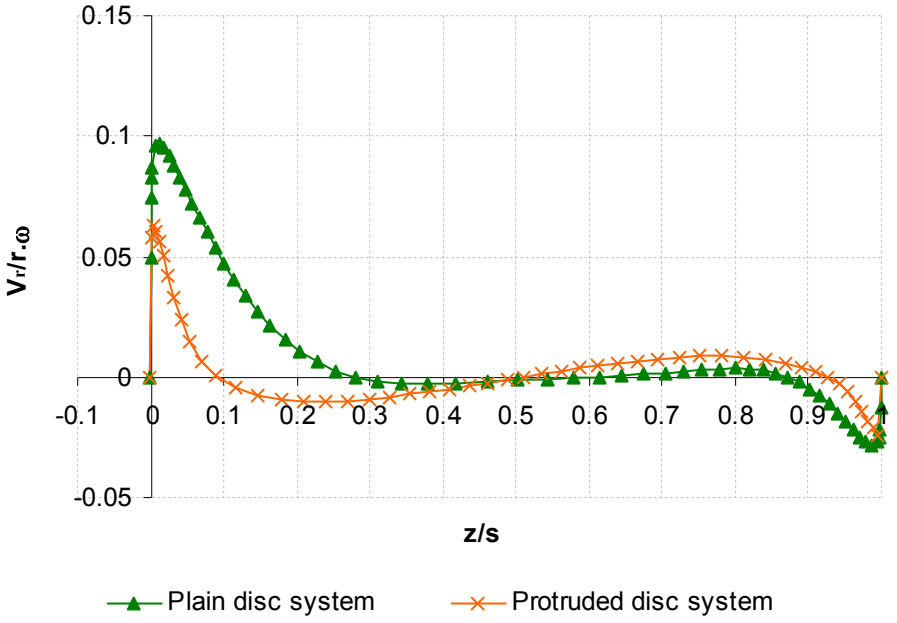

(b)

Figure 5.8: Comparison of the Dimensionless Radial Velocity Distribution between the Plain Disc and Protruded Disc Systems for $Re_\phi = 0.72 \times 10^7$, $C_w = 0.3 \times 10^5$, ($\lambda_T = 0.09$) at (a) r/b =0.62 and (b) r/b = 0.8

It is also interesting to examine the radial pressure distribution in the system with mounted bolts and compare it with the relevant results for the plain disc system. Figure 5.9 demonstrates the simulation results of the dimensionless pressure coefficient $Cp = \frac{(p_b - p_r)\rho b^2}{\mu^2}$ as a function of radius for the two mentioned flow conditions.

Inspection of Figure 5.9 reveals that for the rotationally dominated case, a small pressure variation exists from the lower radial locations up to the radius where the bottom of the bolt (r/b = 0.85) is located. Subsequently, pressure rapidly increases when approaching the peripheral seal. Based on these results, for the rotationally dominated condition the pressure difference between the inlet and the outlet of the cavity noticeably rises for the protruded disc system in comparison to the plain disc cavity. However, it appears that the radial pressure gradient is very close to zero for both the plain disc and protruded disc systems under the throughflow dominated condition.

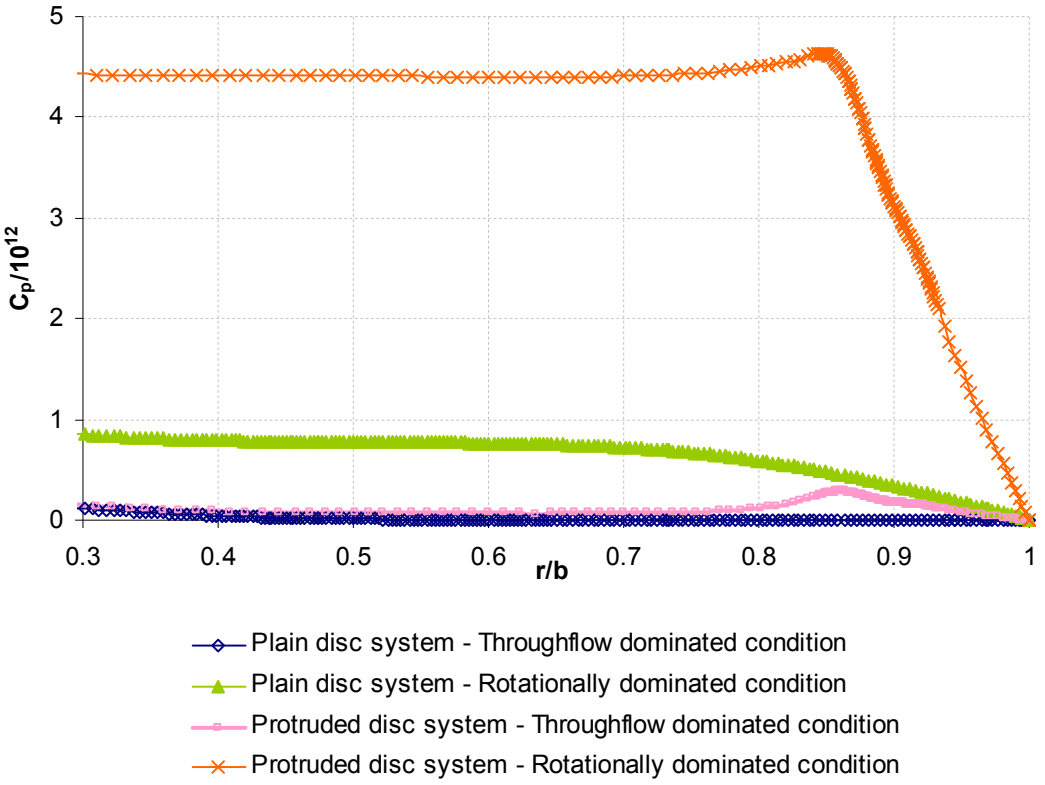

Figure 5.9: Comparison of the Radial Pressure Distribution between the Plain Disc and Protruded Disc Systems for the Rotationally Dominated Condition (Re_ϕ = 0.72 x 10^7, C_w = 0.3 x 10^5, (λ_T = 0.09)) and Throughflow Dominated Condition (Re_ϕ = 0.177 x 10^7, C_w = 0.3 x 10^5, (λ_T = 0.31)) at z/s = 0.52

It is also interesting to investigate the axial pressure gradient for the rotor-mounted bolt system. The axial pressure difference was found for the flow conditions of $Re_\phi = 0.177 \times 10^7$, $C_w = 0.3 \times 10^5$, ($\lambda_T = 0.31$) and $Re_\phi = 0.72 \times 10^7$, $C_w = 0.3 \times 10^5$, ($\lambda_T = 0.09$) at $r/b = 0.6$ and $r/b = 0.8$. Based on the simulation results, there is a small pressure difference (less than 2 Pa) between the rotor and stator at lower radial locations. This was also the case for the plain disc cases. However, in contrast to the plain disc cases, the axial pressure difference increases noticeably at higher radial locations, particularly for the flow condition with the lower turbulent flow parameter. For instance, the pressure difference between the rotor and stator was found to be about 1000 Pa for $\lambda_T = 0.09$ at $r/b = 0.8$.

The axial pressure difference produces an axial velocity in the negative direction of the z-axis (from the stator towards the rotor). This result was also found by Farthing (1988) during his experimental investigation of flow structure in a rotating cavity with mounted protrusions. He observed that mounting protrusions in the rotating cavity produces an axial flow between the rotating discs.

5.3.2 Investigation of the effects of mounting protrusions on the flow structure in the range of interference of the bolts for a specific flow condition

The focus in this section is on investigating the flow structure and different parameter variations in the vicinity of the bolts for a specific flow condition. The impact of changing the flow conditions will be explored in Section 5.3.3. The analysis provides a valuable insight into the key flow phenomena in protruded rotor-stator systems. Investigations were conducted for $Re_\phi = 0.177 \times 10^7$ and $C_w = 0.3 \times 10^5$, ($\lambda_T = 0.31$). While both the disc and the bolts are rotating with a constant angular speed in a moving fluid, it is more convenient to look at the fluid in the relative frame.

The flow field around the bolt can be explained by simultaneously studying flow streamlines, pressure distribution and wall shear stress distribution around the bolt.

Figure 5.10 (a) illustrates the relative velocity vectors around the bolt on a typical cross-sectional plane located close to the root of the bolt at z/s = 0.045. The angular locations of the corners of the bolt are shown in Figure 5.10 (b). Static pressure distribution around the bolt is plotted in Figure 5.11 (a) demonstrating the pressure coefficient (see Equation 5.1) as a function of angular location. Figure 5.11 (b) displays the static pressure contour at z/s = 0.045. In addition, Figure 5.12 exhibits the ϕ-wall shear stress distribution around the bolt at z/s = 0.045. ϕ-wall shear stress is the angular component of the force acting tangential to the surface of the bolt due to friction, and its unit quantity is pressure. Finally, Figure 5.13 displays the relative total velocity contour at z/s = 0.045.

$$C_p = \frac{(p_s - p_\infty)}{\frac{1}{2}\rho V_{rel}^{\ 2}} \tag{5.1}$$

Where p_s is the static pressure, p_∞ is the free-stream static pressure and V_{rel} is the free-stream relative total velocity.

It is important to note that the selected axial location (z/s = 0.045) is located in the rotor boundary layer. Therefore, the flow parameter variations are also influenced by the boundary layer effects of the rotor.

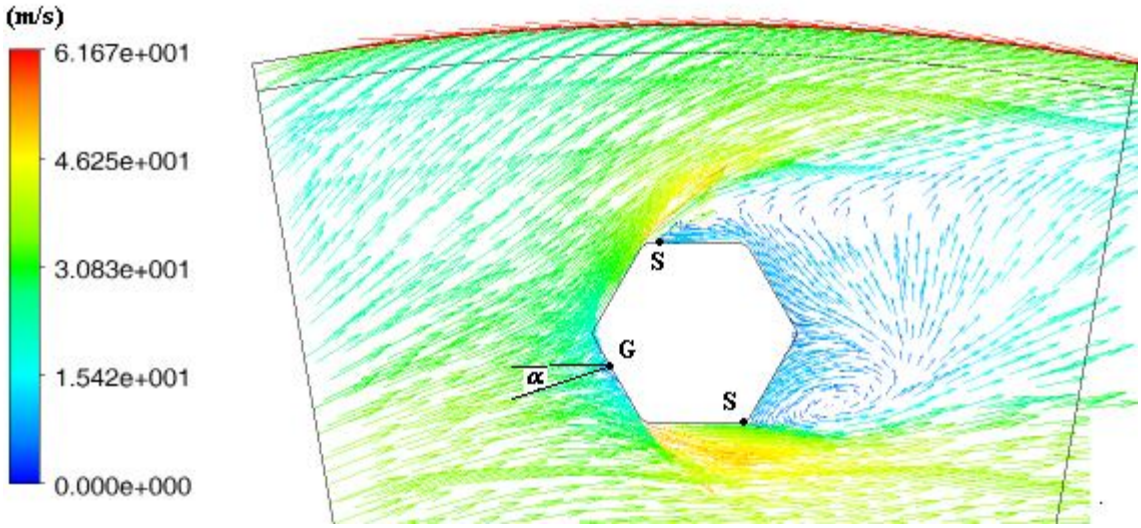

(a)

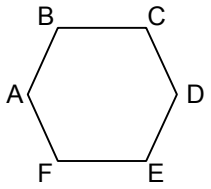

$\phi_A = 87.36^\circ, \phi_D = 92.64^\circ$

$\phi_F = 88.62^\circ, \phi_E = 91.38^\circ$

$\phi_B = 88.73^\circ, \phi_C = 91.27^\circ$

(b)

Figure 5.10: Relative Total Velocity Vectors around the Bolt at $z/s = 0.045$ for $Re_\phi = 0.177 \times 10^7$, $C_w = 0.3 \times 10^5$ ($\lambda_T = 0.31$). Rotor Rotates in Anti-clockwise Direction.

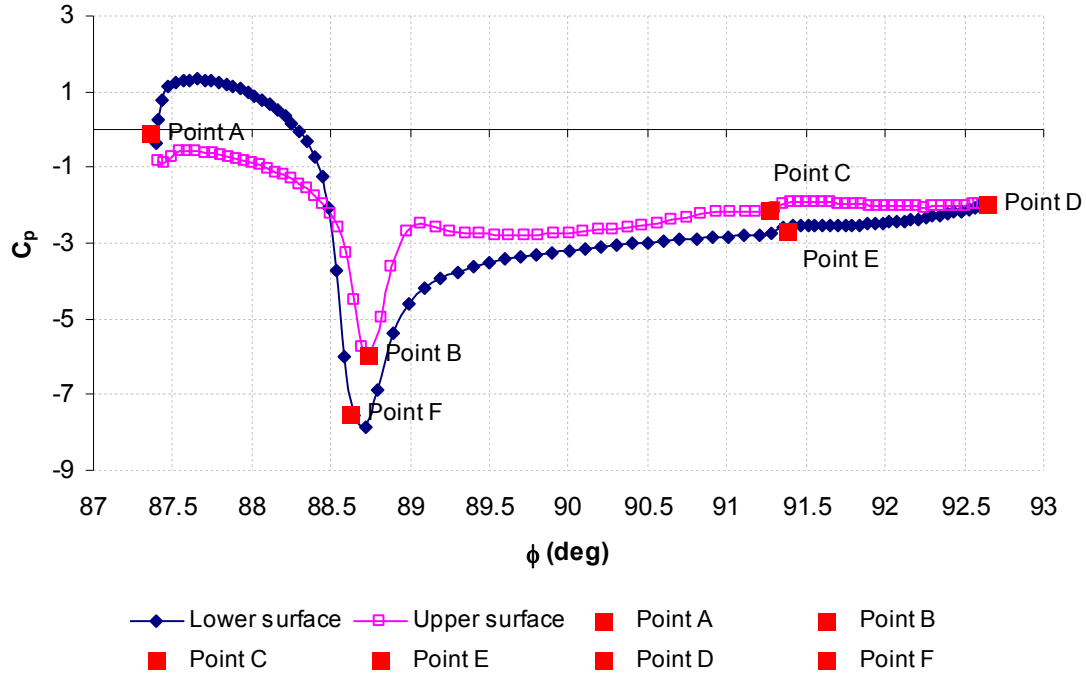

(a)

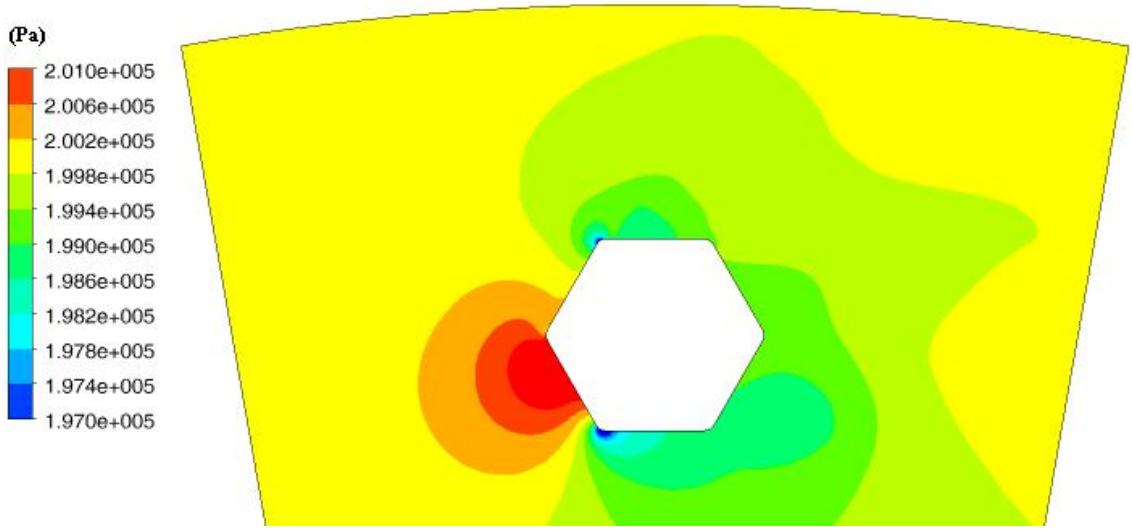

(b)

Figure 5.11: Static Pressure Distribution on the Bolt Surface at z/s = 0.045 for Re_ϕ = 0.177 x 10^7, C_w = 0.3 x 10^5 (λ_T = 0.31); (a) Pressure Coefficient Distribution, (b) Static Pressure Contour. Note: The Angular Coordinates of the Corners of the Bolt are also shown in the Figure (a) and Rotor Rotates in Anti-clockwise Direction.

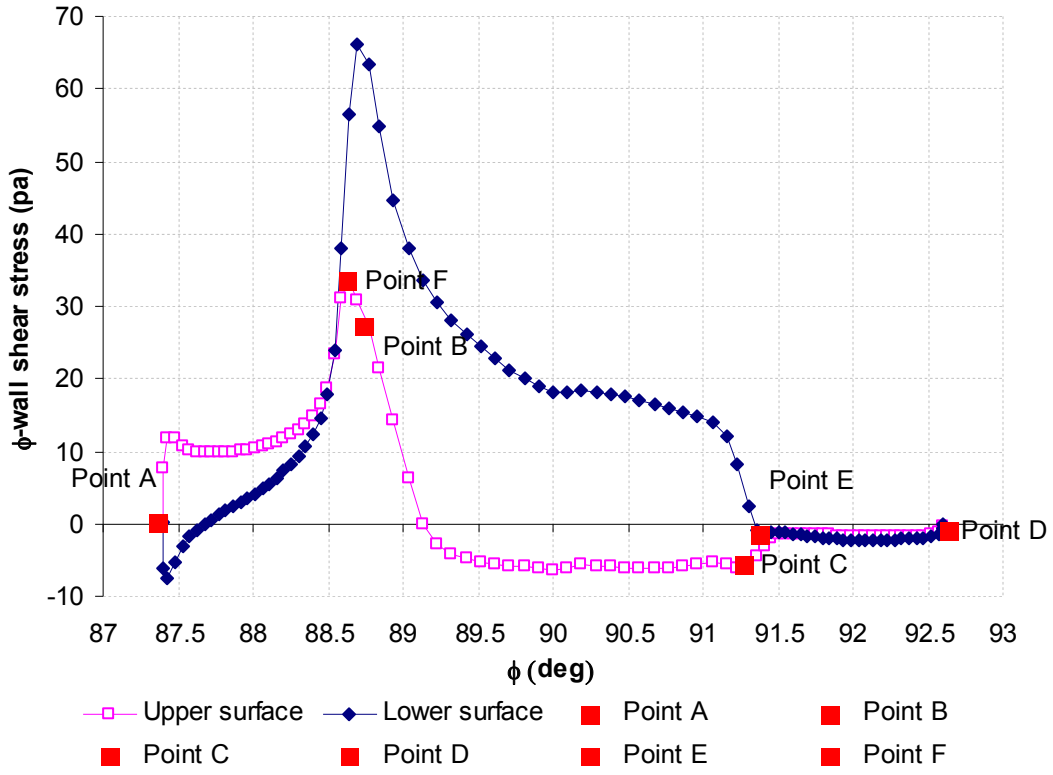

Figure 5.12: ϕ-Wall Shear Stress Distribution on the Bolt Surface at z/s = 0.045 for Re_ϕ = 0.177 x 10^7, C_w = 0.3 x 10^5 (λ_T = 0.31).
Note: The Angular Coordinates of the Corners of the Bolt are also shown in the Figure and Rotor Rotates in Anti-clockwise Direction.

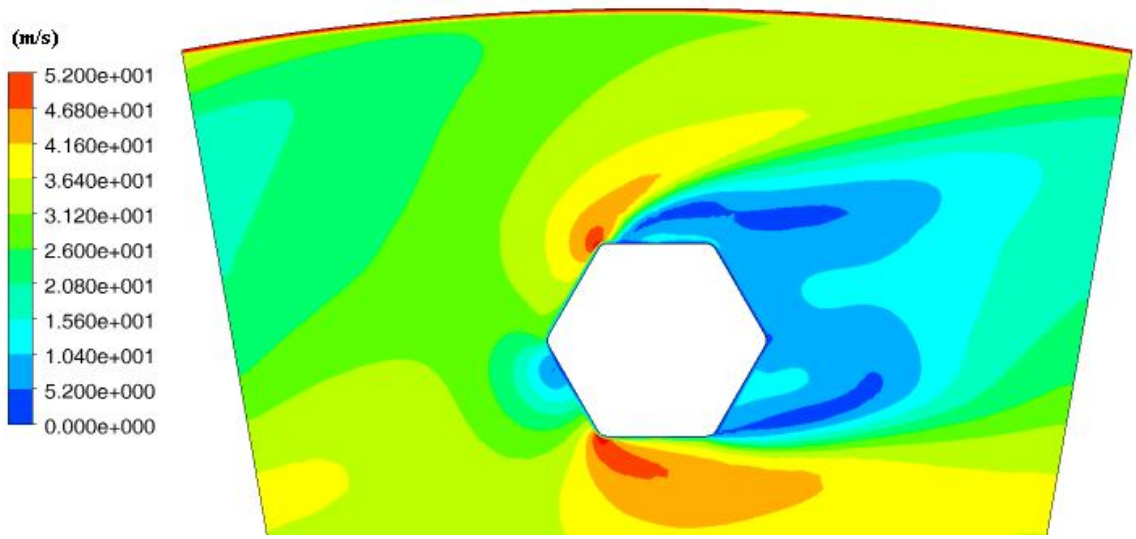

Figure 5.13: Total Relative Velocity Contour at z/s = 0.045 for Re_ϕ = 0.177 x 10^7, C_w = 0.3 x 10^5 (λ_T = 0.31)

As shown in Figure 5.10, flow having both radial and tangential velocities hits the bolt with a non-zero angle of attack. The point at which the flow hits the bolt and is brought to rest is called the stagnation point, G. The location of the stagnation point can be found using the pressure distribution plot around the bolt. The pressure coefficient is 1 at the stagnation point. According to Figure 5.11, the stagnation point is at $\varphi = 87.97^{\circ}$.

Inspection of Figure 5.11 reveals that, aside from the region close to the stagnation point, the static pressure of the bolt is lower than the free-stream static pressure. In addition, aside from the region near the stagnation point, the static pressure of the upper surface of the bolt is higher than the static pressure of its lower surface (see Figure 5.11 (a)). The reason is that the velocity on the upper side of the bolt is lower than its lower side.

It can be seen in Figure 5.11 (a) that there is a high static pressure zone near the stagnation point where the pressure coefficient peaks. From the stagnation point, a noticeable drop in pressure occurs and the boundary layer develops under a negative pressure gradient. Eventually, the pressure reaches a minimum near the front upper and lower corners of the bolt, and after that the boundary layer develops with a positive or adverse pressure gradient. Based on Bernoulli's equation, as the pressure of fluid increases in the adverse pressure region, its velocity reduces. The pressure increases up to a point at which the velocity gradient becomes zero (points S in Figure 5.10 (a)). At these points, the flow encounters separation, where the momentum of fluid cannot overcome the adverse pressure gradient. Separation causes the boundary layer to detach from the bolt, making the fluid be pushed backward by the pressure gradient and a wake region to be formed. This region is the source of the form drag of the bolt and is characterised by a vortex formation. The separation points in the adverse pressure region can be approximately identified as the start of the region over which the surface static pressure is nearly constant (Tani, 1964). According to Figure 5.11, this constant-pressure region extends to the trailing edge of the bolt. Based on the findings obtained by Tani (1964), the extension of the constant pressure region to the trailing edge of an airfoil indicates that the flow fails to reattach to the surface. This appears to also be the case for the flow around the bolt with this specific flow condition where there is no reattachment of flow after the separation points.

In order to completely analyse the flow field around the bolt, it is also necessary to investigate the wall shear stress distribution around it. Wall shear stress varies along the bolt surface, reflecting the influence of the pressure gradient and the flow phenomena, such as separation, reattachment and laminar to turbulent transition of the boundary layer over the bolt. Moreover, it would be helpful to simultaneously study the velocity variations around the bolt. As can be seen in Figure 5.12, the ϕ-wall shear stress distribution along the bolt shows a small negative region close to the stagnation point. This region is restricted by the points of zero wall shear stress; one corresponds to the front middle corner of the bolt, and the other corresponds to a point close to the stagnation point. The negative values of wall shear stress over the bolt in that region can be attributed to the changing direction of the flow as it stagnates on the bolt.

Following the flow from this region, it can be seen that the wall shear stress increases on the top and bottom surfaces of the bolt. This is due to the pressure reduction along these regions. Wall shear stress is then reduced and reaches zero at around $\varphi = 89.17^{\circ}$ on the upper surface and $\varphi = 91.34^{\circ}$ on the lower surface of the bolt. These points are the locations where the flow separates from the bolt surface. The region between these two points is the recirculation or wake region, in which the wall shear stress stays at small negative values. According to Figure 5.12, wall shear stress does not change sign from negative to positive after the separation points, which means that flow does not reattach to the surface of the bolts. This confirms the result concluded from the pressure distribution investigations around the bolt.

Considering Figure 5.13, it can be seen that there is a low velocity region near the stagnation point, which is followed by an increase in the velocity along the bolt surface. Velocity reaches a maximum at the upper and lower front corners of the bolt, where the wall shear stress also peaks and the pressure coefficient reaches its minimum value. The wake region is characterised as a near zero velocity region at the rear side of the bolt.

As mentioned above, since the selected axial location ($z/s = 0.045$) for the discussed variations of flow parameters is in the rotor boundary layer, the flow parameter variations are influenced by the boundary layer effects of the rotor. Hence, in order to study the effects of the bolt alone, it is necessary to re-examine flow parameter variations at other axial locations out of the rotor boundary layer. Accordingly, two

axial locations, one at z/s = 0.22 and the other at z/s = 0.4 were selected for analysis. Note that z/s = 0.5 is the axial location of the tip of the bolt.

Before analysing the simulation results at z/s = 0.4 and z/s =0.22, it is of interest to study the extent of the influence of the bolts on the boundary layer thickness of the rotor in the range of their interference. Therefore, the tangential velocity profiles were plotted at different radial and angular locations around the bolt. Inspection of the tangential velocity plots reveals that the thickness of the boundary layer attached to the rotor reduces when moving from the bottom to the top of the bolt. For instance, the rotor boundary layer thickness at r/b = 0.86 and $\varphi = 87.28^{\circ}$ is δ = 3.3mm, which reduces to δ = 1.2mm at r/b = 0.92 and $\varphi = 87.28^{\circ}$. This is due to the increased effects of the bolts on the dimensionless tangential velocity of the core. As was mentioned in Chapter 4, the rotor boundary layer thickness is a function of (1-β). Hence, increasing the core swirl ratio ends up with a reduction of the boundary layer thickness.

In contrast to the radial variations of the rotor boundary layer thickness, variations in the boundary layer thickness along the angular direction do not follow a regular pattern with the increase of the angular distance from the bolts, and depend instead on the selected radial location.

Figures 5.14 through 5.18 illustrate respectively relative velocity vectors, static pressure distribution, ϕ-wall shear stress distribution, static pressure contour, and total relative velocity contour at z/s = 0.4 and z/s = 0.22.

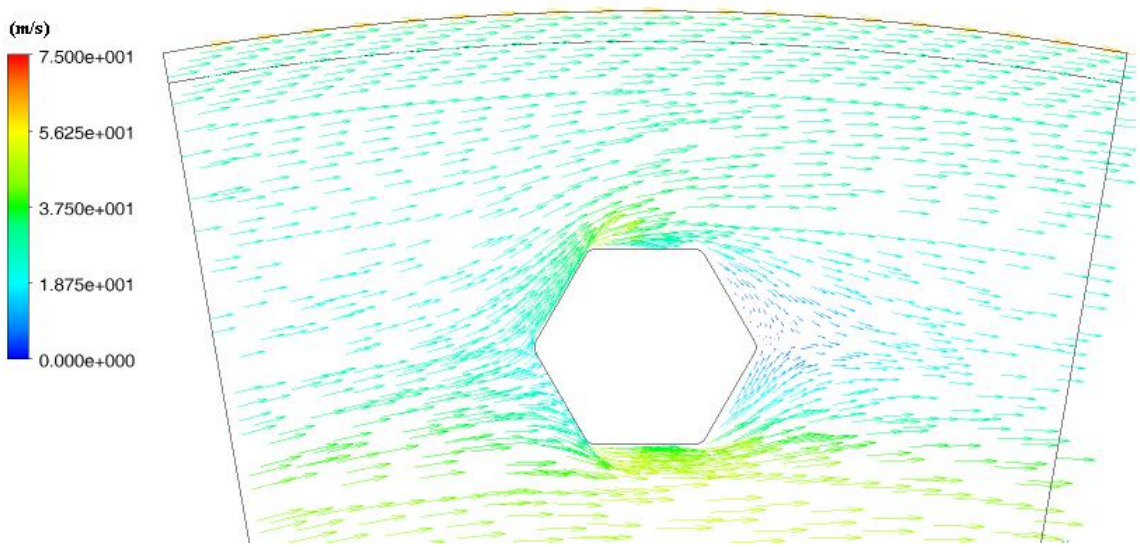

(a)

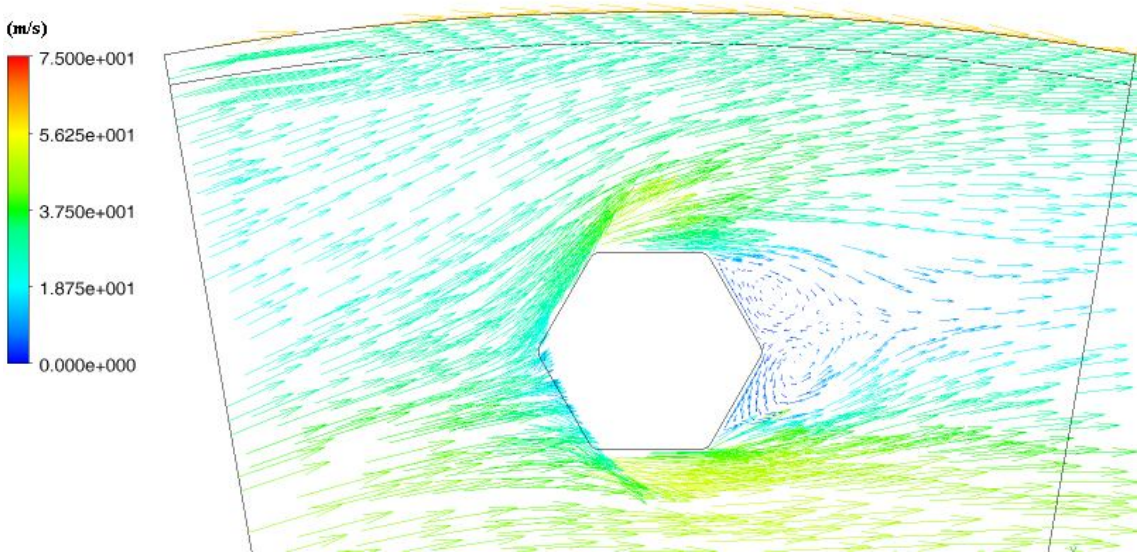

(b)

Figure 5.14: Relative Velocity Vectors around the Bolt for Re_{ϕ} = 0.177 x 10^7, C_w = 0.3 x 10^5 (λ_T = 0.31) at (a): z/s = 0.4 and (b): z/s = 0.22

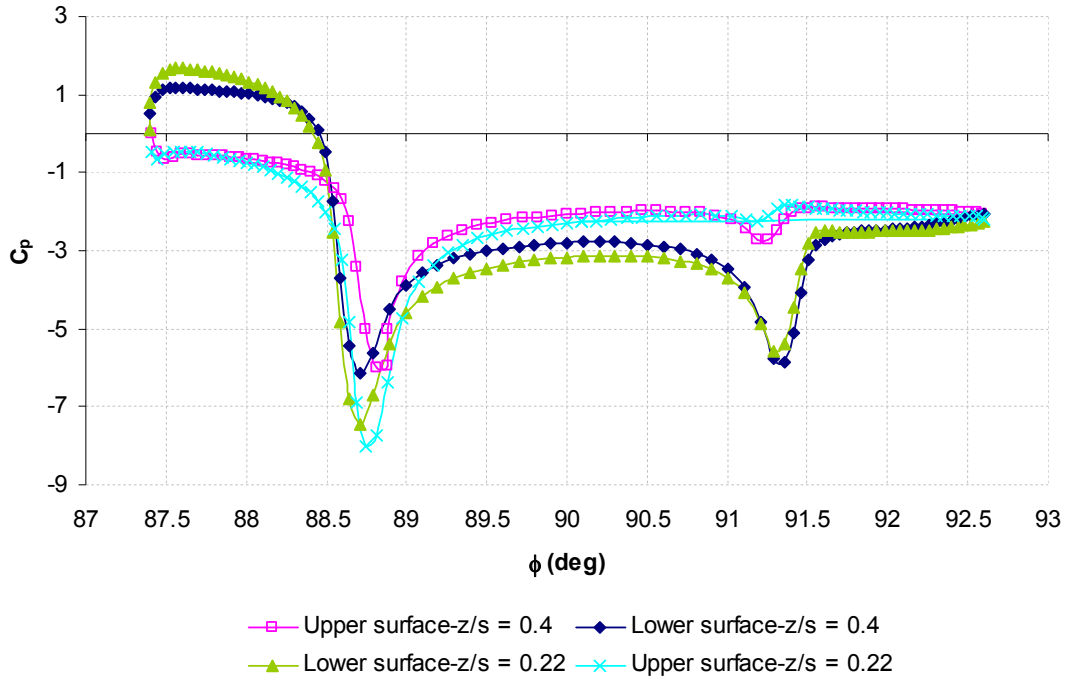

Figure 5.15: Pressure Coefficient Distribution on the Bolt Surface at *z/s* = 0.4 and *z/s* = 0.22 for Re_ϕ = 0.177 x 10^7, C_w = 0.3 x 10^5 (λ_T = 0.31

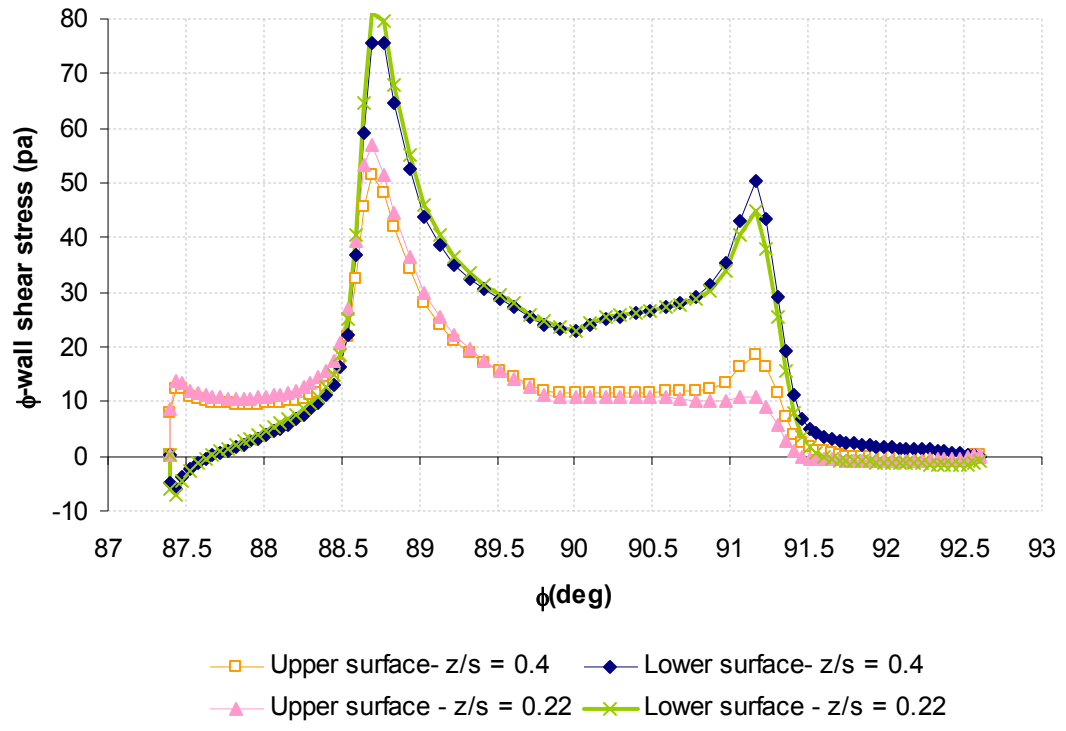

Figure 5.16: ϕ-Wall Shear stress Distribution on the Bolt Surface at *z/s* = 0.4 and *z/s* = 0.22 for Re_ϕ = 0.177 x 10^7, C_w = 0.3 x 10^5 (λ_T = 0.31)

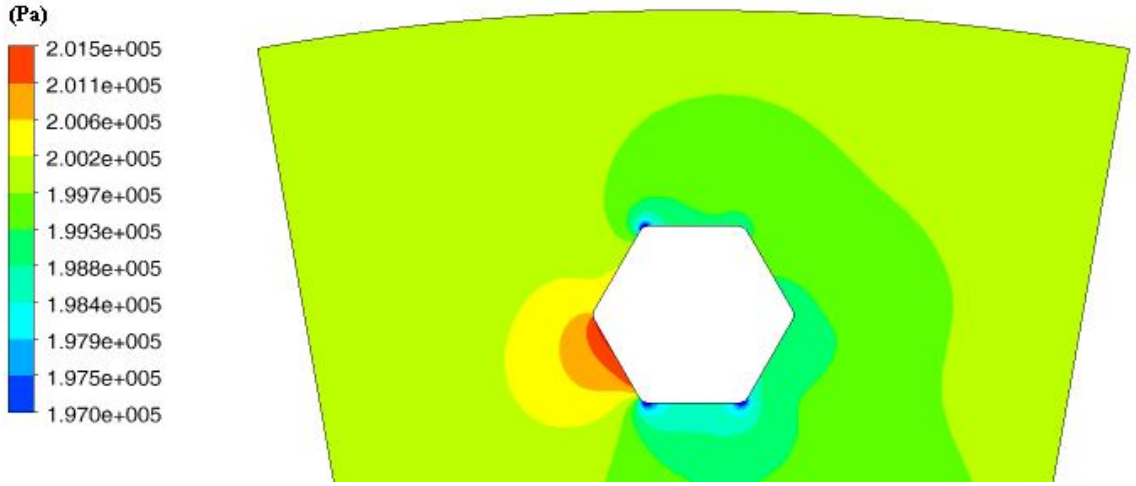

(a)

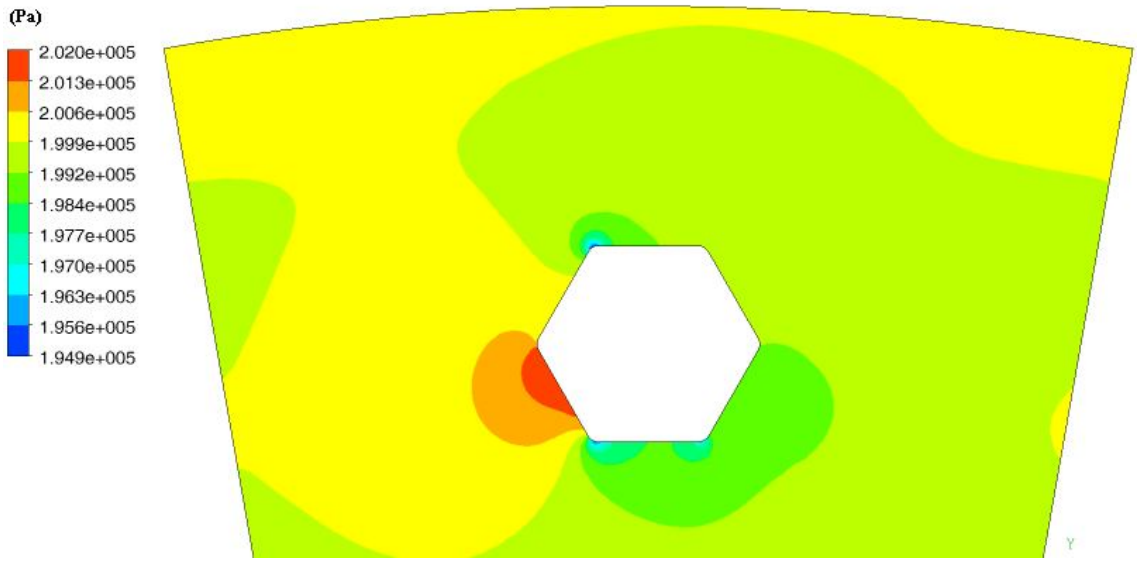

(b)

Figure 5.17: Static Pressure Contour around the Bolt Surface for $Re_{\phi} = 0.177 \times 10^7$, $C_w = 0.3 \times 10^5$ ($\lambda_T = 0.31$) at (a): $z/s = 0.4$ and (b): $z/s = 0.22$

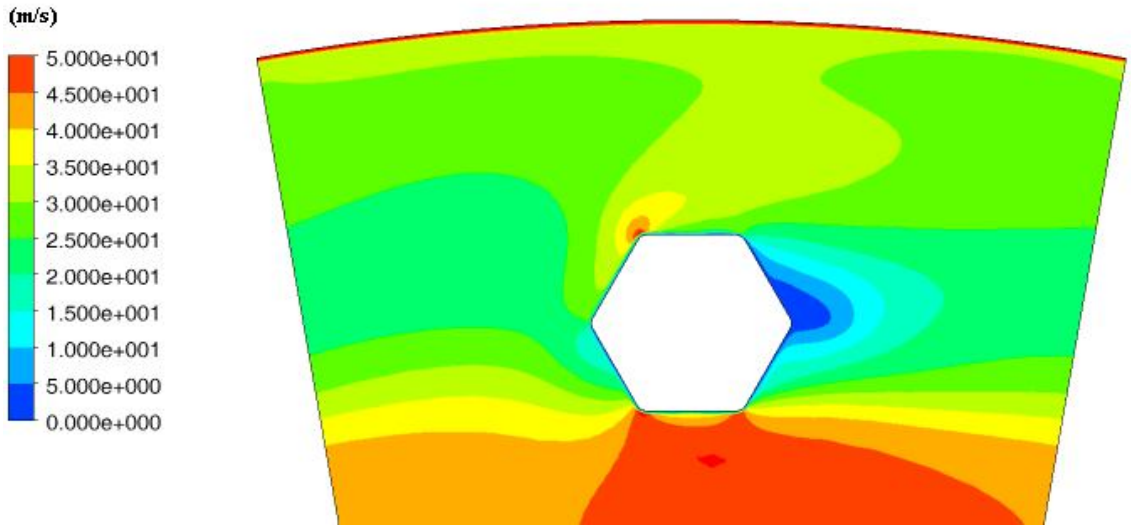

(a)

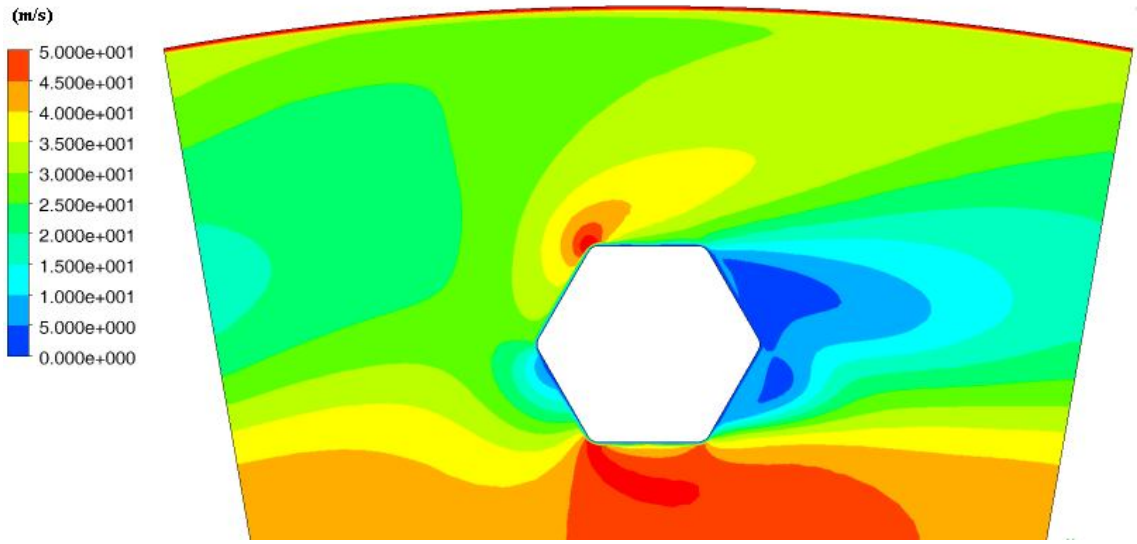

(b)

Figure 5.18: Total Relative Velocity Contour for Re_{ϕ} = 0.177 x 10^7, C_w = 0.3 x 10^5 (λ_T = 0.31) at (a): *z/s* = 0.4 and (b): *z/s* = 0.22

Considering Figure 5.14 and comparing it with Figure 5.10, it can be seen that the wake region is moved towards the rear section of the bolt and is significantly smaller than the wake region at *z/s* = 0.045. Comparison of Figures 5.16 and 5.12 shows that the separation point on the upper side of the bolt was moved from around φ = 89.17˚ at *z/s* = 0.045 to φ = 91.41˚ at *z/s* = 0.22 and then to φ = 91.67˚ at *z/s* = 0.4. In addition, the

separation point on the lower side of the bolt was moved from around φ = 91.34˚ at *z/s* = 0.045 to φ = 91.64˚ at *z/s* = 0.22 and then to φ = 92.35˚ at *z/s* = 0.4. The mentioned displacements result in a smaller wake region, and confirm the results obtained by comparing the two flow streamline plots.

Further inspection of Figure 5.16 reveals that the ϕ-wall shear stress profile at *z/s* = 0.22 and *z/s* = 0.4 has two peaks. This is contrary to the relevant plot at *z/s* = 0.045. The location of the second maximum in the wall shear stress plot at *z/s* = 0.22 and *z/s* = 0.4 corresponds to the second minimum in the pressure distribution plot (see Figure 5.15). Similarly, this second minimum was not observed in the pressure distribution profile at *z/s* = 0.045. Hence, since the bolt is located in the rotor boundary layer at *z/s* = 0.045, the reason for the different patterns observed in the wall shear stress and pressure plots at *z/s* = 0.045 could be attributed to the interaction of the flow around the bolt with the boundary layer of the rotor.

Considering the pressure distribution, comparison of the two relevant plots (Figures 5.11 and 5.15) demonstrates that the stagnation point is moved toward the lower surface of the bolt at around φ = 88.04˚.

In order to explain the reasons for the mentioned variations of flow parameters along the axial direction, it is required to calculate the three key parameters that affect the flow structure around immersed bodies. As mentioned by Schlichting and Gersten (1999), the mean flow around immersed bodies is mainly governed by three control parameters: the free-stream Reynolds number, $\mathrm{Re_D}$ (see Equation 5.2), the angle of attack, α (see Equation 5.3), and the Mach number of the flow approaching the bodies. However, the effects of the Mach number are only important for Mach numbers greater than about 0.4 (White, 1998).

$$\mathrm{Re}_D = \frac{\rho V_{rel} D}{\mu} \qquad 5.2$$

$$\alpha = \tan^{-1}\left(\frac{V_r}{V_{\varphi-rel}}\right) \qquad 5.3$$

Where V_r, $V_{\phi\text{-}rel}$ and V_{rel} are, respectively, the radial, relative tangential and relative total velocities, and D is the diameter of the bolt.

In order to calculate the Mach number, free-stream Reynolds number and angle of attack of the flow approaching the bolt, it is necessary to first calculate the relevant velocity magnitudes used in the equations. However, finding these velocity components is not a simple task. The reason is that the velocity field of the flow approaching the bolts is highly non-uniform and three-dimensional. Hence, the only applicable method for calculating the necessary velocity components is to average each of them on a plane downstream from the bolt. This plane is used for calculating the total values of the free-stream Reynolds number, angle of attack and Mach number, and is selected at a distance from the bolt where velocity variations due to the boundary layer effects of the bolts are negligible. Accordingly, a bounded plane with a width of 11mm (the height of the bolt) and a length of 16mm (the diameter of the bolt) located at $\varphi = 87.28^\circ$ is selected for the averaging calculations. Using the resulting values of the averaged velocity components, it is possible to obtain the Mach number, free-stream Reynolds number and angle of attack.

As mentioned, averaging the velocity components over the selected plane yields the total amounts of Re_D, α and Ma. However, in order to determine the local values of these parameters at z/s = 0.045, z/s = 0.22 and z/s = 0.4 it is required to average the velocity components on three lines located on the selected plane at the axial locations under investigation. The results of the total values as well as the local values of the free-stream Reynolds number, angle of attack and Mach number at the mentioned axial locations are tabulated in Table 5.2.

Table 5.2: Results of the Free-stream Reynolds Number, Angle of Attack and Mach Number of The Flow Approaching the Bolt for $Re_\phi = 0.177 \times 10^7$ and $C_w = 0.3 \times 10^5$, ($\lambda_T = 0.31$)

	Re_D ($/10^5$)	α (deg)	Ma
Local value at z/s = 0.045	0.51	40	0.12
Local value at z/s = 0.22	0.52	32	0.115
Local value at z/s = 0.4	0.53	28	0.11
Total value	0.54	30	0.11

According to the results presented in Table 5.2, since the Mach number is lower than 0.4, it is expected that compressibility effects do not influence the flow structure around the bolt. In addition, it can be seen that the free-stream Reynolds number did not vary noticeably from the root to the tip of the bolt. This is in contrast to the angle of attack, which had significant variations along the axial direction. Based on these results, it appears that it is the angle of attack rather than the free-stream Reynolds number that affects the flow structure variations around the bolts in z-direction.

Schlichting and Gersten (1999) found that for a NACA 4412 airfoil, both the pressure distribution and the lift coefficient are dependent on the angle of attack. According to their measurements at a constant Reynolds number, increasing the angle of attack from $\alpha = 0^\circ$ to $\alpha = 8^\circ$ changes the symmetric pressure distribution to a significantly different pressure profile at the upper and lower sides, and reduces the pressure difference around the airfoil. In addition, it was found by Tani (1964) that increasing the angle of attack for an airfoil advances the separation and reattachment points toward the leading edge. Although the geometric shape of the hexagonal bolt is very different from an airfoil, similar trends of movement of the separation point could be observed for the flow passing the bolt in the rotor-stator cavity.

It would be of interest to restudy the flow structure variations along z-direction in order to identify the presence of Taylor columns. The occurrence of Taylor columns was investigated by Farthing (1988). Farthing performed experimental measurements inside a rotating cavity with a radial outflow of air and four cylindrical protrusions. Using smoke injections, he observed the flow pattern inside the cavity and compared it with the relevant pattern in a rotating cavity without protrusions. According to his experimental measurements, for both the turbulent and laminar flows Taylor columns could be produced in the system up to very high Rossby numbers (about 0.4 for turbulent flow).

Taylor columns are imaginary cylinders projected above and below a real cylinder in a steady flow with strong rotations. According to the Taylor-Proudman theorem, the flow will curve around this cylinder and the directional derivatives of velocity in the direction of the axis of rotation will vanish. Since the existence of strong rotation ($Ro \ll 1$) is necessary for producing Taylor columns, Rossby number, Ro, can be used as an

indicator. Equation 5.4 displays the Rossby number as a function of the core swirl ratio (Farthing, 1988 and Gartner, 1998).

$$Ro = 1 - \frac{V_\phi}{r\omega} \qquad 5.4$$

For the case of the rotor-stator cavity under investigation and for $Re_\phi = 0.177 \times 10^7$ and $C_w = 0.3 \times 10^5$ ($\lambda_T = 0.31$), the Rossby number is 0.6. Although the magnitude of the Rossby number is near the maximum value obtained by Farthing for a rotating cavity with mounted protrusions, the simulation results show no evidence of any imaginary cylinder above the bolts. This result is obtained by looking at the velocity vectors in planes located at different axial locations perpendicular to the axis of rotation above the bolts. Accordingly, no imaginary cylinder and, as a result, no Taylor column is formed above the bolt in the system.

Further investigation of the flow around the bolts could be conducted by studying the flow structure variations along the radial direction. Figure 5.19 illustrates the flow streamlines around the bolt at three different radial locations: $r/b = 0.86$, $r/b = 0.89$ and $r/b = 0.92$. As can be observed, the area of the wake region increases, moving from the bottom to the middle section of the bolt and then decreases, moving from the middle section towards the top of the bolt. This could be explained by comparing the local values of angle of attack and free-stream Reynolds number for the flow approaching the bolt at the mentioned radial locations. Based on the simulation results, the free-stream Reynolds number reduces by moving from $r/b = 0.86$ to $r/b = 0.89$ and then increases with the further increase of the radial location up to $r/b = 0.92$. Regarding the angle of attack, it can be seen that it increases from $r/b = 0.86$ to $r/b = 0.89$ and is then reduced by moving to $r/b = 0.92$. These variations could be attributed to the variation of both direction and magnitude of the radial and relative tangential velocity vectors in the upper and lower sections of the bolt. Based on the simulation results, radial velocity increases by moving from the bottom towards the middle section of the bolt and then reduces towards its upper surface. However, the relative tangential velocity has a reverse trend and it reduces by moving from the lower section of the bolt towards the middle of it, and it is then increased by further movement towards the upper section of the bolt. The trend of variations of the total relative velocity magnitude is similar to that described for the relative tangential velocity.

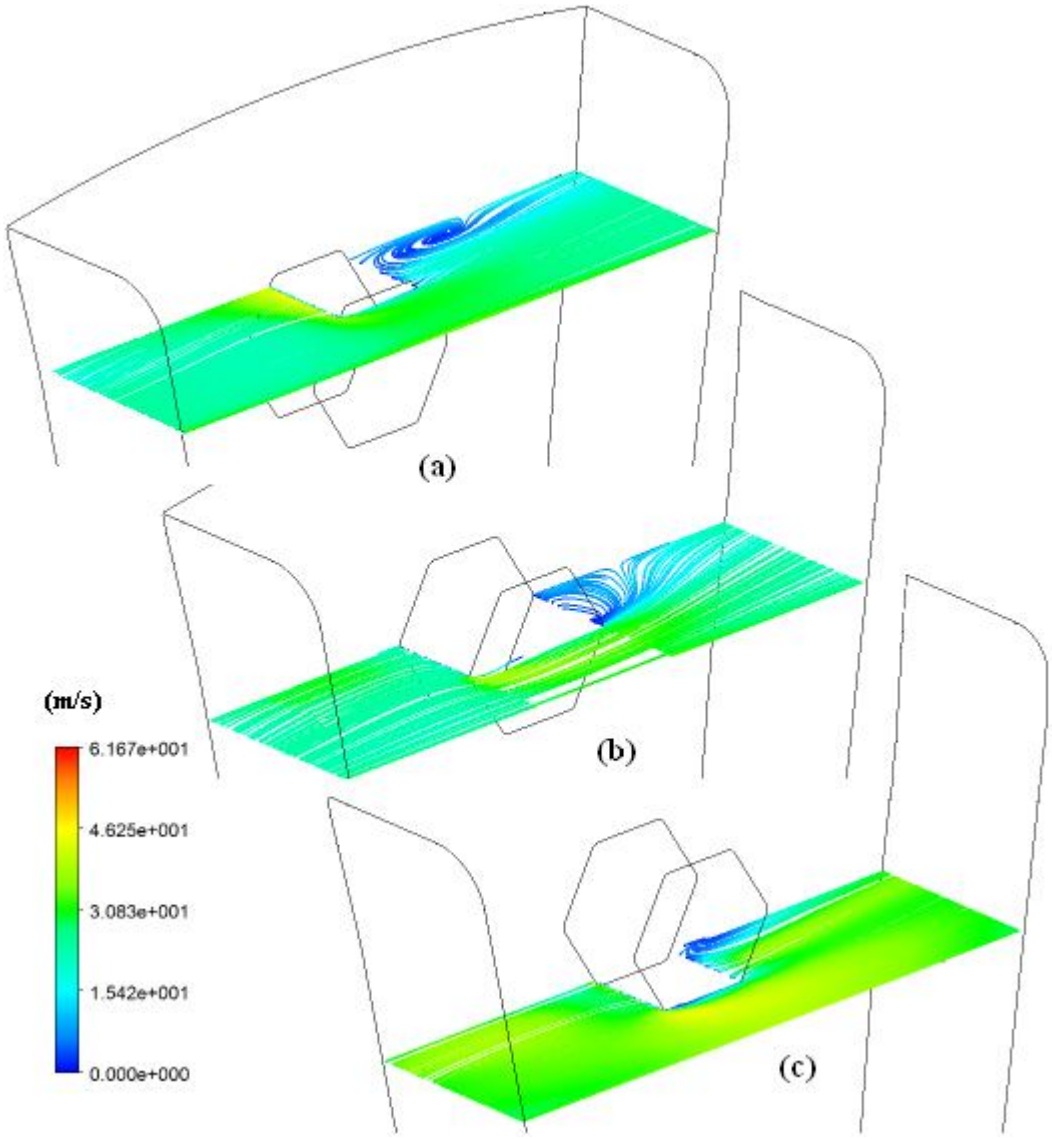

Figure 5.19: Flow Streamlines around the Bolt for $Re_\phi = 0.177 \times 10^7$, $C_w = 0.3 \times 10^5$ ($\lambda_T = 0.31$) at (a) $r/b = 0.92$, (b) $r/b = 0.89$ and (c) $r/b = 0.86$

5.3.3 Investigation of the effects of changing the flow conditions on the flow structure in the range of interference of the bolt

The results of the flow structure analysis for $Re_\phi = 0.177 \times 10^7$ and $C_w = 0.3 \times 10^5$ ($\lambda_T = 0.31$) showed that the free-stream Reynolds number and angle of attack of the flow approaching the bolt are the governing parameters that affect the flow structure variations in three dimensions around the bolt. In addition, it is expected that variations

of the rotational Reynolds number and the throughflow rate indirectly affect the flow structure around the bolt by varying the free-stream Reynolds number and angle of attack of the flow hitting the bolt. These effects are graphically displayed in Figure 5.20, which shows relative velocity vectors around the bolt at z/s = 0.045 for the matrix of flow conditions presented in Table 5.1. This axial location was selected because at z/s = 0.045 the angle of attack of the flow hitting the bolt, the size of the wake region and, as a result, the boundary layer effects of the bolt have their highest values. However, the results of changing the axial location are also described in the following pages. Figures 5.21 and 5.22 show the pressure and ϕ-wall shear stress distributions around the bolt at z/s = 0.045 for a constant C_w and two different values of Re_ϕ. Figures 5.23 and 5.24 display similar results for approximately similar values of Re_ϕ and two different values of C_w.

To complement the discussions about the effects of changing the flow conditions on the flow structure around the bolt, it is necessary to calculate the local free-stream Reynolds number and angle of attack of the flow approaching the bolt at z/s = 0.045. The results are tabulated in Table 5.3. It should be noted that the total Mach number of the flow approaching the bolt ranges from about 0.08 for $\mathrm{Re}_\phi = 0.362 \times 10^7$ and $C_w = 10^5$ (λ_T = 0.58) to about 0.41 for $\mathrm{Re}_\phi = 0.933 \times 10^7$ and $C_w = 0.3 \times 10^5$ (λ_T = 0.06). Accordingly, it appears that compressibility effects do not influence the flow structure around the bolts for the range of the simulated non-dimensional parameters. In addition, Table 5.4 compares the stagnation and separation points at z/s = 0.045 for the flow conditions presented in Table 5.3.

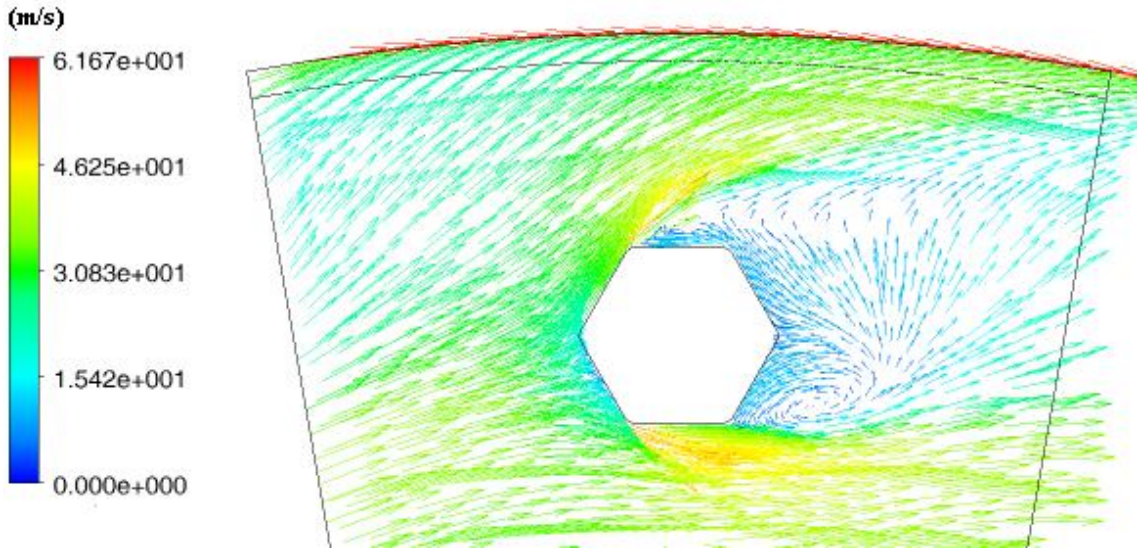

(a): C_w = 0.3 x 10^5, Re_ϕ = 0.177 x 10^7, λ_T = 0.31

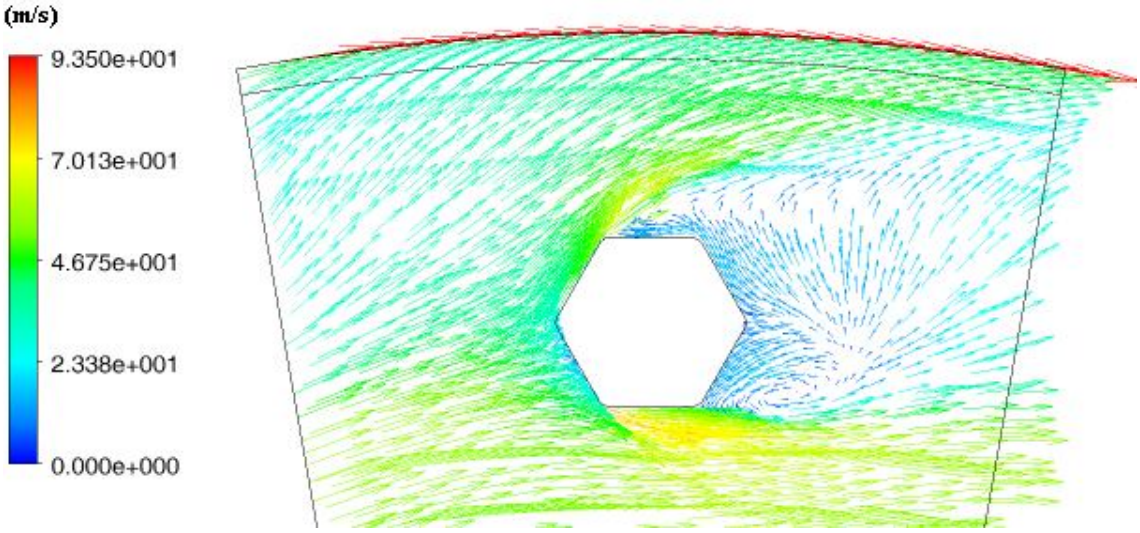

(b): C_w = 0.3 x 10^5, Re_ϕ = 0.272 x 10^7, λ_T = 0.22

Figure 5.20: Comparison of Relative Velocity Vectors at *z/s* = 0.045 for Different Flow Conditions (Continued)

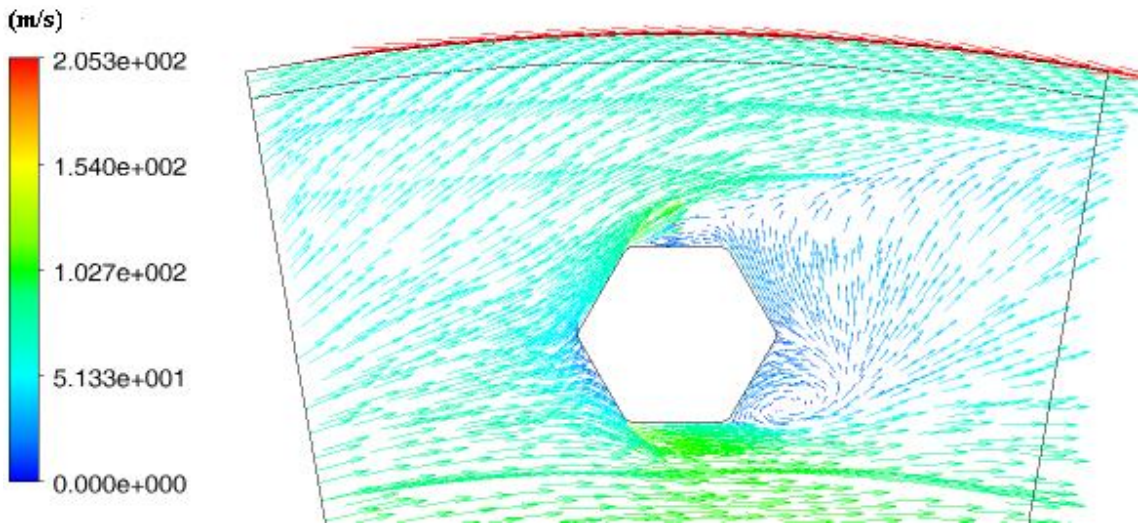

(c): C_w = 0.3 x 10^5, Re_ϕ = 0.716 x 10^7, $\lambda_{T=}$ 0.088

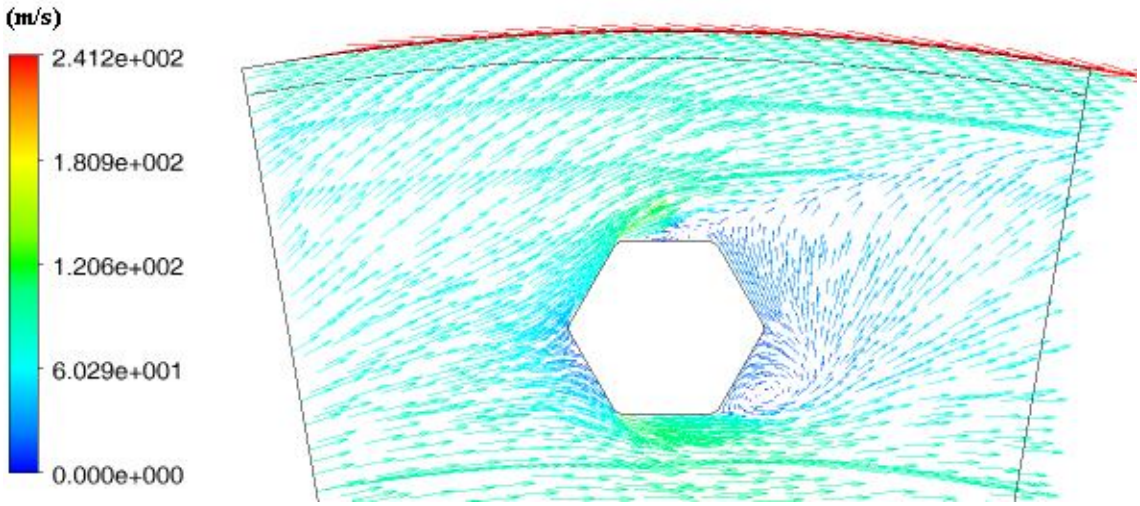

(d): C_w = 0.3 x 10^5, Re_ϕ = 0.933 x 10^7, $\lambda_{T=}$ 0.064

Figure 5.20: Comparison of Relative Velocity Vectors at *z/s* = 0.045 for Different Flow Conditions

(Continued)

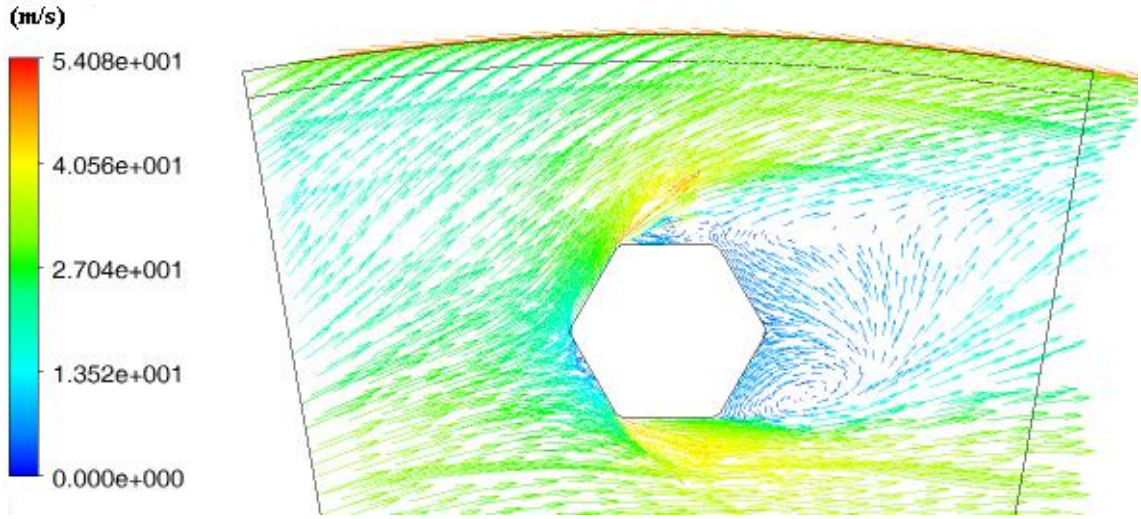

(e): $C_w = 10^5$, $Re_\phi = 0.362 \times 10^7$, $\lambda_{T=} 0.58$

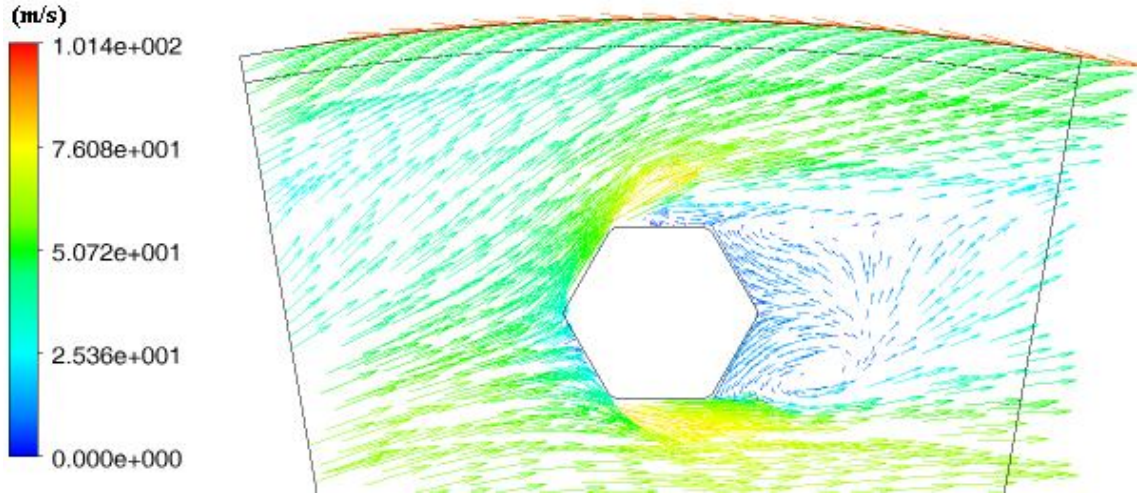

(f): $C_w = 10^5$, $Re_\phi = 0.668 \times 10^7$, $\lambda_{T=} 0.35$

Figure 5.20: Comparison of Relative Velocity Vectors at $z/s = 0.045$ for Different Flow Conditions

(Continued)

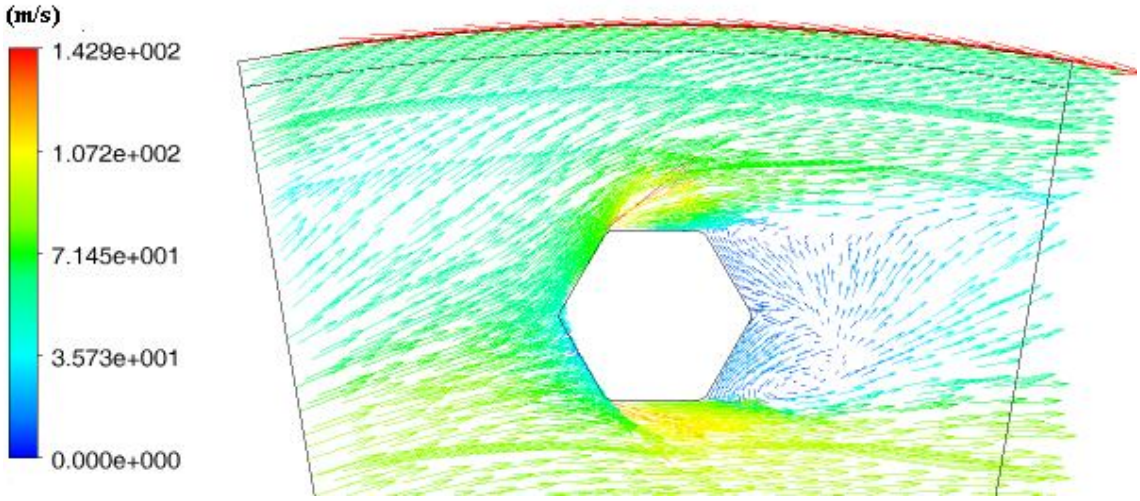

(g): $C_w = 10^5$, $Re_\phi = 0.999 \times 10^7$, $\lambda_{T=} 0.25$

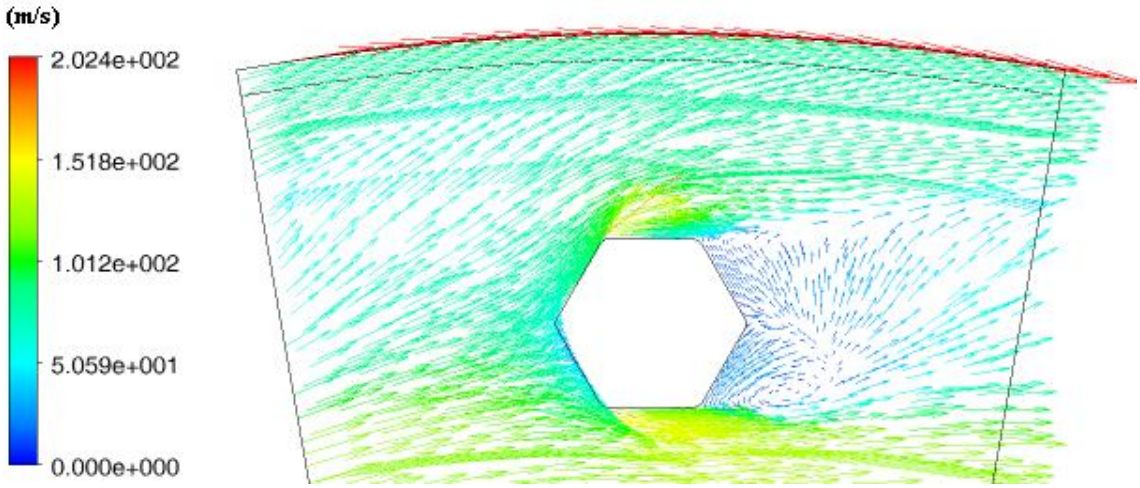

(h): $C_w = 10^5$, $Re_\phi = 1.323 \times 10^7$, $\lambda_{T=} 0.19$

Figure 5.20: Comparison of Relative Velocity Vectors at $z/s = 0.045$ for Different Flow Conditions

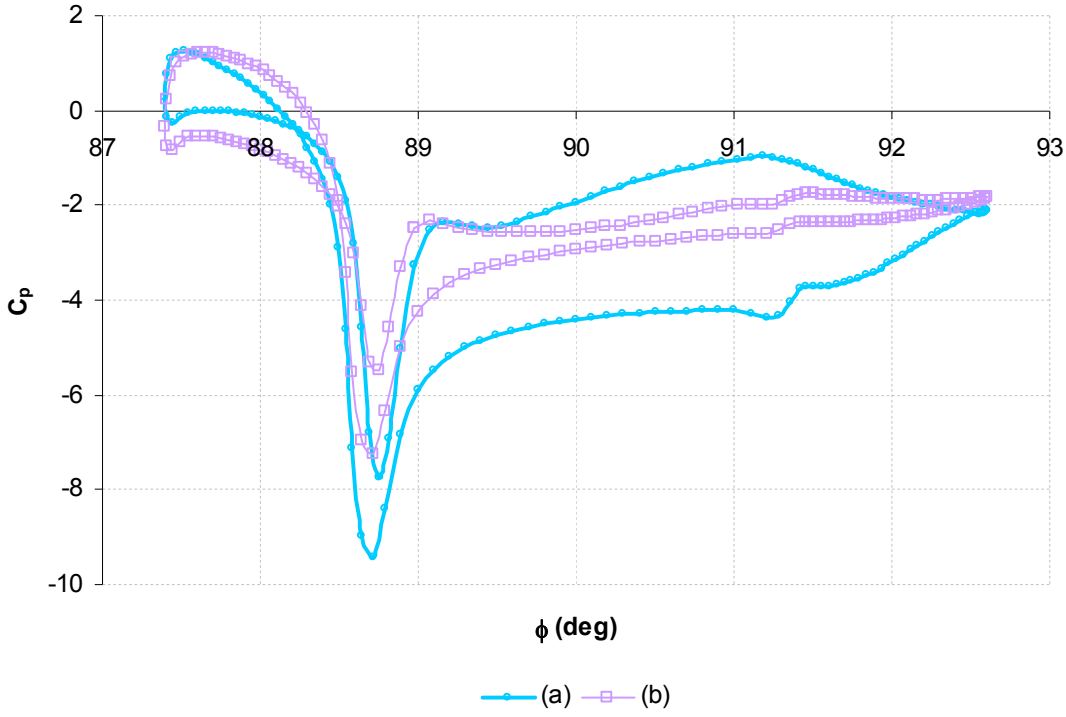

Figure 5.21: Comparison of the Pressure Distribution around the Bolt at *z/s* = 0.045 between (a): C_w = 0.3 x 10^5, Re_ϕ = 0.9 x 10^7, (λ_T = 0.064) and (b): C_w = 0.3 x 10^5, Re_ϕ = 0.177 x 10^7 (λ_T = 0.31)

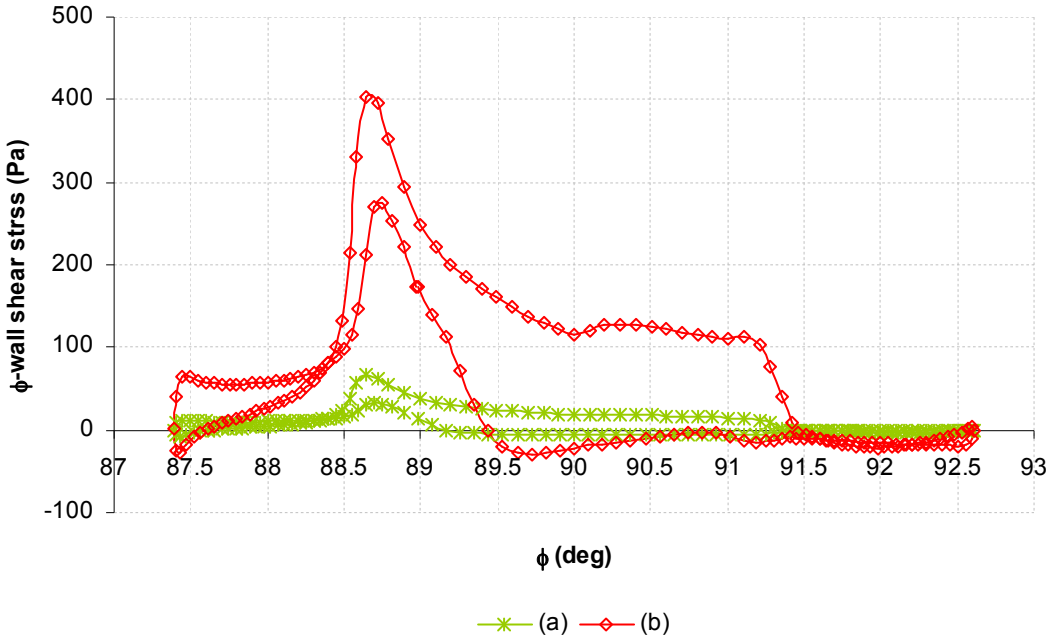

Figure 5.22: Comparison of the ϕ-wall Shear Stress Distribution around the Bolt at z/s = 0.045 between (a) C_w = 0.3 x 10^5, Re_ϕ = 0.177 x 10^7 (λ_T = 0.31) and (b) C_w = 0.3 x 10^5, Re_ϕ = 0.9 x 10^7, (λ_T = 0.064)

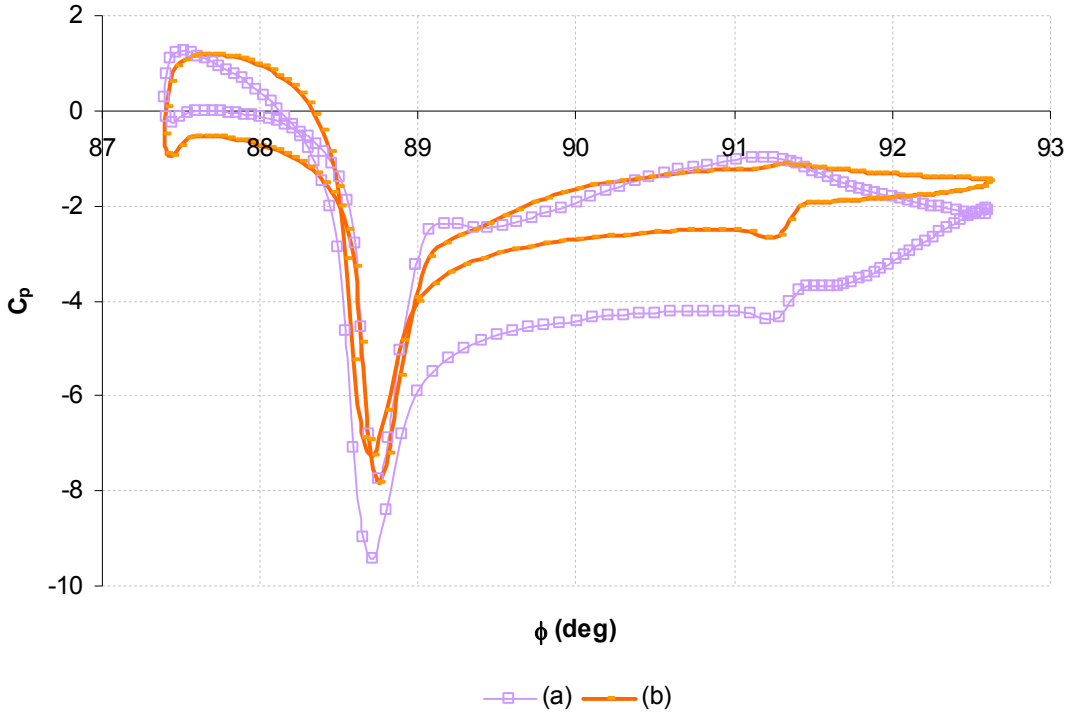

Figure 5.23: Comparison of the Pressure Distribution around the Bolt at z/s = 0.045 between (a): C_w = 0.3 x 10^5, Re_ϕ = 0.9 x 10^7, (λ_T = 0.064) and (b): C_w = 10^5, Re_ϕ = 0.9 x 10^7, (λ_T = 0.25)

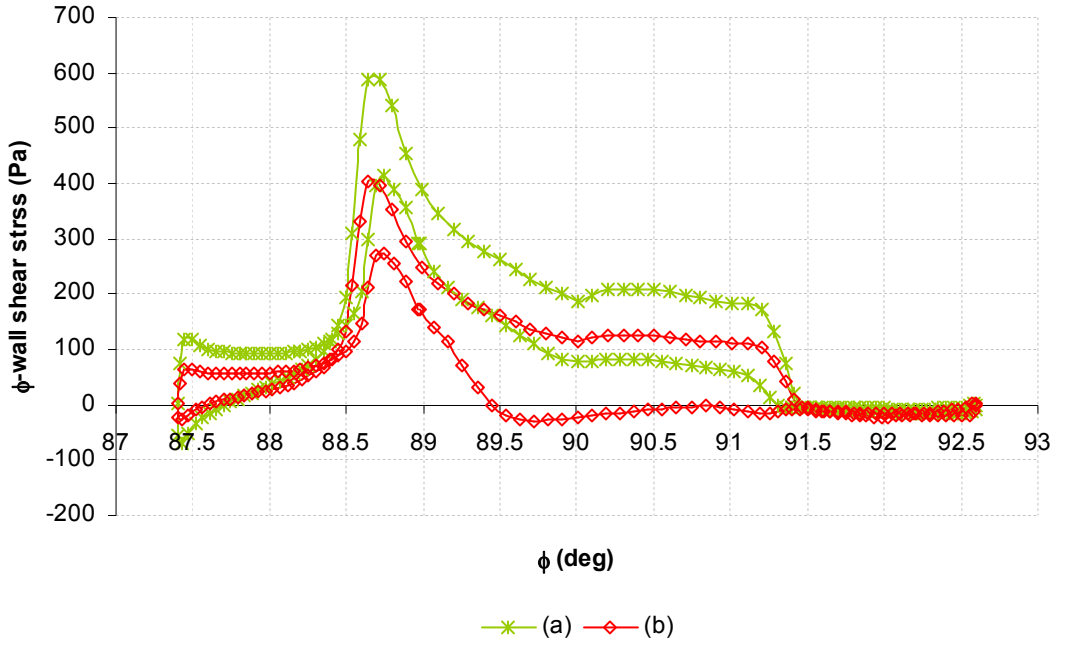

Figure 5.24: Comparison of the ϕ-wall Shear Stress Distribution around the Bolt at z/s = 0.045 between (a): C_w = 10^5, Re_ϕ = 0.9 x 10^7, (λ_T = 0.25) and (b): C_w = 0.3 x 10^5, Re_ϕ = 0.9 x 10^7, (λ_T = 0.064)

Table 5.3: Comparison of the Local Free-stream Reynolds Number and Angle of Attack at *z/s* = 0.045 for Different Flow Conditions

ω (rad/s)	Re_{φ} ($/10^7$)	C_w ($/10^5$)	α (deg)	Re_D ($/10^5$)
264.5	0.177	0.311	40	0.51
411	0.272	0.307	38.6	0.73
902.5	0.716	0.268	30.1	1.24
1060.1	0.933	0.242	27	1.38
211.9	0.362	1.022	41.4	1.06
409.5	0.668	1.017	39.3	2.25
618.8	0.999	0.994	35.8	2.8
889.5	1.323	0.963	32.9	3.3

Table 5.4: Comparison of the Stagnation and Separation Points on a Plane Cut at *z/s* = 0.045 for Different Flow Conditions

ω (rad/s)	Re_{φ} ($/10^7$)	C_w ($/10^5$)	$\varphi_{stagnation}$ (deg)	$\varphi_{separation-upper\ surface}$ (deg)	$\varphi_{separation-lower\ surface}$ (deg)
264.5	0.177	0.311	87.97	89.17	91.399
411	0.272	0.307	87.95	89.2	91.4
902.5	0.716	0.268	87.84	89.3	91.41
1060.1	0.933	0.242	87.72	89.31	91.45
211.9	0.362	1.022	87.96	89.24	91.42
409.5	0.668	1.017	87.95	89.298*	91.45
618.8	0.999	0.994	87.91	91.27	91.455
889.5	1.323	0.963	87.88	91.29	91.46

*The angular location corresponds to the first separation point.

According to the results demonstrated in Table 5.3, for a constant value of throughflow rate, increasing Re_{ϕ} increases the free-stream Reynolds number and reduces the angle of attack of the flow approaching the bolt. It is therefore expected that a delayed separation occurs on the surface of the bolt. Inspection of the flow streamlines shown in Figure 5.20 (a) to (h) confirms this expectation and reveals that increasing the rotational

Reynolds number gradually moves the separation point toward the trailing edge of the bolt and reduces the area of the wake region. This result agrees with the results obtained by Schlichting and Gersten (1999) for a cylinder immersed in a flow with different values of Re_D.

For a constant value of Re_ϕ, increasing C_w increases the angle of attack and the free-stream Reynolds number of the flow hitting the bolt. Based on the findings of Schlichting and Gersten (1999), while increasing Re_D delays the separation and produces a wake region with a smaller area, increasing the angle of attack moves the separation point downstream from the bolt and produces a wake region with a larger size. Hence, in order to identify which of the mentioned variations affects the location of the separation point more than the others, it is necessary to compare the results displayed in Table 5.4. Accordingly, it can be seen that increasing the throughflow rate for approximately similar values of rotational Reynolds numbers noticeably delays the separation and reduces the area of the wake region. As a result, it appears that it is the free-stream Reynolds number that has the major effect on the flow structure around the bolt. This is due to, as will be discussed later in this chapter, laminar to turbulent transition of the boundary layer over the bolt for higher values of C_w ($C_w = 10^5$). Such a transition delays the separation and, as will be discussed later, reduces the amount of form drag.

Comparison of the shape of the wakes in Figure 5.20 (a) to (h) shows that decreasing the throughflow rate causes the wakes to become more circumferential in their path around the bolt. In addition, a decrease in λ_T causes an increase in the wake shed from the trailing edge of one bolt to the leading edge of the next, which reduces the area of the wake region (compare Figure 5.20 (a) with (d) or (e) with (h)).

It is apparent from the velocity vector plots for $C_w = 10^5$ that a separation bubble is formed over the upper surface of the bolt for the two rotational Reynolds numbers of $Re_\phi = 0.362 \times 10^7$ and $Re_\phi = 0.67 \times 10^7$. As was mentioned by Tani (1964), a separation bubble is formed over an airfoil when a reattachment of flow occurs downstream from the separation point. Careful inspection of the ϕ-wall shear stress distribution plots for the two mentioned flow conditions reveals that for $Re_\phi = 0.362 \times 10^7$, the wall shear stress closely approaches the x-axis (after the separation point) but does not meet it.

Therefore, reattachment of flow has not occurred for this value of Re_ϕ. However, the wall shear stress distribution for $Re_\phi = 0.67 \times 10^7$ shows that flow reattaches to the surface of the bolt at $\varphi = 90.32^\circ$ downstream from the separation point, which is located at $\varphi = 89.298^\circ$. In addition, there is another separation of flow following the reattachment point at $\varphi = 91.24^\circ$. As will be discussed later in this chapter, the free-stream Reynolds number for $C_w = 10^5$ and $Re_\phi = 0.67 \times 10^7$ corresponds to a fully turbulent regime. For $C_w = 10^5$ and higher values of rotational Reynolds numbers ($Re_\phi = 0.999 \times 10^7$ and 1.323×10^7) the extent of turbulence has increased so that the separation point was moved towards the trailing edge of the bolt.

According to Figure 5.21, for a constant value of C_w, increasing the rotational Reynolds number increases the static pressure difference between the upper and lower surfaces of the bolt. Simulation results also show that, with an increase in Re_ϕ the relative total pressure difference between the upper and lower surfaces of the bolt noticeably increases. In addition, increasing Re_ϕ moves the stagnation point toward the lower surface of the bolt.

Regarding Figure 5.23, it can be seen that for a constant value of Re_ϕ, increasing C_w moves the stagnation point towards the lower surface of the bolt and reduces the static pressure difference around the bolt. Using the simulation results to plot the relative total pressure around the bolt, it can be found that increasing the throughflow rate reduces the relative total pressure difference between the upper and lower sides of the bolt.

Considering the wall shear stress distribution, it is clear from Figures 5.22 and 5.24 that the wall shear stress has higher values for higher amounts of C_w and Re_ϕ. In addition, increasing the rotational Reynolds number and throughflow rate increases the maximum ϕ-wall shear stress at both the upper and lower sides of the bolt as well as the wall shear stress difference around the bolt. Furthermore, for higher values of C_w and Re_ϕ a delayed separation can be observed.

Variations of different flow parameters were also examined along the axial direction for different flow conditions. Accordingly, it was found that the rate of reduction of the angle of attack along the axial direction (from the root to the tip of the bolt) reduces when decreasing the turbulent flow parameter. However, the free-stream Reynolds

number was shown to have very small variations along this direction. It was also found that for the higher value of λ_T, the location of the separation point has minor variations, moving from the root to the tip of the bolt. This contrasts with lower turbulent flow conditions, in which both the angle of attack and the area of the wake region noticeably reduce when moving from the root towards the tip of the bolt.

Regarding the radial variations of different flow parameters around the bolt, similar trends to those observed for the specific flow condition discussed in the previous section were also found for the other flow conditions.

It is interesting to study how the boundary layer thickness of the rotor, in the range of interference of the bolt, varies with changing the flow conditions. The results of the tangential velocity distribution along the axial location at r/b = 0.91 and φ = 87.28° show that, for a specific value of C_w, increasing Re_ϕ reduces the boundary layer thickness of the rotor. For instance, the rotor boundary layer thickness for $C_w = 0.3 \times 10^5$ and $Re_\phi = 0.177 \times 10^7$ is δ = 1.54mm, which is reduced to δ = 0.2mm for $C_w = 0.3 \times 10^5$ and $Re_\phi = 0.933 \times 10^7$. This is due to the increase in the tangential velocity of the core. In addition, comparison of the boundary layer thickness of the rotor for two typical flow conditions with similar values of Re_ϕ and different throughflow rates reveals that increasing C_w increases the boundary layer thickness of the rotor. For example, the thickness of the rotor boundary layer for $C_w = 10^5$ and $Re_\phi = 0.9 \times 10^7$ at r/b = 0.91 and φ = 87.28° is δ = 1.2mm, which reduces to δ = 0.4mm for $C_w = 0.3 \times 10^5$ and $Re_\phi = 0.9 \times 10^7$.

The occurrence of Taylor columns above the bolts can also be investigated for the different flow conditions studied in this section. Table 5.5 displays the Rossby number at the location of the bolts for different values of Re_ϕ and C_w. According to the results shown in this table, the condition of strong rotation ($Ro \ll 1$), which is crucial for occurrence of Taylor columns, was not satisfied and, as a result, it is expected that no Taylor column is produced above the bolts. This is confirmed by looking at the velocity vectors above the bolts for the different flow conditions investigated. In conclusion, it appears that, contrary to the findings of Farthing (1988), for a rotating cavity with mounted bolts, Taylor columns cannot be produced in this specific configuration of a rotor-stator system with rotor-mounted bolts.

Table 5.5: Comparison of the Rossby Number at the Location of the Bolts for Different Flow Conditions

ω (rad/s)	Re_ϕ ($/10^7$)	C_w ($/10^5$)	Ro
264.5	0.177	0.311	0.6
411	0.272	0.307	0.51
902.5	0.716	0.268	0.32
1060.1	0.933	0.242	0.25
211.9	0.362	1.022	0.89
409.5	0.668	1.017	0.52
618.8	0.999	0.994	0.42
889.5	1.323	0.963	0.36

5.4 Investigation of bolt drag coefficient

In the previous section, variations of flow structure in and out of the range of interference of the bolts were investigated for different flow conditions. This section examines the relation between those variations and the amounts of losses in the system.

A body moving relative to a fluid experiences a drag force, which is usually divided into two components: frictional or viscous drag, and pressure or form drag. Viscous drag comes from the wall shear stress in the direction of flow, and pressure drag comes from the pressure component in the direction of flow. It is common to report the drag force with the indicative factor of the drag coefficient. Drag coefficient, C_D, is a useful parameter for analysing the flow past immersed bodies, and is defined in Equation 5.5.

$$C_D = \frac{\frac{F_D}{A_p}}{\frac{1}{2}\rho V^2} \qquad 5.5$$

Where F_D is the drag force, A_p is the projected area of the body on a plane perpendicular to the direction of flow, and V is the velocity of the approaching stream.

In addition to the shape of the body that affects the drag force, the angle of attack of the flow hitting it and the velocity distribution of the approaching stream are the two other important parameters that can significantly change the pressure distribution and flow structure around the body. For symmetric pressure distribution around the body, the pressure gradient between the top and bottom sections is zero or very small and, as a result, pressure drag is only produced due to the pressure losses in the wake region. This symmetric pressure distribution occurs when the angle of attack is zero or very small and also when the velocity distribution of the approaching flow is uniform. However, for non-uniform velocity distributions of approaching flow or large angles of attack, the pressure difference between the top and bottom sections of the body increases. In these cases the pressure drag is not only produced by the pressure losses in the wake region but also by the high pressure difference around the body, which makes it act like a pump. Accordingly, the three elements producing the bolts' moment and moment coefficient that were considered by Zimmerman *et al*. (1986) can be recognised for the drag force and drag coefficient as well: the drag force produced by the wakes, the drag force produced by the pressure difference around the bolt (pumping losses), and the viscous drag. The pressure or form drag includes the first two elements of the drag force.

In order to calculate the drag force, it is necessary to first calculate the total angle of attack for the flow approaching the bolt and, consequently, project the forces in *x*-, *z*-, and *y*- directions in the direction of the calculated angle of attack. In addition, the angle of attack can be used to calculate the projected area of the bolts in the direction of flow. Using the calculated values of the total drag force and the projected area, it is possible to calculate the drag coefficient using Equation 5.5. Table 5.6 gives the drag coefficient of the bolts for different flow conditions. In addition, the results of the total free-stream Reynolds number and angle of attack that were presented in the previous section are re-displayed in Table 5.6 in order to use them to explain the variations in the drag coefficient for different flow conditions. Furthermore, Figure 5.25 graphically demonstrates the drag coefficient of individual bolts versus Re_D for $C_w = 0.3 \times 10^5$ and $C_w = 10^5$. Also included in Figure 5.25 are the results of the drag coefficient of a circular cylinder and a sphere proposed by Schlichting and Gersten (1999).

Table 5.6: Comparison of the Total Free-stream Reynolds Number and Angle of Attack of the Flow Approaching the Bolt as well as the Individual Bolts Drag Coefficient for Different Flow Conditions

ω (rad/s)	Re_φ ($/10^7$)	C_w ($/10^5$)	α (deg)	Re_D ($/10^5$)	C_D
264.5	0.177	0.311	30	0.54	1.28
411	0.272	0.307	29.6	0.74	1.23
902.5	0.716	0.268	27	1.26	1.22
1060.1	0.933	0.242	26.9	1.41	1.06
211.9	0.362	1.022	32.4	1.14	1.52
409.5	0.668	1.017	32	2.07	0.89
618.8	0.999	0.994	31.9	2.7	0.82
889.5	1.323	0.963	31.5	3.06	0.8

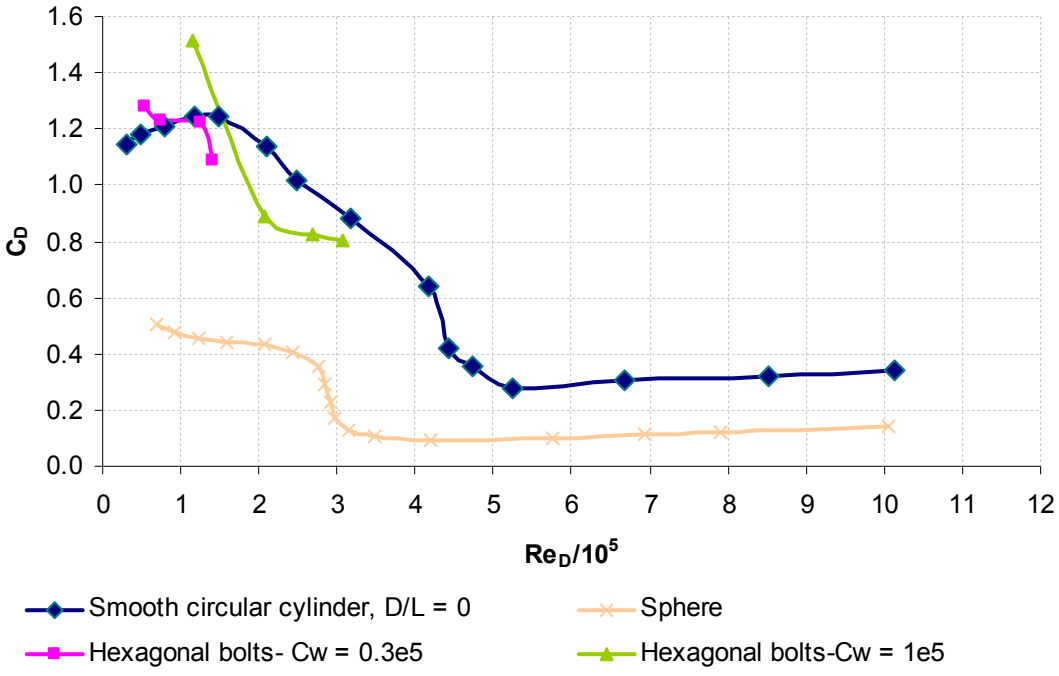

Figure 5.25: Variations of the Drag Coefficient as a Function of Re_D. Comparison between the Drag Coefficient of Hexagonal Bolts Mounted on Rotor with the Drag Coefficient of Circular Cylinder and Sphere using the Results Obtained by Schlichting and Gersten (1999)

According to the results presented in Table 5.6, for a constant C_w, increasing Re_ϕ reduces the angle of attack and increases the free-stream Reynolds number of the flow hitting the bolt. As mentioned in Section 5.3, decreasing the angle of attack delays the separation (see also Table 5.4) and reduces the area of the wake region and, as a consequence, reduces the form drag produced by the pressure losses of the wakes. Regarding the free-stream Reynolds number, increasing Re_D (up to the critical free-stream Reynolds number at which transition of laminar to turbulent boundary layer occurs) increases the shear stress and the frictional force between the fluid and the bolt, and consequently its viscous drag (Schlichting an Gersten, 1999). In addition, as discussed before, increasing the rotational Reynolds number increases both the static and relative total pressure differences between the upper and lower surfaces of the bolts and, as a result, the pressure drag produced by the pumping losses. Based on the simulation results, the overall effect of increasing Re_ϕ is an increase in the total drag force of the bolt. However, since the relative total velocity magnitude also noticeably increases when increasing Re_ϕ and it is squared in the denominator of the drag coefficient formula, drag coefficient decreases when increasing the disc's rotational speed.

Comparison of the results given in Table 5.6 reveals that increasing the throughflow rate for approximately similar values of Re_ϕ results in an increase in the angle of attack and the free-stream Reynolds number of the flow hitting the bolt. According to the results displayed in Table 5.5, the overall effect of increasing C_w is a noticeable reduction in the total drag coefficient. While increasing the angle of attack of the flow approaching the bolt increases the total drag coefficient, the only reason for this reduction could be attributed to the boundary layer transition from laminar to turbulent, which delays the separation and results in a sudden decrease in the drag coefficient (Schlichting and Gersten, 1999). The critical Re_D at which the transition occurs could be found by plotting the drag coefficient as a function of Re_D (see Figure 5.25). The location where a sudden drop of drag coefficient could be captured indicates the critical Reynolds number. Based on the presented results, laminar to turbulent transition of the boundary layer occurs approximately in the range of $2 \times 10^5 < Re_D < 4.5 \times 10^5$ for a circular cylinder. However, the transition of the boundary layer above the bolt from laminar to turbulent occurs earlier and in the range of Re_D between 1×10^5 and 2×10^5. Hence, For $C_w = 10^5$ the boundary layer above the bolt encounters laminar to turbulent

transition between $Re_\phi = 0.36 \times 10^7$ and 0.67×10^7 and is turbulent for $Re_\phi \geq 0.67 \times 10^7$. However, for $C_w = 0.3 \times 10^5$ the boundary layer above the bolt is laminar for $Re_\phi < 0.72 \times 10^7$ and becomes transient for higher values of Re_ϕ. In addition, it can be seen from Figure 5.25 that the maximum drag coefficient obtained in the present study for $N = 18$ and $D = 16$mm is about 1.52, which occurs for a free-stream Reynolds number of about 1.14×10^5.

5.5 Moment coefficient variations

The simulation results of the moment coefficient are shown in Figures 5.26 and 5.27 as a function of, respectively, Re_ϕ and λ_T for $C_w = 0.3 \times 10^5$. Figures 5.28 and 5.29 show the results for $C_w = 10^5$. The results displayed in Figures 5.26 to 5.29 are given as five separate plots including the experimental results for the total moment coefficient, the CFD results for the plain disc moment coefficient and the CFD results for the viscous, pressure, and total moment coefficient of the rotor-mounted bolt system. Note that all of the moment coefficient results (experimental and numerical) shown in this chapter were obtained for one side of the disc.

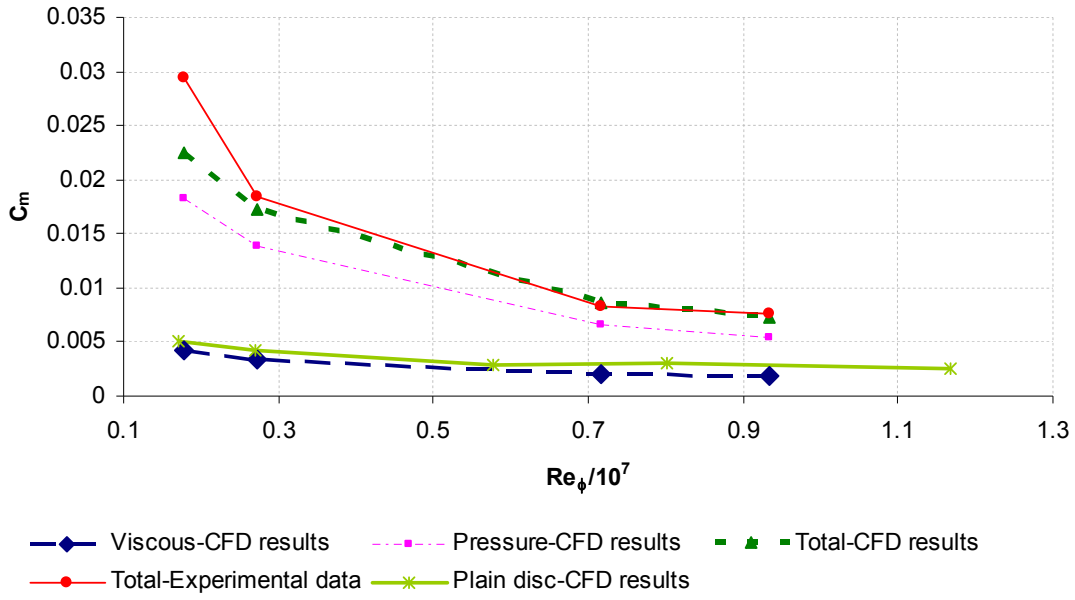

Figure 5.26: Variation of Moment Coefficient with Rotational Reynolds Number, $C_w = 0.3 \times 10^5$

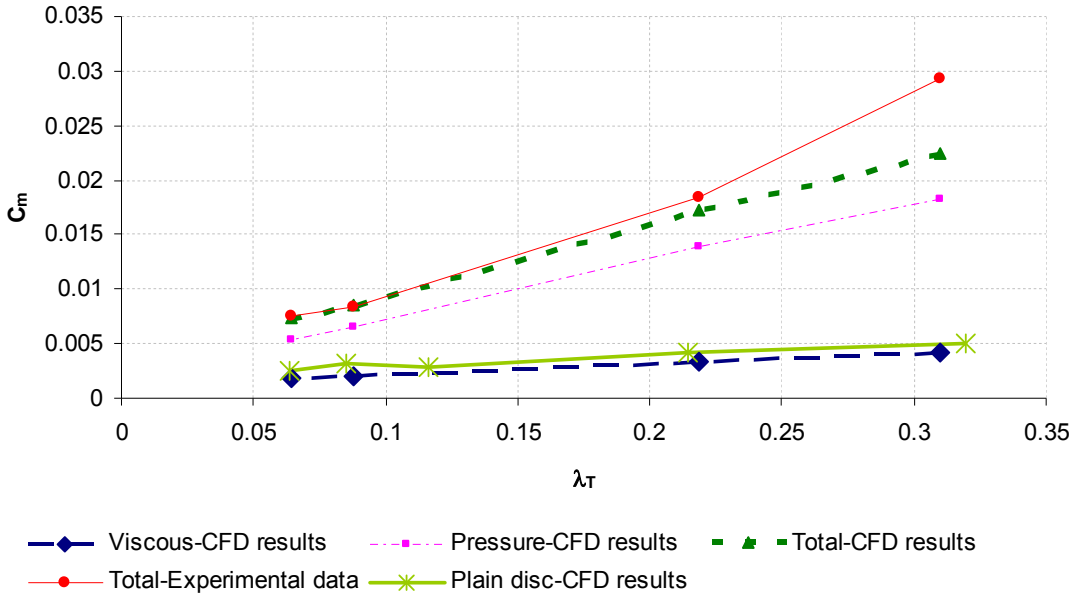

Figure 5.27: Variation of Moment Coefficient with Turbulent Flow Parameter, $C_w = 0.3 \times 10^5$

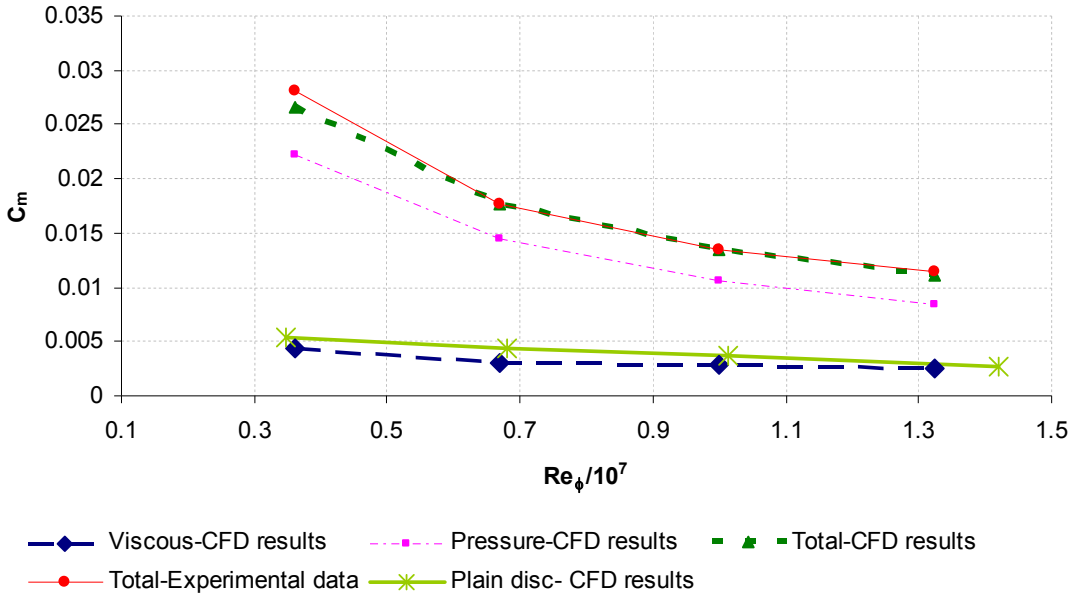

Figure 5.2816: Variation of Moment Coefficient with Rotational Reynolds Number, $C_w = 10^5$

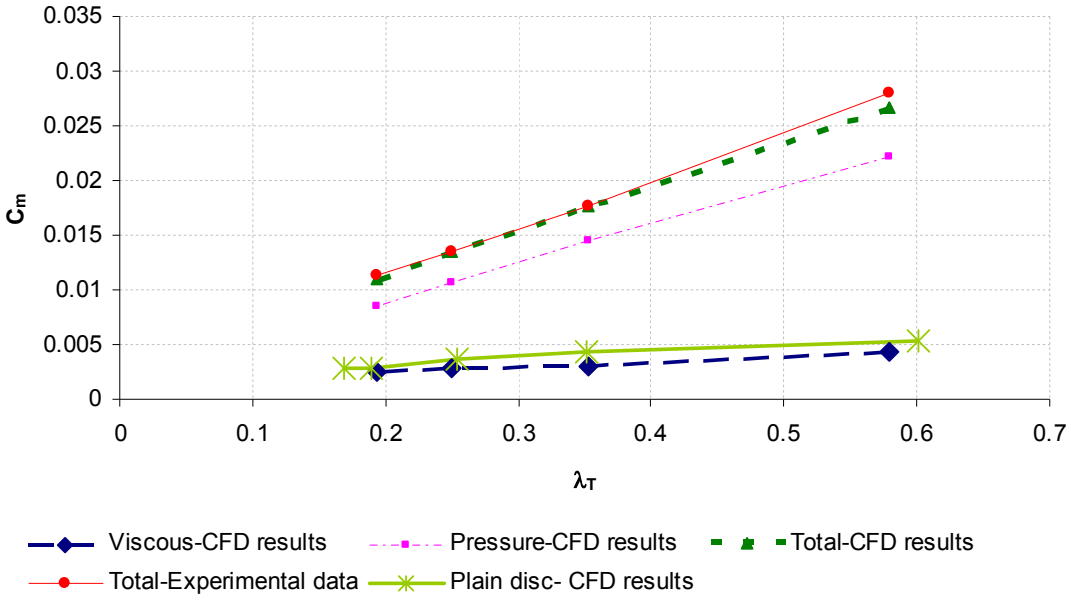

Figure 5.29: Variation of Moment Coefficient with Turbulent Flow Parameter, $C_w = 10^5$

According to Figures 5.26 to 5.29, there is very good agreement between the simulation results and the experimental data for both of the throughflow Reynolds numbers. Similar to the results obtained for the plain disc simulations, there is a divergence and a change of slope between the total moment coefficient plots of the experimental measurements and the numerical results for lower values of Re_ϕ and higher values of λ_T. The reason for this discrepancy is similar to that explained for the plain disc system (see Section 4.5).

Comparison of the moment coefficient results between the rotor-mounted bolt system and the plain disc system shows that, as expected, the presence of bolts causes a significant rise in the moment coefficient above that of a plain disc. In order to investigate the reasons for this noticeable difference, it is necessary to break down the total amount of moment coefficient into its components. One of the advantages of CFD is the ability to look at the individual contributions to the total moment coefficient. Total moment is composed of pressure and viscous moments.

Examination of the results shown in Figures 5.26 to 5.29 reveals that the pressure moment coefficient contributes the highest part of the total moment coefficient. Hence, it is the pressure moment that increases the moment coefficient of the rotor-mounted bolt system well beyond that of the plain disc system.

It is interesting to note that the three elements of total moment coefficient for a protruded rotor-stator cavity that were considered by Zimmerman *et al.* (1986) can be recognised here as well: the pressure moment produced by the wakes, the pressure moment produced by the pressure difference around the bolts (pumping losses) and the viscous moment. It should be noted that since FLUENT reports only the viscous moment and the pressure moment (which includes both the moment produced by the wakes and by the pumping action) separately, it is not possible to report the pressure moment produced by the wakes and that produced by the pumping losses separately.

Further inspection of Figures 5.26 through 5.29 reveals that both of the two components (viscous and pressure) of total moment coefficient increase when increasing λ_T and decreasing Re_ϕ. It can also be seen that the moment coefficient of the throughflow dominated cases is significantly higher than that of the rotationally dominated cases. The reason could be because of the reduction in the core tangential velocity produced by increasing the throughflow rate. This occurs due to the conservation of angular momentum and is a well-known phenomenon in a plain disc rotor-stator cavity (Owen and Rogers, 1989); as it has been shown, it is also true in a rotor-stator system with rotor-mounted bolts. Consequently, the relative (rotor to core) tangential velocity is increased with an increase in superimposed flow, and this leads to an increase in the moment coefficient due to an increase in skin friction.

It would also be of interest to study whether any equivalency could be found between the moment coefficient of individual bolts and their drag coefficient. Miles *et al*. (2009) suggested such an equivalency by assuming the bolts as cylinders having the same diameter D and the same height H. They also assumed that the velocity of the flow approaching the bolt is uniform and equal to the relative tangential velocity of the bolts and the core ($U = (1 - \beta)r\omega$). In addition, they assumed that the flow hits the bolt with a zero angle of attack. Considering these assumptions, the free-stream Reynolds number and drag coefficient of individual bolts can be written as below:

$$\mathrm{Re}_D = \frac{r_b D}{b^2}(1-\beta)\,\mathrm{Re}_\phi \qquad 5.6$$

$$C_D = \frac{b^5}{D H\, r_b^3 (1-\beta)^2} C_{m,bolt} \qquad 5.7$$

Where r_b is the radial location of the centre of the bolts, $C_{m,bolt}$ is the moment coefficient of the individual bolt, and b is the diameter of the disc.

The above equations were also used by Gartner (1998) in order to calculate the moment coefficient of the bolts from their drag coefficient. He assumed that the drag coefficient of the bolts could be obtained from the experimental data of the drag coefficient of a smooth circular cylinder.

The two equations above give the transformation between the dimensionless groups used in rotor-stator systems and those appropriate to drag over shapes. Although the mentioned assumptions are not realistic, it is worth investigating the extent to which the calculated drag coefficients and free-stream Reynolds numbers differ from those calculated in the previous section. Table 5.7 shows the results of such a comparison. Additionally, Figure 5.30 graphically displays the results tabulated in Table 5.7.

Table 5.7:Comparison of the Drag Coefficient and Free-stream Reynolds Number Obtained by the Simulation Results with Those Calculated Using Equations 5. 6 and 5.7 for the Simulated Matrix of Flow Conditions

ω (rad/s)	λ_T	Re_φ ($/10^7$)	C_w ($/10^5$)	$\mathrm{Re_D}$($/10^5$)		C_D	
				Simulation results	Using Equation 5.6	Simulation results	Using Equation 5.7
264.5	0.31	0.177	0.311	0.54	0.67	1.28	1.16
411	0.22	0.272	0.307	0.74	0.84	1.23	1.33
902.5	0.09	0.716	0.268	1.26	1.49	1.22	1.43
1060.1	0.06	0.933	0.242	1.4	1.71	1.06	1.45
211.9	0.58	0.362	1.022	1.1	1.9	1.52	0.74
409.5	0.35	0.668	1.017	2.07	2.3	0.89	1.13
618.8	0.25	0.999	0.994	2.7	2.8	0.82	1.28
889.5	0.19	1.323	0.963	3.06	3.28	0.8	1.3

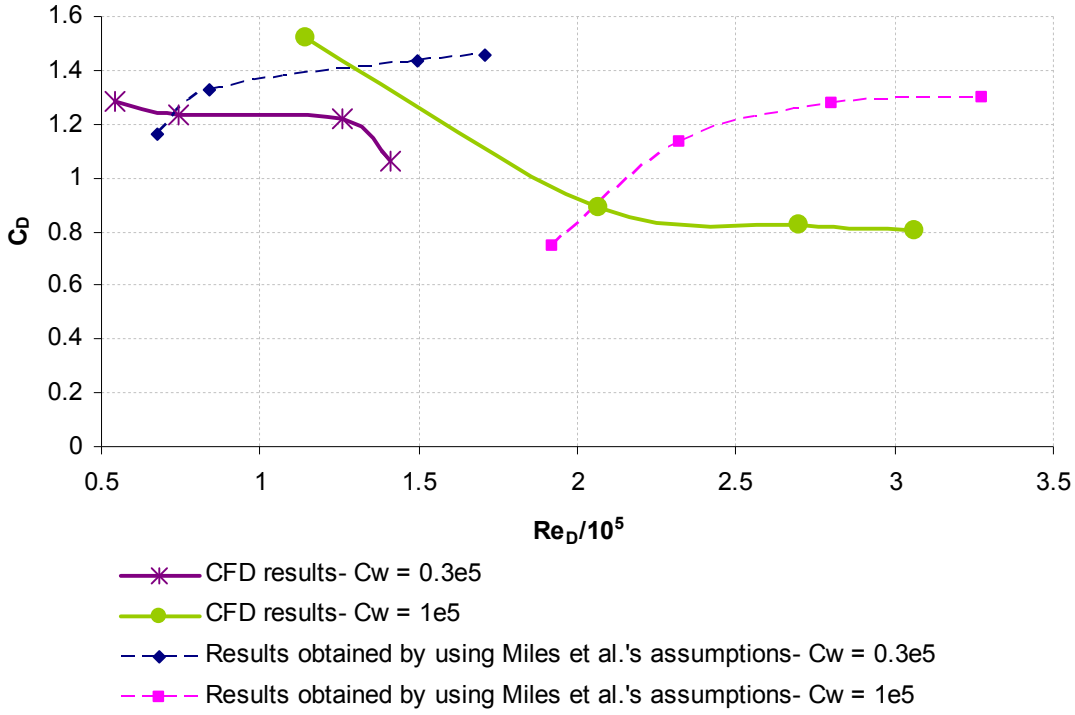

Figure 5.30: Comparison of the Drag Coefficient Obtained by the Simulation Results with Those Calculated Using Equation 5.7

According to the results demonstrated in Table 5.7 and Figure 5.30, as was expected, there are significant differences not only in the magnitude of the drag coefficients obtained using the simulation results and those obtained using Miles *et al.*'s assumptions, but also in the trend of the their variations with Re_D. It should be noted that, aside from the non-realistic assumptions about considering the bolts as cylinders and the free-stream velocity to be equal to $U = (1 - \beta)r\omega$, since the angles of attack of the flow hitting the bolts are noticeably larger than zero, the forces that produce the moment of the bolt are not the same as the forces producing the total drag. Hence, it is not reasonable to consider the moment and drag coefficients of the bolts to be equivalent.

5.6 The standard k-ε model and protrusions

As mentioned in Chapter 3, selection of the appropriate turbulence model influences the accuracy and reliability of the simulation results. Each turbulence model has its strengths and weaknesses. Based on the discussions presented in Section 3.2, among the different simulation turbulence models, the standard and realizable k-ε models were proposed to be more suitable for simulating the plain disc cavity. However, while the two models predicted similar results with acceptable accuracy, it was the standard k-ε model that was finally selected as the turbulence model for the subsequent simulations. This was due to the much higher CPU time and the higher calculation tuning required getting converged results for the realizable k-ε model compared to the standard k-ε model. However, the standard k-ε model in literature is normally known to have inaccurate predictions for three-dimensional flows with boundary layer separation and rotation. Therefore, it seems necessary to compare the results obtained by three-dimensional simulations using the standard k-ε model with those obtained by the turbulence models that in theory are suggested for flows with curvature and boundary layer separation.

Hence, in order to validate the superior adequacy of the standard k-ε model compared to other turbulence models, the condition of $Re_\phi = 0.27 \times 10^7$ and $C_w = 0.3 \times 10^5$ ($\lambda_T = 0.22$) was randomly selected in which the results of the realizable k-ε, the RSM and SST-k-ω compared with each other.

Figures 5.31 and 5.32 show comparisons of the simulation results for the pressure and ϕ-wall shear stress distributions respectively at z/s = 0.045. Also, Table 5.8 shows a comparison of the simulation results of the total Re_D and α of the flow approaching the bolt as well as the C_D and the C_m of individual bolts between the simulated models.

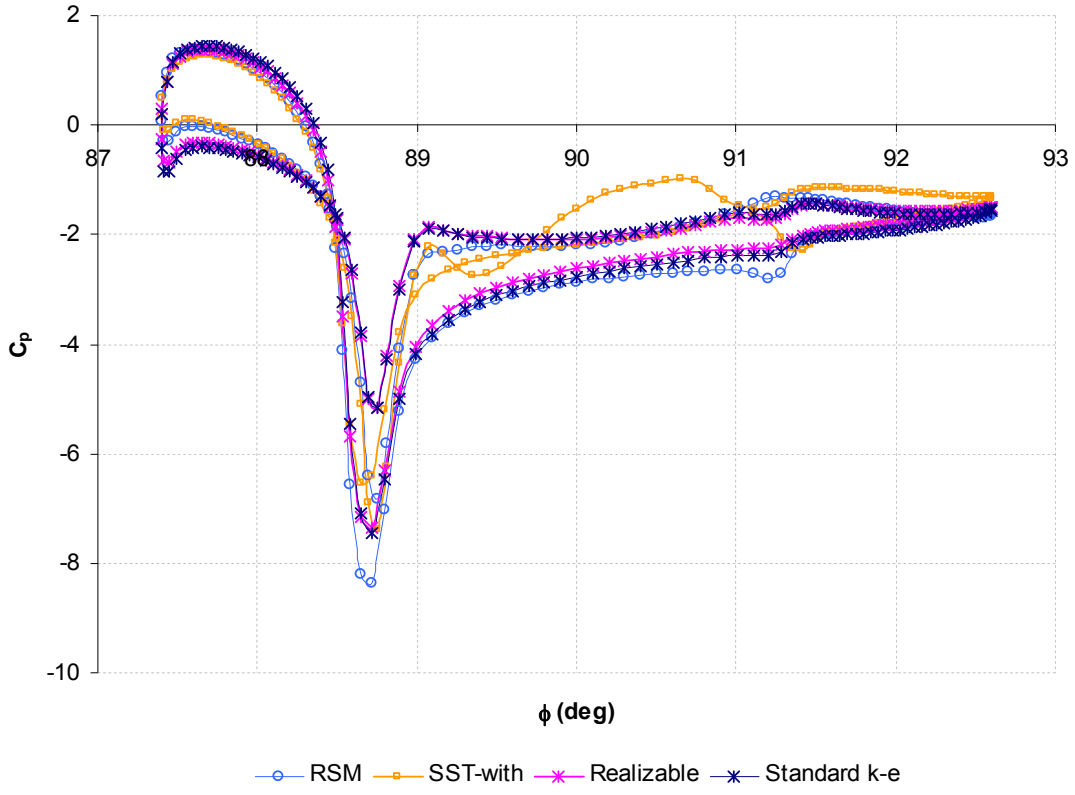

Figure 5.31: Comparison of the Pressure Distribution Predicted by the Standard k-ε Model with that Predicted by the Realizable k-ε, SST-k-ω and RSM at z/s = 0.045; Re_ϕ = 0.27 x 10^7, C_w = 0.3 x 10^5 (λ_T = 0.22)

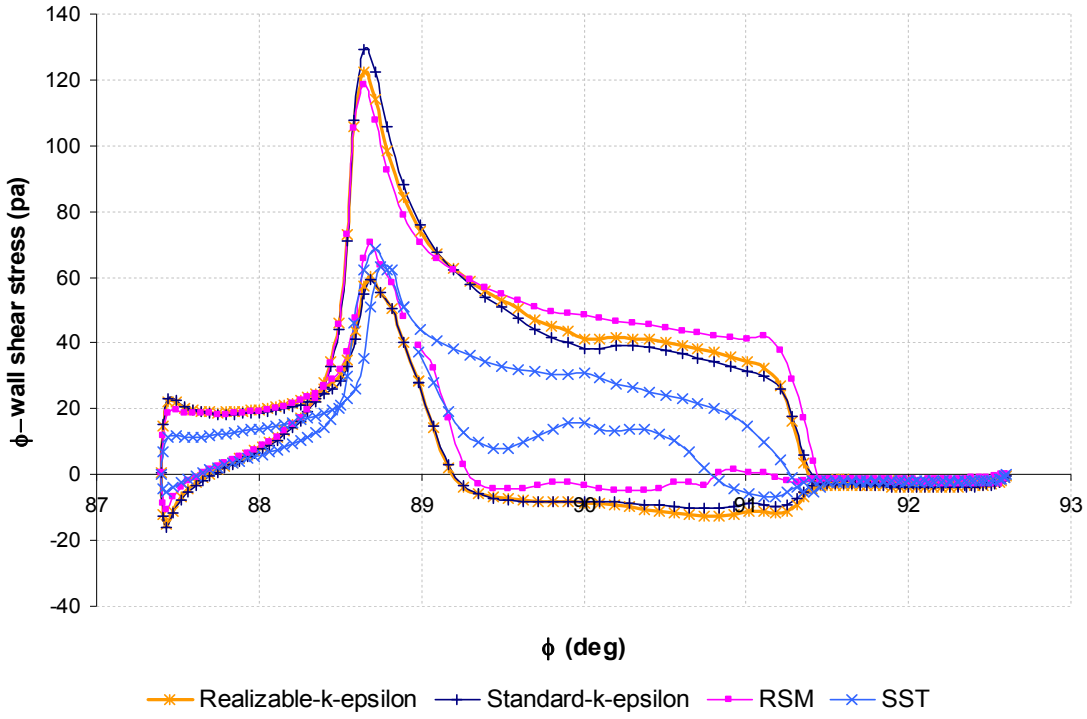

Figure 5.32: Comparison of the ϕ-Wall Shear Stress Distribution Predicted by the Standard k-ε Model with that Predicted by the Realizable k-ε, SST-k-ω and RSM at z/s = 0.045; Re_ϕ = 0.27 x 10^7, C_w = 0.3 x 10^5 (λ_T = 0.22)

Table 5.8: Comparison of the Total Free-stream Reynolds Number and Angle of Attack of the Flow approaching the Bolt as well as the drag coefficient and Moment coefficient of Individual Bolts Resulted from the Predictions of Realizable k-ε, Standard k-ε , SST-k-ω and RSM Turbulence Models; $Re_\phi = 0.27 \times 10^7$, $C_w = 0.3 \times 10^5$ ($\lambda_T = 0.22$)

Turbulence model	Re_D ($/10^5$)	α (deg)	C_D	C_m
Realizable- k-ε	0.765	29.15	1.19	0.0162
Standard-k-ε	0.742	29.65	1.23	0.0167
SST-k-ω	0.78	25.3	0.9	0.014
RSM	0.72	28.2	0.99	0.015

Note: The experimental amount of the moment coefficient for one side of the total system is $C_m = 0.0175$ (Miles, 2011).

According to the results shown in Figures 5.31 and Figure 5.32, the pressure and wall shear stress distributions can similarly be predicted by the simulated models, except the SST-k-ω. In addition, based on the simulation results, the location of the upper and lower separation points were closely predicted by the realizable and standard k-ε models (about $\phi = 89.2^\circ$) and the RSM ($\phi = 89.35^\circ$) with the exception of the SST k-ω model which predicted a delayed separation about $\phi = 90.8^\circ$. Therefore, the area of the wake region would also be similar for the standard k-ε, realizable k-ε and RSM and is considerably larger than that predicted by the SST k-ω. Considering Table 5.8, it can be seen that while the standard and realizable k-ε models have similar results in terms of the moment and drag coefficients, the RSM and SST-k-ω models under-predicted the moment coefficient in comparison with the experimental data. Based on these results, it appears that although the standard k-ε model is known to have inaccurate predictions for three-dimensional flows with separation and rotation, for the flow simulations analysed in this research this is not valid. This could be due to the near wall modeling (the enhanced wall treatment) used for the simulations with the standard k-ε, which is able to model the near wall region around the bolt very well. Therefore, it appears that the standard k-ε model used in conjunction with enhanced wall treatment provides both the accuracy and efficiency of time and CPU usage for the three-dimensional

simulations. This gives confidence in using the results of the standard k-ε model for the rest of the simulations in this thesis.

There is still one limitation for the standard k-ε model in predicting the flow around the bolts. The analysis of the simulation results (see Section 5.4) showed that the boundary layer around the bolt may have laminar-to-turbulent transition depending on the conditions of the flow approaching it. Therefore, a transitional model should be used to simulate the flow phenomena in the transitional boundary layer around the bolts. Modelling three-dimensional transition is difficult almost for all the turbulence models since they are unable to consider the physics of the transition process. Although the transition process could be mimicked by the low-Reynolds- number turbulence models, the positions and the growth rate of the transition is often poorly predicted and thus empirical correlations are needed to complement modelling of the transition process (Fadai-Ghotbi, 2007). In addition, the application of the transitional model for the protruded rotor-stator cavity in this study is only necessary for modelling the narrow boundary layer region around the bolts. With respect to these considerations, the strategy of this research is to continue with the standard k-ε model and suggests future research projects to complement the findings of this thesis by using or developing a suitable transitional model.

5.7 Summary

The simulation results of 18 bolts with 16mm diameters have been investigated in this chapter. Compared to the relevant plain disc cases, it was found that the flow structure in the rotor-mounted bolt system is almost unaffected at low radial locations out of the range of interference of the bolts. However, radial and axial pressure gradients as well as the tangential velocity increase when increasing the radial location in the protruded system in comparison with the plain disc system.

It was found that the flow structure around the bolts is governed by the angle of attack and the free-stream Reynolds number of the flow approaching the bolts. In addition, local values of these two parameters affect the local variations of flow structure in terms

of the location of the separation point and the area of the wake region, as well as the velocity and pressure distributions around the bolt.

Based on the simulation results, for a constant value of throughflow rate, increasing Re_ϕ increases the free-stream Reynolds number and decreases the angle of attack of the flow approaching the bolt, causing a delayed separation on the surface of the bolt, which reduces the area of the wake region. In addition, the overall effect of increasing the rotational Reynolds number is a reduction in the bolt's drag coefficient.

For a constant value of Re_ϕ, increasing C_w increases the angle of attack and the free-stream Reynolds number of the flow hitting the bolt, which delays the separation and reduces the area of the wake region. The overall effect of increasing C_w is a noticeable reduction in the total drag coefficient. This could be attributed to the boundary layer transition from laminar to turbulent, which results in a sudden decrease in the drag coefficient. Furthermore, it was found that decreasing the throughflow rate causes the wakes to become more circumferential in their path around the bolt; additionally, a decrease in λ_T causes an increase in the wake shed from the trailing edge of one bolt to the leading edge of the next, which reduces the area of the wake region.

Regarding the production of Taylor columns, it was found that Taylor columns cannot be produced in this specific configuration of a rotor-stator system with rotor-mounted bolts.

6. Rotor-Stator System with Mounted Bolts: Investigation of the Effects of Changing the Number and Diameter of Bolts

6.1 Introduction

One of the most important questions in analysing the rotor-stator cavity with mounted bolts is the extent to which the moment coefficient and flow structure vary with the number and diameter of bolts. This chapter aims to shed light on this question and generalise the findings obtained in Chapter 5. The effects of changing the number and diameter of the bolts are investigated for two typical flow conditions, one representing a throughflow dominated regime and the other representing a rotationally dominated one. Also included are data comparing the disc moment coefficient in the plain disc system with that in the protruded disc system. Such a comparison validates the assumption used in the empirical measurements, in which the disc moment coefficient was considered to be equal for the two systems.

This chapter is composed of six sections. Section 6.2 discusses the simulation results of different numbers of bolts, keeping the diameter of bolts constant. Section 6.3 provides a discussion for a specific number of bolts but with different diameters. Section 6.4 investigates the effects of varying both the diameter and the number of bolts on the amount of losses. Section 6.5 examines the validity of the assumption made in the experimental measurements. Finally, Section 6.6 gives a summary of the chapter.

6.2 Investigation of the variations of flow structure and the amount of losses for a specific diameter and different number of bolts

Two different flow conditions were selected for the analysis: $\mathrm{Re}_\phi = 0.67 \times 10^7$, $C_w = 10^5$, ($\lambda_T = 0.35$) and $\mathrm{Re}_\phi = 0.72 \times 10^7$, $C_w = 0.3 \times 10^5$, ($\lambda_T = 0.09$). The former

corresponds to a throughflow dominated regime, and the latter a regime where rotational effects are expected to dominate. Other dimensional parameters are given in Table 6.1.

Simulations were performed in this section for D = 16mm, and different number of bolts N = 0 (plain disc), 3, 9, 18, 36, 45 and 60 (for N = 60, the circumferential spacing between one bolt and the next is less than D/4). In addition, another geometry was built using a continuous ring with 16mm radial thickness and 11mm height at r = 0.2m on the rotor, representing the case of an infinite number of bolts. Figure 6.1 displays the front view, in r-ϕ plane, of the simulated geometries for N = 9, 18, 36, 45 and 60. The angular extent of the sector simulated depends on the number of bolts, so for three bolts a 120° sector is used, for nine bolts a 40° sector is used, for 18 bolts a 20° sector is used, and so on. The simulation specifications were the same as those used in Chapter 5.

Table 6.1: Matrix of Flow Conditions

ω (rad/s)	$\dot{m}$ (kg/s)	Re_φ ($/10^7$)	C_w ($/10^5$)	λ_T	P_{in}* (bar)	T_{in}** (K)
902.5	0.1188	0.716	0.268	0.09	3	292
409.5	0.4152	0.668	1.017	0.35	5.1	296.7

*: Static pressure
**: Static temperature

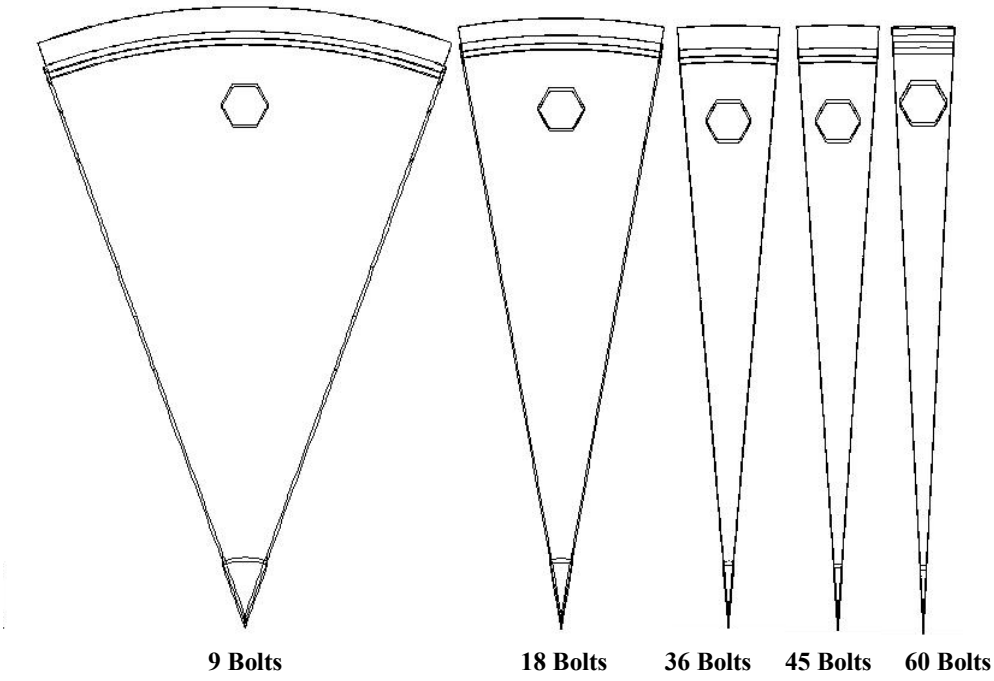

Figure 6.1: Simulated Geometries for Different Number of Bolts in r-ϕ Plane

6.2.1 Flow structure analysis

Increasing the number of bolts reduces the distance between two neighbouring bolts. For the bolts located in close proximity, the flow field and the forces experienced by them are entirely different from those observed when the bolts are far from each other and isolated in the fluid stream. The differences become more important when the distance between two bolts is so small that one of them is immersed in the wake of the other.

The situation of bodies in close proximity to each other was investigated for parallel circular cylinders of diameter D, separated by a centre-to-centre distance of L (the Tandem arrangement) by Zdravkovich (1977), Zdravkovich (1987) and Zdravkovich (1997). Based on these investigations, the pressure distribution and drag coefficient of the two cylinders depends on the Reynolds number and the L/D or the spacing between them. It was also found that the pressure distribution around each cylinder and the

amount of its drag coefficient does not follow a regular pattern, as *L/D* varies and is a unique function of the spacing for the given Reynolds Number.

In the same manner, for the case of the bolts mounted on the rotor in the rotor-stator cavity under investigation, the extent of interference of one bolt on the flow structure and power losses of the neighbouring bolt strongly depends on the number of bolts, or the bolts' spacing. An inspection of the wake region in relative velocity vector plots around the bolts could help to find the number of bolts above which the flow structure of the downstream bolt is affected by the upstream one. As was found in the previous chapter, the largest area of the wake region and, as a result, the greatest extent of interference between the wake of one bolt and the flow structure of the neighbouring bolt occurs at the axial locations close to the root of the bolt. Therefore, the cross-sectional plane at $z/s = 0.045$ was selected for flow structure analysis. Figures 6.2 and 6.3 illustrate relative velocity vectors around the bolts for $N = 9$, 18, 45 and 60, and the two mentioned flow conditions. Also included in Figures 6.2 and 6.3 are the bolts' spacing, which is defined as the ratio of the bolt pitch arc length, x_{pr}, to the bolt diameter.

$$X_b = \frac{x_{pr}}{D} \tag{6.1}$$

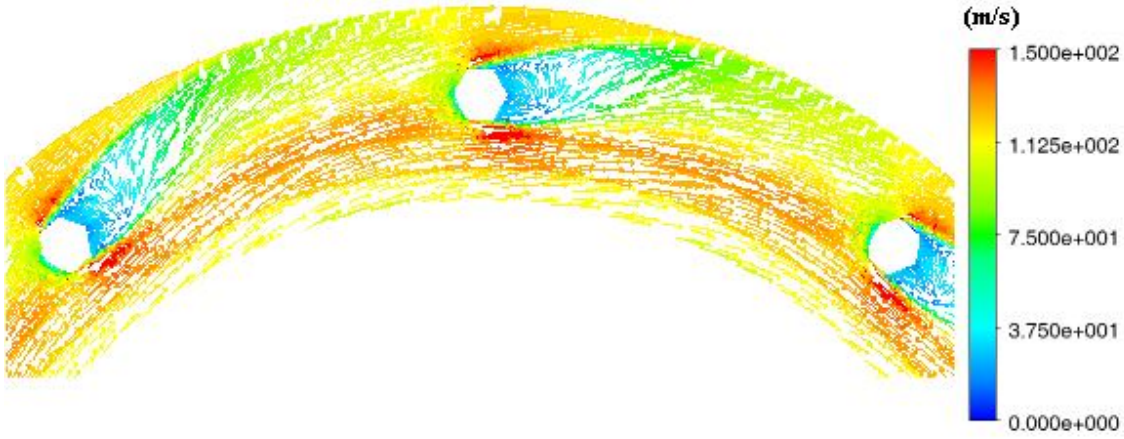

$N = 9,\ X_b = 8.7$

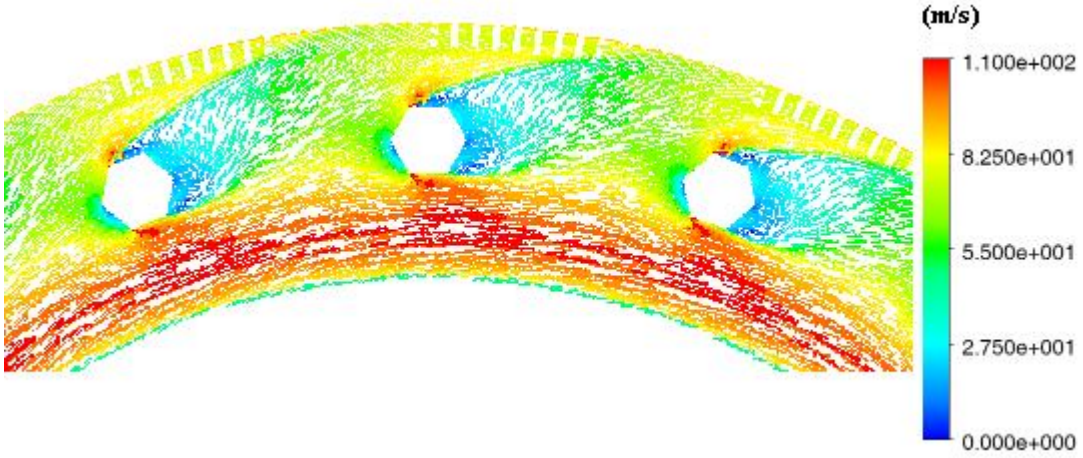

$N = 18,\ X_b = 4.36$

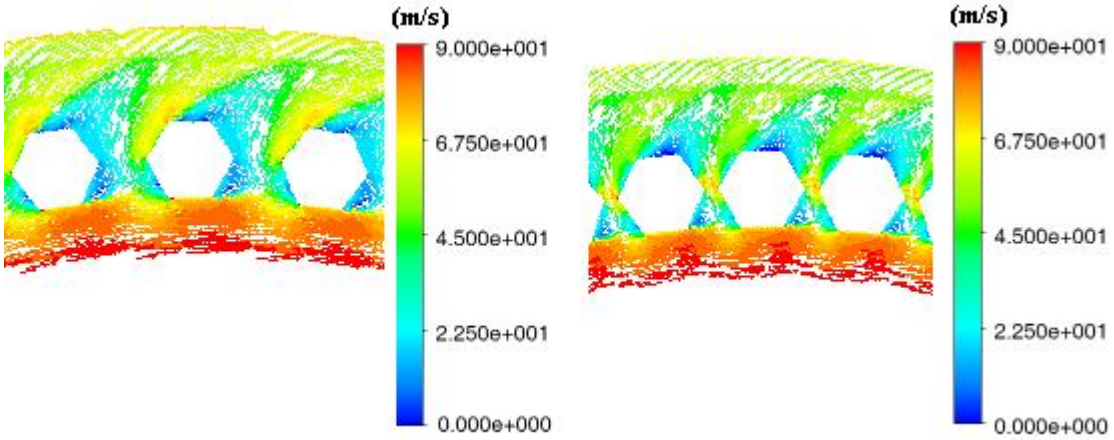

$N = 45,\ X_b = 1.74$ $N = 60,\ X_b = 1.31$

Figure 6.2: Relative Velocity Vectors at z/s = 0.045 for Different Number of Bolts; $Re_\phi = 0.72 \times 10^7$ and $C_w = 0.3 \times 10^5$ ($\lambda_T = 0.09$)

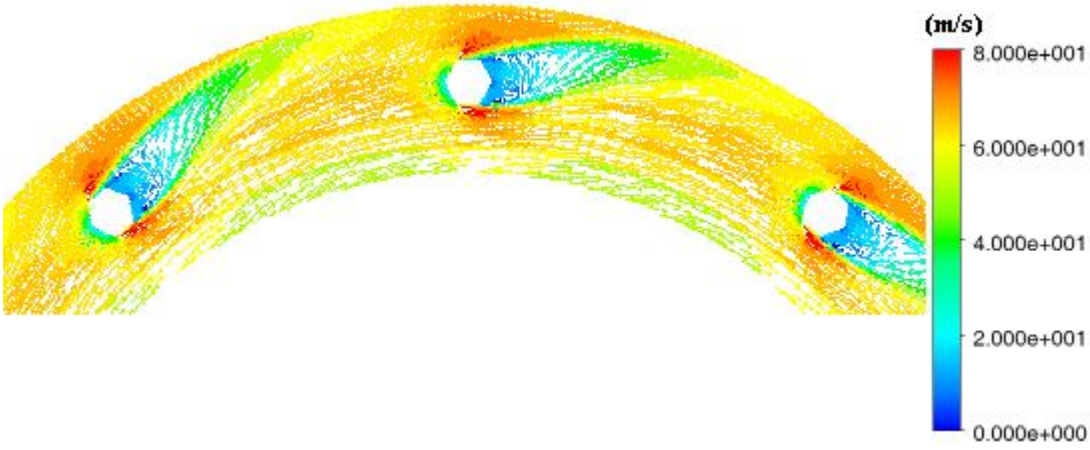

$N = 9,\ X_b = 8.7$

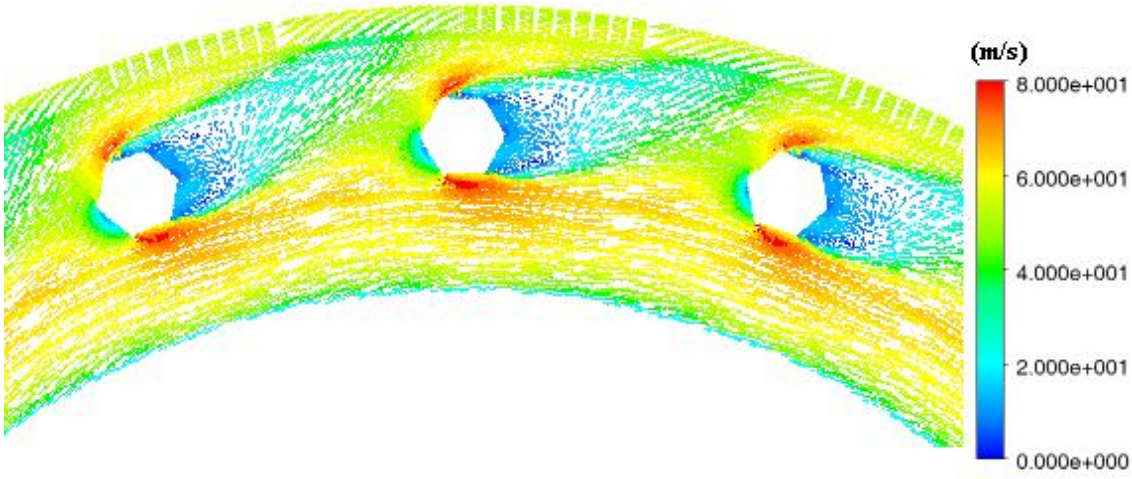

$N = 18,\ X_b = 4.36$

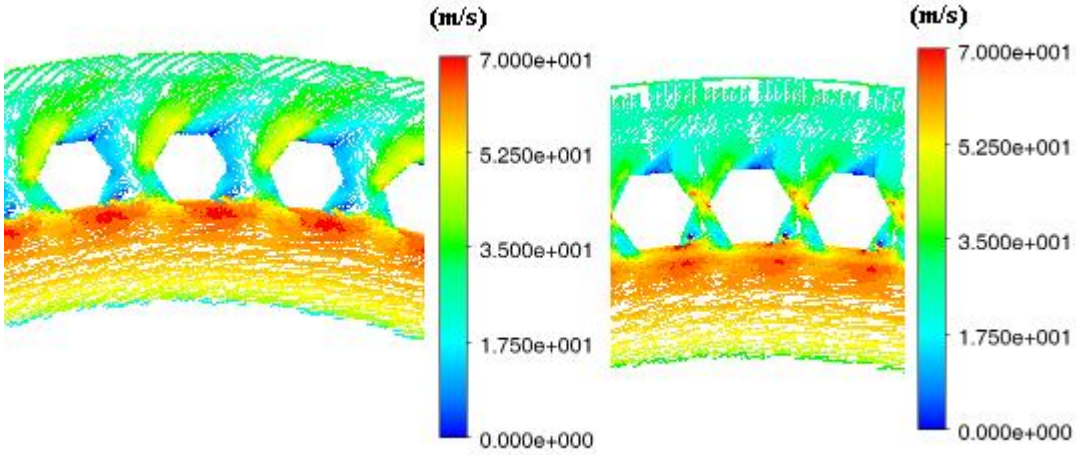

$N = 45,\ X_b = 1.74$ $N = 60,\ X_b = 1.31$

Figure 6.3: Relative Velocity Vectors at z/s = 0.045 for Different Number of Bolts; $Re_\phi = 0.67 \times 10^7$ and $C_w = 10^5$ ($\lambda_T = 0.35$)

Based on the results obtained by Zdravkovich (1987), the flow structure around the tandem arrangement of cylinders could be categorised into two different types. Accordingly, for the first type of flow regime ($1 < L/D < 3.4$ to 3.8), the wake formation of the upstream cylinder is affected by the presence of the downstream cylinder. However, for the second type of flow regime ($L/D > 3.4$ to 3.8), a complete wake was formed in the gap between the cylinders. It is apparent from Figures 6.2 and 6.3 that the mentioned flow patterns could also be observed around the bolts in the rotor-stator system. It appears that there is a minor interaction between the wake of one bolt and the flow field of the neighbouring bolt for $N \leq 18$. This makes the shear layers from the front bolt not impinge directly on the rear bolt. However, when the number of bolts increases ($N > 18$), the downstream bolt is immersed in the wake region of the upstream bolt and the shear layers from the front bolt either envelop or impinge directly on the rear bolt. The extent of this interference increases when increasing the number of bolts.

Considering Figures 6.2 and 6.3, it is evident that the form of the wake changes with the number of bolts fitted to the rotor. For $N > 18$ the wake falls on the upper section of the bolt. Comparing the shape of the wakes in Figures 6.2 and 6.3, it can also be seen that decreasing the throughflow rate (or decreasing λ_T) pushes the wakes toward the rear section of the bolt and increases their interference with the flow field of the neighbouring bolt. This agrees with the predictions of Zimmerman *et al*. (1986). They found that the interference effects of the wakes are reduced by increasing the throughflow rate.

In order to gain further insight into the interaction of the gap flow with the bolts, pressure and wall shear stress distributions were examined. Accordingly, Figures 6.4 and 6.5 respectively illustrate the ϕ-wall shear stress and pressure coefficient distributions on the bolt for $Re_\phi = 0.67 \times 10^7$, $C_w = 10^5$ and $N = 3$, 18, 45 and 60 at $z/s = 0.045$. Figures 6.6 and 6.7 show the plots for $Re_\phi = 0.72 \times 10^7$, $C_w = 0.3 \times 10^5$. Additionally, angular locations of stagnation and separation points are tabulated in Tables 6.2 and 6.3 for the simulated flow conditions. Also included in Tables 6.2 and 6.3 are the calculated values of local free-stream Reynolds numbers and angles of attack of the flow approaching the bolt at $z/s = 0.045$. Figure 6.8 zooms in the relative velocity vector plot of a typical simulated case ($N = 45$, $Re_\phi = 0.67 \times 10^7$, $C_w = 10^5$ ($\lambda_T = 0.35$))

in order to graphically show the locations of the first and second upper separation and the reattachment points.

It should be noted that the results presented in Tables 6.2 and 6.3 for Re_D and α were obtained by averaging the relevant velocity components on a bounded line located at φ = 87.28°. The angular location of this line is selected where the boundary layer effects of the bolt have approximately vanished for different numbers of bolts. Regarding the length of the line, it was reduced by increasing the number of bolts in order to evaluate the angle of attack of the flow hitting the bolt. This was due to the movement of the stagnation point towards the lower section of the bolt. However, the length of the selected line for determining Re_D for different number of bolts was constant and equal to the bolts' diameter.

Based on the simulation results, the Mach number ranges from 0.05 for the plain disc to 0.23 for 60 bolts for $Re_\phi = 0.67 \times 10^7$, $C_w = 10^5$ and from 0.15 for the plain disc to 0.42 for 60 bolts for $Re_\phi = 0.72 \times 10^7$, $C_w = 0.3 \times 10^5$. Hence, it appears that compressibility effects do not have a considerable influence on the flow structure around the bolt when varying the number of bolts.

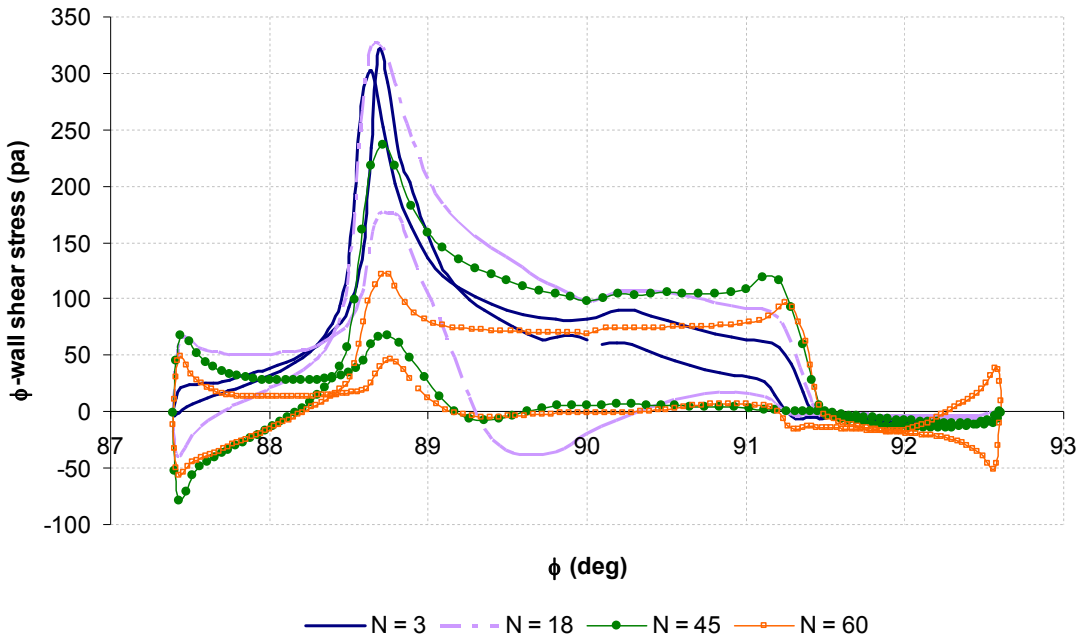

Figure 6.4: ϕ-wall Shear Stress Distribution on the Bolt at $z/s = 0.045$ for $Re_\phi = 0.67 \times 10^7$, $C_w = 10^5$ ($\lambda_T = 0.35$); $N = 3$, 18, 45 and 60

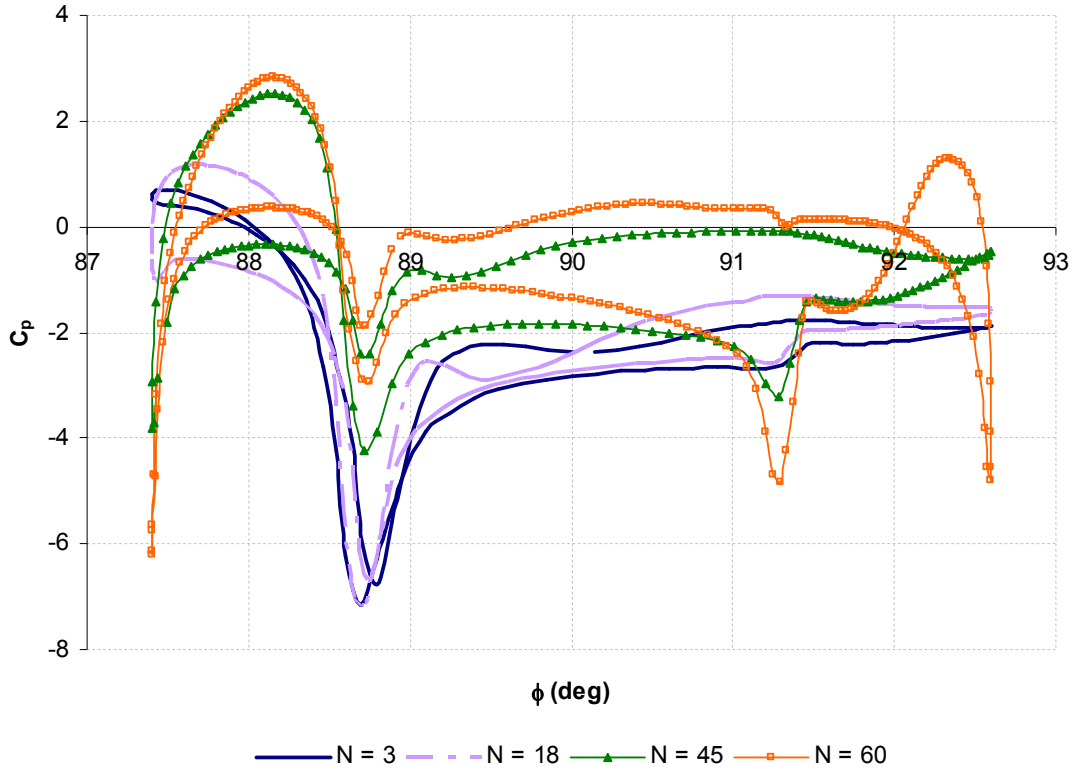

Figure 6.5: Pressure Coefficient Distribution on the Bolt at $z/s = 0.045$ for $Re_\phi = 0.67 \times 10^7$, $C_w = 10^5$ ($\lambda_T = 0.35$); $N = 3, 18, 45$ and 60

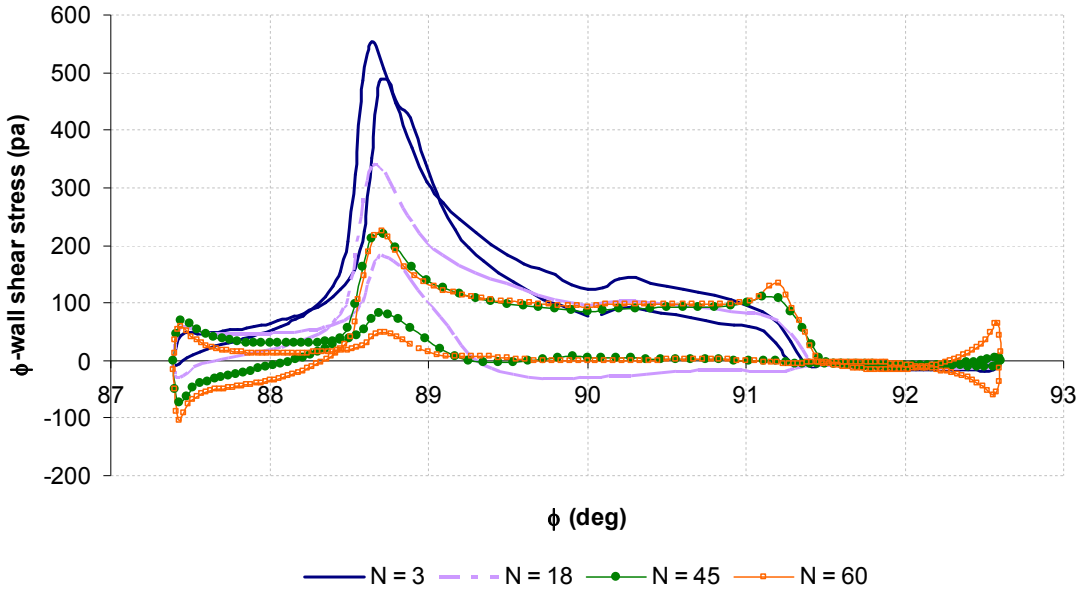

Figure 6.6: ϕ-wall Shear Stress Distribution on the Bolt at $z/s = 0.045$ for $Re_\phi = 0.72 \times 10^7$, $C_w = 0.3 \times 10^5$ ($\lambda_T = 0.09$); $N = 3, 18, 45$ and 60

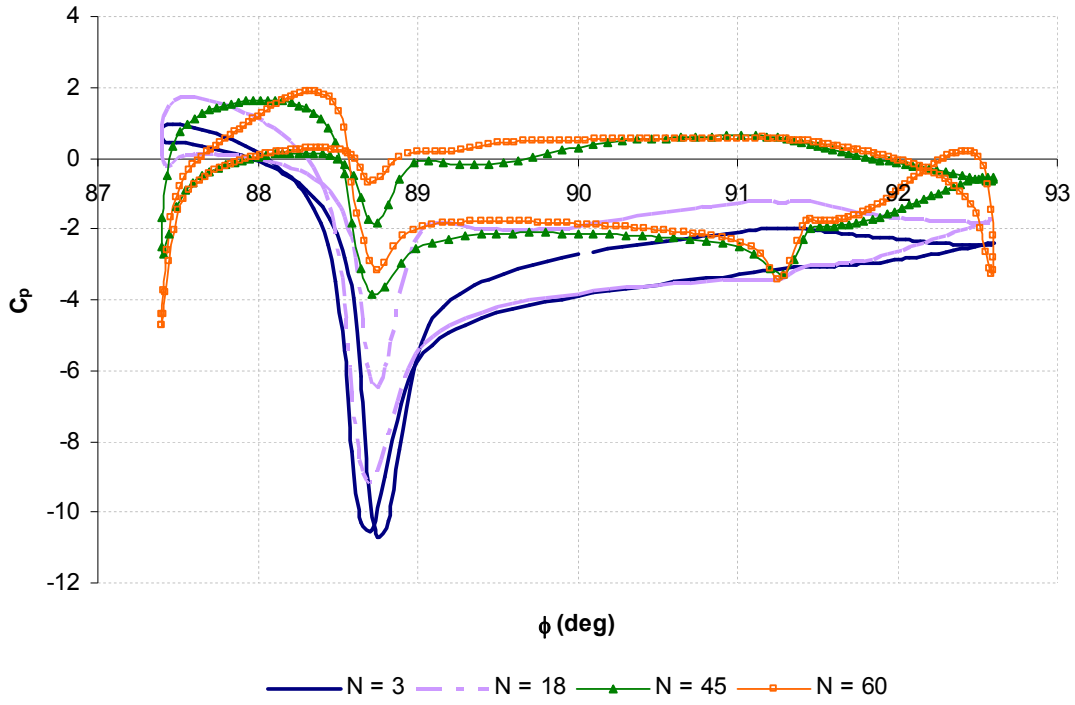

Figure 6.7: Pressure Coefficient Distribution on the Bolt at z/s = 0.045 for Re_ϕ = 0.72 x 10^7, C_w = 0.3 x 10^5 (λ_T = 0.09); N = 3, 18, 45 and 60

Table 6.2: Comparison of the Free-stream Reynolds Number and Angle of Attack of the Flow Approaching the Bolt at z/s =0.045 as well as the Location of the Stagnation and Separation Points for Different Number of Bolts; Re_ϕ = 0.72 x 10^7, C_w = 0.3 x 10^5 (λ_T = 0.09)

N	α (deg)	Re_D (/10^5)	$\phi_{stagnation}$ (deg)	$\phi_{separation\text{-}upper\ surface}$ (deg)	$\phi_{separation\text{-}lower\ surface}$ (deg)
3	18.1	1.91	87.6	90.6	91.42
9	22	1.53	87.74	89.8	91.42
18	30.1	1.24	87.84	89.3	91.41
36	38.8	1.2	88.3	89.17	91.4
45	47.2	1.16	88.4	89.13	91.4
60	49.2	1.14	88.5	89.02	91.39

*Note that the angular locations reported in Table 6.2 corresponds to the first separation points. This is also the case for Table 6.3.

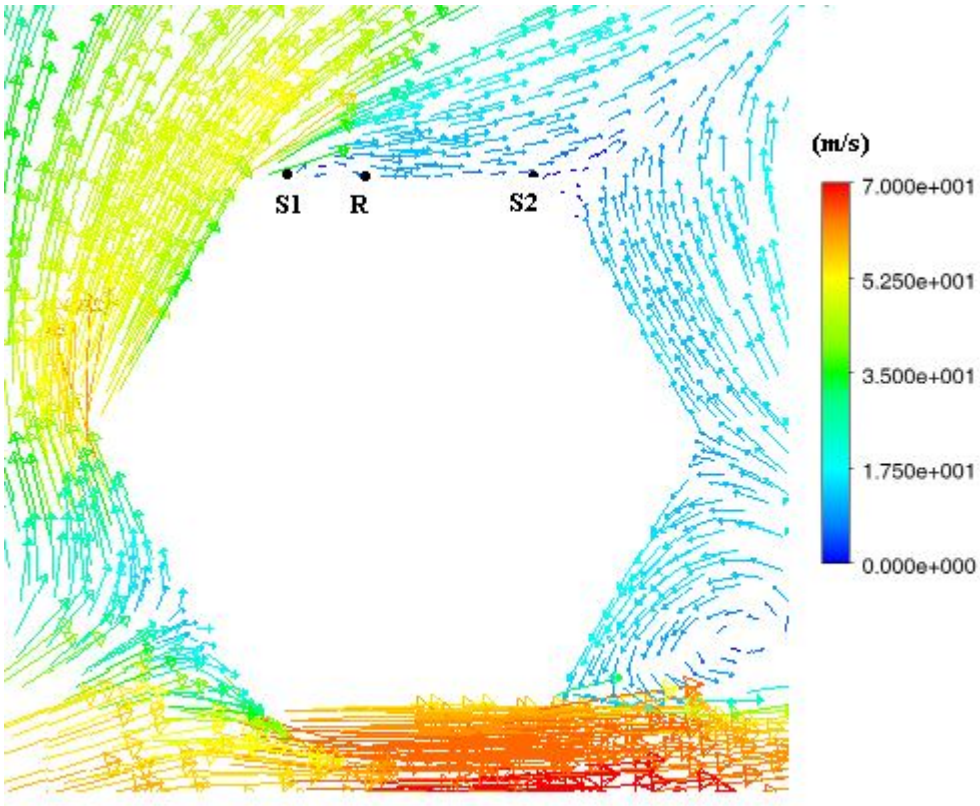

Figure 6.8: Relative Velocity Vectors around the Bolt for $N = 45$, $Re_{\phi} = 0.67 \times 10^7$, $C_w = 10^5$ ($\lambda_T = 0.35$), Zooming on the Locations of the First and Second Separation (S1 and S2) and Reattachment (R) Points

Table 6.3: Comparison of the Free-stream Reynolds Number and Angle of Attack of the Flow Approaching the Bolt *at z/s* =0.045 as well as the Location of the Stagnation and Separation Points for Different Number of Bolts; $Re_{\phi} = 0.67 \times 10^7$, $C_w = 10^5$ ($\lambda_T = 0.35$)

N	α (deg)	Re_D ($/10^5$)	$\phi_{stagnation}$ (deg)	$\phi_{separation\text{-}upper\ surface}$ (deg)	$\phi_{separation\text{-}lower\ surface}$ (deg)
3	16.3	2.9	87.7	91.25	91.47
9	26.9	2.56	87.82	91	91.47
18	39.3	2.25	87.95	89.298	91.45
36	44.8	2.15	88.44	89.26	91.45
45	50.6	2.1	88.49	89.17	91.44
60	53.4	2	88.54	89.14	91.44

Inspection of Figures 6.4 through 6.7 as well as Tables 6.2 and 6.3 permits several conclusions to be made about the flow.

Based on the results presented in Tables 6.2 and 6.3, increasing the number of bolts noticeably increases the angle of attack of the flow approaching the bolt. However, the decreasing trend of Re_D with the number of bolts is slightly lower than that observed for the angle of attack. The trend of the increase for both of the parameters slows down for $N > 36$.

As discussed in Chapter 5, the combined effects of these variations of angle of attack and free-stream Reynolds number with an increasing number of bolts end up with a forward movement of the separation points, particularly at the upper side of the bolt. It is interesting to note that for both of the flow conditions, increasing the number of bolts beyond $N = 18$ makes the separated shear layer reattach to the upper surface of the bolt and separate again at a distance downstream. Hence, for $N > 18$ a separation bubble is formed over the top surface of the bolt. This can be observed by inspecting the wall shear stress distribution plots (Figures 6.4 and 6.6). The second zero in the wall shear stress distribution of the upper surface of the bolt indicates the location of the reattachment point.

It can be seen in Table 6.3 that increasing the number of bolts from 18 to 45 for $Re_\phi = 0.67 \times 10^7$ and $C_w = 10^5$ ($\lambda_T = 0.35$) advances the separation location from $\phi = 89.298^\circ$ to 89.17°. On the basis of the simulation results, for $N = 45$, flow reattaches to the bolts' surface at $\phi = 90.34^\circ$ and forms a separation bubble over the upper surface of the bolt. Following the reattachment point, another separation of flow occurs at $\phi = 91.22^\circ$. Hence, a wake region is formed behind the bolt between $\phi = 91.27^\circ$ (located on the upper side of the bolt) and $\phi = 91.44^\circ$, which is the location of the separation point on the lower side of the bolt. Increasing the number of bolts from $N = 45$ to $N = 60$ further advances the location of the separation bubble at the top surface and places it between $\phi = 89.14^\circ$ and $\phi = 90.37^\circ$. Flow separates again from the upper surface of the bolt at $\phi = 91.19^\circ$, which is slightly upstream from the second separation point for $N = 45$. Comparison of the separation and reattachment locations between $N = 45$ and $N = 60$ reveals that the length of the separation bubble increases with increasing the number of bolts. Since increasing the number of bolts reduces the free-stream Reynolds number of

the flow approaching the bolt, it could be concluded that the increase in the length of the separation bubble is because of a reduction in the free-stream Reynolds number. This result agrees with the findings obtained by Tani (1964) for an airfoil. Tani proposed that increasing the Reynolds number decreases the separation bubble length.

Inspection of the results in Table 6.2 for $Re_{\phi} = 0.72 \times 10^7$ and $C_w = 0.3 \times 10^5$ ($\lambda_T = 0.09$) shows a similar trend of displacement of separation and reattachment points.

It is also evident in Figures 6.4 and 6.6 that increasing the number of bolts noticeably increases the wall shear stress difference between the bottom side and the top side of the bolt. However, the trend of this increase reduces for $N > 45$. This could be representative of the large differences between the viscous forces exerted on the top and bottom sections of the bolts. In addition, increasing the number of bolts reduces the peak of shear stress as well as the shear stresses of the lower and upper sides of the bolt.

Regarding the pressure distribution around the bolt, it can be observed in Figures 6.5 and 6.7 that increasing the number of bolts increases the peak of static pressure as well as the static pressure difference across each individual bolt. However, it should be noted that increasing the number of bolts reduces the relative total pressure difference between the upper and lower surfaces of the bolt, which is more noticeable for the rotationally dominated flow condition. This is due to the reduction of relative total velocity of the flow around the bolt by increasing the number of bolts. In addition, it is evident in Figures 6.5 and 6.7 that the stagnation point is moved toward the bottom section of the bolt when increasing the number of bolts. This is attributed to the increase in the angle of attack for higher numbers of bolts (Tani, 1964). Differences are also noticed in the pressure coefficient of the upper surface of the bolt for $N = 45$ and 60. Accordingly, the constant pressure region is followed by a slight increase of pressure, showing the reattachment of flow (Tani, 1964).

Variations of different parameters were also investigated at another axial location, $z/s = 0.4$, which is close to the tip of the bolt. Based on the simulation results, for $N = 60$ and $Re_{\phi} = 0.67 \times 10^7$ and $C_w = 10^5$ ($\lambda_T = 0.35$), both the angle of attack and the free-stream Reynolds number slightly reduce when moving from the root to the tip of the bolt. However, since the differences were not considerable, very minor differences were observed for the location of the separation points when moving from the root to the tip

of the bolt. This result is similar to the results obtained for N =18 and similar flow condition in Chapter 5.

It is also interesting to investigate the effect of the number of bolts on the axial variation of the dimensionless tangential velocity. Hence, Figures 6.9 and 6.10 illustrate the tangential velocity distribution at r/b = 0.9 for the two flow conditions investigated in Figures 6.2 to 6.7. The horizontal axis starts at z/s = 0.5, which corresponds to the axial location of the tip of the bolt or the ring. The tangential velocity varies around the circumference of the bolt radius, and the value used in these graphs is that obtained at the location of the centreline of the bolt.

It is clear from Figures 6.9 and 6.10 that the presence of bolts on the rotor brings about an increase in the tangential velocity of the core ($V_\phi/r\omega$). Although increasing N generally increases $V_\phi/r\omega$, there is a levelling off. It is also interesting to note that although the plain disc (N = 0) values of $V_\phi/r\omega$ for λ_T = 0.35 and λ_T = 0.09 are quite different ($V_\phi/r\omega \approx$ 0.04 and 0.3 respectively), this discrepancy reduces with the presence of bolts. In the limit of N = 60, $V_\phi/r\omega \approx$ 0.8 for both λ_T = 0.35 and λ_T = 0.09.

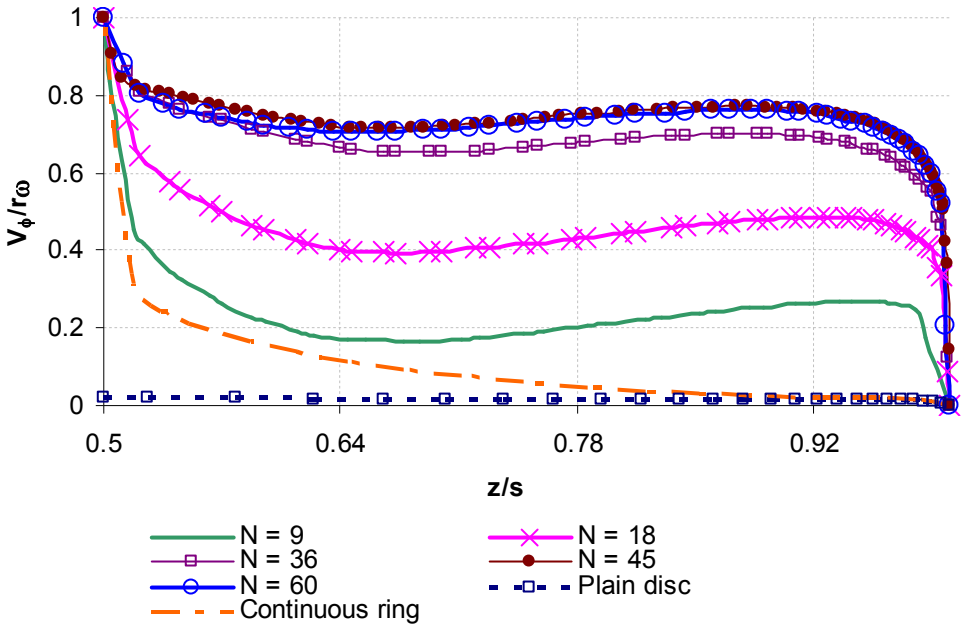

Figure 6.9: Predicted Axial Variation of Dimensionless Tangential Velocity at r/b = 0.9, Re_ϕ = 0.67 x 10^7 and C_w = 10^5 (λ_T = 0.35)
Note: z/s = 0 is located on rotor. This is also the case for Figure 6.10.

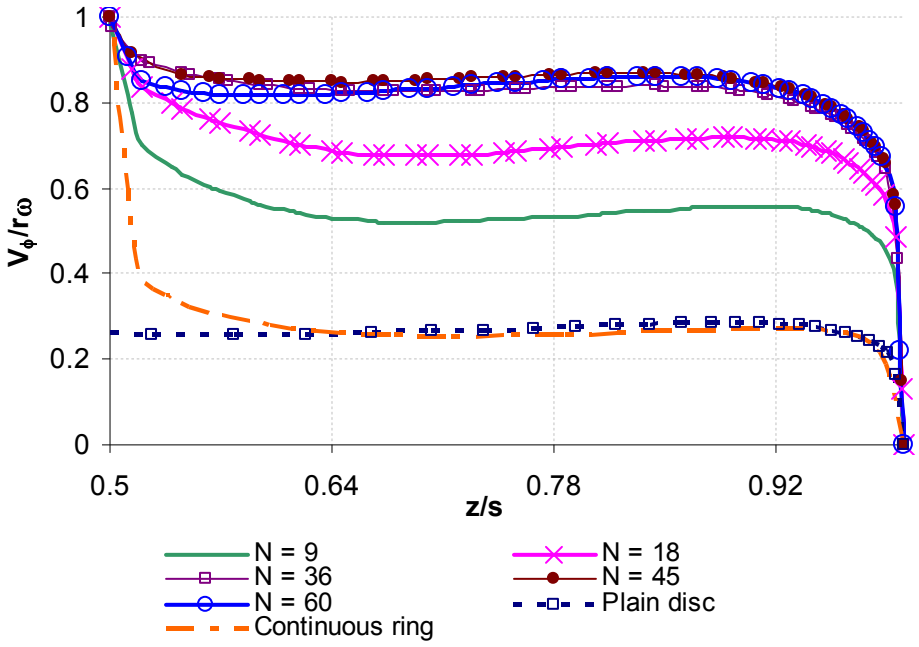

Figure 6.10: Predicted Axial Variation of Dimensionless Tangential Velocity at r/b = 0.9, Re_ϕ = 0.72 x 10^7 and C_w = 0.3 x10^5 (λ_T = 0.09)

It is of interest to study how the boundary layer thickness of the disc varies with increasing the number of bolts. This can be achieved by plotting the dimensionless tangential velocity profile versus the axial location and calculating the distance from the rotor at which the dimensionless tangential velocity reaches 1.1β. Table 6.4 compares the simulation results of rotor boundary layer thickness for the plain disc as well as N = 18, 36 and 60 for the two simulated flow conditions at r/b = 0.91 and φ = 87.28˚.

Inspection of these tangential velocity profiles reveals that increasing the number of bolts reduces the thickness of the boundary layer attached to the rotor. This is due to the increase in the tangential velocity of the core with the increasing number of bolts.

Table 6.4: Comparison of the Rotor Boundary Layer Thickness for Different Number of attached Bolts at $r/b = 0.91$ and $\varphi = 87.28^{\circ}$

N	δ (mm)	
	$Re_\phi = 0.67 \times 10^7$ $C_w = 10^5$ ($\lambda_T = 0.35$)	$Re_\phi = 0.72 \times 10^7$ $C_w = 0.3 \times 10^5$ ($\lambda_T = 0.09$)
Plain disc	4.1	2.2
18	0.9	0.4
36	0.5	0.1
60	0.2	0.04

The occurrence of Taylor columns could also be investigated for different numbers of bolts. As mentioned in Chapter 5, a Rossby number can be used as an indicator of the occurrence of Taylor columns. Based on the simulation results, Rossby numbers ranged from 0.98 for the plain disc to 0.27 for 60 bolts for the flow condition of $Re_\phi = 0.67 \times 10^7$, $C_w = 10^5$ and from 0.74 for the plain disc to 0.14 for 60 bolts for $Re_\phi = 0.72 \times 10^7$, $C_w = 0.3 \times 10^5$. According to these ranges of Rossby numbers, there is an intermediate rotation for the two flow conditions for all the numbers of bolts used in the system (except for the 60 bolts under the rotationally dominated condition). As a result, it is expected that no Taylor columns are produced in the system. Inspection of the velocity vectors above the bolts confirms this expectation.

6.2.2 Moment and drag coefficients

Figures 6.11 and 6.12 illustrate the moment coefficient variations with number of bolts N for $Re_\phi = 0.67 \times 10^7$, $C_w = 10^5$, ($\lambda_T = 0.35$) and $Re_\phi = 0.72 \times 10^7$, $C_w = 0.3 \times 10^5$, ($\lambda_T = 0.09$). The experimental results, together with those from the CFD simulations, are shown for $N = 3$, 9 and 18 bolts as well as for a plain disc. As can be seen, there is good overall agreement between the predictions and the experimental data. Figures 6.13 and 6.14 demonstrate the variations of the moment coefficient with the number of bolts $N = 3$, 9, 18, 36, 45 and 60 and the plain disc as well as the continuous ring for the two flow conditions. The CFD results shown in Figures 6.13 and 6.14 extend the range of those

shown in Figures 6.11 and 6.12 and provide a consistent picture of the effect of the number of bolts on the moment coefficient. In addition, the contribution of skin friction and pressure-related (form drag and radial pumping) losses to the overall moment coefficient for the two flow conditions are presented in Figures 6.15 and 6.16.

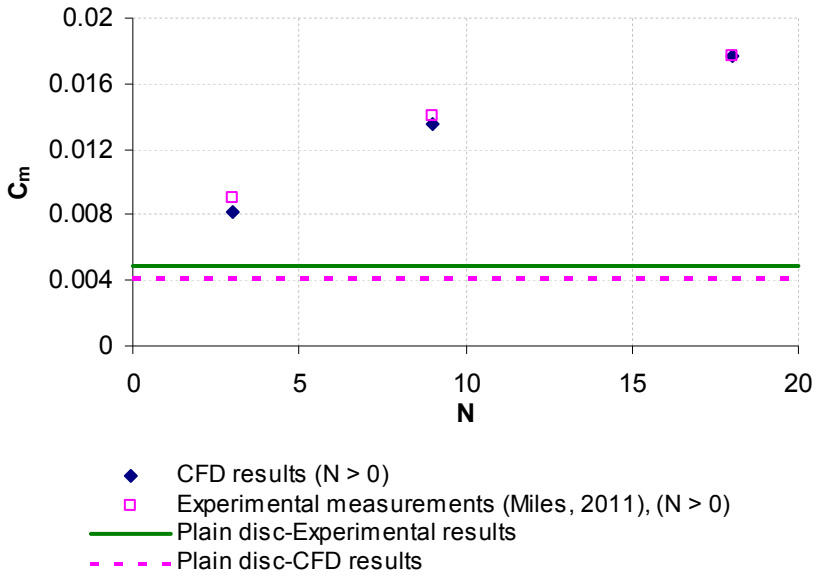

Figure 6.11: Variation of Moment Coefficient with Number of Bolts *N*. Comparison Between Numerical and Experimental Results for 3, 9 and 18 Bolts and a Plain Disc: $Re_\phi = 0.67 \times 10^7$, $C_w = 10^5$ ($\lambda_T = 0.35$)

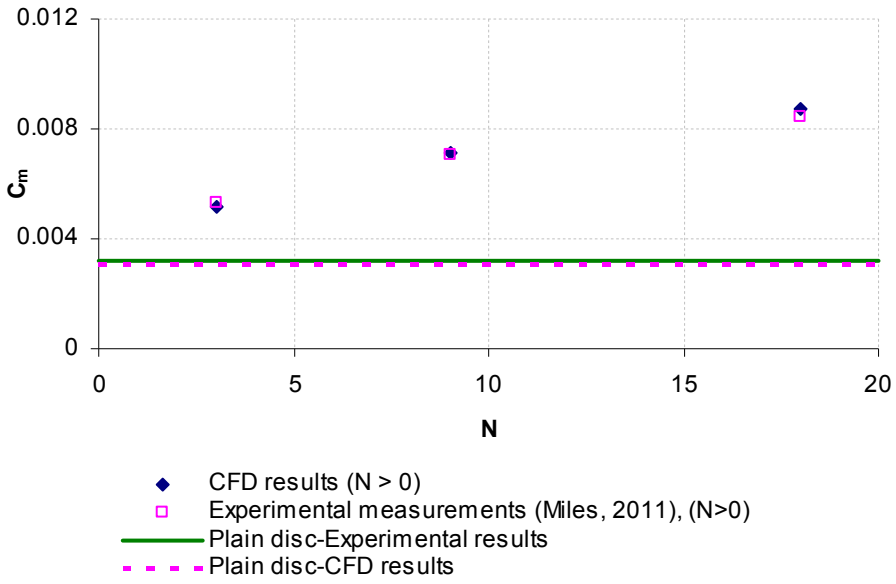

Figure 6.12: Variation of Moment Coefficient with Number of Bolts *N*. Comparison Between Numerical and Experimental Results for 3, 9 and 18 Bolts and a Plain Disc: $Re_\phi = 0.72 \times 10^7$, $C_w = 0.3 \times 10^5$ ($\lambda_T = 0.09$)

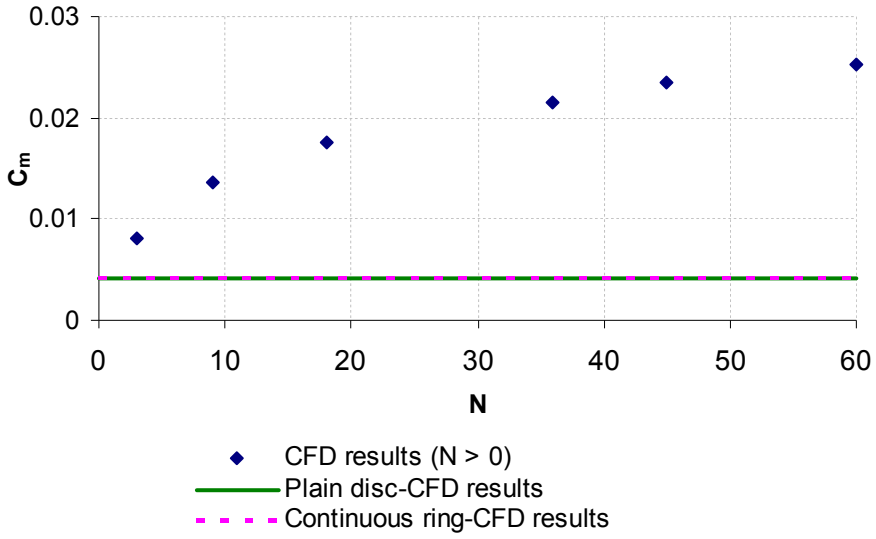

Figure 6.13: Predicted Variation of Moment Coefficient with Number of Bolts, *N* for $Re_\phi = 0.67 \times 10^7$, $C_w = 10^5$ ($\lambda_T = 0.35$)

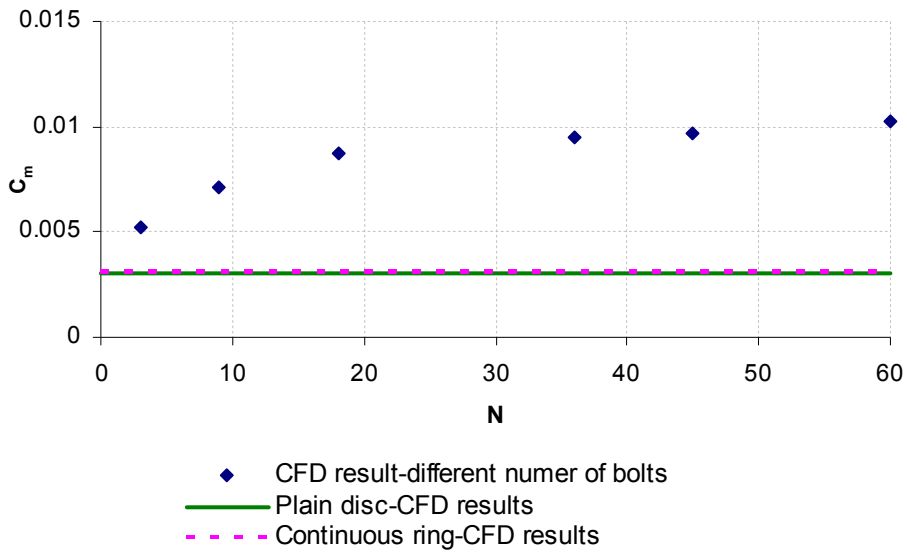

Figure 6.14: Predicted Variation of Moment Coefficient with Number of Bolts, *N* for Re_ϕ = 0.72 x 10^7, C_w =0.3 x 10^5 (λ_T = 0.09)

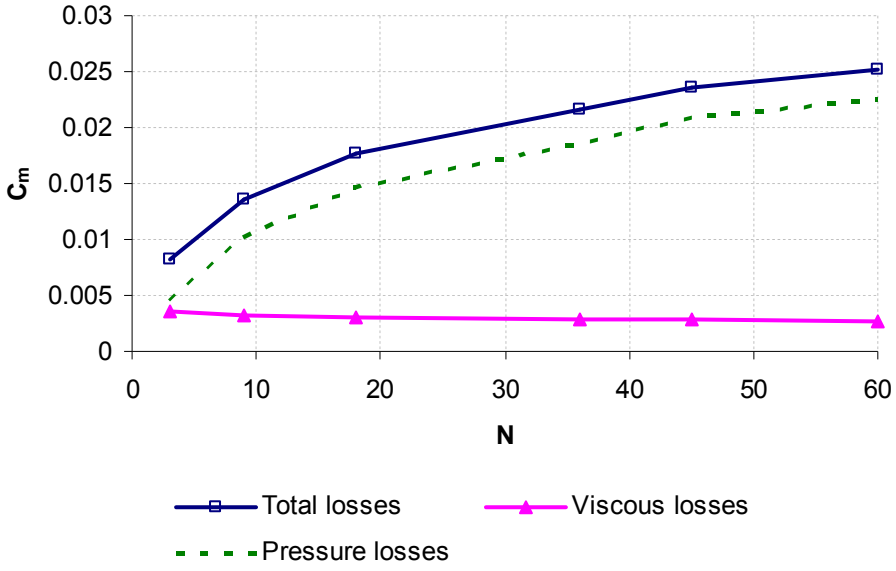

Figure 6.15: Variation of the Overall Moment Coefficient, Viscous and Pressure-related (Form Drag and Radial Pumping) Contributions with Number of Bolts (Re_ϕ = 0.67 x 10^7, C_w = 10^5 and λ_T = 0.35)

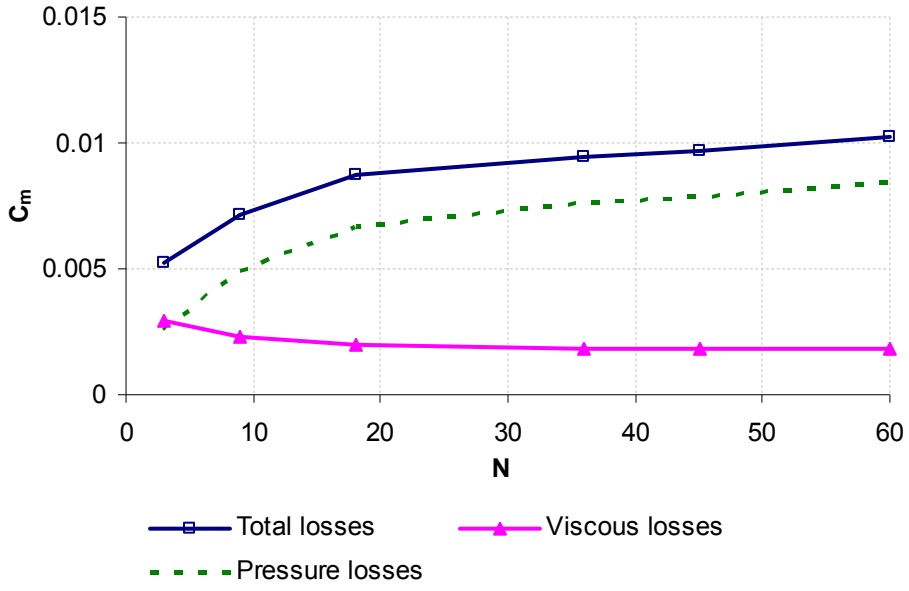

Figure 6.16: Variation of the Overall Moment Coefficient, Viscous and Pressure-related (Form Drag and Radial Pumping) Contributions with Number of Bolts (Re_ϕ = 0.72 x 10^7, C_w =0.3 x10^5 and λ_T = 0.09)

It can be seen that, not surprisingly, increasing the number of bolts increases C_m. There also appears to be a value of N for which the rate of increase of C_m noticeably reduces when further increasing the number of bolts. For λ_T = 0.35, this occurs when approximately $N > 50$ and for $\lambda_T = 0.09$ when $N > 20$. It is interesting to see in Figures 6.13 and 6.14 that the moment coefficient of the ring is approximately equal to the moment coefficient of a plain disc. This is in agreement with the investigations of Millward and Robinson (1989).

Considering Figures 6.15 and 6.16, it can be seen that the skin friction contributes less to the overall moment coefficient than the pressure does. This agrees with the predictions of Zimmerman *et al*. (1986). They proposed that the moment coefficient produced because of the viscous effects is always relatively small. Note that, since the amount of viscous moment coefficient is noticeably less than the pressure moment coefficient, its variation with the number of bolts could not be easily seen in these figures.

The total drag and moment coefficient of individual bolts continuously reduce when increasing the number of bolts. This is contrary to the theoretical predictions made by Zimmerman *et al*. (1986). They proposed that the moment coefficient of the bolts increases when increasing the number of bolts up to approximately N = 13, and then reduces when mounting more bolts into the system.

Based on the simulation results, increasing the number of bolts reduces the area of the wake region and causes an increase in the wake shed from the trailing edge of one bolt to the leading edge of the next. This also brings about a reduction in C_m through the mechanism of form drag. In addition, there is the (reversible) loss associated with the pumping mechanism of the bolts. It would be of interest to further investigate the contribution to C_m. However, since FLUENT reports only the viscous moment and the pressure moment (which includes both the moment produced by the wakes and by the pumping action) separately, it is not possible to find the amount of moment produced by the wakes alone. As mentioned, increasing the number of bolts decreases the relative total pressure difference across each individual bolt. This leads to a net decrease in the moment. However, since there are more bolts, the contribution of the pressure-related moment of all the bolts together increases. Therefore, the simulation results show that the net effect of increasing the number of bolts is to increase the overall moment coefficient. However, for the reasons explained above concerning the structure of the wakes, the rate at which C_m increases with N decreases as N becomes larger.

It is also important to study the variations of the bolt drag coefficient with the number of bolts. Tables 6.5 and 6.6 display the results of the total angle of attack and the free-stream Reynolds number of the flow approaching the bolts as well as the drag coefficient of individual bolts for different N and the two simulated flow conditions. Additionally, Figures 6.17 and 6.18 graphically exhibit the drag coefficient and the moment coefficient respectively of individual bolts as a function of N.

Table 6.5: Comparison of the Total Free-stream Reynolds Number and Angle of Attack of the Flow Approaching the Bolts as well as the Drag Coefficient of Individual Bolts for N = 3, 9, 18, 36, 45, and 60; Re_ϕ = 0.72 x 10^7, C_w = 0.3 x 10^5 (λ_T = 0.09)

N	α (deg)	Re_D (/10^5)	C_D
3	10	1.76	1.99
9	18.7	1.4	1.65
18	27	1.26	1.22
36	35.5	1.03	0.85
45	42	1	0.65
60	43	0.99	0.5

Table 6.6: Comparison of the Total Free-stream Reynolds Number and Angle of Attack of the Flow Approaching the Bolts as well as the Drag Coefficient of Individual Bolts for N = 3, 9, 18, 36, 45, and 60;Re_ϕ = 0.67 x 10^7, C_w = 10^5 (λ_T = 0.35)

N	α (deg)	Re_D (/10^5)	C_D
3	10.5	2.49	1.6
9	19.4	2.27	1.32
18	32	2.07	0.89
36	38	1.8	0.58
45	43.5	1.7	0.4
60	45	1.65	0.32

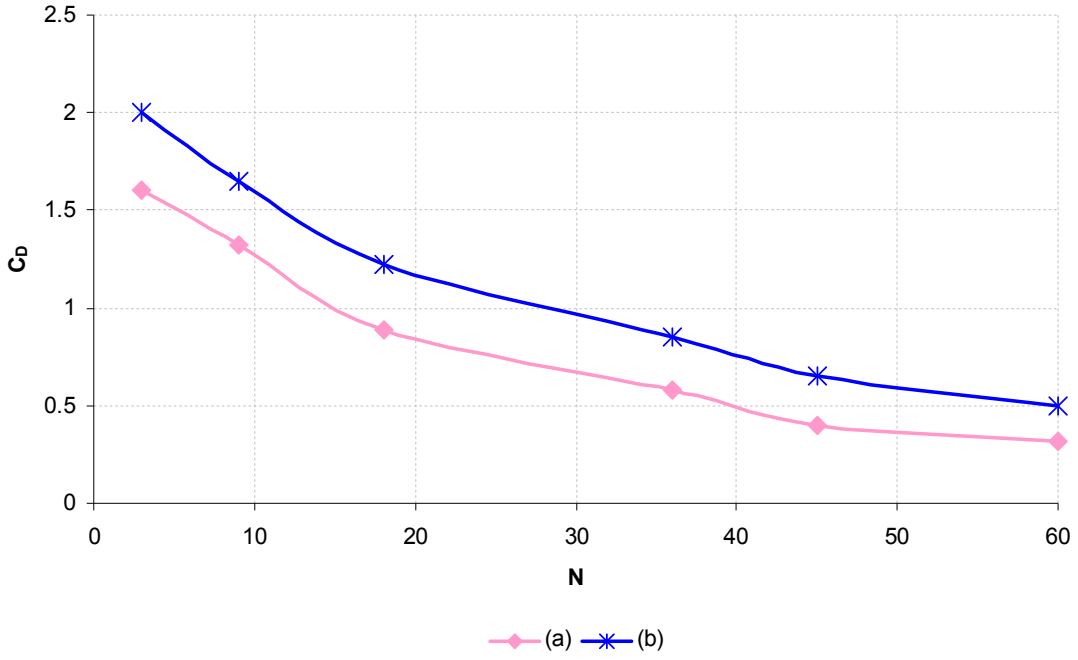

Figure 6.17: Comparison of the Drag Coefficient of Individual Bolts as a Function of *N* for (a): $Re_\phi = 0.67 \times 10^7$, $C_w = 10^5$ ($\lambda_T = 0.35$), and (b): $Re_\phi = 0.72 \times 10^7$, $C_w = 0.3 \times 10^5$ ($\lambda_T = 0.09$)

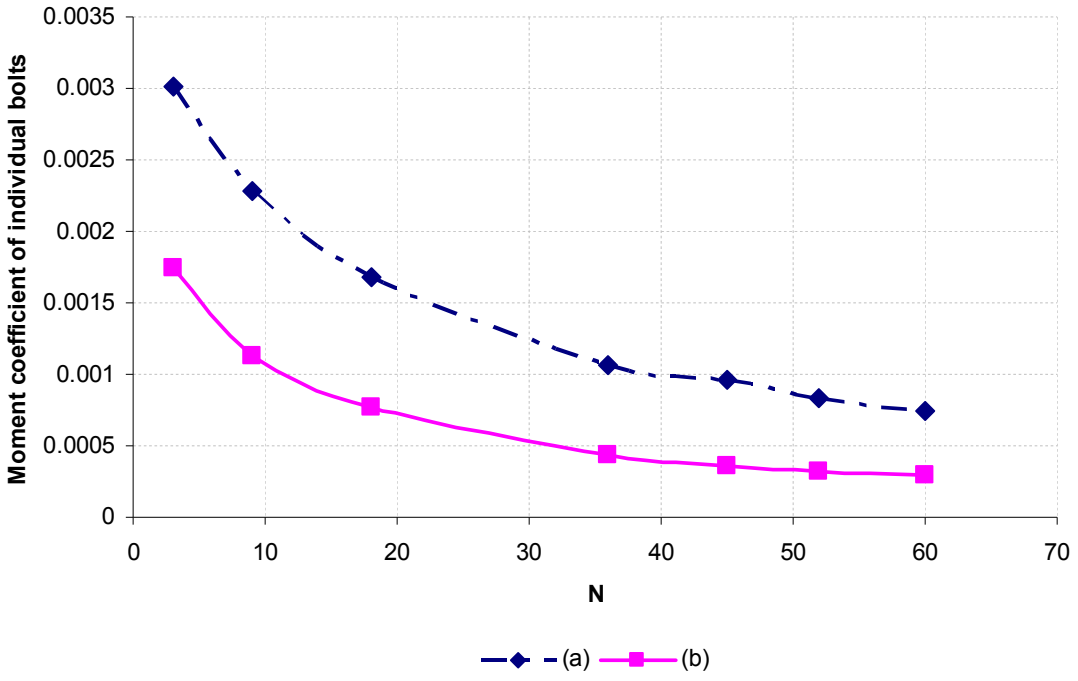

Figure 6.18: Comparison of the Moment Coefficient of Individual Bolts as a Function of *N* for (a): $Re_\phi = 0.67 \times 10^7$, $C_w = 10^5$ ($\lambda_T = 0.35$), and (b): $Re_\phi = 0.72 \times 10^7$, $C_w = 0.3 \times 10^5$ ($\lambda_T = 0.09$)

According to the results presented in Tables 6.5 and 6.6, increasing the number of bolts reduces the total free-stream Reynolds number and increases the total angle of attack of the approaching flow. These variations are similar to those obtained for the local free-stream Reynolds number and the angle of attack (see Tables 6.2 and 6.3). As was discussed earlier, it is expected that the combined effects of these variations end up with an increase in the total drag coefficient of individual bolts. However, inspection of the drag coefficient variations in Tables 6.5 and 6.6, as well as those in Figure 6.17, indicates a reverse trend with increasing *N*. This could be attributed to the fact that increasing the number of bolts and, as a result, decreasing the gap between two neighbouring bolts disturbs the full formation of the wakes behind the bolts. In addition, due to the reduced influence of wakes from upstream bolts, a smaller pressure difference is produced across the bolt. Hence, increasing the number of bolts causes a reduction of the pressure drag coefficient produced by the wakes and that produced by the pumping losses and, as a consequence, reduces the total drag coefficient.

It would be of interest to investigate the boundary layer flow separation regime variations around the bolt by increasing the number of bolts. It was concluded in Chapter 5 that for N = 18 laminar to turbulent transition of the boundary layer above the bolt occurs in the range of Re_D between about 1.2×10^5 and 2×10^5. However, increasing the number of bolts increases the interaction of upstream and downstream bolt and, as a result, increases the degree of unsteadiness and disturbance of the boundary layer over the bolt due to the impingement of the upstream wake. Therefore, it is not only the free-stream Reynolds number that can affect the transition of the boundary layer over the bolt but also it is affected by the wake impingement of upstream bolt. Transition due to the wake impingement also occurs in the boundary layer over the blades of a multi-stage turbomachinery. The situation was studied by Wu *et al.* (1999) and Lien *et al.* (1998). Accordingly, they found that three types of boundary layer transition are typical in gas turbine engines: the bypass transition, the separated-flow transition and the wake-induced transition. In the first type the free-stream turbulence produces the disturbances in the boundary layer. The second type of transition occurs close to the reattachment point of a laminar separation bubble. Finally, the third type of transition is caused by the passing wakes from upstream airfoil. It appears that all of the mentioned mechanisms of transition could cause the transition of flow in the boundary layer above the bolts for N> 18. However, detailed detection of the

transitional mechanisms and the boundary layer regime variations over the bolts requires using unsteady simulations with transitional modelling of the boundary layer which is not the subject of investigation in this research.

6.3 Investigation of the variations of flow structure and amount of losses for a specific number and different diameters of bolts

Investigations were carried out in this section for 18 bolts with three different diameters: D = 10, 13 and 16mm. The flow conditions studied in Section 6.2 were used in this section as well: $Re_\phi = 0.67 \times 10^7$, $C_w = 10^5$ ($\lambda_T = 0.35$) and $Re_\phi = 0.72 \times 10^7$, $C_w = 0.3 \times 10^5$ ($\lambda_T = 0.09$).

The flow structure is studied by plotting relative velocity vectors as well as static pressure and ϕ-wall shear stress distributions on the bolt at z/s = 0.045. Accordingly, Figures 6.19 and 6.20 exhibit the relative velocity vectors for $Re_\phi = 0.67 \times 10^7$, $C_w = 10^5$ ($\lambda_T = 0.35$) and $Re_\phi = 0.72 \times 10^7$, $C_w = 0.3 \times 10^5$ ($\lambda_T = 0.09$), respectively. Figures 6.21 and 6.22 respectively demonstrate the ϕ-wall shear stress and pressure coefficient distributions for $Re_\phi = 0.67 \times 10^7$, $C_w = 10^5$ ($\lambda_T = 0.35$). Similar plots to those shown in Figures 6.21 and 6.22 are displayed in Figures 6.23 and 6.24 for $Re_\phi = 0.72 \times 10^7$ and $C_w = 0.3 \times 10^5$ ($\lambda_T = 0.09$). In addition, results of the local free-stream Reynolds numbers and angles of attack of the flow approaching the bolt at z/s = 0.045 as well as the locations of the stagnation and separation points are tabulated in Tables 6.7 and 6.8.

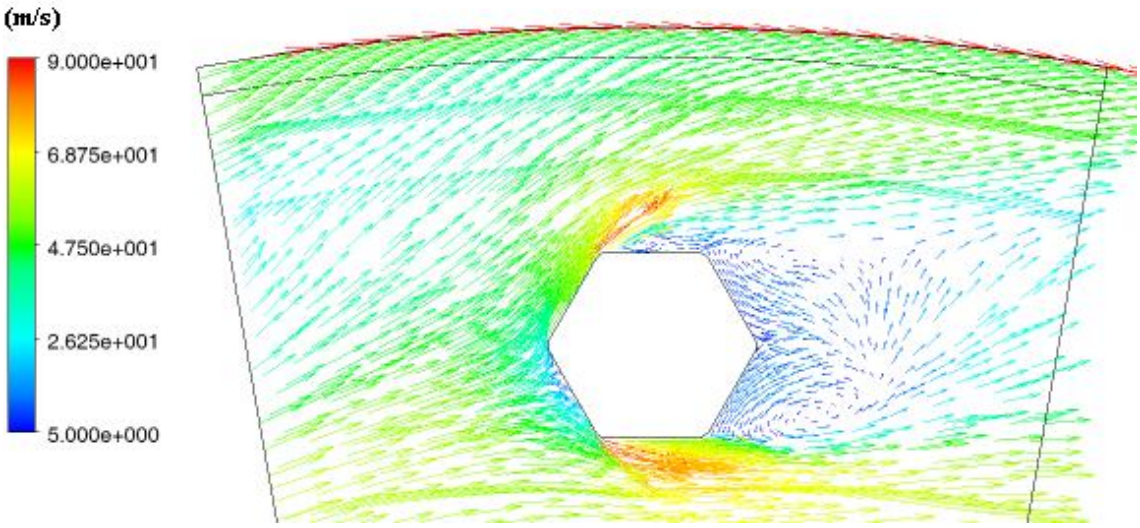

(a)

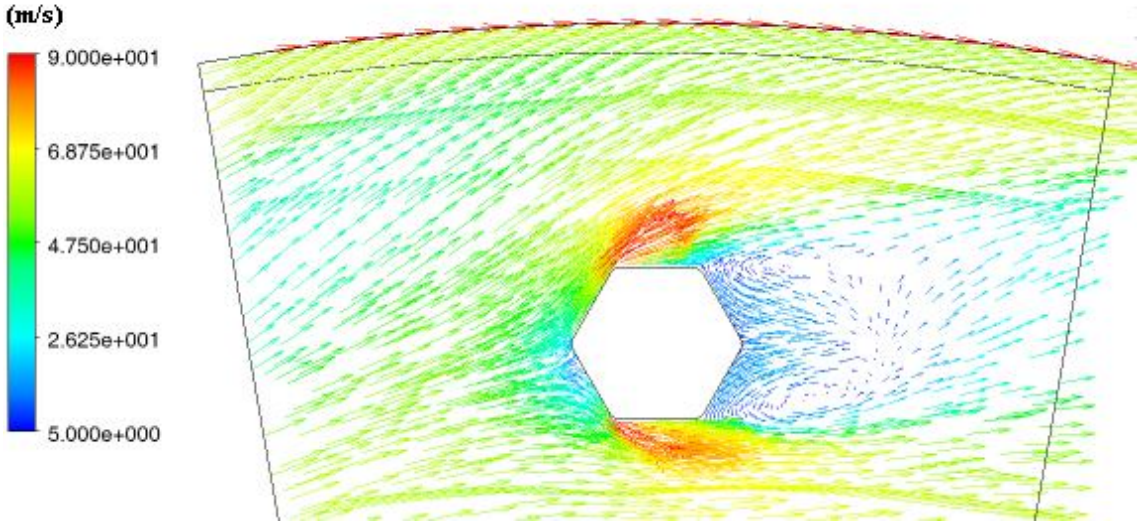

(b)

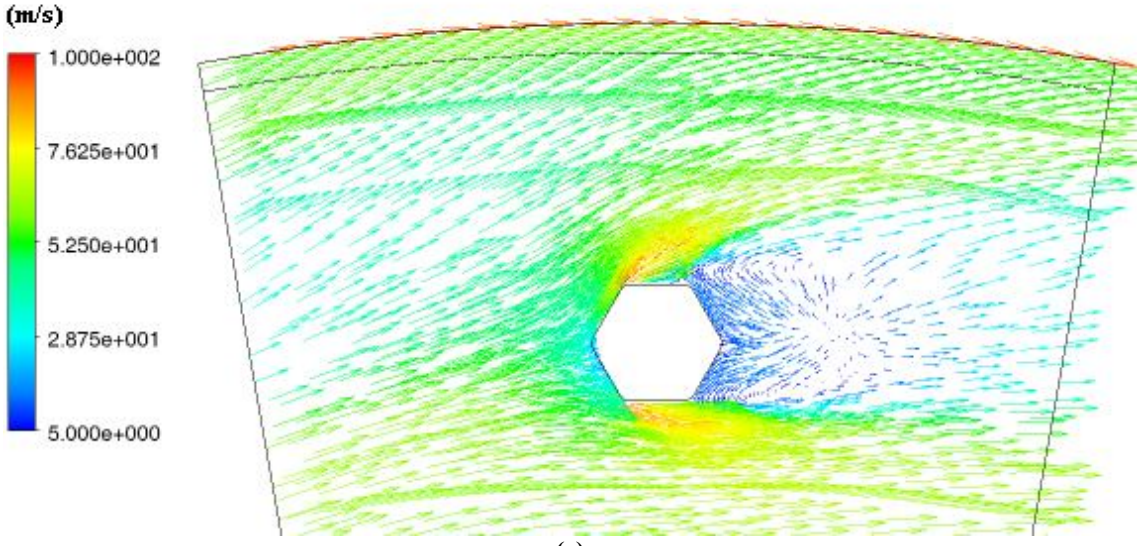

(c)

Figure 6.19: Relative Velocity Vectors for $Re_\phi = 0.67 \times 10^7$, $C_w = 10^5$ ($\lambda_T = 0.35$) at $z/s = 0.045$; N =18, (a) D =1 6 mm, (b) D = 13 mm, and (c) D = 10 mm

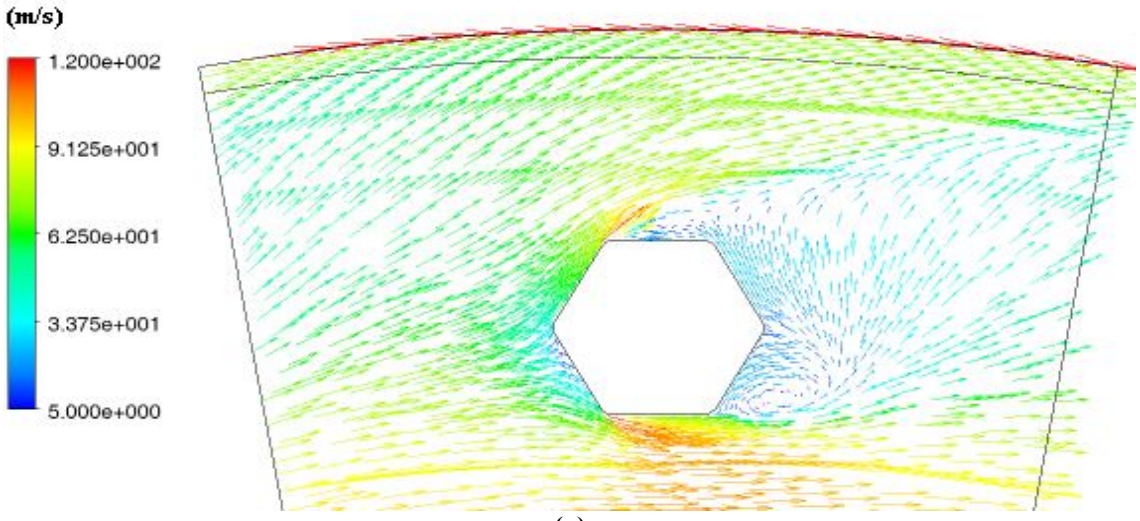

(a)

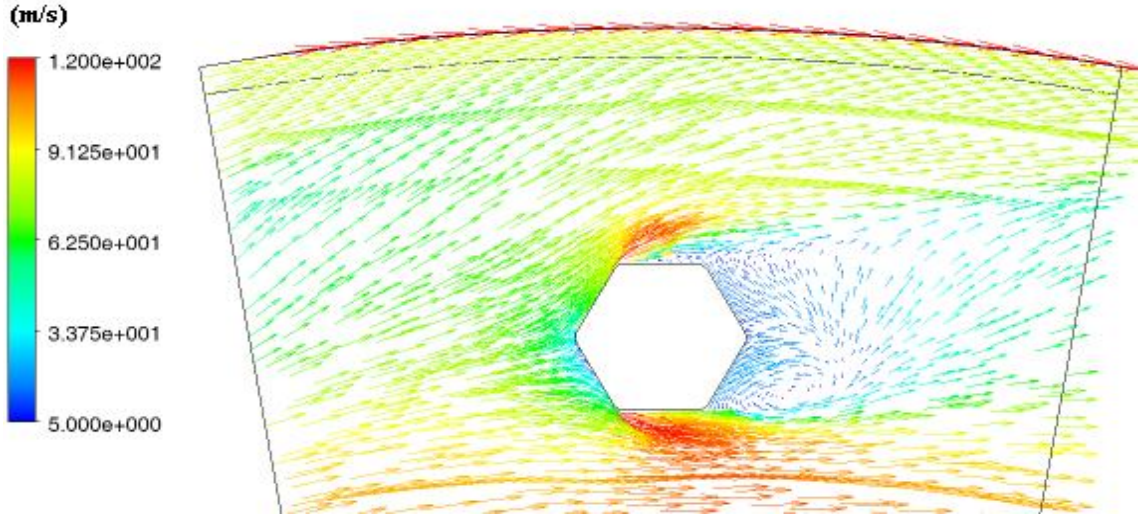

(b)

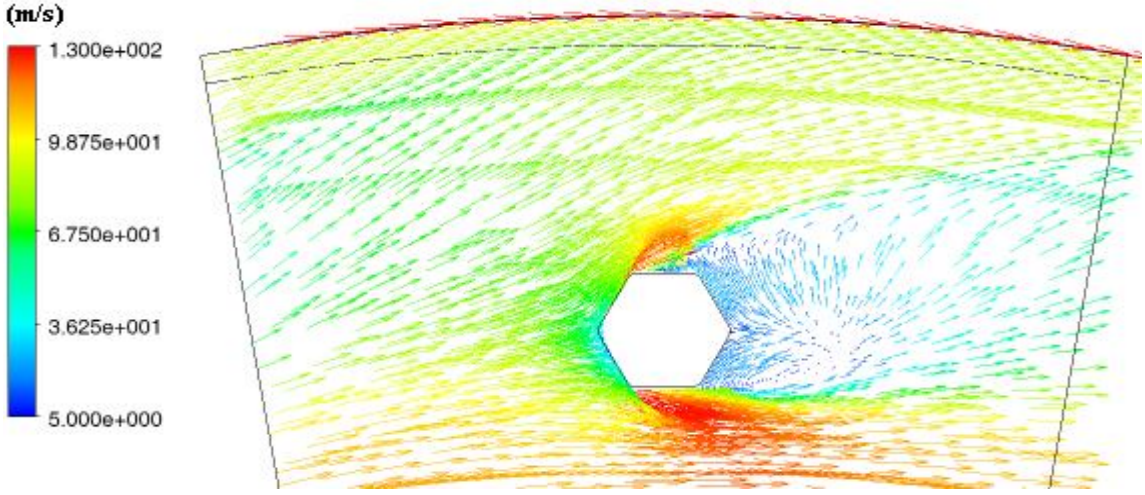

(c)

Figure 6.20: Relative Velocity Vectors for $Re_{\phi} = 0.72 \times 10^7$, $C_w = 0.3 \times 10^5$ ($\lambda_T = 0.09$) at $z/s = 0.045$, $N = 18$, (a) $D = 16$ mm, (b) $D = 13$ mm, and (c) $D = 10$ mm

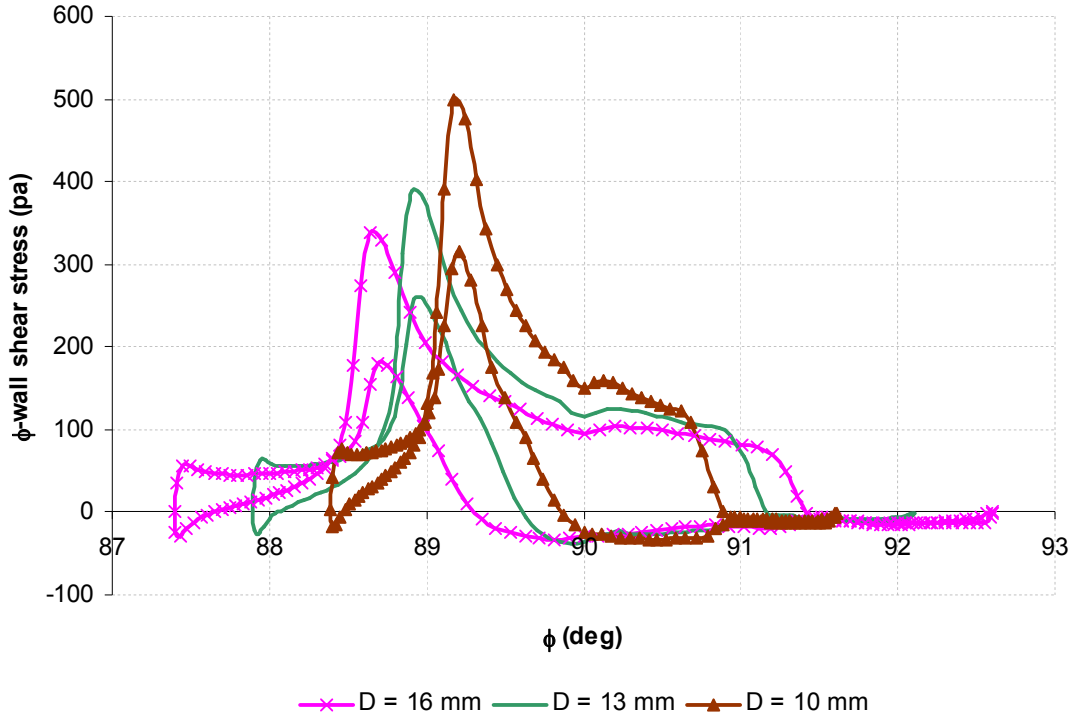

Figure 6.21: Variations of ϕ-wall Shear Stress Distribution on the Bolt for Different Diameters of Bolts at z/s = 0.045, Re_ϕ = 0.72 x 10^7, C_w = 0.3 x 10^5 (λ_T = 0.09), N =18

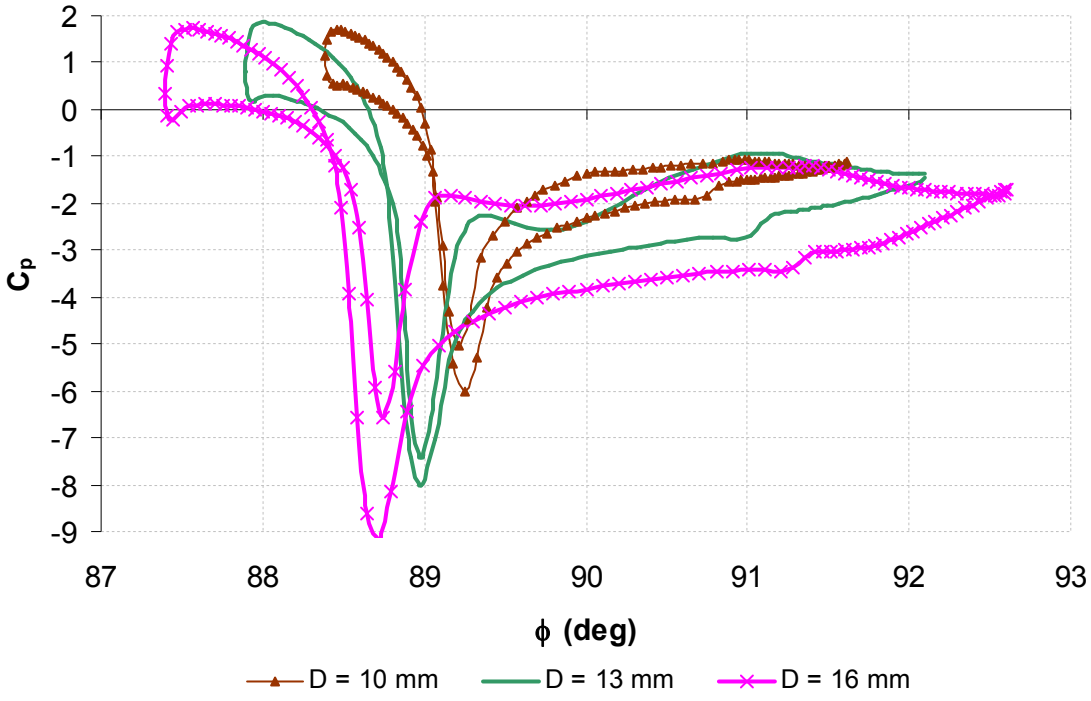

Figure 6.22: Variations of Pressure Distribution on the Bolt for Different Diameters of Bolts at z/s = 0.045, Re_ϕ = 0.72 x 10^7, C_w = 0.3 x 10^5 (λ_T = 0.09), N =18

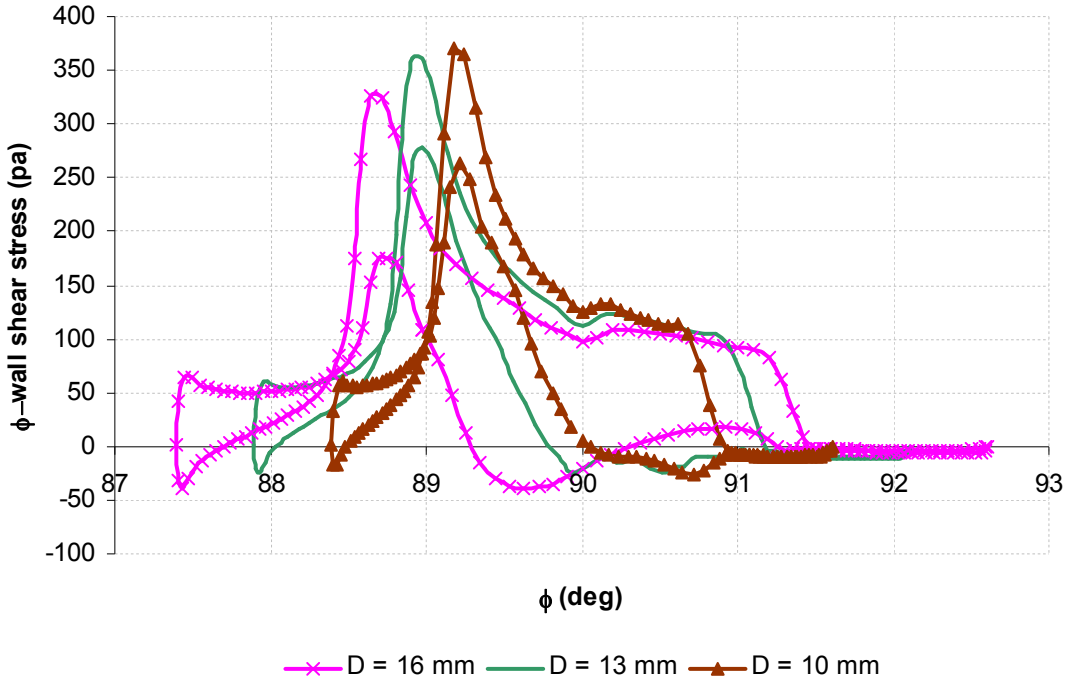

Figure 6.23: Variations of ϕ-wall Shear Stress Distribution on the Bolt for Different Diameters of Bolts at $z/s = 0.045$, $Re_\phi = 0.67 \times 10^7$, $C_w = 10^5$ ($\lambda_T = 0.35$), $N = 18$

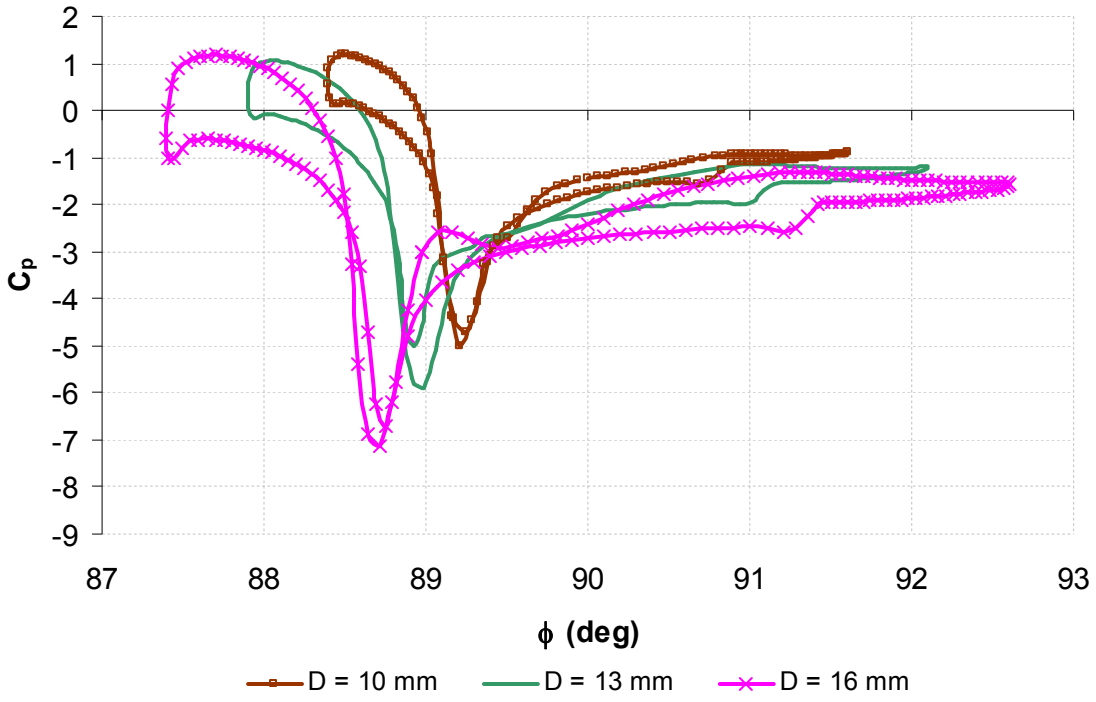

Figure 6.24: Variations of Pressure Distribution on the Bolt for Different Diameters of bolts at $z/s = 0.045$, $Re_\phi = 0.67 \times 10^7$, $C_w = 10^5$ ($\lambda_T = 0.35$), $N = 18$

Table 6.7: Comparison of the Local Free-stream Reynolds Number and Angle of Attack of the Flow Approaching the Bolt at z/s =0.045 as well as the Location of the Stagnation and Separation Points for Different Diameters of bolts, $Re_\phi = 0.67 \times 10^7$, $C_w = 10^5$ ($\lambda_T = 0.35$), $N = 18$

D (mm)	α (deg)	Re_D ($/10^5$)	$\phi_{stagnation}$ (deg)	$\phi_{separation-upper\ surface}$ (deg)	$\phi_{separation-lower\ surface}$ (deg)
10	28.2	1.62	88.65	90.9	91.44
13	33.4	1.93	88.16	90.67	91.44
16	39.3	2.25	87.95	89.298*	91.45

*The angular location corresponds to the first separation point.

Table 6.8: Comparison of the Local Free-stream Reynolds Number and Angle of Attack of the Flow Approaching the Bolt at z/s =0.045 as well as the Location of the Stagnation and Separation Points for Different Diameters of bolts, $Re_\phi = 0.72 \times 10^7$, $C_w = 0.3 \times 10^5$ ($\lambda_T = 0.09$), $N = 18$

D (mm)	α (deg)	Re_D ($/10^5$)	$\phi_{stagnation}$ (deg)	$\phi_{separation-upper\ surface}$ (deg)	$\phi_{separation-lower\ surface}$ (deg)
10	21.7	1.14	88.8	89.85	91.4
13	25.2	1.18	88.46	89.63	91.4
16	30.1	1.24	87.84	89.3	91.41

Based on the results presented in Tables 6.7 and 6.8, increasing the diameter of bolts causes an earlier flow separation, which leads to an increase in the area of the wake region (see also Figures 6.19 and 6.20). This could be attributed to the fact that the angle of attack of the flow approaching the bolt increases when increasing the bolt's diameter. Considering the free-stream Reynolds number, increasing D slightly increases Re_D.

Considering the range of Re_D for laminar to turbulent transition of the boundary layer above the bolt which was obtained for N = 18 (see section 5.4), for $Re_\phi = 0.72 \times 10^7$ and $C_w = 0.3 \times 10^5$ ($\lambda_T = 0.09$), flow in the boundary layer attached to the bolt remains in the laminar regime for the three simulated diameters of the bolts. However, for $Re_\phi = 0.67 \times 10^7$ and $C_w = 10^5$ ($\lambda_T = 0.35$), the boundary layer flow is in the transitional regime for D

= 13mm and 10mm, and is moved to the fully turbulent regime for D = 16mm. Note that the angular location of the separation point for $Re_\phi = 0.67 \times 10^7$ and $C_w = 10^5$ and D = 16mm corresponds to the location of the first separation point. It should be recalled that for $Re_\phi = 0.67 \times 10^7$ and $C_w = 10^5$ and D = 16mm the turbulent boundary layer on the upper surface of the bolt reattaches the flow and forms a separation bubble over its upper side.

Inspection of pressure coefficient distributions reveals that the static pressure difference around the bolt increases when increasing the diameter of the bolts. However, the minimum static pressure as well as the relative total pressure difference between the lower and upper surfaces of the bolt are reduced with increasing D. This can be attributed to the reduction of the relative total velocity between the upper and lower sides of the bolts for the bolts with larger diameters. In addition, increasing D moves the stagnation point toward the upper surface of the bolt. This is due to the increase in the angle of attack with the diameter of the bolts.

It is also interesting to investigate the variations in rotor boundary layer thickness with changing the diameter of bolts in the range of their interference. Table 6.9 displays the boundary layer thickness of the rotor for different diameters of bolts at r/b = 0.91 and φ = 87.28˚. Accordingly, it appears that the boundary layer thickness of the rotor is at its lowest for D = 16mm. The reason is that the core swirl ratio for D = 16mm is at its highest in comparison with that for the two other simulated diameters.

Table 6.9: Comparison of the Boundary Layer Thickness of the Rotor for Different Diameters of attached Bolts at r/b = 0.91 and φ = 87.28˚

D **(mm)**	δ **(mm)**	
	$Re_\phi = 0.67 \times 10^7$ $C_w = 10^5$ ($\lambda_T = 0.35$)	$Re_\phi = 0.72 \times 10^7$ $C_w = 0.3 \times 10^5$ ($\lambda_T = 0.09$)
10	0.99	0.5
13	0.94	0.45
16	0.9	0.4

It is important to investigate the loss coefficients produced by bolts with different diameters. Hence, the results of the moment and drag coefficients of individual bolts with different diameters as well as the total values of the free-stream Reynolds number and the angle of attack of the flow approaching the bolts are tabulated in Tables 6.10 and 6.11 for $Re_\phi = 0.67 \times 10^7$, $C_w = 10^5$ ($\lambda_T = 0.35$) and $Re_\phi = 0.72 \times 10^7$, $C_w = 0.3 \times 10^5$ ($\lambda_T = 0.09$) respectively. In addition, the drag and moment coefficients of individual bolts are graphically presented in Figures 6.25 and 6.26.

Table 6.10: Variations of Total Free-stream Reynolds Number and Angle of Attack of the Flow Approaching the Bolts as well as the Drag and Moment Coefficients of Individual Bolts for Different Diameters, $Re_\phi = 0.67 \times 10^7$, $C_w = 10^5$ ($\lambda_T = 0.35$), $N = 18$

D (mm)	α (deg)	Re_D ($/10^5$)	C_D	C_m
10	21	1.6	1.03	0.0007
13	27	1.97	0.98	0.00085
16	32	2.07	0.89	0.00098

Table 6.11: Variations of the Total Free-stream Reynolds Number and Angle of Attack of the Flow Approaching the Bolts as well as the Drag and Moment Coefficients of Individual Bolts for Different Diameters of Bolts, $Re_\phi = 0.72 \times 10^7$, $C_w = 0.3 \times 10^5$ ($\lambda_T = 0.09$), $N = 18$

D (mm)	α (deg)	Re_D ($/10^5$)	C_D	C_m
10	19	1.05	1.13	0.00033
13	22.6	1.12	1.18	0.00037
16	27	1.26	1.22	0.00047

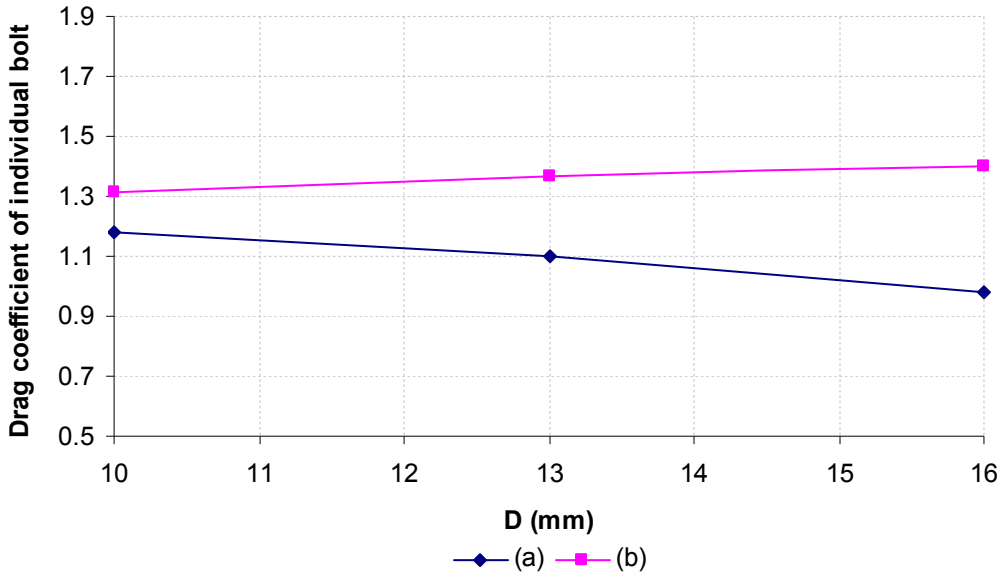

Figure 6.25: Variations of the Drag Coefficient of Individual Bolts for $N = 18$ (a): $Re_\phi = 0.67 \times 10^7$, $C_w = 10^5$ (λ_T=0.35) and (b): $Re_\phi = 0.72 \times 10^7$, $C_w = 0.3 \times 10^5$ (λ_T=0.09)

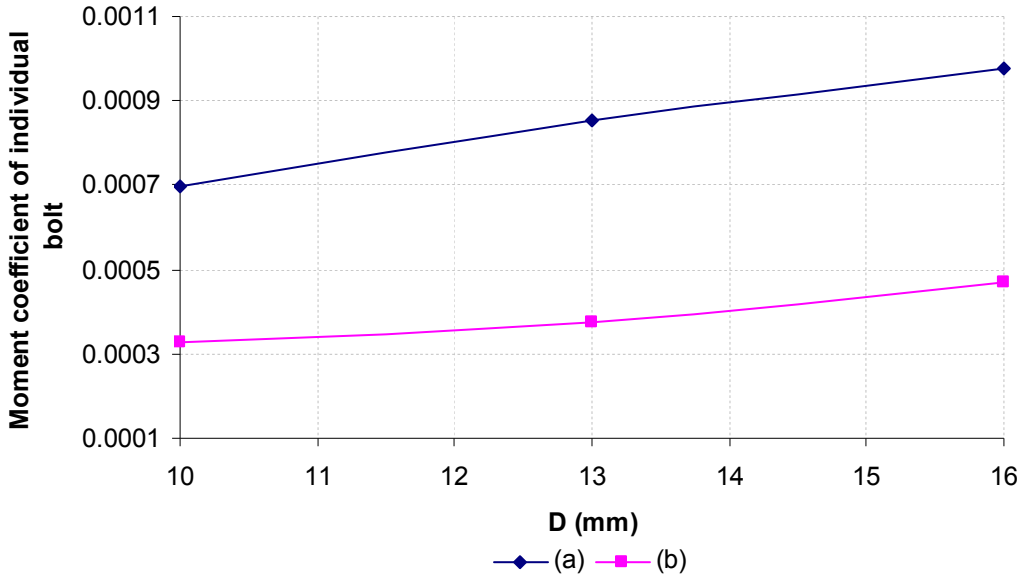

Figure 6.26: Variations of the Moment Coefficient of Individual Bolts for $N = 18$ (a): $Re_\phi = 0.67 \times 10^7$, $C_w = 10^5$ (λ_T=0.35) and (b): $Re_\phi = 0.72 \times 10^7$, $C_w = 0.3 \times 10^5$ (λ_T=0.09)

As mentioned by Schlichting and Gersten (1999), the relative contribution of viscous and pressure drags depends on the thickness of the body. For small thicknesses of the body, viscous drag has the major contribution to the total drag. However, as the thickness of the body increases, viscous drag decreases, and for blunt bodies like cylinders it is dominated significantly by pressure drag. The same observations were obtained from the simulation results of the bolts with different diameters.

Miles (2011) could not find a measurable increase of the moment coefficient between D = 10mm and D = 13mm due to the uncertainty of measurements at low rotational Reynolds numbers. However, on the basis of the results presented in Tables 6.10 and 6.11, increasing the diameter of the bolts consistently increases the moment and drag coefficients for $\mathrm{Re}_\phi = 0.72 \times 10^7$ and $C_w = 0.3 \times 10^5$ ($\lambda_T = 0.09$). Although the moment coefficient of the bolts increases with increasing D for $\mathrm{Re}_\phi = 0.67 \times 10^7$ and $C_w = 10^5$ ($\lambda_T = 0.35$), a reducing trend is evident for the variations of the bolts' drag coefficient. This could be explained by examining the flow regimes around the bolts with different diameters for the mentioned flow conditions. According to the results shown in Table 6.11, flow is in the transitional regime for D = 10mm and 13mm, and moves to the fully turbulent regime for D = 16mm. This is contrary to the flow regime in the boundary layer over the bolt for $\mathrm{Re}_\phi = 0.72 \times 10^7$ and $C_w = 0.3 \times 10^5$ where flow is in the laminar regime for all of the three diameters of bolts simulated. As a result, it appears that the predictions proposed by Schlichting and Gersten (1999) are only valid for variations of the bolts' drag coefficient with diameters for $\mathrm{Re}_\phi = 0.72 \times 10^7$ and $C_w = 0.3 \times 10^5$ ($\lambda_T = 0.09$).

It also appears from Figure 6.25 that the rate of drag coefficient variations is higher between D = 13mm and D = 16mm in comparison to its variations between D = 10mm and D = 13mm for $\mathrm{Re}_\phi = 0.67 \times 10^7$ and $C_w = 10^5$ ($\lambda_T = 0.35$). In addition, it appears that the total variations of the bolts' drag coefficient between D = 10mm and D = 16mm for the mentioned flow conditions are higher than their variations for $\mathrm{Re}_\phi = 0.72 \times 10^7$ and $C_w = 0.3 \times 10^5$ ($\lambda_T = 0.09$). A similar observation could be made by comparing the moment coefficient variations between the two flow conditions.

6.4 Investigation of the moment and drag coefficient variations by varying the diameter and number of bolts simultaneously

In Sections 6.2 and 6.3, variations of the moment coefficient in the rotor-stator system were investigated by varying either the number or diameter of the bolts. However, it is interesting to investigate whether it is possible to find a general trend between the moment coefficient and the number of bolts, independent of their diameter. Hence, two sets of simulations were conducted, one for D = 10mm in which N ranges from 3 to 96, and the other for D = 13mm in which N ranges from 3 to 75. These sets of simulations as well as the simulations performed for D = 16mm in which N ranges from 3 to 60 provide a large database for analysis. Note that N = 60 for simulations with D = 16mm, N = 75 for simulations with D = 13mm and N = 96 for simulation with D = 10mm are the maximum possible number of bolts that can circumferentially be placed on the rotor at r/b = 0.9. The bolts were made non-dimensional by defining the ratio of the bolts' pitch arc length, x_{pr}, to the bolts' diameter and the bolts spacing, as displayed in Equation 6.1.

Figures 6.27 and 6.28 show the variations of the total moment coefficient for different numbers of bolts as a function of X_b for Re_ϕ = 0.67 x 10^7, C_w = 10^5 (λ_T = 0.35) and Re_ϕ = 0.72 x 10^7, C_w = 0.3 x 10^5 (λ_T = 0.09) respectively. Also included in Figures 6.27 and 6.28 are the results of the correlation obtained by the experimental measurements of Miles (2011). The correlation suggests a relation between the dimensionless parameters and the bolts' spacing (see Equation 6.2).

$$C_m = 12.15 \mathrm{Re}_\phi^{-0.67} C_w^{0.44} \left(\frac{D}{x_{pr}} \right)^{0.27} \qquad 6.2$$

In addition, variations of the drag coefficient of the individual bolts as a function of X_b are shown in Figures 6.29 and 6.30 for the two simulated flow conditions. The range of applicability of Equation 6.2 is as follows:

$0.17 \times 10^7 \leq Re_\phi \leq 1.5 \times 10^7$

$0.24 \times 10^5 \leq C_w \leq 1.06 \times 10^5$

$4 \leq (p/D) \leq 42$

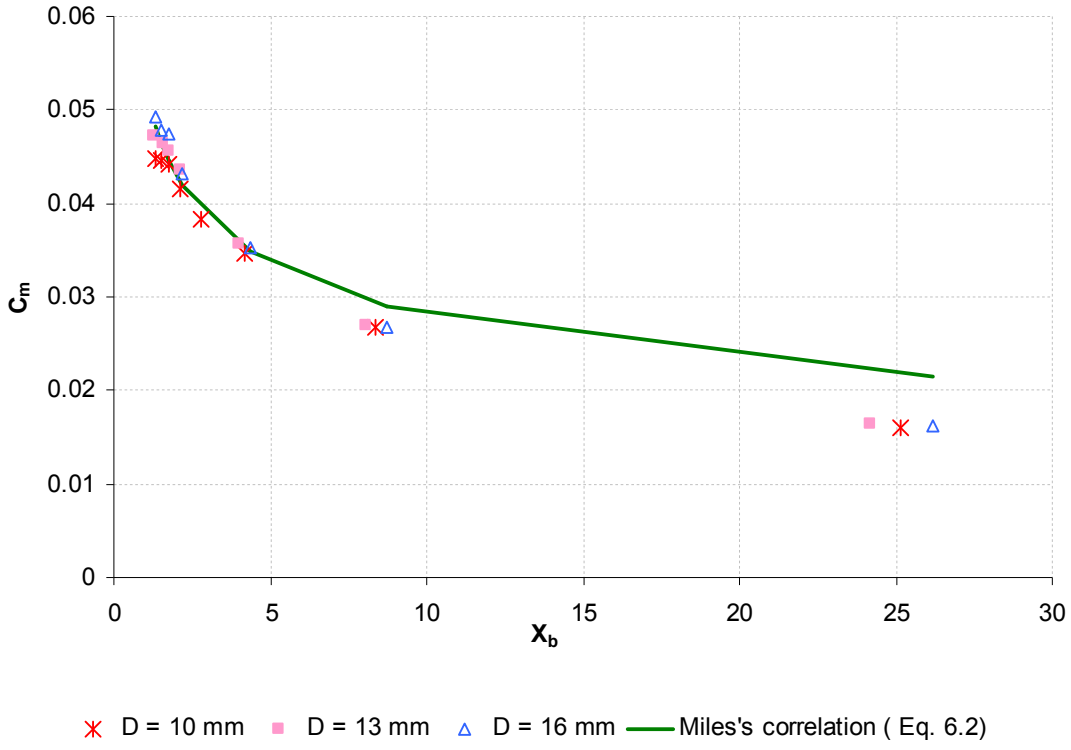

Figure 6.27: Variations of Total Moment Coefficient as a Function of Bolts Spacing for Different Diameters of Bolts; $Re_\phi = 0.67 \times 10^7$, $C_w = 10^5$ ($\lambda_T = 0.35$)

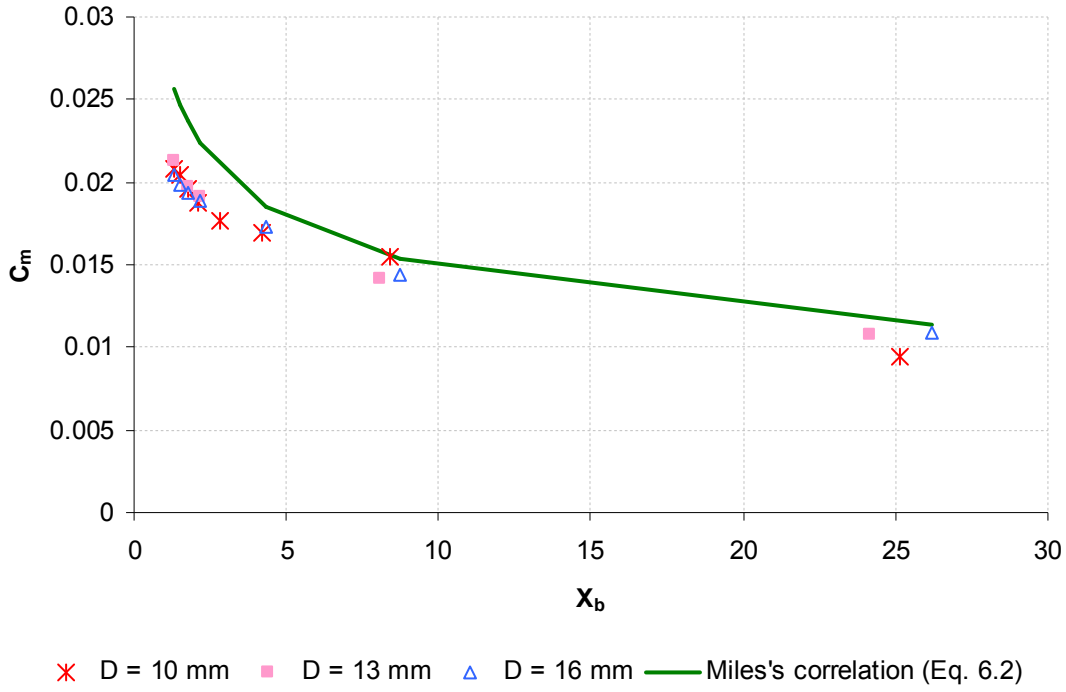

Figure 6.28: Variations of Total Moment Coefficient as a Function of Bolts Spacing for Different Diameters of Bolts; $Re_\phi = 0.72 \times 10^7$, $C_w = 0.3 \times 10^5$ ($\lambda_T = 0.09$)

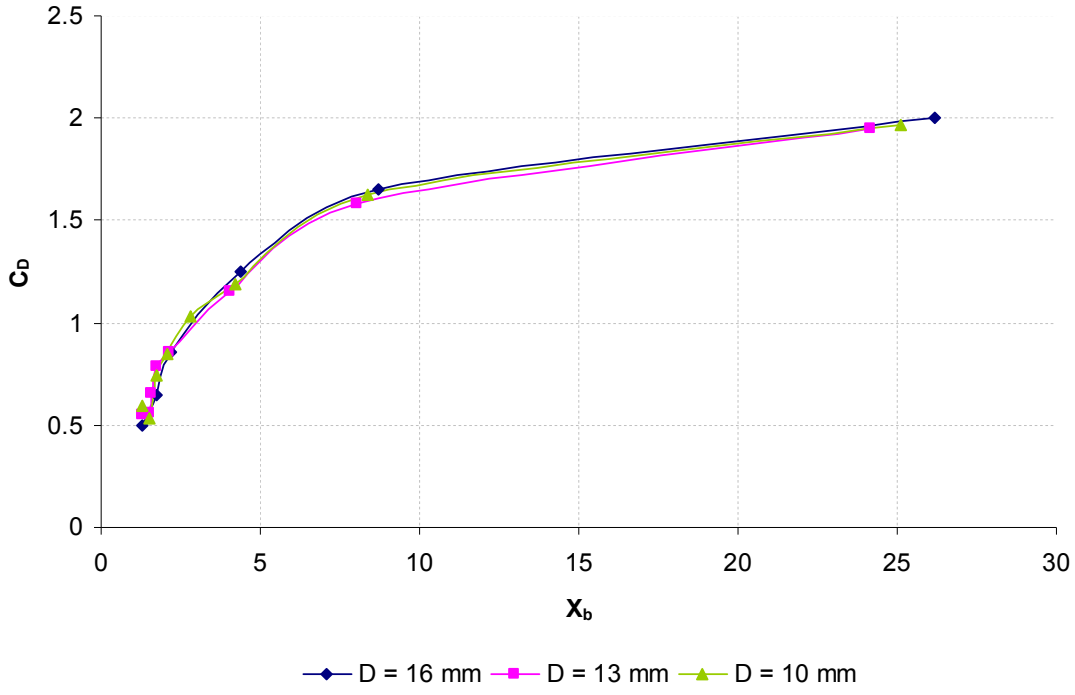

Figure 6.29: Variations of Drag Coefficient of Individual Bolts as a Function of Bolts Spacing for $Re_\phi = 0.67 \times 10^7$, $C_w = 10^5$ ($\lambda_T = 0.35$)

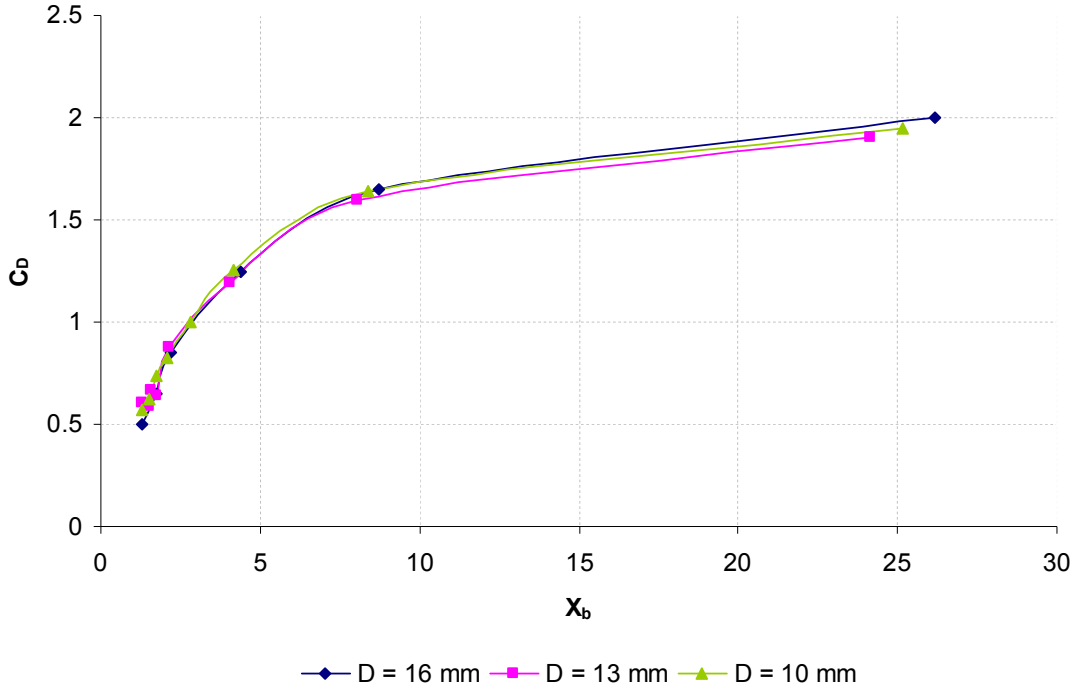

Figure 6.30: Variations of Drag Coefficient of Individual Bolts as a Function of Bolts Spacing for $Re_\phi = 0.72 \times 10^7$, $C_w = 0.3 \times 10^5$ ($\lambda_T = 0.09$)

As can be observed, the moment coefficients of the bolts with equal values of X_b are approximately equal in almost the whole range of X_b apart from at its lower values. The reason for this observed discrepancy is that for a specific value of X_b the difference between the number of bolts for each diameter becomes larger. For example, at $X_b = 25$ the number of bolts for D = 16mm, 13mm, and 10mm is three, four and five respectively,, while for $X_b = 1.3$ it is 60, 75 and 96 respectively.

In addition, apart from the lower values of X_b ($X_b < 4$), a good overall agreement could be observed between the simulation results and the results obtained using Miles's correlation. However, it should be noted that the maximum number of bolts used in the experimental measurements conducted by Miles was $N = 18$. Hence, the validity of their suggested correlation for higher numbers of bolts (lower values of X_b) is doubted. Regarding the drag coefficient, it can be seen from Figures 6.29 and 6.30 that its value is almost the same for different diameters having equal values of X_b.

6.5 Investigation of the validity of experimental measurement assumptions: equal amounts of disc moment coefficients for a system with bolts and a system without bolts

The experimental measurements for windage losses are primarily based on two methods: the first method is to measure the heat added to the fluid by the windage effects, and the second is to measure the additional torque that is produced by windage. However, since there is no direct method to separately measure the windage added by protrusions, an indirect method is used in both of the two experimental measurements. In the indirect method, the torque (or enthalpy change) of the whole system is measured in two cases: the rotor-stator system with mounted bolts, and the rotor-stator system without mounted bolts (plain disc system). Then the torque (or enthalpy change) of the bolts is achieved by subtracting one of these two values from the other (see Equation 6.3). Although this is the only applicable method for measuring the losses produced by the protrusions, the results are based on a specific assumption. The assumption is that the amount of losses produced by the disc is equal for the two systems. However, the validity of this assumption is highly doubted because the presence of protrusions in a rotor-stator system significantly alters the flow phenomena, particularly in the range of their interference.

$$C_{m,bolt} = C_{m,total} - C_{m,plaindisc} \qquad 6.3$$

As mentioned before, it is possible in FLUENT to find the moment coefficient produced by the disc and that produced by the bolts separately. The results could be used in order to validate the assumption mentioned above.

Accordingly, Figure 6.31 displays the moment coefficient of the rotor as a function of Re_ϕ for the plain disc system and the rotor-mounted bolt system with N = 18 and D = 16mm. In addition, Figure 6.32 compares the moment coefficient of the rotor with a different number of mounted bolts (D = 16mm).

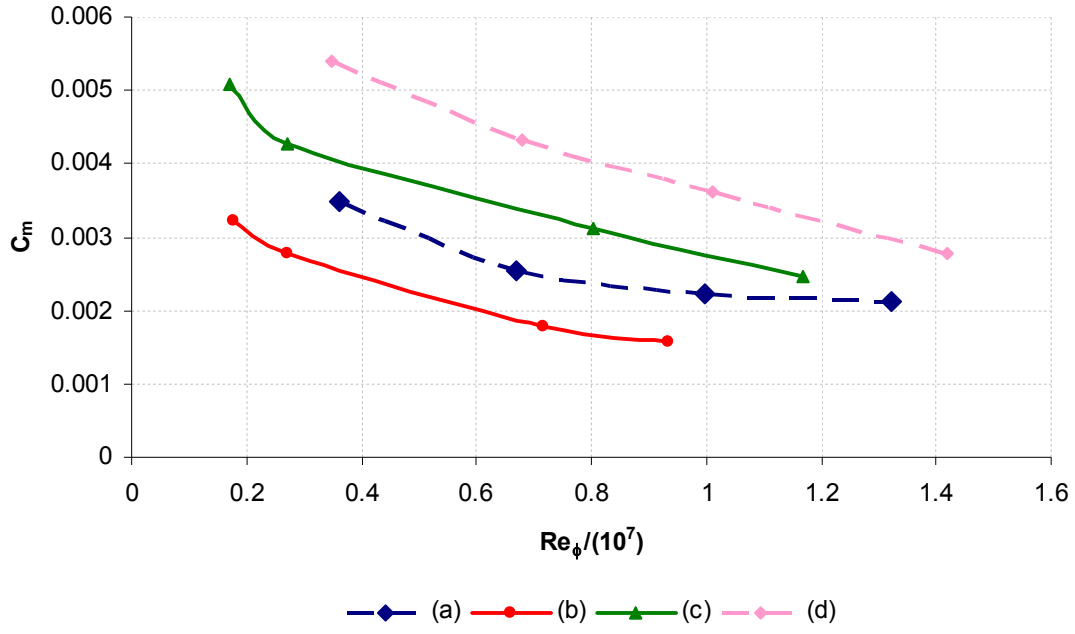

Figure 6.31: Variations of Moment Coefficient Results Produced by the Rotor Between (a): Rotor-mounted Bolts System with $C_w = 10^5$, (b): Rotor-mounted Bolts System with $C_w = 0.3 \times 10^5$, (c): Plain Disc System with $C_w = 10^5$, and (d): Plain disc System with $C_w = 0.3 \times 10^5$

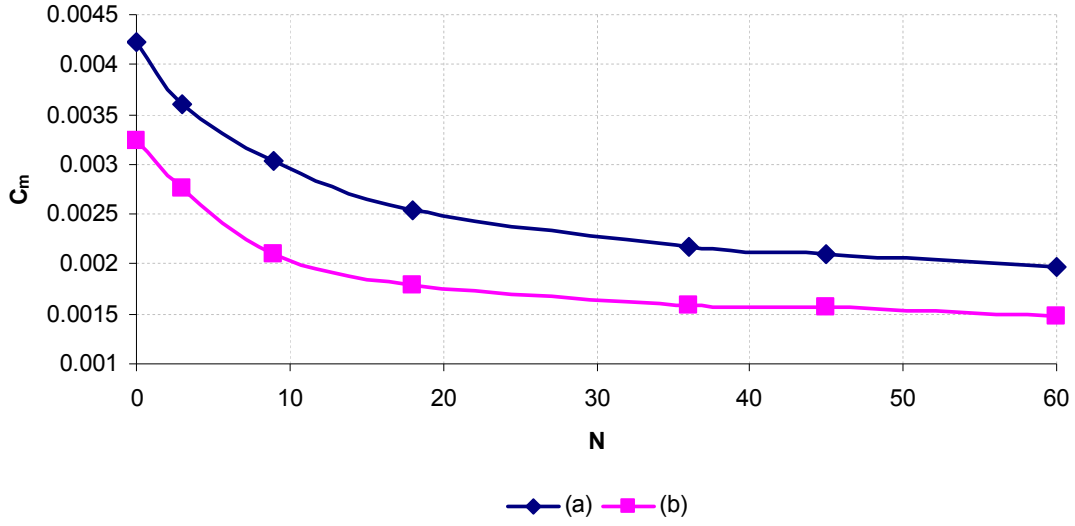

Figure 6.32: Variations of Moment Coefficient Produced by the Rotor with Different Number of Mounted Bolts, $D = 16$ mm; (a) $Re_\phi = 0.67 \times 10^7$, $C_w = 10^5$ ($\lambda_T = 0.35$) and (b) $Re_\phi = 0.72 \times 10^7$, $C_w = 0.3 \times 10^5$ ($\lambda_T = 0.09$)

As can be observed in Figure 6.31, the amount of the moment coefficient produced by the rotor in the plain disc system is considerably higher than that for the protruded disc system. The reason for this difference could be attributed to the shear stress that the fluid exerts on the disc by viscous friction. As mentioned above, the presence of bolts in the system speeds up the tangential velocity of the core. This reduces the shear stress and, as a result, the viscous friction and consequently the viscous moment. In addition, it should be noted that part of the disc is covered by the bolts in the protruded rotor-stator system. This results in a further reduction of the moment coefficient produced by the rotor. Therefore, it can be concluded that the amount of moment coefficient produced by the disc is significantly dependent on the presence and the number and size of the mounted bolts. However, because the amount of viscous moment coefficient produced by the rotor is noticeably less than the amount of moment coefficient produced by the bolts, it is expected that this non-equality does not have a significant effect on the amount of moment coefficient produced by the bolts using Equation 6.3. Nevertheless, it is necessary to make sure that this expectation is reasonable. Hence, Tables 6.12, 6.13 and 6.14 compare the results of the bolts' moment coefficient obtained by the CFD results with those obtained using Equation 6.3.

6.12:Table 6.33: Comparison of the Results of Bolts Moment Coefficient Obtained by the CFD Results with those Obtained Using Equation 6.3 for Different Number of Bolts, D = 16 mm; Reϕ = 0.67 x 107, Cw = 105 (λT = 0.35)

N	$C_{m,total\ bolts}$ calculated by FLUENT	$C_{m,total\ bolts}$ calculated by using Equation 6.3	Percentage of difference between the experimental assumption and CFD results
3	0.004745	0.004026508	15.14699
9	0.010593	0.009309746	12.11236
18	0.015044	0.013264936	11.82784
36	0.019101	0.017181307	10.04898
45	0.021558	0.019332955	10.3206
60	0.023122	0.020770146	10.17276

Table 6.13: Comparison of the Results of Bolts Moment Coefficient Obtained by the CFD Results with those Obtained Using Equation 6.3 for Different Number of Bolts, D =16 mm; Re_ϕ = 0.72 x 10^7, C_w =0.3 x10^5 (λ_T= 0.09)

N	$C_{m,total\ bolts}$ calculated by FLUENT	$C_{m,total\ bolts}$ calculated by using Equation 6.3	Percentage of difference between the experimental assumption and CFD results
3	0.0026	0.00223	14.3899
9	0.005	0.00401	20.369
18	0.0068	0.0055	19.66
36	0.0082	0.0066	18.92
45	0.0091	0.0075	17.0898
60	0.0087	0.00706	18.877

Table 6.14: Comparison of the Results of Bolts Moment Coefficient Obtained by the CFD Results with those Obtained Using Equation 6.3 for Different Flow Conditions, N =18, D = 16 mm

ω (rad/s)	Re_ϕ ($/10^7$)	C_w ($/10^5$)	$C_{m,total\ bolts}$ calculated by FLUENT	$C_{m,total\ bolts}$ calculated by using Equation 6.3	Percentage of difference between the experimental assumption and CFD results
264.5	0.177	0.311	0.01856	0.01693	8.81
411	0.272	0.307	0.01397	0.01249	10.56
902.5	0.716	0.268	0.00685	0.00551	19.59
1060.1	0.933	0.242	0.00537	0.00459	14.67
211.9	0.362	1.022	0.02304	0.02115	8.19
409.5	0.668	1.017	0.01506	0.01328	11.81
618.8	0.999	0.994	0.01107	0.00991	10.47
889.5	1.323	0.963	0.00876	0.00826	5.74

Based on the results given in Tables 6.12 and 6.13, on average the calculated bolt moment coefficient using the two methods has about 11% difference for $Re_\phi = 0.67 \times 10^7$, $C_w = 10^5$ ($\lambda_T = 0.35$), and about 18% difference for $Re_\phi = 0.72 \times 10^7$, $C_w = 0.3 \times 10^5$ ($\lambda_T = 0.09$). Considering the data presented in Table 6.14, the percentage of difference between the two results was about 13% for $C_w = 0.3 \times 10^5$ and about 9% for $C_w = 10^5$. Therefore, it appears that the reported differences should be considered when the assumption of equal rotor moment coefficient for the system with bolts and the system without bolts is applied. It should also be noted that the non-validity of this assumption increases when decreasing λ_T.

6.6 Summary

The effects of changing the number and diameter of bolts on the moment coefficient and flow structure have been investigated in this chapter for one typical rotationally dominated condition and one typical throughflow dominated condition. It was found that for both of the flow conditions the downstream bolt is immersed in the wake region of the upstream bolt for $N > 18$. Also, for $N > 18$ the wake falls on the upper section of the bolt.

Increasing the number of bolts was found to move the separation point towards the leading edge of the bolt. In addition, for both of the flow conditions and for N > 18 a separation bubble was observed over the top surface of the bolt, the length of which increases with an increasing number of bolts. Furthermore, increasing the number of bolts creates an increase in the total moment coefficient. However, a limit was found after which further increases in N do not bring about increases in C_m. There also appears to be very little difference between the values of C_m obtained for a plain disc and those for a continuous ring. In addition, increasing the number of bolts causes a reduction of the pressure drag coefficient and, as a consequence, the total drag coefficient of an individual bolt.

Increasing the diameter of bolts causes an earlier flow separation, which leads to an increase in the area of the wake region. In addition, increasing the diameter of the bolts consistently increases the moment and drag coefficients for the rotationally dominated

condition. However, although the moment coefficient of the bolts increases with increasing D for the throughflow dominated case, a reducing trend was evident for the variations of the bolts' drag coefficient.

It was also found that both the drag and moment coefficients of the bolts with equal values of X_b (the ratio of the bolts' pitch arc length to the bolts' diameter) are approximately equal at almost the whole range of X_b apart from at its lower values. In addition, it was found that increasing the number and diameter of the bolts had no influence on the production of Taylor columns.

The validity of the assumption used during experimental measurements that an equal amount of rotor moment exists for cavities with protrusions and those without protrusion was also investigated in this chapter. It was found that this assumption is subject to noticeable differences in the calculated moment coefficient of the total bolts, and the non-validity of this assumption increases by decreasing λ_T.

7. Conclusions and recommendations for future work

7.1 Introduction

This thesis has aimed to understand the fluid flow in a protruded rotor-stator cavity with superimposed radial outflow using CFD simulations. Extending the theoretical and experimental investigations, this thesis has focused on different parameter variations in the range of interference of the bolts as well as the loss coefficients of hexagonal bolts mounted on the rotor. The effects of changing the flow conditions as well as the number and diameter of the hexagonal bolts have also been examined. In this light, three research questions were posed. In the following paragraphs, the research questions are first recalled and then answered accordingly.

1- *What are the effects of adding protrusions in a rotor-stator cavity in terms of flow structure and flow parameter distributions such as velocity and pressure? How do these parameters vary around protrusions for different flow conditions? Do Taylor columns occur on top of a bolt and extend across the axial width of the cavity from rotor to stator?*

Chapter 5 clarified the effects of adding protrusions in the rotor-stator cavity, both in terms of different parameter variations and loss coefficients. Comparing the relevant plain disc cases, it was found that protrusions do not affect the flow structure in the rotor-mounted bolt system at lower radial locations. However, almost all of the flow aspects are considerably affected by the presence of bolts at higher radial locations close to the bolts. These effects are more noticeable for the rotationally dominated flow conditions where the tangential velocity of the core is increased. The presence of bolts for the rotationally dominated flow condition reduces the rotor boundary layer thickness and increases the radial and axial pressure gradients at higher radial locations.

The analysis of flow structure and different parameter variations in the vicinity of the bolts revealed that the flow structure around the bolts is governed by the angle of attack and the free-stream Reynolds number of the flow approaching the bolts. In addition, local values of these two parameters affect the local variations of flow structure in terms

of the location of the separation point and the area of the wake region as well as the velocity and pressure distributions around the bolt.

It was found that while the free-stream Reynolds number did not vary noticeably from the root to the tip of the bolt for almost all of the simulated flow conditions, the angle of attack had noticeable variations along the axial direction. However, the rate of reduction of the angle of attack along the axial direction reduces when decreasing the turbulent flow parameter. In addition, it was found that the angular distributions of different flow parameters are a function of axial and radial locations. Accordingly, it was found that for higher values of λ_T the location of the separation point has minor variations when moving from the root to the tip of the bolt. This showed to be contrary for lower values of λ_T, at which both the angle of attack and the area of the wake region noticeably reduce when moving from the root towards the tip of the bolt. Regarding the radial variations of flow parameters around the bolts, it was observed that the area of the wake region increases when moving from the bottom to the middle section of the bolt, and then decreases when moving from the middle section towards the top of the bolt. This was attributed to the reduction of the free-stream Reynolds number and the increase of the angle of attack of the flow approaching the bolt when moving from the bottom to the middle section of the bolt, which is followed by an increase of the free-stream Reynolds number and a reduction of the angle of attack from that location towards the top of the bolt.

Based on the simulation results, for a constant value of throughflow rate, increasing Re_ϕ increases the free-stream Reynolds number and reduces the angle of attack of the flow approaching the bolt, causing a delayed separation on the surface of the bolt that reduces the area of the wake region. In addition, increasing the rotational Reynolds number increases the static and relative total pressure differences between the upper and lower surfaces of the bolt.

For a constant value of Re_ϕ, increasing C_w increases the angle of attack and the free-stream Reynolds number of the flow hitting the bolt, which delays the separation and reduces the area of the wake region. In addition, it was found that the flow regime in the boundary layer over the bolt changes from laminar to turbulent for higher rotational Reynolds numbers ($Re_\phi \geq 0.67 \times 10^7$) of the flow conditions with $C_w = 10^5$. However, it

appears that the flow remains in the laminar regime for lower throughflow Reynolds numbers ($C_w = 0.3 \times 10^5$), even when increasing the rotational Reynolds number up to $Re_\phi = 0.716 \times 10^7$, and then becomes transient for higher values of Re_ϕ. Laminar to turbulent transition of the boundary layer over the bolt occurs approximately in the range of $2 \times 10^5 < Re_D < 4.5 \times 10^5$ for a circular cylinder. However, the transition of the boundary layer above the bolt from laminar to turbulent occurs earlier and in the range of Re_D between 1×10^5 and 2×10^5.

In addition, the increased level of turbulence in the turbulent boundary layer over the upper surface of the bolt reattaches the flow, causing a separation bubble for the rotational Reynolds number of $Re_\phi = 0.67 \times 10^7$. The separation bubble is followed by a second separation of flow, which forms the wake region behind the bolt. However, for higher values of rotational Reynolds numbers ($Re_\phi \geq 0.999 \times 10^7$) due to the increased extent of turbulence the separation point is moved toward the trailing edge of the bolt and, as a result, no separation bubble is formed over the bolt.

It was found that for a constant amount of Re_ϕ, increasing C_w reduces the static and relative total pressure differences between the upper and lower surfaces of the bolt.

It was also found that decreasing the throughflow rate causes the wakes to become more circumferential in their paths around the bolt. Furthermore, a decrease in λ_T causes an increase in the wake shed from the trailing edge of one bolt to the leading edge of the next, which reduces the area of the wake region.

In addition, it was found that the boundary layer thickness of the rotor in the vicinity of the bolts is a function of both angular and radial locations. While the rotor boundary layer thickness is reduced when increasing the radial location around the bolt, it does not follow a regular pattern along the angular direction. Additionally, it was found that for a specific value of C_w, increasing Re_ϕ reduces the boundary layer thickness of the rotor. In addition, increasing C_w increases the boundary layer thickness of the rotor.

Regarding the production of Taylor columns, it was found that, contrary to the findings of Farthing (1988) for a rotating cavity with mounted bolts, Taylor columns cannot be produced in this specific configuration of a rotor-stator system with rotor-mounted bolts

for all numbers of bolts mounted on the rotor and under all of the simulated flow conditions.

2- *What are the effects of adding protrusions in a rotor-stator cavity in terms of losses? How does the drag coefficient of the protrusions vary with Reynolds numbers? Does the drag from the bolts have substantially different behaviour in regimes where it is expected to be notionally laminar or notionally turbulent?*

Based on the simulation results, as expected, adding protrusions considerably increases the total moment coefficient of the rotor-stator system. Although the moment coefficient produced by the rotor was reduced when protrusions were added to the system (due to the increased value of the core tangential velocity and the reduction of the relative velocity between the rotor and the core), this reduction was dominated by the moment coefficient produced by the bolts. Similar to the investigations carried out by Zimmerman *et al*. (1986), three elements were considered to contribute into the bolts' moment and drag coefficients, including the pressure losses produced by the wakes, the pressure losses produced by the pressure difference around the bolts (pumping losses), and the viscous losses. Examination of the results shown in Chapter 5 revealed that the pressure loss coefficient (pumping losses and form drag losses) contributes the highest part of the total moment coefficient and is responsible for the significant increases in the moment coefficient of the rotor-mounted bolts system in comparison to the plain disc system.

Variations of the flow conditions in the rotor-stator cavity with rotor-mounted bolts affect the loss coefficients noticeably. It was found that for a constant C_w increasing Re_ϕ reduces the pressure drag produced by the wakes (due to the reduced area of the wake region), increases the pressure drag produced by the pumping losses (due to the increase in both the static and relative total pressure differences between the upper and lower surfaces of the bolts), and increases the viscous drag (due to the increase in the shear stress and the frictional force between the fluid and the bolt). Based on the simulation results, the overall effect of increasing Re_ϕ is an increase in the total drag force of the bolt. However, since the relative total velocity magnitude also noticeably increases when increasing Re_ϕ, the drag coefficient decreases when increasing the disc's rotational speed.

The overall effect of increasing C_w is a noticeable reduction in the total drag coefficient. This was attributed to the boundary layer transition from laminar to turbulent which delays separation and results in a sudden decrease in the drag coefficient.

Investigations were also carried out in order to find out whether any equivalency could be considered between the moment coefficient of individual bolts and their drag coefficient. According to the results demonstrated in Chapter 5, since the angles of attack of the flow hitting the bolts were noticeably larger than zero, the forces that produce the moment of the bolts are not the same as the forces producing the drag. Hence, considering the moment and drag coefficients of the bolts to be equivalent is not reasonable.

The validity of the assumption used during experimental measurements assuming an equal amount of rotor moment for cavities with protrusions and those without protrusion was investigated in Chapter 6. It was found that the amount of moment coefficient produced by the disc is significantly dependent on the presence and also the number and size of mounted bolts. Although the moment coefficient produced by the bolts is significantly higher than that produced by the rotor, and it is expected that the error in calculating the rotor moment coefficient using the assumption does not have a significant effect on the amount of moment coefficient produced by the bolts, the simulation results showed that there are considerable differences between the bolts' moment coefficient obtained using the assumption and that obtained by the simulations. Additionally, the non-validity of this assumption increases when decreasing λ_T.

3- *To what extent do different numbers and sizes of protrusions affect the flow structure and the amount of losses in the cavity?*

Chapter 6 clarified this question. The effects of changing the number and diameter of the bolts were investigated for two typical flow conditions: one representing a throughflow dominated regime and the other representing a rotationally dominated one. Based on the flow analysis results for both of the simulated flow conditions, the flow between two neighbouring bolts could be described by two regimes. For $N \leq 18$ ($X_b \geq 4.36$), the presence of a downstream bolt does not noticeably affect the wake of the upstream bolt. However, for $N > 18$ ($X_b < 4.36$) the wake of the upstream bolt either impinges or envelops the downstream bolt. The extent of the wake interference is

increased with increasing the number of bolts, so that for $N > 45$ the downstream bolt is completely immersed in the wake of the upstream bolt. In addition, it was found that increasing the number of bolts pushes the wakes towards the upper section of the bolts.

The wake interference of two neighbouring bolts significantly affects different parameter distributions around the bolts. Increasing the number of bolts beyond N = 18 noticeably increases the static pressure difference between the upper and lower surfaces of the bolt, so that for $N \geq 45$ the pressure coefficient of the upper section of the bolt can reach positive values. However, it was found that the relative total pressure difference between the upper and lower sides of the bolt reduces when increasing N. The rate of this reduction was higher for the rotationally dominated flow condition. In addition, it was found that the relative total pressure of the leading edge of the bolt approaches approximately that of the trailing edge of the bolt by increasing the number of bolts. Investigations were also carried out in order to examine the variations of the free-stream Reynolds number and the angle of attack of the flow approaching the bolt for different numbers of bolts attached to the rotor. Based on the results presented in Chapter 6, increasing the number of bolts increases the angle of attack of the flow approaching the bolt. However, the reducing trend of Re_D with the number of bolts is slightly lower than that observed for the angle of attack. The trend of the increase for both of the parameters slows down for $N > 36$. Moreover, increasing N increases the tangential velocity of the fluid approaching the bolt as well as the core tangential velocity, and decreases the relative tangential velocity between the rotor and the core.

Increasing the number of bolts ends up with a forward movement of the separation points, particularly at the upper side of the bolt. It is interesting to note that for both of the flow conditions, increasing the number of bolts beyond $N = 18$ makes the separated shear layer reattach to the upper surface of the bolt and separate again at a distance downstream. Hence, for $N > 18$ a separation bubble is formed over the top surface of the bolt, the length of which increases with an increasing number of bolts.

The thickness of the boundary layer attached to the rotor in the vicinity of the bolts was also investigated for different numbers of mounted bolts. It was found that increasing the number of bolts reduces the thickness of the boundary layer attached to the rotor.

There appears to be very little difference between the values of C_m obtained for a plain disc with those obtained for a continuous ring. Increasing the number of bolts creates an increase in the moment coefficient of the total system. However, this reaches a limit where further increases in N do not bring about an increase in C_m. This can be explained by examining the separate contributions that skin friction and pressure-related drag make to the overall moment coefficient. The skin friction actually reduces as the number of bolts is increased. This is because increasing N causes the tangential velocity of the core to increase, which decreases the relative rotor-to-core velocity. The pressure-related drag (it was not possible to distinguish between form drag and pumping loss in this study) is also affected by increasing N. The more bolts attached, the more the wake of the leading bolt affects that of the bolt immediately behind. As a result, the viscous, pressure and total drag for each individual bolt is reduced, but as there are more bolts, the overall drag increases. The direction of the wake shed by one bolt and therefore its influence on another bolt is also found to be affected by λ_T. Decreasing the throughflow rate (or decreasing λ_T) pushes the wakes toward the rear section of the bolt and increases their interference with the flow field of the neighbouring bolt.

Analysis of the flow around bolts with different diameters revealed that increasing the diameter of the bolts causes an earlier flow separation, which leads to an increase in the area of the wake region. This was attributed to the increase of both the angle of attack and the free-stream Reynolds number of the flow approaching the bolt. Inspection of pressure coefficient distributions around the bolts also revealed that the static pressure difference between the upper and lower sides of the bolt increases when increasing the diameter of the bolts.

The thickness of the rotor boundary layer in the vicinity of the bolts was also investigated for the three diameters simulated. Accordingly, it was found that the boundary layer thickness of the rotor is at its lowest for D = 16mm.

As mentioned by Schlichting and Gersten (1999), the relative contribution of viscous and pressure drags depends on the thickness of the body. For small thicknesses of the body, viscous drag has the major contribution to the total drag. However, as the thickness of the body increases, viscous drag decreases and for blunt bodies like

cylinders it is dominated significantly by pressure drags. The same observations were obtained from the simulation results of the bolts with different diameters.

On the basis of the results presented in Chapter 6, increasing the diameter of the bolts consistently increases the moment and drag coefficients for the rotationally dominated flow condition. However, although the moment coefficient of the bolts increases with increasing D for the throughflow dominated case, a reducing trend was evident for the variations of the bolts' drag coefficient. The reason was attributed to the flow regimes in the boundary layer over the bolt. It was found that a laminar boundary layer formed above the bolts for all three simulated diameters and the rotationally dominated condition. However, for the throughflow dominated case, the flow was in the transitional regime for D = 13mm and 10mm, and was moved to the fully turbulent regime for D = 16mm.

The loss coefficients of the bolts were also investigated in Chapter 6 by making the bolts non-dimensional. Accordingly, further simulations were carried out for D = 10mm and D = 13mm with different numbers of bolts ranging from 0 (plain disc system) to the maximum possible number of bolts that can circumferentially be placed on the rotor at r/b = 0.9.

It was found that the moment and drag coefficients of the bolts with equal values of X_b were approximately equal in almost the whole range of X_b apart from at its lower values. The reason for the observed discrepancy for the lower values of X_b was attributed to the fact that for specific low values of X_b the difference between the number of bolts mounted on the rotor for each of the simulated diameters becomes larger. In addition, apart from the lower values of X_b ($X_b < 4$), a good overall agreement was observed between the simulation results and the results obtained using Miles *et al.*'s correlation (2007).

7.2 Recommendations for future work

While the standard k-ε model with the enhanced wall treatment shows acceptable predictions for the flow structure as well as loss coefficients in the protruded rotor-stator

cavity, other complex methods of turbulence modeling such as DNS, and LES (see Appendix 2) may consolidate this thesis findings. Since, the mentioned models are expensive both in terms of CPU memory and time particularly for large number of simulations, they were not used in this study.

In addition, all of the simulations in this thesis were implemented with the assumption of the steady state condition of the flow within the cavity. According to the findings of this thesis, when the number of bolts is increased beyond N > 18 the flow around the bolts is subjected to a substantial degree of unsteadiness. This is because of the impinging wakes of the upstream bolt. Hence, unsteady simulations can be implemented in order to check the validity of the simulation results under steady and unsteady circumstances.

Furthermore, based on the findings of this thesis laminar to turbulent transition may occur in the boundary layer over the bolts. Hence, mechanisms of the laminar to turbulent transition of the boundary layer above the bolt should be examined. It is also interesting to investigate the location of the laminar to turbulent transition of the boundary layer above the bolt in order to find possible relations with the locations of the separation and reattachment points. The complementary studies can also investigate heat transfer effects and temperature distribution around the bolts.

During simulations, the radial location of the mounted bolts on the rotor was constant and close to the cavity outlet. Therefore, further investigations could be carried out in order to examine how the fluid flow is affected by changing the radial locations of the mounted bolts. Further investigations could also be carried out in order to understand the fluid flow phenomena in a cavity with bolts attached both on rotor and stator.

The shape of protrusions could also be changed. Miles (2011) carried out experimental measurements using bi-hexagonal bolts attached to rotor which are common protrusions used in internal structures of gas turbine engines. She found that the use of bi-hexagonal bolts reduces the overall drag and windage heating in the cavity. However, it is also interesting to investigate other shapes of protrusions like cylindrical or staged protrusions.

References

Batchelor, G.K., 1951.

Notes on a Class of Solutions to the Navier-Stokes Equations Representing Steady Rotationally-Symmetric Flow.

Quarterly Journal of Mechanics and Applied Math. Vol. 4, pp. 29-41.

Bayley, F.J., Conway, L., 1964.

Fluid Friction and Leakage Between a Stationary and Rotating Disc.

Journal of Mechanical Engineering Science, Vol. 6, pp. 164-172.

Bayley, F.J., Owen, J.M., 1969,

Flow Between a Rotating and a Stationary Disc.

Aeronautical Quarterly, Vol. 20, pp.333-354.

Bayley, F.J., Owen, J.M., 1970.

The Fluid Dynamics of a Shrouded Disc System with a Radial Outflow of Coolant.

Trans. ASME, Journal of Engineering for Power, Vol. 92, pp.335-341.

Bodewadt, U.T., 1940.

Die Drehströmug über Festem Grunde.

ZAMM- Journal of Applied Mathematics and Mechanics, Vol. 20, pp. 241-253.

Chew, J.W., 1984.

Prediction of Flow in Rotating Disc Systems Using the k-ε Turbulence Model.

ASME Paper No. 84-GT-229.

Chew, J.W., Vaughan, C.M., 1988.

Numerical Predictions for the Flow Induced by an Enclosed Rotating Disc.

ASME conference paper, 88-GT-127.

Chew, J.W., Hills, N.J., 2007.

Computational Fluid Dynamics for Turbomachinery Internal Air Systems.

Philosophical transactions of the Royal Societty (series A), Aerospace CFD Theme Issue.

Childs, P. R. N., 2007.

Flow in Rotating Components – Discs, Cylinders and Cavities.

ESDU Fluid Mechanics, Internal Flow Series, Vol. 4c.

Chou, P.Y., 1945.

On the velocity correlations and the solution of the equations of turbulent fluctuation.

Quart. Appl., Math., Vol. 3, p. 38.

Cochran, W.G., 1934.

The Flow due to a Rotating Disc.

Proceedings Cambridge Philosophical Society, Vol. 30, pp.365-375.

Coren, D., 2007.

Windage due to Protrusions in Rotor-Stator Systems.

Thermo-Fluid Mechanics Research Centre, University of Sussex, D.Phil. Thesis.

Daily, J.W., Nece, R.E., 1960.

Chamber Dimension Effects on Induced Flow and Frictional Resistance of Enclosed Rotating Discs.

Trans. ASME, Journal of Basic Engineering, Vol. 82, pp. 217–232.

Daily, J.W., Ernst, W.D., Asbedian, V.V., 1964.

Enclosed Rotating Discs with Superposed Throughflow.

MIT Department of Civil Engineering, Hydrodynamics Laboratory Report No. 64.

Davidov, B.I., 1961.

On the statistical dynamics of an incompressible fluid.

Doklady Akademia Nauk SSSR, Vol. 136, p. 47.

Dibelius, G., Radtke, F., Ziemann, M., 1984.

Experiments on Friction, Velocity and Pressure Distribution of Rotating Discs.

Heat and mass transfer in rotating machinery (A86-24451 09-34), Washington DC, Hemisphere Publishing Corp., pp. 117-130.

Dorfman, L.A., 1963.

Hydrodynamic Resistance and Heat Loss of Rotating Solids.

Oliver and Boyd.

Elena, L. and Schiestel, R., 1996.

Turbulence Modelling of Rotating Confined Flows.

International Journal of Heat and Fluid Flow, Vol.17, pp. 283-289.

Fadai-Ghotbi, A., 2011.

Modelling and control of separation bubbles in transitional turbomachinery flows.

9th European Conference on Turbomachinery Fluid Dynamics and Thermodynamics, Turkey.

Farthing, P.R, 1988.

The Effect of Geometry on Flow and Heat Transfer in a Rotating Cavity.

D.Phil Thesis, University of Sussex, UK.

Fluent 6.1 User's Guide, 2003.

Gartner, W., 1987.

Analysis of Windage Losses and Velocity Distribution for a Shrouded Rotating Disc.

ASME Conference Paper, 97-GT-204.

Gartner, W. 1997.

A Prediction Method for the Frictional Torque of a Rotating Disc in a Stationary Housing with a Superimposed Radial Outflow.

ASME Conference Paper, 97-GT-204.

Gartner, W., 1998.

A Momentum Integral Method to Predict the Frictional Torque of a Rotating Disc with Protruding Bolts.

ASME Conference Paper, 98-GT-138.

Goldstein, S., 1935.

On the Resistance to the Rotation of a Disc Immersed in a Fluid.

Proceedings of Cambridge Philosophic Society, Vol.31, Pt.2, pp. 232-241.

Gosman, A.D., Ideriah, F.J.K., 1976.

TEACH-T: A General Computer Program for Two-Dimensional, Turbulent Recirculating Flows.

Department of Mechanical Engineering, Imperial College, University of London.

Gosman, A.D., Spalding, D.B., 1970.

Computation of Laminar Flow Between Shrouded Rotating Discs.

Department of Mechanical Engineering, Imperial College, University of London, Report No. EF.TN/A/30.

Graber, D.J., Daniels, W.A., Johnson, B.V., 1987.

Disc Pumping Test.

United Technologies Corporation Report, AFWAL-TR-87-2050.

Harlow, F.H.. and Nakayama, P.I., 1968.

Transport of turbulence energy decay rate.

Los Alamos Sci. Lab., University of California Report LA-3854.

Iacovides, H., Launder, B.E., 1995.

Computational Fluid Dynamics Applied to Internal Gas-Turbine Blade Cooling: a Review.

International Journal of Heat and Fluid Flow, Vol.16, pp.454–470.

Iacovides, H. and Toumpanakis, P.,1993.

Turbulence Modelling of Flow in Axisymmetric Rotor-Stator Systems.

In 5th international symposium on Refined Flow Modelling and Turbulence Measurements, Paris.

Jones, D.A., Clarke, D.B., 2005.

Simulation of a Wing-Body Junction Experiment Using the FLUENT Code.

DSTO-TR-1731.

Kilic, M., Gan, X., Owen, J.M., 1994.

Turbulent Flow Between Two Discs Contra-Rotating at Different Speeds.

ASME Conference paper, 94-GT-54.

Kolmogorov, A.N., 1942.

Equations of turbulent motion of an incompressible fluid.

Izvestia Academy of Scienses, USSR; Physics, Vol. 6, Nos. 1 and 2, p.56.

Lance, G.N. and Rogers, M.H., 1960.

The Rotationally Symmetric Flow of a Viscous Fluid in the Presence of an Infinite Rotating Disc.

Journal of Fluid Mechanics, Vol.7, pp. 617-631.

Launder, B.E., and Spalding, D.B., 1974.

The Numerical Computation of Turbulent Flow.

Computer Methods in Applied Mechanics and Engineering, 3, pp. 269–289.

Launder, B.E., and Sharma, B.I., 1974.

Application of the Energy-Dissipation Model of Turbulence to the Calculation of Flow Near a Spinning Disc.

Letters in Heat and Mass Transfer, 1, pp. 131–138.

Lee, C. W., Palma, P. C., Simmons, K. and Pickering, S. J., 2004.

Comparison of CFD and PIV Data for the Air Flow in an Aero-Engine Bearing Chamber.

In Proc. ASME Turbo Expo. Paper GT2004-53281.

Lien1, F. S., Kalitzin, G. and Durbin, P. A., 1998.

RANS Modeling for compressible and Transitional Flows.

In Proceedings of the Center for Turbulence Research, University of Waterloo, Canada.

Menter, F.R., 1994.

Two-Equation Eddy-Viscosity Turbulence Models for Engineering Applications.

AIAA Journal, Vol. 32, Issue 8, pp.1598–1605.

Mellor, G.L., Chapple, P.J., and Stokes, V.K., 1968.

On the Flow Between a Rotating and a Stationary Disc.

Journal of Fluid Mechanics, 31-1, 95.

Menter, F.R., 1993.

Zonal Two-equation $k-\omega$ Turbulence Model for Aerodynamic Flows.

AIAA Journal, pp. 1993-2906

Menter, F.R., 1994.

Two-Equation Eddy-Viscosity Turbulence Models for Engineering Applications.

AIAA Journal, Vol. 32, Issue 8, pp.1598–1605.

Menter, F.R. , Kuntz, M. , Langtry, R. , 2003.

Ten Years of Industrial Experience with the SST Turbulence Model.

Turbulence Heat and Mass Transfer, V. 4. pp 625–632.

Menter, F.R. , Smirnov, P.E. , 2009.

Sensitization of the SST Turbulence Model to Rotation and Curvature by Applying the Spalart-Shur Correction Term,

Journal of Turbomachinary, V.131.

Millward, J. A. and Edwards, M. F., 1994.

Windage Heating of Air Passing Through Labyrinth Seals.

ASME international gas turbine & aero engine conference paper, 94-GT-56.

Millward, J.A., Robinson, P.H., 1989.

Experimental Investigation into the Effects of Rotating and Static Bolts on Both Windage Heating and local Heat Transfer Coefficients in a Rotor-Stator Cavity.

ASME Conference Paper, 89-GT-196.

Mohammadi, B. and Pironneau, O., 1994.

Analysis of the K-epsilon Turbulence Model.

Paris: MASSON, USA: John Wiley & Sons.

Nydahl, J.E., 1971.

Heat Transfer for the Bodewadt Problem.

Colorado State University Dissertation, Fort Collins, Colorado, USA.

Owen, J.M., Haynes, C.M., Bayley, F.J., 1974.

Heat Transfer from an Air Cooled Rotating Disc.

Proc.R.Soc.Lond.A., Vol.336, pp.453-473.

Owen, J.M., 1988.

An Approximate Solution for the Flow Between a Rotating and a Stationary Disc.

ASME Paper 88-GT-293.

Owen, J.M., Rogers, R.H., 1989.

Flow and Heat Transfer in Rotating-Disc Systems.

Vol. 1: Rotor-Stator Systems, Research Studies Press, USA: Wiley Inc.

Owen, J.M., Rogers, R.H., 1995.

Flow and Heat Transfer in Rotating-Disc Systems.

Vol. 2: Rotating Cavities. UK: Research Studies Press, USA: Wiley Inc.

Pao, H., 1970.

A Numerical Computation of a Confined Rotating Flow.

J. of Applied Mechanics, TRANS ASME, 37, 480

Patankar, S.V., and Spalding, D.B., 1972.

A Calculation Procedure for Heat, Mass and Momentum Transfer in Three-Dimensional Parabolic Flow.

International Journal of Heat and Mass Transfer, 15, 1787.

Randriamampianina, A., Elena, L., Fontaine, J.P., Schiestel, R., 1997.

Numerical prediction of laminar, transitional and turbulent flows in shrouded rotor–stator systems.

Phys. Fluids Vol.9–Issue. 6, pp.1696–1713.

Rodi, W. 1980.

Turbulence models and their application in hydraulics.

Delft, The Netherlands: International Association for Hydraulic Research.

Rodi, W., Bonnin, J.C., Buchal, T., and Laurence, D., 1998.

Testing of Calculation Methods for Turbulent Flows.

Workshop results for 5 test cases", Electricite' de France Report 98NB00004

Romero-Hernandez, S., Etemad, M.R.E., Pullen, K.R., 2001.

Numerical determination of windage losses on high-speed rotating discs.

Computational fluid dynamics in practice, Bury St Edmunds, Professional Engineering Publishing, pp.91-98.

Schlichting, H., Gersten, K., 1999.

Boundary Layer Theory.

8th edition, McGraw Hill.

Schultz-Grunow, F. 1935.

The Frictional Resistance of Rotating Discs in Housings.

ZAMM- Journal of Applied Mathematics and Mechanics, Vol.15, Pt. 4, pp.191–204.

Shih,T.H., Liou, W.W., Shabbir, A., Yang, Z., and Zhu, J., 1995.

A New k-ε Eddy-Viscosity Model for High Reynolds Number Turbulent Flows - Model Development and Validation.

Computers Fluids, 24(3):227–238.

Spalart, P.R , and Allmaras, S.R. , 1992.

A One Equation Turbulence Model for Aeorodynamic Flows.

AIAA paper 92, pp. 439

Spalart, P.R. and Shur. M. , 1997.

On the Sensitization of Turbulence Models to Rotation and Curvature.

Aerosp. Sci. Technology, 1(5), pp.297-302.

Spalart, P.R , and Allmaras, S.R., 1992.

A One Equation Turbulence Model for Aeorodynamic Flows.

AIAA Journal paper, V.92, pp. 439

Sparrow, E.M., Goldstein, J.L., 1976.

Effect of Rotation and Coolant Throughflow on the Heat Transfer and Temperature Field in an Enclosure.

J. Heat Transfer, 98, pp. 387-394

Stewartson, K., 1953.

On the Flow Between Two Rotating Coaxial Discs.

Proceedings of the Cambridge Philosophical Society,Proc. Camb. Phil. Soc. Vol.49, pp. 333-341.

Tani, I., 1964,

Low-Speed Flows Involving Bubble Separations,

Progress in Aerospace Sciences, Vol. 5, pp. 70–103.

Taniguchi, S., Sakamoto, H. and Arie, M., 1981.

Flow around Circular Cylinders of Finite Height Placed Vertically in Turbulent

Boundary Layers.

Bulleting of the JSME, Vol. 24, No. 187.

Theodorson, T., Regier, A., 1944.

Experiments on Drag of Revolving Discs, Cylinders, and Streamline Rods at High Speed.

NACA- National Advisory Committee Aeronautics, Report No. 793.

Ton, F.K., Lin, C.A., 1994.

Predictions of Turbulent Flows Between a Rotating and a Stationary Disc.

In: Proceedings of Symposium on Turbulent Heat andMass Transfer, Lisbon, Portugal.

Vaughan, C.M., 1987.

A Numerical Investigation into the Effect of an External Flow Field on the Sealing of a Rotor-Stator Cavity.

Phd thesis, University of Sussex.

Virr, G. P., Chew, J. W. and Coupland, J., 1993.

Application of Computational Fluid Dynamics to Turbine Disc Cavities.

ASME Conference paper, 93-GT-89.

Von Karman, T., 1921.

Über laminare und turbulent reibung.

Zeitschrift für Angewandte Mathematik und Mechanik, Vol.1, pp. 233-252.

Wilcox, D.C., 2006.

Turbulence Modeling for CFD.

Third ed. DCW Industries.

White, F. M., 1998

Fluid Mechanics.

McGraw-Hill.

WU, X., JACOBS, R. G., HUNT, J. R. and DURBIN, P. A., 1999.

Simulation of Boundary Layer Transition Induced by Periodically Passing Wakes

Journal of Fluid Mechanics, vol. 398, pp. 109-153.

Yakhot, V. and Orszag, S.A., 1986.

Renormalization Group Analysis of Turbulence: I.Basic Theory.

Journal of Scientific Computing, 1(1):1–51.

Zdravkovich, M.M., 1977.

Review of Flow Interference Between Two Circular Cylinders in Various Arrangements.

ASME Journal of Fluids Engineering, Vol. 99, pp. 618–633.

Zdravkovich, M.M., 1987.

The Effects of Interference Between Circular Cylinders in Cross Flow.

Journal of Fluids and Structures, Vol. 1, Pt. 2, pp. 239–261.

Zdravkovich, M.M., 1997.

Flow around Circular Cylinders – Volume 1: Fundamentals.

Oxford University Press.

Zimmerman, H., Firsching, A., Dibelius, G.H., Ziemann, M., 1986.

Friction Losses and Flow Distribution for Rotating Discs with Shielded and Protruding Bolts.

ASME Conference Paper, 86-GT-158.

Appendix 1: CFD Procedure

In this research, the well-recognised CFD code, FLUENT, was used for modelling the flow. FLUENT numerically solves the governing differential equations of mass, momentum, energy and other equations such as turbulence and chemical species. FLUENT uses the finite volume method for integrating the governing differential equations over the total control volume. The resultant discretised equations are linearised and then iteratively solved to yield approximate values of variables, which are stored at the cell-centres.

Simulation in FLUENT primarily consists of three general steps: 1-Pre-processing; 2-Solver; 3-Post-processing.

In further detail, these steps include:

- **Pre-processing section:**

The first step of the simulation process in FLUENT is the pre-processing step, in which the flow domain is described and the physics of problem is identified. The geometry that was meshed is loaded into FLUENT and checked. Then the solver options (including pressure-based, density-based, unsteady, etc.), the physical models (including turbulence, multiphase, combustion, etc.) are set and the material properties are defined. Subsequently, the appropriate operating conditions and boundary conditions at each boundary zone are defined. The solution methods including the appropriate solution scheme and spatial discretisation are also selected.

In this research, the pressure-based solver with relative velocity formulation under the steady state condition was used for simulations. The difference between the two approaches of pressure-based and density-based solvers is in the way that the continuity, momentum, energy and species equations are solved. Since the density-based solver was defined for high-speed compressible flows, the pressure-based approach was

selected as the solver type in this research. In addition, the segregated algorithm (with SIMPLE type), in which the governing equations are solved sequentially, segregated from one another, was selected for the simulations. Moreover, since the flow is rotating in the flow domain, the relative velocity formulation was preferred.

Since the geometry is meshed with the triangular grids (in the r-ϕ plane) and as a result, the flow is not aligned with the grids, second-order discretisation was selected for obtaining more accurate results.

- **Solver section:**

The simulation starts with an initial solution and then iteratively continues to reach convergence. The convergence criteria are generally reached when the variables' residuals could be considered negligible and the overall property conservation is achieved within the system. During the solution process the residuals and the lift, drag, and moment coefficients can be monitored continuously in order to identify the convergence.

- **Post-processing section:**

In this section the results are analysed and the desired flow properties, including the forces, moments, velocities, flow pattern, etc., are extracted from the solution of the flow field.

Appendix 2: Turbulence Modelling

An overview of the turbulence models, particularly that provided by FLUENT, is given in this Appendix. Wilcox (2006) defined a turbulence model as "a mathematical model that approximates the physical behaviour of turbulent flows". He mentioned that "the function of turbulence modelling is to devise approximations for the unknown correlations in terms of flow properties that are known so that a sufficient number of equations exist. In making such approximations, we close the system".

Turbulent flows are described as velocity fields that have fluctuations in all scales and frequencies. Simulating both small scale and small frequency fluctuations is computationally very expensive. Therefore, a method should be provided that can eliminate the resolving of these fluctuations. There are two methods that can do this job: Reynolds averaging and filtering.

There is another method of modelling turbulent flows, which is called "direct numerical simulation" (DNS). In this method, the complete three-dimensional time-dependent Navier Stokes equations as well as the continuity equation are solved.

Reynolds averaging approach

The basis of the Reynolds averaging models is to convert the simultaneous variables in the Navier Stokes equations to time-averaged variables. The only difference between the time-averaged and the original Navier Stokes equations is the appearance of the term $\overline{u_i' u_j'}$. Equation A2.1 shows the general averaged Navier Stokes equation for incompressible fluids:

$$\rho \frac{\partial U_i}{\partial t} + \rho U_j \frac{\partial U_i}{\partial x_j} = -\frac{\partial p}{\partial x_i} + \frac{\partial}{\partial x_j}(2\mu S_{ji} - \rho \overline{u_i' u_j'}) \qquad \text{A2.1}$$

The above equation is the well-known Reynolds-averaged Navier Stokes equation (RANS), and the term $-\rho\overline{u_i'u_j'}$ is the Reynolds stress tensor. The Reynolds stress tensor is denoted by $\rho\tau_{ij}$, where τ_{ij} is the specific Reynolds stress tensor (Wilcox, 2006). In order to solve equation 3.13, a presentation for computing $\overline{u_i'u_j'}$ is needed.

$$\tau_{ij} = -\overline{u_i'u_j'} \qquad \text{A2.2}$$

There are different turbulence models that can compute the Reynolds stress tensor, such as the Spalart Allmaras, the k-ε and its variants, the k-ω and its variants, and the RSM. The first three models use an assumption called the Boussinesq eddy viscosity approximation in order to calculate the Reynolds stress tensor, while the latter model (the RSM) computes the $\overline{u_i'u_j'}$ terms without any pre-assumption.

A simple way to compute the Reynolds stress tensor is to use the Boussinesq eddy viscosity approximation, which defines the Reynolds stress terms as the product of an eddy viscosity (which is a flow property rather than a fluid property) and the mean strain-rate tensor. The limitation of the Boussinesq approximation is the assumption of isotropic eddy viscosity. In the isotropic assumption, the values of ν_T (turbulent eddy viscosity) are assumed to be the same for different $\overline{u_i'u_j'}$ terms. Therefore the effects of rotation, curvature and buoyancy forces will be neglected, and in order to be considered, they should be modelled separately.

There are different turbulence models that use the Boussinesq approximation. However, FLUENT only provides the Spalart Allmaras model, the k-ε models, and the k-ω models.

The Spalart Allmaras model

The Spalart Allmaras model is a one-equation turbulence model that was developed by Spalart and Allmaras (1992). This model solves only one additional transport equation representing the turbulent eddy viscosity. The defining equations of the model are as follows.

Kinematic eddy viscosity:

$$\nu_T = \tilde{\nu} f_{v1} \qquad \text{A2.3}$$

Eddy viscosity

$$\frac{\partial \tilde{\nu}}{\partial t} + U_j \frac{\partial \tilde{\nu}}{\partial x_j} = c_{b1} \tilde{S} \tilde{\nu} - c_{w1} f_w \left(\frac{\tilde{\nu}}{d} \right)^2 + \frac{1}{\sigma} \frac{\partial}{\partial x_k} \left[(\nu + \tilde{\nu}) \frac{\partial \tilde{\nu}}{\partial x_k} \right] + \frac{c_{b2}}{\sigma} \frac{\partial \tilde{\nu}}{\partial x_k} \frac{\partial \tilde{\nu}}{\partial x_k} \qquad \text{A2.4}$$

Closure coefficients and auxiliary relations

$$c_{b1} = 0.1355 \quad c2 = 0.622 \quad c_{v1} = 7.1 \quad \sigma = \frac{2}{3}$$

$$c_{w1} = \frac{c_{b1}}{\kappa^2} + \frac{(1 + c_{b2})}{\sigma} \qquad c_{w2} = 0.3 \qquad c_{w3} = 2 \qquad \kappa = 0.41$$

$$f_{v1} = \frac{\chi^3}{\chi^3 + {c_{v1}}^3} \qquad f_{v2} = 1 - \frac{\chi}{1 + f_{v1}\chi} \qquad f_w = g \left[\frac{1 + {c_{w3}}^6}{g^6 + {c_{w3}}^6} \right]^{\frac{1}{6}}$$

$$\chi = \frac{\tilde{\nu}}{\nu} \qquad g = r + c_{w2}(r^6 - r) \qquad r = \frac{\tilde{\nu}}{\tilde{S} \kappa^2 d^2}$$

$$\tilde{S} = S + \frac{\tilde{\nu}}{\kappa^2 d^2} f_{v2} \qquad S = \sqrt{2\Omega_{ij}\Omega_{ij}} \qquad \Omega_{ij} = \frac{1}{2}\left(\frac{\partial U_i}{\partial x_j} - \frac{\partial U_j}{\partial x_i} \right)$$

Spalart and Allmaras suggested their model for aerospace applications, but it has been used for many engineering applications, especially for wall-bounded flows. Furthermore, it has been widely used in turbomachinery applications.

FLUENT provides two versions of the Spalart Allmaras model: vorticity-based, which is the original model, and strain/vorticity based, which is a modified version and considers the effect of rotation and strain tensors in the definition of the production term. It should be noted that the Spalart Allmaras model was designed for wall-bounded

flows. Therefore, fine grids are needed near the walls to properly resolve the laminar-sub-layer region.

The k-ε model

The k-ε model is a two-equation models and has been widely used in industrial flow and heat transfer simulations. Two equation models provide two additional transport equations for calculating turbulent kinetic energy as well as equations for calculating the turbulent length scale or its equivalent (Wilcox, 2006). Therefore two equation models are complete. The first k-ε model is based on the efforts of Chou (1945), Davidov (1961), and Harlow and Nakayana (1968). FLUENT provides three versions of the k-ε model: the standard k-ε, the renormalization group (RNG) k-ε, and the realizable k-ε.

The standard k-ε model was introduced by Launder and Sharma (1974). It is a semi-empirical model that computes turbulent viscosity as a function of turbulent kinetic energy (k) and the turbulent dissipation rate (ε). The exact equations of turbulent viscosity are summarised by Wilcox (2006) as follows.

$$\nu_T = \frac{C_\mu k^2}{\varepsilon} \tag{A2.5}$$

Turbulence Kinetic Energy:

$$\frac{\partial k}{\partial t} + U_j \frac{\partial k}{\partial x_j} = \tau_{ij} \frac{\partial U_i}{\partial x_j} - \varepsilon + \frac{\partial}{\partial x_j}\left[\left(\nu + \frac{\nu_T}{\sigma_k}\right)\frac{\partial k}{\partial x_j}\right] \tag{A2.6}$$

Dissipation Rate:

$$\frac{\partial \varepsilon}{\partial t} + U_j \frac{\partial \varepsilon}{\partial x_j} = C_{\varepsilon 1} \frac{\varepsilon}{k} \tau_{ij} \frac{\partial U_i}{\partial x_j} - C_{\varepsilon 2} \frac{\varepsilon^2}{k} + \frac{\partial}{\partial x_j}\left[\left(\nu + \frac{\nu_T}{\sigma_\varepsilon}\right)\frac{\partial \varepsilon}{\partial x_j}\right] \tag{A2.7}$$

Closure Coefficients and Auxiliary Relations:

$$C_{\varepsilon 1} = 1.44, \quad C_{\varepsilon 2} = 1.92, \quad C_\mu = 0.09, \quad \sigma_k = 1.0, \quad \sigma_\varepsilon = 1.3$$

$$\omega = \frac{\varepsilon}{(C_\mu k)} \qquad \text{and} \qquad \ell = \frac{C_\mu k^{\frac{3}{2}}}{\varepsilon}$$

The second version of the k-ε model is the RNG model, which was developed by Yakhot and Orszag (1986). RNG stands for the renormalization group, and is a mathematical technique for solving instantaneous Navier Stokes equations. The equations of eddy viscosity, k, and ε are the same as the standard k-ε model, while a modified coefficient, $C_{\varepsilon 2}$ was defined for the RNG model. This model has the capability of modelling turbulence in rapidly strained and swirling flows. Furthermore, FLUENT provides two other options for the RNG model, which are the swirl modification, and the differential viscosity. The exact equations of turbulent viscosity are summarised by Wilcox (2006) as follows.

$$C_{\varepsilon 2} \equiv \tilde{C}_{\varepsilon 2} + \frac{C_\mu \lambda^3 (1 - \frac{\lambda}{\lambda_o})}{1 + \beta \lambda^3} \qquad , \qquad \lambda \equiv \frac{k}{\varepsilon} \sqrt{2 S_{ij} S_{ji}}$$

The closure coefficients for the RNG model are:

$$C_{\varepsilon 1} = 1.42 \quad , \quad \widetilde{C}_{\varepsilon 2} = 1.68 \quad , \quad C_\mu = 0.085 \quad , \quad \sigma_k = 0.72$$

$$\sigma_\varepsilon = 0.72 \quad , \quad \beta = 0.012 \quad , \quad \lambda_o = 4.38$$

The third version of the k-ε model is the realizable k-ε model, which was developed by Shih *et al*. (1995). This model was proposed to improve the ability of the standard k-ε model to predict complex turbulent flows. It suggests new equations for both the dissipation rate and the eddy viscosity. The new equations for ε are based on the dynamic equation for fluctuating vorticity, while the new equation for eddy viscosity contains the effect of mean rotation on turbulence stresses and ensures realizability, which are certain mathematical constraints on the Reynolds stresses in consistent with the physical behaviour of turbulent flow (Shih *et al.,* 1995). This model has been validated for various flows, including rotating homogenous shear flows, boundary-free shear flows, channel and flat boundary layer flows with and without pressure gradients,

and backward facing step flows (Shih *et al*.). The results of these validation cases show better flow predictions in comparison with the standard k-ε model (Shih *et al.,* 1995). The formulations of the realizable model are given bellow.

$$\frac{\partial}{\partial t}(\rho k)+\frac{\partial}{\partial x_j}(\rho k u_j)=\frac{\partial}{\partial x_j}\left[\left(\mu+\frac{\mu_t}{\sigma_k}\right)\frac{\partial k}{\partial x_j}\right]+G_k+G_b-\rho\varepsilon-Y_M+S_k$$

$$\frac{\partial}{\partial t}(\rho \varepsilon)+\frac{\partial}{\partial x_j}(\rho \varepsilon u_j)=\frac{\partial}{\partial x_j}\left[\left(\mu+\frac{\mu_t}{\sigma_\varepsilon}\right)\frac{\partial \varepsilon}{\partial x_j}\right]+\rho C_1 S\varepsilon-\rho C_2\frac{\varepsilon^2}{k+\sqrt{\nu\varepsilon}}+C_{1\varepsilon}\frac{\varepsilon}{k}C_{3\varepsilon}G_b+S_\varepsilon$$

$$C_1=\max\left[0.43,\frac{\eta}{\eta+5}\right] \qquad \eta=S\frac{k}{\varepsilon} \qquad S=\sqrt{2S_{ij}S_{ij}} \qquad G_k=\mu_t S^2$$

$$G_b=\beta g_i\frac{\mu_t}{\mathrm{Pr}_t}\frac{\partial T}{\partial x_i} \qquad \beta=-\frac{1}{\rho}\left(\frac{\partial \rho}{\partial T}\right)_p \qquad C_{3\varepsilon}=\tanh\left|\frac{v}{u}\right|$$

$$C_{1\varepsilon}=1.44 \quad C_2=1.9 \quad \sigma_k=1.0 \quad \sigma_\varepsilon=1.2$$

Mohammadi and Pironneau (1994) investigated the k-ε models. They mentioned that the viscous sub-layer and the log-law region should be removed from the computational domain and the log-law should be used as the boundary condition. This idea works only if $20\le\frac{\delta}{y^*}\le 100$ (where $Y^+=\frac{\delta}{y^*}$) and when there is no boundary layer separation.

The k-ε models are valid in fully turbulent (log-law) regions. The log-law for mean velocity is valid for Y^+ > 30-60. In FLUENT, the log-law is employed when Y^+ > 11.225. In order to use finer meshes near the walls, the enhanced wall treatment option in FLUENT should be enabled, in which the viscous sub-layer can be modelled. When the enhanced wall treatment is enabled, Y^+ should be in the order of 1.

The k-ω model

The k-ω model is another popular two-equation turbulence model. It computes the turbulent eddy viscosity as a function of turbulent kinetic energy (k) and the specific

dissipation rate (ω). FLUENT provides the standard k-ω model and the SST k-ω model. The first k-ω model was proposed by Kolmogorov (1942). Since then, different modifications have been offered. The most well-known k-ω model is the Wilcox k-ω model. The advantage of the k-ω model compared with the k-ε model is its ability to model the flow near the walls, and its success in modelling flows with moderate adverse pressure gradients (Menter, 1994). However, the standard k-ω model has limitations for flows with pressure-induced separation. These limitations have been eliminated in the SST k-ω model, which predicts flows with strong adverse pressure gradients and separation (Menter *et.al*., 2003).

The standard k-ω model in FLUENT is based on the model proposed by Wilcox (1998). It computes the eddy viscosity as a function of turbulent kinetic energy (k) and the specific dissipation rate (ω), which itself can be thought of as the ratio of ε to k.

Wilcox described his model using the following equations (Wilcox, 2006):

Kinematic Eddy Viscosity:

$$\nu_T = \frac{k}{\tilde{\omega}}, \qquad \tilde{\omega} = \max\left\{\omega, C_{\lim}\sqrt{\frac{2S_{ij}S_{ij}}{\beta^*}}\right\}, \qquad C_{\lim} = \frac{7}{8}$$

Turbulence Kinetic Energy:

$$\frac{\partial k}{\partial t} + U_j \frac{\partial k}{\partial x_j} = \tau_{ij}\frac{\partial U_i}{\partial x_j} - \beta^* k\,\omega + \frac{\partial}{\partial x_j}\left[\left(\nu + \sigma^*\frac{k}{\omega}\right)\frac{\partial k}{\partial x_j}\right] \qquad \text{A2.8}$$

Specific Dissipation Rate:

$$\frac{\partial \omega}{\partial t} + U_j \frac{\partial \omega}{\partial x_j} = \alpha\frac{\omega}{k}\tau_{ij}\frac{\partial U_i}{\partial x_j} - \beta\omega^2 + \frac{\sigma_d}{\omega}\frac{\partial k}{\partial x_j}\frac{\partial \omega}{\partial x_j} + \frac{\partial}{\partial x_j}\left[\left(\nu + \sigma\frac{k}{\omega}\right)\frac{\partial \omega}{\partial x_j}\right] \qquad \text{A2.9}$$

Closure Coefficients and Auxiliary Relations:

$$\alpha = \frac{13}{25}, \quad \beta = \beta_\omega f_\beta, \quad \beta^* = \frac{9}{100}, \quad \sigma = \frac{1}{2}, \quad \sigma^* = \frac{3}{5}, \quad \sigma_{do} = \frac{1}{8}$$

$$\sigma_d = \begin{cases} 0, \dfrac{\partial k}{\partial x_j}\dfrac{\partial \omega}{\partial x_j} \le 0 \\ \sigma_{do}, \dfrac{\partial k}{\partial x_j}\dfrac{\partial \omega}{\partial x_j} \rangle 0 \end{cases}$$

$$\beta_o = 0.0708, \qquad f_\beta = \frac{1+85\chi_\omega}{1+100\chi_\omega}, \qquad \chi_\omega \equiv \left| \frac{\Omega_{ij}\Omega_{jk}S_{ki}}{(\beta^*\omega)^3} \right|$$

$$\varepsilon = \beta^*\omega k \qquad \text{and} \qquad \ell = \frac{k^{\frac{1}{2}}}{\omega}$$

$$\Omega_{ij} = \frac{1}{2}\left(\frac{\partial U_i}{\partial x_j} - \frac{\partial U_j}{\partial x_i} \right), \qquad S_{ij} = \frac{1}{2}\left(\frac{\partial U_i}{\partial x_j} + \frac{\partial U_j}{\partial x_i} \right)$$

Another version of the k-ω model is the shear stress transport (SST) k-ω model, which was developed by Menter (1994) and was originally used for aeronautics applications. This model has a modification to account for the principal turbulent shear stress in the eddy viscosity equation. It blends the standard k-ω model with the k-ε model so that the k-ω model will be activated near the walls and will be put to zero far from the walls, while activating the k-ε model.

Considering the limitations of the Boussinesq approximation, Mentor and Smirnov (2009) modified the SST model with the rotation-curvature correction (CC), and validated it for a wide range of turbulent flows.

Wilcox (2006) investigated the influence of a solid surface on flow behaviour. He described different numerical considerations for his turbulence model, and mentioned that “quantities such as the dissipation rate, ε, and specific dissipation rate, ω, grow so rapidly approaching a solid boundary that they appear to be singular. In fact, ω is singular for a perfectly-smooth wall. Also, at interfaces between turbulent and nonturbulent regions, velocity and other properties have nearly discontinuous slopes approaching the interface. Because wall-bounded flows typically involve both types of

boundaries, accurate numerical solutions must account for the spatial problems presented by this unusual solution behaviour".

For the k-ω turbulence model, the exact solution of the ω equation in the viscous sub-layer is given by Wilcox (2006). As he stated, this equation should be used for the first seven to ten grid points above the surface, where the wall Y^+ should lie below $Y^+ = 2.5$ (Wilcox, 2006).

In FLUENT, the Y^+ criteria for k-ω models (standard and SST) are the same as those of the k-ε models when the enhanced wall treatment is enabled.

$$\frac{\partial}{\partial t}(\rho k) + \frac{\partial}{\partial x_i}(\rho k u_i) = \frac{\partial}{\partial x_j}(\Gamma_k \frac{\partial k}{\partial x_j}) + \widetilde{G}_k - Y_k + S_k \qquad \text{A2.10}$$

$$\frac{\partial}{\partial t}(\rho \omega) + \frac{\partial}{\partial x_i}(\rho \omega u_i) = \frac{\partial}{\partial x_j}(\Gamma_w \frac{\partial \omega}{\partial x_j}) + G_\omega - Y_\omega + D_\omega + S_\omega \qquad \text{A2.11}$$

$$\Gamma_k = \mu + \frac{\mu_t}{\sigma_k} \qquad \Gamma_\omega = \mu + \frac{\mu_t}{\sigma_\omega} \qquad \mu_t = \frac{\rho k}{\omega} \frac{1}{\max\left[\frac{1}{\alpha^*}, \frac{SF_2}{\alpha_1 \omega}\right]}$$

$$\sigma_k = \frac{1}{\frac{F_1}{\sigma_{k,1}} + \frac{(1-F_1)}{\sigma_{k,2}}} \qquad \sigma_\omega = \frac{1}{\frac{F_1}{\sigma_{\omega,1}} + \frac{(1-F_1)}{\sigma_{\omega,2}}}$$

$$F_1 = \tanh(\Phi^4) \qquad \Phi_1 = \min\left[\max\left(\frac{\sqrt{k}}{0.09\omega y}, \frac{500\mu}{\rho y^2 \omega}\right), \frac{4\rho k}{\sigma_{\omega,2} D_\omega^{+} y^2}\right]$$

$$D_\omega^{+} = \max\left[2\rho \frac{1}{\sigma_{\omega,2}} \frac{1}{\omega} \frac{\partial k}{\partial x_j} \frac{\partial \omega}{\partial x_j}, 10^{-10}\right] \qquad F_2 = \tanh(\Phi_2^{\,2})$$

$$\Phi_2 = \max\left[2\frac{\sqrt{k}}{0.09\omega y}, \frac{500\mu}{\rho y^2 \omega}\right] \qquad \widetilde{G}_k = \min(G_k, 10\rho\beta^* k\omega)$$

$$G_\omega = \frac{\alpha}{\nu_t}\widetilde{G}_k \qquad Y_k = \rho\beta\omega^2 \qquad D_\omega = 2(1-F_1)\rho\sigma_{\omega,2} \frac{1}{\omega} \frac{\partial k}{\partial x_j} \frac{\partial \omega}{\partial x_j}$$

$\sigma_{k,1} = 1.176$ $\sigma_{\omega,1} = 2.0$ $\sigma_{k,2} = 1.0$ $\sigma_{\omega,2} = 1.168$ $a_1 = 0.31$ $\beta_{i,1} = 0.075$

$\beta_{i,2} = 0.0828$

All additional model constants have the same values as the standard k-ω model.

The Reynolds stress model (RSM)

The alternative approach to the Boussinesq eddy viscosity approximation is the RSM, which solves each of the terms in the Reynolds stress tensor and suggests an equation for determining the scale of turbulence (usually for ε). Therefore, it generates seven additional equations in 3D, and five additional equations in 2D.

ANSYS FLUENT provides three options for modelling the pressure-strain term in the RSM, which are the linear pressure-strain model, the quadratic pressure-strain model, and the low-Re stress-Omega model.

The quadratic pressure-strain model has the advantage of good predictions for shear flows, and flows with streamlined curvature. The low-Re stress-Omega model is based on the omega equation and LRR, which has a good performance in flows over curved surfaces and swirling flows. It is similar to the k-ω model and can predict a wide range of turbulent flows very well. The exact transport equation of RSM is as follows:

$$\frac{\partial}{\partial t}(\rho\overline{u_i' u_j'}) + \underbrace{\frac{\partial}{\partial x_k}(\rho u_k \overline{u_i' u_j'})}_{C_{ij}} = \underbrace{\frac{\partial}{\partial x_k}\left[\mu\frac{\partial}{\partial x_k}(\overline{u_i' u_j'})\right]}_{D_{L,ij}} - \underbrace{\frac{\partial}{\partial x_k}\left[\rho\overline{u_i' u_j' u_k'} + \overline{p(\delta_{kj}u_i' + \delta_{ik}u_j')}\right]}_{D_{T,ij}}$$

$$\underbrace{-\rho\left(\overline{u_i' u_j'}\frac{\partial u_j}{\partial x_k} + \overline{u_j' u_k'}\frac{\partial u_i}{\partial x_k}\right)}_{P_{ij}} \underbrace{-\rho\beta\left(g_i\overline{u_j'\theta} + g_j\overline{u_i'\theta}\right)}_{G_{ij}} + \underbrace{\overline{p\left(\frac{\partial u_i'}{\partial x_j} + \frac{\partial u_j'}{\partial x_i}\right)}}_{\phi_{ij}} \underbrace{-2\mu\overline{\frac{\partial u_i'}{\partial x_k}\frac{\partial u_j'}{\partial x_k}}}_{\varepsilon_{ij}}$$

$$\underbrace{-2\rho\Omega_k(\overline{u_i' u_m'}\varepsilon_{ikm} + \overline{u_i' u_m'}\varepsilon_{jkm})}_{F_{ij}} \qquad \text{A2.12}$$

While the terms $D_{T,ij}$, G_{ij}, ϕ_{ij} and ε_{ij} need to be modelled, the terms C_{ij}, $D_{L,ij}$, P_{ij} and F_{ij} do not require any modelling.

$$D_{T,ij} = \frac{\partial}{\partial x_k}\left[\frac{\mu_t}{\sigma_k}\frac{\partial \overline{u_i u_j}}{\partial x_k}\right] \qquad G_{ij} = \beta\frac{\mu_t}{\mathrm{Pr}_t}\left(g_i\frac{\partial T}{\partial x_j} + g_j\frac{\partial T}{\partial x_i}\right)$$

$$\phi_{ij} = \phi_{ij,1} + \phi_{ij,2} + \phi_{w,ij} \qquad \phi_{ij,1} = -C_1\rho\frac{\varepsilon}{k}\left[\overline{u_i u_j} - \frac{2}{3}\delta_{ij}k\right]$$

$$\phi_{ij,2} = -C_2\left[(P_{ij} + F_{ij} + \frac{5}{6}G_{ij} - C_{ij}) - \frac{1}{3}\delta_{ij}(p_{kk} + G_{kk} - C_{kk})\right]$$

$$\phi_{w,ij} = C_1{}'\frac{\varepsilon}{k}\left(\overline{u_k u_m}n_k n_m\delta_{ij} - \frac{3}{2}\overline{u_i u_k}n_j n_k - \frac{3}{2}\overline{u_j u_k}n_i n_k\right)\frac{k^{\frac{3}{2}}}{C_l\varepsilon d} +$$

$$C_2{}'\left(\phi_{km,2}n_k n_m\delta_{ij} - \frac{3}{2}\phi_{ik,2}n_j n_k - \frac{3}{2}\phi_{jk,2}n_i n_k\right)\frac{k^{\frac{3}{2}}}{C_l\varepsilon d}$$

$$C_l = \frac{C_\mu{}^{\frac{3}{4}}}{\kappa} \quad C_1 = 1.8 \quad C_2 = 0.6 \quad C_1{}' = 0.5 \quad C_2{}' = 0.3 \quad C_\mu = 0.09 \quad \kappa = 0.4187$$

$$\varepsilon_{ij} = -2\mu\overline{\frac{\partial u_i}{\partial x_k}\frac{\partial u_j}{\partial x_k}}$$

Filtering

Filtering is another general method for solving Navier Stokes equations, which has not been used as widely as the RANS method in engineering applications. The basis of the method is to filter all turbulent eddies which are smaller than the filter size, using either Fourier (wave-number) space or configuration (physical) space in time-dependent Navier Stokes equations. The filter works similarly to the averaging process and separates the resolvable scales from the sub-grid scale (Wilcox, 2006). This method is

used in the large eddy simulation (LES), in which large eddies are computed and the smallest, sub-grid scale (SGS) eddies are modelled (Wilcox, 2006).

There is another method called detached eddy simulation (DES), which is a blending of LES and RANS, so that the largest eddies are modelled by LES, while the boundary layers and thin shear layers are handled with RANS (Wilcox, 2006).

Near wall treatment

As mentioned above, the k-ε models, LES and RSM are not applicable in viscosity-affected near wall regions. Therefore, it is necessary to bridge the viscous region by using semi-empirical formulae called wall functions. The near-wall region is divided into three zones, as follows:

- Viscous or laminar sub-layer (y+ < 5)
- Buffer layer (5 < y+ < 30)
- Fully turbulent or log-law region (y+ > 30 to 60)

The dimensionless wall distance, y^+, is an important parameter for resolving the boundary layer in a numerical simulation.

$$y^+ = \frac{y u_\tau \rho}{\mu} \qquad \text{A2.13}$$

$$u_\tau = \sqrt{\frac{\tau_w}{\rho}} \qquad \text{A2.14}$$

Where u_τ is the friction velocity, y is the actual distance from the wall and τ_w is the shear stress (based on the velocity gradient in the direction normal to the surface of the wall) at the wall.

The position of the first cell near the walls depends on whether it is desirable that the calculations cover the laminar sub-layer or be started from the turbulent core. The near

wall region can be modelled using two approaches. In the first approach, the laminar sub-layer is modelled using a semi-empirical formula called wall function, which bridges the wall to the fully turbulent region. The wall functions provided in FLUENT, depending on the turbulence model selected, are: standard wall function and non-equilibrium wall function. In the second approach, turbulence models are modified so that they can model the laminar sub-layer region. In the second approach, enhanced wall treatment is used for near wall modelling.

The standard wall function in FLUENT is based on the model suggested by Launder and Spalding (1974) which uses the logarithmic law-of-the-wall for modelling the mean velocity, and a similar logarithmic law for modelling the temperature. The standard wall function assumes constant shear stress and local equilibrium hypotheses for modelling the flow. Hence, it is not reliable to model the near wall region when there are severe pressure gradients and when the flows are in strong non-equilibrium. The effects of pressure gradient and non-equilibrium conditions are included in the non-equilibrium wall functions. However, the applicability of the wall function approach remains limited due to the ideal conditions underlying the wall functions. These conditions include severe pressure gradients leading to boundary layer separation, strong body forces, and high three-dimensional flows near the walls. In such situations, enhanced wall treatment should be used for modelling the near wall region, which combines a two-layer model with enhanced wall functions. Since the viscosity-affected region is modelled by the enhanced wall treatment, the quality of the meshes near the walls should be fine enough ($y+ < 4$ or 5) (Fluent Inc. 2003).